NTNU
Norwegian University of
Science and Technology

# Analysis and Design of Bjørnefjorden Floating Cable-Stayed Bridge subjected to Large Ship Collisions and Extreme Environmental Loads

**Ida Fagerli Osvoll**

| | |
|---|---|
| Marine Technology | |
| Submission date: | June 2018 |
| Supervisor: | Jørgen Amdahl, IMT |
| Co-supervisor: | Yanyan Sha, IMT |

Norwegian University of Science and Technology
Department of Marine Technology

**MASTER THESIS 2018**

for

Stud. Techn. Ida Fagerli Osvoll

# Analysis and Design of Bjørnefjorden Floating Cable-Stayed Bridge subjected to Large Ship Collisions and Extreme Environmental Loads

*Analyse og dimensjonering Bjørnefjorden flytende skråstagbro utsatt for støt fra store skip og ekstreme miljølaster*

The Norwegian Public Roads Administration (NPRA) is running a project "Ferry free coastal route E39", where suspension bridges, floating bridges or submerged tunnels would be installed across fjords in Western Norway. The straits are up 5 kilometres wide and will call for significant extension of present technology. Several innovative crossing concepts have been proposed. One of them is the combined floating-cable stayed bridge concept.

GLOBAL MARITIME

The bridge has to resist extreme environmental loads and accidental actions with acceptable safety levels. One of the concerns are accidental ship collisions with energies 100-1500 MJ. The proposed concepts cannot be designed adequately using existing methods and design rules. Consequently, advanced scenario-based analyses have to be conducted based on accurate simulation of the governing physical processes.

For crossing of Bjørnefjorden one of the most relevant concept is floating side-anchored - or end-anchored bridge with a cable stayed section in the south end.

The purpose of the project and (later) master thesis work is to perform scenario-based and advanced analysis of ship collision with the bridge and to assess the response of the bridge exposed to extreme environmental loads, both in intact and damaged condition.

.

**Scope of work:**

1. Complete the finite element model of the single deck girder end anchored bridge for USFOS analysis. Special emphasis is placed on obtaining the correct representation of the pontoons with respect to hydrodynamic properties. Describe the modelling principles. Perform eigenvalue analysis and compare with results obtained with alternative software.

2. To further enhance the possibility to get better insight in the fundamental behaviour of the bridge establish simplified models of the bridge girder where the cable stayed section is omitted and the bridge girder/pontoons is uniform over the entire length. It shall be considered to have both a curved and a straight bridge model.

3. Perform introductory studies of ship impacts with the bridge. Discuss the impact impulse with respect to various eigenperiods for the bridge. Ship force-deformation curve obtained form LS_DYNA may be modelled with a nonlinear spring and the ship with a nodal mass with initial velocity. The impulse may, however, be varied beyond the expected range to obtain further insight into the problem. Discuss how shear forces, inertia forces, bending moments etc. in the bridge girder balance the collision force and how the motions travels along the girder. Establish a one degree of freedom model simplified response analysis. Perform a review of literature that may be relevant for analysis of this problem.

4. Describe the environmental conditions and environmental loads that should be considered for this bridge. The spatial and temporal variations of wind and wave loads relevant for extreme response calculations with USFOS shall be discussed and time series be established using alternative software to the extent needed. Prepare scripts to conduct numerous simulations of extreme storm conditions.

5. Perform static analysis of the bridge subjected extreme wave and wind loads. Determine characteristic values for selected load effects and compare the results with respect to structural resistance.

6. Perform time-domain analysis of the bridge subjected stochastic extreme wave and wind loads. It may be considered to start with the uniform curved bridge, before the complete model is used. Calculate extreme response quantities and corresponding utilizations using for example the contour line method. Compare the results with static calculations.

7. Establish a simplified model for USFOS analysis that represents approximately the behaviour of the bridge girder in damaged condition after ship impacts. Perform time-domain residual strength analysis with characteristic environmental loads

.

8. For selected damage condition as concerns girder damage or pontoon flooding, assess the residual strength of the bridge subjected to relevant environmental loads

9. Conclusions and recommendations for further work.

Literature studies of specific topics relevant to the thesis work may be included.

The work scope may prove to be larger than initially anticipated. Subject to approval from the supervisor, topics may be deleted from the list above or reduced in extent.

In the thesis the candidate shall present his personal contribution to the resolution of problems within the scope of the thesis work.

Theories and conclusions should be based on mathematical derivations and/or logic reasoning identifying the various steps in the deduction.

The candidate should utilise the existing possibilities for obtaining relevant literature.

The thesis should be organised in a rational manner to give a clear exposition of results, assessments, and conclusions. The text should be brief and to the point, with a clear language. Telegraphic language should be avoided.

The thesis shall contain the following elements: A text defining the scope, preface, list of contents, summary, main body of thesis, conclusions with recommendations for further work, list of symbols and acronyms, references and (optional) appendices. All figures, tables and equations shall be numerated.

The supervisor may require that the candidate, in an early stage of the work, presents a written plan for the completion of the work. The plan should include a budget for the use of computer and laboratory resources, which will be charged to the department. Overruns shall be reported to the supervisor.

The original contribution of the candidate and material taken from other sources shall be clearly defined. Work from other sources shall be properly referenced using an acknowledged referencing system.

The report shall be submitted in two copies:
- Signed by the candidate
- The text defining the scope included
- In bound volume(s)
- Drawings and/or computer prints which cannot be bound should be organised in a separate folder.

**Supervisor:**
Prof. Jørgen Amdahl

**Co-supervisor:**
Postdoc Yanyan Sha

**Contact person at Entail**: Mads Heiervang

**Deadline:, June 11, 2018**

Trondheim, January 15, 2018

Jørgen Amdahl

# Preface

This master thesis is written as a final part of the Master of Science degree in Marine Technology at the Norwegian University of science and Technology, and is finalized in June 2018. The problem description has been formulated by Professor Jørgen Amdahl.

The topics of this thesis are large ship collisions and extreme environmental loads on the Bjørnafjorden end-anchored floating bridge. Analyses are carried out in USFOS, a nonlinear FEM-tool. A model was prepared during the work with the project thesis, “Prestudy: Analysis and Design of Bjørnafjorden Floating Cable-Stayed Bridge subjected to Large Ship Collisions and Extreme Environmental Loads”. The modelling principles in chapter 4 are taken from the project thesis, but the description of the pontoons has been altered.

The majority of the time has been spent on the ship collision analyses, which proved to be more challenging than initially expected. As a consequence, there has not been enough time to thoroughly consider extreme environmental loads.

I would like to thank my supervisor Professor Jørgen Amdahl, who has contributed with both expertise and enthusiasm. I would also like to thank my co-supervisor Postdoc Yanyan Sha, who has answered all my questions. Finally, I would also like to thank Tore Holmås for all the assistance with USFOS, which has been essential for the project.

Ida Fagerli Osvoll

Ida Fagerli Osvoll
Trondheim, June 2018

# Summary

The objective of this master thesis is to study the global behaviour of the end-anchored floating bridge across the Bjørnafjord when it is subjected to high energy ship collision and extreme environmental loads. The end-anchored floating bridge is one of the proposed concepts for the crossing of the Bjørnafjord, which is a part of of a national project, where the aim is to replace ferries with bridges and undersea tunnels. The end-anchored bridge is curved in the horizontal plane, and has a total length of 5.5 $km$. The bridge is supported by 46 steel pontoons, which are placed with a spacing of 100 $m$ between each. At the south end of the bridge, the bridge girder is elevated in order to serve as a transit channel for ship traffic. This is the cable-stayed section, where the bridge girder is supported by a 230 $m$ tall tower. According to the Norwegian Public Road Administration (NPRA), the crossing of the Bjørnafjord will be the longest floating bridge in the world, and existing design regulations are therefore not applicable. Scenario-based analyses are therefore required in order to predict governing physical processes and to assess the capacity of the bridge to withstand them.

The scope of work for this thesis is structural analysis of global bridge response in the ultimate and accidental limit state. The analyses of the bridge are carried out in USFOS, a computer program for nonlinear structural analysis. During the project thesis, which served as preparatory work for the master thesis, a model of the end-anchored floating bridge was created in USFOS. During the master thesis, the model has been developed further, in order to better represent the hydrodynamic properties of the pontoons. This involves modelling of added mass and drag properties, as well as including rotational waterplane stiffness. An eigenvalue analysis is carried out, and it is found that the fundamental eigenperiod of the bridge is 119.6 $s$, and that the vertical modes in the floating low bridge have periods close to 6 $s$. The results of the eigenvalue analysis coincide well with results obtained in alternative software.

Ship impact is modelled by applying a mass with an initial velocity, connected to the bridge through a nonlinear spring. The spring represents the combined force-deformation curve for the ship and bridge. The design collision energies determined by the NPRA are in the range of 250 to 660 $MJ$. In addition to the design energies, a 1000 $MJ$ collision is studied. Both collisions with pontoons and with the bridge girder are considered. In collisions where the ship strikes the bridge perpendicularly to its longitudinal axis, the impact force is balanced by bending moments in the bridge girder. The maximum bending moment is reached at the collision site, but due to interference between propagating and reflected bending waves, high bending moments can also be reached at the end-supports of the bridge. In the case of a 660 $MJ$ collision with the pontoon closest to the transit channel, the bending moment in the bridge exceeds the capacity, both at the impact site and at the end-supports. When considering lower energy collisions further from the transit channel, the bridge seems to have sufficient strength to survive. However, in collisions between a ship deckhouse and the bridge girder, the bending moment at the collision site is close to the capacity of the undamaged girder. Since local deformations will reduce the capacity of the girder, more thorough analyses are required in order to assess if the bridge can survive these impacts.

The response of the bridge in a 100-year storm is also considered in this thesis. Stochastic wind speed as a function of time is generated in WindSim, while wave loads are calculated in MATLAB and applied as nodal loads. The results indicate that there is an issue with numerical drift in the wave analyses, and it is therefore decided to focus on wind loads. Wind is applied both statically and dynamically. It is found that wind loads are mainly carried by bending moments in the bridge girder. When dynamic effects are accounted for, about one third of the bending capacity is utilized. If wave loads, self-weight and ULS safety factors are also taken into account, the utilization of the girder will be high at the end-supports.

# Norsk samandrag

Målet med denne masteroppgåva er å studere den endeforankra flytebrua over Bjørnafjorden når den er utsatt for skipsstøt og ekstremvér. Den endeforankra flytebrua er eit av forslaga for kryssinga av Bjørnafjorden, som er ein del av prosjektet “Fergefritt E39”. Den endeforankra brua er krumma i det horisontale planet, og har ei total lengde på omlag 5.5 $km$. Brua står på 46 flytande pontongar av stål, som er plassert med 100 $m$ mellomrom. Sørenden av brua er heva, slik at store skip skal kunne passere. Denne delen er utforma som ei strekkstagbru, der brubjelken er støtta av eit 230 $m$ høgt tårn. I følge Statens Vegvesen vil brua verte verdas lengste flytebru, og ekstisterande regelverk er difor ikkje anvendeleg. Det er av den grunn nødvendeg å utføre scenariobaserte analyser for å forstå korleis brua vil oppføre seg, og for å undersøke om den har tilstrekkeleg styrke.

Temaet for denne masteroppgåva er strukturell analyse i bruddgrensetilstanden og ulykkesgrensetilstanden. Analysene av brua er uftørt i USFOS, som er eit dataprogram for ikkjelineær strukturell analyse. I løpet av prosjektoppgåva, som var eit forarbeid til masteroppgåva, vart det laga ein USFOS-modell av den endeforankra flytebrua. I arbeidet med masteroppgåva har modellen vorte vidareutvikla for å betre dei hydrodynamiske eigenskapane til pontongane. Ei eigenverdianalyse av den utbetra modellen viser at den fundamentale eigenperioda til brua er 119.6 $s$, og at dei vertikale modene har perioder på omlag 6 $s$. Resultata av eigenverdianalysa stemmer godt med resultat frå analyser i andre program.

Skipsstøt er simulert ved å sette på ei punktmasse med ei gitt hastigheit, der massa er kopla til brua gjennom ei ikkje-linneær fjør. Fjøra representerar den kombinerte kraftdeformasjonskurva for skipet og brua. Designenergiane som har vorte bestemt av Statens Vegvesen er på mellom 250 og 660 $MJ$. I tilleg til desse energiane er ein 1000 $MJ$ kollisjon studert. Både støt med pontongar og med brubjelken er tatt i betraktning. I støt der skipet treff brua perpendikulært til den langsgåande aksen, vil bøyemomentet om den sterke aksen til brubjelken vere den kritiske responsen. Det største momentet oppstår der skipet treff brua, men på grunn av bøyebølger vil momentet også verte høgt ved endeforankringane. Ved ein kollisjon på 660 $MJ$ med pontongen nærmast sørenden av brua, vil bøyemomentet i bjelken overstige kapastiteten. Dei mest kritiske områda er kollisjonsstaden og endeforankringane. Dersom ein ser på mindre støt lengre frå skråstagbrua, verkar det som brua har tilstrekkelig styrke. Samtidig, dersom ein ser på støt mellom skip og brubjelken, ser ein at reaksjonskreftene er nærme kapasiteten til det uskada tverrsnittet. Ettersom lokale deformasjonar truleg vil redusere styrka til brubjelken, er det nødvendig med grundigere analyser der dette er tatt hensyn til.

Responsen til brua når den er utsatt for ein hundreårsstorm er også undersøkt i denne oppgåva. Stokastisk vindhastigheit er generert i WindSim, mens bølgjelaster er utrekna i MATLAB og påsatt som punktlastar. Resultata avdekkjer numerisk drift i analysene, og det er difor valgt å fokusere på vindlastar. Både statisk og dynamisk vind er betrakta. Resultata frå analysene viser at vind hovudsakeleg er tatt opp av bøyemoment i brubjelken. Omtrent ein tredjedel av bøyekapasiteten er utnytta når dynamiske effekter er tatt høgde for. Dersom ein inkluderar bølgjelastar, eigenvekt og sikkerheitsfaktorar, vil utnyttelsen av kapasiten vere høg.

# Contents

**List of Figures** **xi**

**List of Tables** **xviii**

**List Of Symbols And Abbreviations** **xxi**
List Of Symbols And Abbreviations . . . . . . . . . . . . . . . . . . . . . . . . . xxi

**1 Introduction** **1**
1.1 Background . . . . . . . . . . . . . . . . . . . . . . . . . . . . . . . 1
1.2 Objective . . . . . . . . . . . . . . . . . . . . . . . . . . . . . . . . 2
1.3 Scope and limitations . . . . . . . . . . . . . . . . . . . . . . . . . 3

**2 Literature Review** **5**
2.1 Single degree of freedom modelling of ship collision . . . . . . . . . . 5
2.2 Impact on long beams . . . . . . . . . . . . . . . . . . . . . . . . . 6
2.2.1 Reflection of elastic flexural waves in simply supported beam . . . . . 6
2.2.2 Flexural waves in thin rods . . . . . . . . . . . . . . . . . . . . . 7
2.2.3 Travelling plastic hinges . . . . . . . . . . . . . . . . . . . . . . . 9

**3 Theory** **11**
3.1 Definition of limit states . . . . . . . . . . . . . . . . . . . . . . . . 11
3.2 Definition of the eigenvalue problem . . . . . . . . . . . . . . . . . . 12
3.2.1 Rayleigh-damping . . . . . . . . . . . . . . . . . . . . . . . . . . 14
3.2.2 Short impulse model . . . . . . . . . . . . . . . . . . . . . . . . . 15
3.3 Buckling of curved beams . . . . . . . . . . . . . . . . . . . . . . . 16
3.4 Ship collision . . . . . . . . . . . . . . . . . . . . . . . . . . . . . . 17
3.4.1 Terms and design principles . . . . . . . . . . . . . . . . . . . . . 17
3.4.2 Collision mechanics . . . . . . . . . . . . . . . . . . . . . . . . . 19
3.4.3 Current codes and regulations on determining design loads . . . . . . 20
3.5 Environmental loads . . . . . . . . . . . . . . . . . . . . . . . . . . 21
3.5.1 Wave theory . . . . . . . . . . . . . . . . . . . . . . . . . . . . . 21
3.5.2 Linear wave theory . . . . . . . . . . . . . . . . . . . . . . . . . . 22
3.5.3 Difference-frequency effects . . . . . . . . . . . . . . . . . . . . . 24
3.5.4 JONSWAP spectrum . . . . . . . . . . . . . . . . . . . . . . . . . 25
3.5.5 Predicting extreme wave loads . . . . . . . . . . . . . . . . . . . . 26

3.5.6 The contour line method . . . . . . . . . . . . . . . . . . . . . . . . . 27
3.5.7 Distribution of the largest wave height and response . . . . . . . . . . 28
3.5.8 Wind theory . . . . . . . . . . . . . . . . . . . . . . . . . . . . . . . . 29

**4 Modelling of the Bridge in USFOS 31**
4.1 Description of bridge design . . . . . . . . . . . . . . . . . . . . . . . . . 31
4.2 Modelling of the bridge girder . . . . . . . . . . . . . . . . . . . . . . . . 33
4.3 Modelling of the cable tower . . . . . . . . . . . . . . . . . . . . . . . . . 36
4.4 Modelling of the stay-cables . . . . . . . . . . . . . . . . . . . . . . . . . 38
4.5 Modelling of the columns . . . . . . . . . . . . . . . . . . . . . . . . . . . 40
4.6 Modelling of the pontoons . . . . . . . . . . . . . . . . . . . . . . . . . . 41
4.7 Modelling of wind parameters . . . . . . . . . . . . . . . . . . . . . . . . 46
4.8 Eigenvalue analysis . . . . . . . . . . . . . . . . . . . . . . . . . . . . . . 46
4.8.1 Method . . . . . . . . . . . . . . . . . . . . . . . . . . . . . . . . . . . 47
4.8.2 Results . . . . . . . . . . . . . . . . . . . . . . . . . . . . . . . . . . . 47
4.8.3 Comparison to eigenperiods obtained in alternative software . . . . . 49
4.8.4 Discussion of eigenvalue analysis . . . . . . . . . . . . . . . . . . . . . 50
4.8.5 Simple control of modes with vertical motions in the floating low bridge 50
4.9 Structural damping . . . . . . . . . . . . . . . . . . . . . . . . . . . . . . 53

**5 Applicability of Plastic Hinge Theory on Ship Collision 55**
5.1 Method for comparing theory to results from USFOS-analysis . . . . . . . . 55
5.2 Results and discussion . . . . . . . . . . . . . . . . . . . . . . . . . . . . 56
5.3 Relevance of model with respect to ship collision analysis . . . . . . . . . . 59

**6 Analysis of Ship Collision 61**
6.1 Design Ship . . . . . . . . . . . . . . . . . . . . . . . . . . . . . . . . . . 61
6.2 Modelling of ship collision in USFOS . . . . . . . . . . . . . . . . . . . . . 62
6.2.1 Added mass and structural damping . . . . . . . . . . . . . . . . . . . 63
6.2.2 Pontoon collision . . . . . . . . . . . . . . . . . . . . . . . . . . . . . . 64
6.2.3 Girder collision . . . . . . . . . . . . . . . . . . . . . . . . . . . . . . . 66
6.3 Results and discussion of pontoon collision analyses . . . . . . . . . . . . . 68
6.3.1 Local deformations caused by pontoon collision . . . . . . . . . . . . . 69
6.3.2 Description of impact load as a function of time . . . . . . . . . . . . 72
6.3.3 Critical bridge regions in case of pontoon collision . . . . . . . . . . . 74
6.3.4 Global motions of bridge after impact . . . . . . . . . . . . . . . . . . 78
6.3.5 Single degree of freedom model for ship impact at midspan . . . . . . 82
6.3.6 Study of flexural wave propagation after impact . . . . . . . . . . . . 83
6.3.7 Collision analysis with new pontoon design . . . . . . . . . . . . . . . 86
6.4 Results and discussion of deckhouse-girder collision analyses . . . . . . . . 90
6.5 Analysis of bridge with flooded pontoon compartments . . . . . . . . . . . 93
6.5.1 Method for modelling flooding of compartments . . . . . . . . . . . . 93
6.5.2 Results and discussion of analysis with flooded compartments . . . . 94
6.6 Limitations of ship collision modelling . . . . . . . . . . . . . . . . . . . . 95

**7 Analysis of the Bridge Exposed to Extreme Environmental Loads 97**
7.1 Description of environmental conditions at the Bjørnafjord . . . 97
7.1.1 Combination of load cases in the ultimate limit state . . . 97
7.1.2 Wind generated waves . . . 98
7.1.3 Swell . . . 99
7.1.4 Wind . . . 99
7.2 Modelling of wave loads . . . 99
7.2.1 Wave spectrum . . . 100
7.2.2 Linear transfer functions . . . 101
7.2.3 Linear wave forces . . . 102
7.2.4 Mean drift coefficients . . . 104
7.2.5 Nonlinear wave loads . . . 107
7.3 Modelling of wind loads . . . 109
7.4 Studied combinations of environmental loads . . . 112
7.5 Wave analyses considering 100-year sea states . . . 113
7.5.1 Determining worst sea state based on static analysis . . . 113
7.5.2 Mean drift in time domain analyses caused by numerical issues . . . 116
7.5.3 Dynamic analysis of long crested wind sea and swell from northwest . 118
7.5.4 Relative importance of swell . . . 121
7.5.5 Relative importance of difference-frequency forces . . . 121
7.6 Wind analyses considering 100-year storms . . . 123
7.6.1 Static analysis of wind loads . . . 123
7.6.2 Time domain analysis of wind loads . . . 124
7.6.3 Utilization of bridge girder at locations damaged by ship collision . . 126
7.6.4 Comparison of static and stochastic wind analyses . . . 127
7.7 Combined environmental load analysis . . . 129
7.8 Discussion of environmental load analyses . . . 129

**8 Conclusions 131**

**9 Recommendations for Further Work 133**

**Appendices**

**A Modelling of the Bridge I**
A.1 Cable properties . . . II
A.2 Added mass for pontoons . . . III

**B Eigenmodes V**
B.1 Illustrations of a selection of eigenmodes . . . V
B.2 Eigenmodes found in USFOS . . . VII
B.3 Eigenmodes from USFOS analysis compared to results obtained with alternative software . . . IX

**C Ship Collision XI**

C.1 Force-deformation curves . . . . . . . . . . . . . . . . . . . . . . . . . . . . . XI
C.1.1 Pontoon collision . . . . . . . . . . . . . . . . . . . . . . . . . . . . . XI
C.1.2 Pontoon collision - new pontoon design . . . . . . . . . . . . . . . . . . XIV
C.1.3 Alternative extrapolations of the force-deformation curves for the new pontoon design . . . . . . . . . . . . . . . . . . . . . . . . . . . . . XV
C.1.4 Girder collision . . . . . . . . . . . . . . . . . . . . . . . . . . . . . XVI
C.2 Force history plots . . . . . . . . . . . . . . . . . . . . . . . . . . . . . . XVII
C.2.1 Pontoon collision . . . . . . . . . . . . . . . . . . . . . . . . . . . . . XVII
C.2.2 Pontoon collision - new pontoon design . . . . . . . . . . . . . . . . . . XVIII
C.2.3 Girder collision . . . . . . . . . . . . . . . . . . . . . . . . . . . . . XIX
C.3 Bending waves in the floating high bridge . . . . . . . . . . . . . . . . . . . XX

**D Wave Loads on Pontoons** **XXV**
D.1 Comparison of linear transfer functions obtained with different mesh sizes . . XXV
D.2 Linear transfer functions for a selection of heading angles . . . . . . . . . . . XXVI
D.3 Mean drift coefficients . . . . . . . . . . . . . . . . . . . . . . . . . . . . . XXVII
D.4 Force spectra . . . . . . . . . . . . . . . . . . . . . . . . . . . . . . . . . XXXI

**E Example of Wave Forces on a Single Pontoon** **XXXIII**

# List of Figures

1.1 USFOS-model of the end-achored floating bridge. . . . . . . . . . . . . . . . 2

2.1 Illustration of the simplified interaction model described by W. Fan. $P_s$ is the load level, $a$ is the deformation, $m_v$ is the vessel mass and $dm_v$ is the hydrodynamic added mass. From: (Fan et al., 2011) . . . . . . . . . . . . . 6
2.2 Moment diagrams for the first two phases in the transient beam behaviour described by Yu et al. From: (Yu et al., 1996) . . . . . . . . . . . . . . . . . . 7
2.3 Propagation of bending waves in infinite beam subjected to initial disturbance. Results given by the solid line. From: (Graff, 1975) . . . . . . . . . . . . . . 8
2.4 Yield criterion applied in the theory presented by Jones. . . . . . . . . . . . 9
2.5 (a) Illustration of a mass $G$ with initial velocity $V_0$ hitting a long beam. (b) Illustration of the velocity profile of the beam in the first phase of motion, $0 \leq t \leq T_1$. (c) Illustration of the velocity profile of the beam in the second phase of motion, $t \geq T_1$. . . . . . . . . . . . . . . . . . . . . . . . . . . . 10

3.1 Combinations of environmental loads in both the ultimate and the accidental limit states. From: (NORSOK, 2007). . . . . . . . . . . . . . . . . . . . . . . 12
3.2 Damping ratio as a function of eigenfrequency for Rayleigh-damping. From: (Langen and Sigbjörnsson, 1979) . . . . . . . . . . . . . . . . . . . . . . . 15
3.3 Illustration of the snap-through phenomenon. . . . . . . . . . . . . . . . . . 17
3.4 Load-deformation curve for a simple truss-model. From: (Moan, 2003) . . . 17
3.5 Design principles for dissipation of energy in ship collisions. From: (NORSOK, 2004) . . . . . . . . . . . . . . . . . . . . . . . . . . . . . . . . . . . . . . 18
3.6 Example of a combined load-deformation curve for a ship and an installation. The total dissipated strain energy for the given load level is equal to the grey area below the curves. From: (NORSOK, 2004) . . . . . . . . . . . . . . . . 20
3.7 Illustration of folding about the Nyquist frequency. From: (Lehn, 2009) . . . 23
3.8 Example of contour lines. From: (Haver, 2017) . . . . . . . . . . . . . . . . . 28

4.1 USFOS-model of the bridge seen from the south end. . . . . . . . . . . . . . 31
4.2 Orientation of the bridge as seen from above. The arrow indicates geographic north. From: (Norconsult AS, 2017a) . . . . . . . . . . . . . . . . . . . . . . 32
4.3 General cross section of the bridge girder. From: (Norconsult AS, 2017a) . . 33
4.4 Figures of the cable-tower. . . . . . . . . . . . . . . . . . . . . . . . . . . . 37

4.5 Bending moment about the strong axis of the bridge girder at the south end of the bridge due to pretension in the stay-cables. . . . . . . . . . . . . . . . 39
4.6 Geometry and local coordinate system for the pontoons. . . . . . . . . . . . 42
4.7 Connection points for the spring to ground elements attached to the pontoons. 42
4.8 Nonlinear spring applied for modelling buoyancy. Equilibrium position indicated with orange circle. . . . . . . . . . . . . . . . . . . . . . . . . . . . . 43
4.9 Illustration of eigenmode 2. . . . . . . . . . . . . . . . . . . . . . . . . . . 49
4.10 Illustration of eigenmode 13. . . . . . . . . . . . . . . . . . . . . . . . . . 49
4.11 Repetitive component in the floating low bridge. . . . . . . . . . . . . . . . 51
4.12 Illustration of the mode applied when determining the maximum eigenperiod in heave. The bridge is seen from the side. . . . . . . . . . . . . . . . . . . . 51
4.13 Illustration of the mode applied when determining the minimum eigenperiod in heave. The bridge is seen from the side. . . . . . . . . . . . . . . . . . . . 52
4.14 Illustration of eigenmode 97. . . . . . . . . . . . . . . . . . . . . . . . . . 53
4.15 Applied damping ratio for structural damping. . . . . . . . . . . . . . . . . 54

5.1 Illustration of the deformations and plastic utilization of the straight bridge model after impact. The deformations are scaled by a factor of 5. . . . . . . 57
5.2 Position of travelling hinge found in USFOS compared to theoretical solution by Jones. Position given by distance from impact point. . . . . . . . . . . . 58

6.1 Illustration of the general spring configuration for modelling ship collision. . 63
6.2 Position of the three pontoons subjected to ship collision, and the direction of the impacts. . . . . . . . . . . . . . . . . . . . . . . . . . . . . . . . . . . 64
6.3 Impact points between ship bow and pontoon. The illustrations are screenshots from LSDYNA, obtained from Postdoc Yanyan Sha. . . . . . . . . . . 65
6.4 Spring configuration for the ship-pontoon impact, here for a head-on collision. For illustrative purposes, the connection element is shortened. . . . . . . . 65
6.5 Applied force-deformation curve versus the curve found in LSDYNA for the head-on collision between the container vessel and pontoon 1. . . . . . . . 66
6.6 Position of the two areas subjected to girder impact, and the direction of the impacts. . . . . . . . . . . . . . . . . . . . . . . . . . . . . . . . . . . . . 66
6.7 Force-deformation curve for deckhouse-girder collision. . . . . . . . . . . . 67
6.8 Measured force-deformation relationship in collision springs compared to curve from LSDYNA. Collision scenario 2. . . . . . . . . . . . . . . . . . . . . . . 69
6.9 Force-deformation curves obtained in the 660 $MJ$ head-on collision and the 400 $MJ$ perpendicular collision. The forces in the bulb-spring and forecastle-spring are added together in the figure. . . . . . . . . . . . . . . . . . . . . 71
6.10 Measured force-deformation relationship in collision springs compared to curve from LSDYNA. Collision scenario 3. . . . . . . . . . . . . . . . . . . . . . . 72
6.11 Axial force in the collision springs as a function of time. . . . . . . . . . . . 72
6.12 Velocity of the ship mass as a function of time. Collision scenario 2. . . . . . 73
6.13 Position of the struck pontoon in the direction of the impact, i.e. in the global y-direction, plotted along with the impact force. Collision scenario 5. . . . . 74
6.14 Accumulated plastic work as a function of time. Collision scenario 2. . . . . 75

6.15 Torsional moment in column between pontoon 1 and bridge girder. Collision scenario 3. . . . . . . . . . . . . . . . . . . . . . . . . . . . . . . . . . . 77
6.16 Bridge deformations caused by collision scenario 1. The deformations are scaled by a factor of 10. The disturbance at the struck pontoon are the collision springs and connection elements, and can be ignored. . . . . . . . . . . . . 78
6.17 Displacement of the struck pontoon in the global y-direction caused by collision scenario 2. . . . . . . . . . . . . . . . . . . . . . . . . . . . . . . . . . . 79
6.18 Torsion in high bridge caused by collision scenario 1 at time 9.3 $s$. The deformations are scaled by a factor of 10. . . . . . . . . . . . . . . . . . . . . . . 79
6.19 Bridge deformations caused by collision scenario 3. The deformations are scaled by a factor of 15. . . . . . . . . . . . . . . . . . . . . . . . . . . . 80
6.20 Bridge deformations caused by collision scenario 5. The deformations are scaled by a factor of 15. . . . . . . . . . . . . . . . . . . . . . . . . . . . 81
6.21 Position of the struck pontoon in the direction of the impact, i.e. in the global y-direction. Collision scenario 5. . . . . . . . . . . . . . . . . . . . . . . . . 81
6.22 Axial force in the collision springs as a function of time, collision scenario 5. 82
6.23 Fitted impulse model for the transverse displacement of pontoon 20 after the central pontoon collision. . . . . . . . . . . . . . . . . . . . . . . . . . . . . 83
6.24 Clamped beam subjected to a point load $P$. . . . . . . . . . . . . . . . . . . . 84
6.25 Bending moment in the bridge girder north of pontoon 1. Collision scenario 1, structural damping included. . . . . . . . . . . . . . . . . . . . . . . . . . 84
6.26 Horizontal displacement of the bridge girder in the transverse direction. Collision scenario 1, structural damping included. . . . . . . . . . . . . . . . . . . 86
6.27 Measured force-deformation relationship in collision springs compared to curve from LSDYNA. Collision scenario 2, new pontoon design. . . . . . . . . . . 89
6.28 Impact-force characteristics for collision between deckhouse and girder at location $A$. . . . . . . . . . . . . . . . . . . . . . . . . . . . . . . . . . . . . . 91
6.29 Force histories for the collision springs in deckhouse-girder collision scenarios 2 and 3. . . . . . . . . . . . . . . . . . . . . . . . . . . . . . . . . . . . . . 92
6.30 Drawing of pontoon 1 with numbering of pontoon compartments. From: (Norconsult AS, 2017a) . . . . . . . . . . . . . . . . . . . . . . . . . . . . . . . 93

7.1 Sea states corresponding to a 100 year return period. From: (Norconsult AS, 2017b) . . . . . . . . . . . . . . . . . . . . . . . . . . . . . . . . . . . . . . 98
7.2 Applied coordinate system when describing wave loads. . . . . . . . . . . . 100
7.3 Transfer function on surge with four different mesh sizes for a head-on wave, pontoon 4. . . . . . . . . . . . . . . . . . . . . . . . . . . . . . . . . . . . . . 101
7.4 Linear transfer functions in heave and pitch for all four pontoon types, head-on wave. . . . . . . . . . . . . . . . . . . . . . . . . . . . . . . . . . . . . . . 102
7.5 Linear wave force due to wind sea calculated with $N$=250. . . . . . . . . . . 103
7.6 Selection of mean drift coefficients for pontoon type 4. . . . . . . . . . . . 104
7.7 Mean drift coefficient in surge for four different mesh sizes. The heading angle is 30 degrees. . . . . . . . . . . . . . . . . . . . . . . . . . . . . . . . . . . 105
7.8 Geometry of body in Faltinsen's example. . . . . . . . . . . . . . . . . . . . 106
7.9 Example of slowly varying drift force before and after low-pass filtering. . . . 108

7.10 Example of wave force in 100-year sea state with wind sea from 270° and swell from 330°. Direction of incoming waves defined in figure 7.1. Force history in surge for pontoon 1. Characteristic 1-hour wave load from wind sea indicated by the dashed line. . . . . . . . . . . . . . . . . . . . . . . . . . . . 109
7.11 Kaimal wind spectrum with parameters according to DnV-OS-J10 recommended practice. . . . . . . . . . . . . . . . . . . . . . . . . . . . . . . 110
7.12 Coherence as a function of distance when f = 1/120 $Hz$. . . . . . . . . . . 110
7.13 Mean wind profile for the 100-year storm. . . . . . . . . . . . . . . . . . . 111
7.14 Wind gust speed at a random grid point calculated with a time step of 0.1 $s$. 112
7.15 Deformation of bridge when the characteristic load from wave condition 6 is applied to pontoons 15 to 24. Direction of applied load indicated by the arrows. 115
7.16 Considered directions of wind sea in static and dynamic analyses. . . . . . 115
7.17 Displacement of the midpoint on the bridge girder in the global y-direction when the bridge is subjected to swell sea. . . . . . . . . . . . . . . . . . . 116
7.18 Drift motion of bridge girder when only subjected to swell. Displacement scaled by a factor of 40. . . . . . . . . . . . . . . . . . . . . . . . . . . . 116
7.19 Moment about strong axis of bridge girder at the north anchoring. The bridge is subjected to long-crested swell. . . . . . . . . . . . . . . . . . . . . . 117
7.20 Force at pontoon 21 as a function of time in the case of swell sea from 330°. 117
7.21 Drift motion over a period of 2500 $s$ when the bridge is subjected to linear and nonlinear wave forces from wind sea and swell. The results are scaled by a factor of 1.0. . . . . . . . . . . . . . . . . . . . . . . . . . . . . . . . . 119
7.22 Bending moment at the north end-anchoring when subjected to long-crested wind sea and swell from 330°. . . . . . . . . . . . . . . . . . . . . . . . . 119
7.23 Force at pontoon 7 as a function of time in the case of long-crested wind sea and swell from 330°. . . . . . . . . . . . . . . . . . . . . . . . . . . . . 120
7.24 Vertical displacement of bridge girder plotted as a function of frequency. . . 120
7.25 Displacement in the global y-direction when the bridge is subjected to slowly varying drift forces from 330°. See figure 7.21 for position of node. . . . . . 122
7.26 Considered wind directions in static and dynamic analyses. . . . . . . . . . . 123
7.27 Snapshots of bridge deformation due to stochastic wind. Deformations are scaled by a factor of 20. Bending moment about strong axis is indicated by color. . . . . . . . . . . . . . . . . . . . . . . . . . . . . . . . . . . . . . 125
7.28 Displacement of node 10900 in the global y-direction along with the axial force in the bridge girder. . . . . . . . . . . . . . . . . . . . . . . . . . . . . . 126
7.29 Displacement of the bridge girder at midspan in the global y-direction. The results are based on a 5000 $s$ simulation of wind from 100°. . . . . . . . . . 128

A.1 Added mass in surge as a function of oscillation period. WAMIT30 is the smallest pontoon, WAMIT33 is the largest pontoon. From: (Norconsult AS, 2017f). . . . . . . . . . . . . . . . . . . . . . . . . . . . . . . . . . . . . . III
A.2 Added mass in sway as a function of oscillation period. WAMIT30 is the smallest pontoon, WAMIT33 is the largest pontoon. From: (Norconsult AS, 2017f). . . . . . . . . . . . . . . . . . . . . . . . . . . . . . . . . . . . . . III

A.3 Added mass in heave as a function of oscillation period. WAMIT30 is the smallest pontoon, WAMIT33 is the largest pontoon. From: (Norconsult AS, 2017f). . . . . IV

B.1 Illustration of eigenmode 1. . . . . V
B.2 Illustration of eigenmode 4. . . . . V
B.3 Illustration of eigenmode 5. . . . . V
B.4 Illustration of eigenmode 9. . . . . VI
B.5 Illustration of eigenmode 19. . . . . VI
B.6 Illustration of eigenmode 23. . . . . VI
B.7 Illustration of eigenmode 31. . . . . VI
B.8 Illustration of eigenmode 35. . . . . VI

C.1 Measured force-deformation relationship in collision springs compared to curve from LSDYNA. Collision scenario 1. . . . . XI
C.2 Measured force-deformation relationship in collision springs compared to curve from LSDYNA. Collision scenario 2. . . . . XII
C.3 Measured force-deformation relationship in collision springs compared to curve from LSDYNA. Collision scenario 3. . . . . XII
C.4 Measured force-deformation relationship in collision springs compared to curve from LSDYNA. Collision scenario 4. . . . . XIII
C.5 Measured force-deformation relationship in collision springs compared to curve from LSDYNA. Collision scenario 5. . . . . XIII
C.6 Measured force-deformation relationship in collision springs compared to curve from LSDYNA. Collision scenario 2, new pontoon design. . . . . XIV
C.7 Measured force-deformation relationship in collision springs compared to curve from LSDYNA. Collision scenario 2a, new pontoon design. . . . . XIV
C.8 Measured force-deformation relationship in collision springs compared to curve from LSDYNA. Collision scenario 3, new pontoon design. . . . . XV
C.9 Measured force-deformation relationship in collision springs compared to curve from LSDYNA. Collision scenario 2, new pontoon design; flat extrapolation. XV
C.10 Measured force-deformation relationship in collision springs compared to curve from LSDYNA. Collision scenario 2, new pontoon design; steep extrapolation. XVI
C.11 Force-deformation curves for the collisions between deckhouse and girder. . . XVI
C.12 Force histories for the collision springs in USFOS analyses. Pontoon collisions. XVII
C.13 Force histories for the collision springs obtained with USFOS analyses. Pontoon collisions with the new pontoon design. . . . . XVIII
C.14 Force histories for the collision springs obtained with USFOS analyses. Girder collisions. . . . . XIX
C.15 Bending moment in the bridge girder at the north side of the impact point, time interval 1. Collision scenario 1, structural damping included. . . . . XX
C.16 Bending moment in the bridge girder at the north side of the impact point, time interval 2. Collision scenario 1, structural damping included. . . . . XXI
C.17 Bending moment in the bridge girder at the north side of the impact point. Collision scenario 1, structural damping NOT included. . . . . XXII

C.18 Bending moment about the strong axis of the bridge girder, given as a function of time at a selection of locations. Position given by distance from the struck pontoon. . . . . . . . . . . . . . . . . . . . . . . . . . . . . . . . . . . . . XXIII

D.1 Non-zero transfer functions for a head-on wave with four different mesh sizes, pontoon type 4. . . . . . . . . . . . . . . . . . . . . . . . . . . . . . . . . XXV
D.2 Transfer functions for pontoon 4 for a selection of heading angles. . . . . . . XXVI
D.3 Mean drift coefficient in surge compared to coefficient obtained by Norconsult. Angle is relative to the longitudinal axis of the pontoon. . . . . . . . . . . XXVII
D.4 Mean drift coefficient in surge compared to coefficient obtained by Norconsult. Angle is relative to the longitudinal axis of the pontoon. . . . . . . . . . . XXVIII
D.5 Mean drift coefficient in sway compared to coefficient obtained by Norconsult. Angle is relative to the longitudinal axis of the pontoon. . . . . . . . . . . XXIX
D.6 Mean drift coefficient in yaw compared to coefficient obtained by Norconsult. Angle is relative to the longitudinal axis of the pontoon. . . . . . . . . . . XXX
D.7 Force spectrum for pontoon type 4, force 1, 2 and 3. Motion according to the pontoon's local coordinate system. Heading angle relative to pontoon longitudinal axis. . . . . . . . . . . . . . . . . . . . . . . . . . . . . . . . XXXI
D.8 Force spectrum for pontoon type 4, force 4, 5 and 6. Motion according to the pontoon's local coordinate system. Heading angle relative to pontoon longitudinal axis. . . . . . . . . . . . . . . . . . . . . . . . . . . . . . . . XXXII

E.1 Example of wave force in 100-year sea state with wind sea from 270° and swell from 330°. Direction of incoming waves defined in figure 7.1. Force history in local surge for pontoon 1. Characteristic 1-hour wave load from wind sea indicated by dashed line. . . . . . . . . . . . . . . . . . . . . . . . . . . XXXIII
E.2 Example of wave force in 100-year sea state with wind sea from 270° and swell from 330°. Direction of incoming waves defined in figure 7.1. Force history in sway for pontoon 1. Characteristic 1-hour wave load from wind sea indicated by dashed line. . . . . . . . . . . . . . . . . . . . . . . . . . . . XXXIV
E.3 Example of wave force in 100-year sea state with wind sea from 270° and swell from 330°. Direction of incoming waves defined in figure 7.1. Force history in local heave for pontoon 1. Characteristic 1-hour wave load from wind sea indicated by dashed line. . . . . . . . . . . . . . . . . . . . . . . . . . . XXXV
E.4 Example of wave force in 100-year sea state with wind sea from 270° and swell from 330°. Direction of incoming waves defined in figure 7.1. Force history in local roll for pontoon 1. Characteristic 1-hour wave load from wind sea indicated by dashed line. . . . . . . . . . . . . . . . . . . . . . . . . . . XXXVI
E.5 Example of wave force in 100-year sea state with wind sea from 270° and swell from 330°. Direction of incoming waves defined in figure 7.1. Force history in local pitch for pontoon 1. Characteristic 1-hour wave load from wind sea indicated by dashed line. . . . . . . . . . . . . . . . . . . . . . . . . . . XXXVII

E.6 Example of wave force in 100-year sea state with wind sea from 270° and swell from 330°. Direction of incoming waves defined in figure 7.1. Force history in local yaw for pontoon 1. Characteristic 1-hour wave load from wind sea indicated by dashed line. . . . . . . . . . . . . . . . . . . . . . . . . . . . . . XXXVIII

# List of Tables

4.1 Properties of the main girder cross sections. . . . . . . . . . . . . . . . . . . 34
4.2 Steel properties for the bridge girder. . . . . . . . . . . . . . . . . . . . . . . 35
4.3 Equivalent density for the three bridge girder cross sections. . . . . . . . . . 35
4.4 Masses of cable anchors. . . . . . . . . . . . . . . . . . . . . . . . . . . . . . 36
4.5 Additional steel mass at column tops. . . . . . . . . . . . . . . . . . . . . . . 36
4.6 Geometry of tower components. . . . . . . . . . . . . . . . . . . . . . . . . . 36
4.7 Input parameters for tower top. . . . . . . . . . . . . . . . . . . . . . . . . . 37
4.8 Properties of tower material. . . . . . . . . . . . . . . . . . . . . . . . . . . . 38
4.9 Properties of the columns as implemented in USFOS. . . . . . . . . . . . . . 41
4.10 Material properties applied for the pontoons. . . . . . . . . . . . . . . . . . . 41
4.11 Geometry and spring stiffness of the four pontoon types. . . . . . . . . . . 43
4.12 Material density for the pontoons . . . . . . . . . . . . . . . . . . . . . . . . 44
4.13 Added mass in surge, sway and yaw relative to the local pontoon coordinate system. . . . . . . . . . . . . . . . . . . . . . . . . . . . . . . . . . . . . . . 45
4.14 Drag coefficients and characteristic diameters for the pontoons. . . . . . . . . 46
4.15 Drag, lift and moment coefficients for wind drag. . . . . . . . . . . . . . . . . 46
4.16 The first 20 eigenmodes of the USFOS model. The valid range for the applied added mass is given in the last column. . . . . . . . . . . . . . . . . . . . . . 48
4.17 Applied values in the control calculations of eigenperiods in heave. . . . . . . 52
4.18 Theoretical upper and lower limit for the eigenperiods in heave in the floating low bridge. . . . . . . . . . . . . . . . . . . . . . . . . . . . . . . . . . . . . 52

5.1 Characteristics of the impact scenarios applied in the comparison to the theory presented by Jones. . . . . . . . . . . . . . . . . . . . . . . . . . . . . . . 56
5.2 Input parameters implemented in the equations by Jones. . . . . . . . . . . . 56

6.1 Overview of the design ships recommended by the NPRA for pontoon collision. 61
6.2 Overview and results of the ship-pontoon collision analyses. . . . . . . . . . . 68
6.3 Overview and results of the collision analyses with the new pontoon design. . 87
6.4 Maximum torsion in the column between the struck pontoon and the bridge girder. . . . . . . . . . . . . . . . . . . . . . . . . . . . . . . . . . . . . . . 89
6.5 Overview and results of the ship-girder collision analyses. . . . . . . . . . . . 90
6.6 Results from static analysis of the bridge when four compartments of pontoon 1 are flooded. . . . . . . . . . . . . . . . . . . . . . . . . . . . . . . . . . . . 94

7.1 Load cases applied in ultimate limit state considerations. . . . . . . . . . . . 97
7.2 Significant wave height and maximum spectral peak period for the 100-year sea states. . . . . . . . . . . . . . . . . . . . . . . . . . . . . . . . . . . . . 98
7.3 Significant wave height and spectral peak periods for the 10-year sea state. . 99
7.4 Mean wind reduction factor $n^2$ as a function of wind direction. . . . . . . . . 99
7.5 Applied JONSWAP-parameters for wind sea and swell. . . . . . . . . . . . . 100
7.6 Mean drift coefficients for high frequencies in the case of $\beta = 40°$, $R = 5\ m$ and $L = 24\ m$. . . . . . . . . . . . . . . . . . . . . . . . . . . . . . . . . 106
7.7 Wind properties applied when modelling wind in WindSim. . . . . . . . . . . 110
7.8 Most severe wind generated sea states corresponding to a 100-year return period. 113
7.9 Characteristic wave loads for pontoon 22 when subjected the sea states in table 7.8. Loads are given according to the global coordinate system. . . . . . . 114
7.10 Main findings in static wave load analysis. . . . . . . . . . . . . . . . . . . 114
7.11 Main findings in dynamic analysis of long-crested swell and wind sea from 330°. Drift motions have been roughly filtered out of the results. . . . . . . . 118
7.12 Main findings in dynamic analysis of long-crested swell from 330°. Drift motions have been roughly filtered out of the results. . . . . . . . . . . . . . . 121
7.13 Main findings in dynamic analysis of difference-frequency forces when long-crested wind sea from 330° is considered. . . . . . . . . . . . . . . . . . . . 122
7.14 Wind conditions applied statically to the bridge. The direction is relative to the north, measured clockwise. . . . . . . . . . . . . . . . . . . . . . . . . 123
7.15 Main findings in static wind load analysis. . . . . . . . . . . . . . . . . . . 124
7.16 Main findings in dynamic wind load analyses. . . . . . . . . . . . . . . . . 125
7.17 Bending moment about strong axis at areas damaged by ship collision. . . . 127
7.18 Increase in reaction forces and displacements when including wind gusts compared to results obtained in the static analysis. . . . . . . . . . . . . . . . 128

A.1 Properties of the cables in the various cable pairs. The cable pairs are numbered from the south end of the bridge. . . . . . . . . . . . . . . . . . . . . . II

B.1 The first 20 eigenmodes of the USFOS model. The valid range for the applied added mass is given in the last column. . . . . . . . . . . . . . . . . . . . . VII
B.2 Eigenmode 20 to 40 obtained with the USFOS model. The valid range for the applied added mass is given in the last column. . . . . . . . . . . . . . . . VIII
B.3 Eigenmodes obtained in USFOS compared to eigenmodes obtained in 3DFloat. IX

# List Of Symbols And Abbreviations

## Latin Symbols

| | |
|---|---|
| $A$ | Cross sectional area |
| $A_{33}$ | Added mass in heave |
| $A_{WP}$ | Waterplane area |
| $C_{33}$ | Waterplane stiffness in heave |
| $C_{44}$ | Waterplane stiffness in roll |
| $C_{55}$ | Waterplane stiffness in pitch |
| $C_D$ | Drag coefficient |
| $C_L$ | Lift coefficient |
| $C_D$ | Moment coefficient |
| $c_i$ | Decay constant |
| $D$ | Characteristic diameter |
| $E$ | Elastic modulus |
| $\bar{F}_i$ | Mean drift force in direction $i$ |
| $F_D(t)$ | Drag force |
| $F_i^{SV}$ | Slowly varying drift force in direction $i$ |
| $F_{M,i}$ | Characteristic wave load in direction $i$ |
| $f_N$ | Nyquist frequency in $Hz$ |
| $G$ | Mass in impact model by Jones |
| $H(\omega)$ | Transfer function |
| $H_s$ | Significant wave height |
| $I$ | Impulse |
| $I_i$ | Turbulence intensity for wind |
| $I_t$ | Torsional moment of inertia |
| $I_y$ | Moment of inertia about local $y$-axis |
| $I_z$ | Moment of inertia about local $z$-axis |

|  |  |
|---|---|
| $k$ | Wave number |
| $M$ | Mass |
| $M_0$ | Bending moment capacity in theory by Jones |
| $m$ | Mass per unit length |
| $m_0$ | Zeroth moment of spectrum |
| $N$ | Number of frequency intervals |
| $n^2$ | Decay factor for mean wind speed |
| $P(t)$ | Impulse load as a function of time |
| $Q$ | Shear force in theory by Jones |
| $Q_0$ | Shear force capacity in theory by Jones |
| $S_{FF}(\omega)$ | Force spectrum |
| $S_i(f)$ | Spectrum for wind gust |
| $S_{\zeta\zeta}(\omega)$ | Wave spectrum |
| $Sh_y$ | Shear area in $y$-direction |
| $Sh_z$ | Shear area in $z$-direction |
| $T_1$ | Duration of first phase of motion in theory by Jones |
| $T_{jj}^{ic}$ | Mean drift coefficient |
| $T_{jk}^{ic}$ | Constants corresponding to cosine term in slowly varying drift force |
| $T_{jk}^{is}$ | Constants corresponding to sine term in slowly varying drift force |
| $T_n$ | Eigenperiod for mode $n$ |
| $T_p$ | Spectral peak period |
| $t$ | Time |
| $\Delta t$ | Time step in time domain analysis |
| $t_d$ | Duration of impulse load |
| $U(z)$ | Wind speed |
| $\bar{U}_{10}$ | Mean wind speed at 10 $m$ |
| $\bar{U}_{10min}$ | Average wind speed over a 10 minute period |
| $u$ | Velocity of water particle |
| $V_0$ | Impact velocity in theory by Jones |
| $W_{pi}$ | Plastic section modulus about axis $i$ |

**Greek Symbols**

| | |
|---|---|
| $\alpha$ | Shape parameter for wind profile |
| $\alpha_1$, $\alpha_2$ | Parameters for Rayleigh damping |
| $\beta$ | Angle between wave direction and longitudinal axis of pontoon |
| $\gamma$ | Peak shape parameter for JONSWAP spectrum |
| $\delta$ | Phase angle between wave and response |
| $\epsilon$ | Random phase angle |
| $\zeta$ | Surface elevation |
| $\zeta_a$ | Wave amplitude |
| $\lambda$ | Damping ratio |
| $\xi$ | Position of plastic hinge in theory by Jones |
| $\xi_0$ | Position of stationary plastic hinge in theory by Jones |
| $\rho$ | Material density |
| $\sigma$ | Spectral width parameter for JONSWAP spectrum |
| $\tau$ | Shear stress |
| $\omega$ | Angular frequency of wave component |
| $\Delta\omega$ | Frequency step in $rad/s$ |
| $\omega_0$ | Fundamental eigenfrequency in $rad/s$ |
| $\omega_n$ | Eigenfrequency for mode $n$ |
| $\omega_p$ | Spectral peak period in $rad/s$ |

**Abbreviations**

| | |
|---|---|
| $ALS$ | Accidental Limit State |
| $CFM$ | Conservation of Fluid Momentum |
| $DWT$ | Deadweight tonnage |
| $DPI$ | Direct Pressure Integration |
| $LOA$ | Length Over All |
| $NPRA$ | Norwegian Public Roads Administration (Statens Vegvesen) |
| $ULS$ | Ultimate Limit State |

# Chapter 1

# Introduction

## 1.1 Background

During the presentation and discussion of the National Transport Plan (NTP) for 2018-2029, the long-term goal of developing an improved and continuous E39 was confirmed by the Storting(Statens Vegvesen, 2017a). The Norwegian Public Roads Adminitstration (NPRA), i.e. Statens Vegvesen, is in charge of the project, commissioned by the Ministry of Transport and Communications. The E39 is a route of approximately 1100 km that connects Kristiansand in the south to Trondheim in the north. The route also runs through the cities Stavanger, Bergen, Ålesund and Molde. Today, the route includes seven different ferry connections, and the travel time is estimated to 21 hours. The plan is to reduce the travel time to 11 hours by replacing the ferries with bridges and tunnels, and by upgrading and replacing road sections(Statens Vegvesen, 2017a). In addition to reducing the travel time, the reduction in distance is expected to have a positive effect on the emission of greenhouse gases(Statens Vegvesen, 2017b).

In order to achieve the goal of a continuous E39, the ferries that are operated today must be replaced by bridges and undersea tunnels. However, several of the fjords that the route travels by are too deep for tunnels to be a realistic alternative. In addition, the straits are up to 5 $km$ wide, which implies that bridges cannot be designed according to present technology and design rules(Statens Vegvesen, 2017c).

The Bjørnafjord is one of the challenging straits that the E39 is planned to cross. The fjord is about 5 $km$ wide at the crossing site and has a maximum depth of up to 600 $m$(Statens Vegvesen, 2017d). Due to the depth of the fjord, an undersea tunnel is not a good option, which means that a bridge is the only alternative. The planned bridge will be the longest in the world, and an expansion of present technology is therefore required(Statens Vegvesen, 2017d). Until now, there are about 50 Phd- and Postdoc-candidates engaged in the project(Statens Vegvesen, 2017d). Various concepts have been considered for crossing the Bjørnafjord, both for bridges and for floating tunnels. At the present time, the NPRA has recommended to proceed with two of the proposed bridge designs; the end-anchored floating bridge and the side-anchored floating bridge(Statens Vegvesen, 2017d). It is the end-anchored bridge that will be the topic of this thesis.

The end-anchored floating bridge is, as the name suggests, fixed at the ends, and the bridge girder is curved in the horizontal plane, see figure 1.1. In the initial design, the girder of the end-anchored bridge consisted of two box-sections placed side by side, connected by transverse beams. Later, this design has been discarded in favour of a single-girder solution. As a result, the slenderness of the bridge is increased. Due to the length of the bridge, and the complexity of the design, simulations will necessary in order to predict the structural response under various loading scenarios. Norconsult AS, along with Dr. Techn. Olav Olsen, Aker Solutions and ife, are currently involved in the concept development. Additional work that is being conducted involves measuring of waves, winds and currents, geotechnical analyses of the foundation and mapping of the ship traffic(Statens Vegvesen, 2017d).

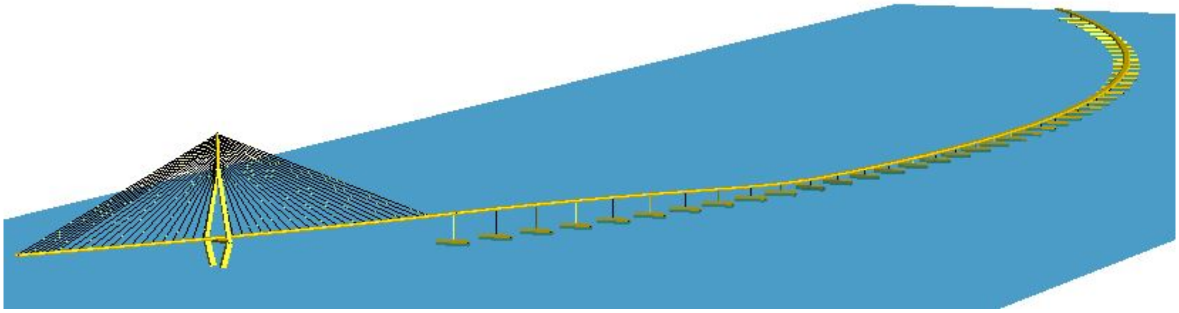

Figure 1.1: USFOS-model of the end-achored floating bridge.

## 1.2 Objective

One of the design criteria for the bridge is that it will have to withstand extreme environmental loads from wind and waves, as well as the loads from high energy ship impacts. Since the behaviour of the bridge is unknown, scenario-based analyses must be carried out in order to reveal the governing vulnerabilities of the design. The aim is to use USFOS to study the response of the bridge when subjected to such extreme load cases.

A model of the bridge was created in USFOS during the work with the project thesis. Before the extreme loading scenarios can be analyzed, the model must be developed further, such that the hydrodynamic properties of the pontoons are represented more accurately. Firstly, added mass and drag must be modelled. Secondly, rotational waterplane stiffness should be modelled in a way such that the properties follows the motions of the pontoons.

The accidental limit state criterion states that the bridge must have sufficient strength to withstand ship collisions with only local damages, i.e. the global integrity of the bridge must not be threatened(Moan, 2001). The resistance of the bridge towards ship impact must therefore be assessed; both for impacts where the ship strikes the pontoons and for impacts between ship deckhouse and bridge girder. Further, the design criterion states that the bridge must have sufficient capacity to survive an extreme storm after the collision. Therefore, analyses where the bridge is exposed to environmental loads with a 100-year return period will be conducted. Due to the slender nature of the bridge, it will be especially interesting to study if the bridge girder is susceptible to global buckling in the horizontal plane. Based on previous work carried out by Norconsult on behalf of the NPRA, wind is believed to be the governing environmental load with respect to snap-through buckling.

## 1.3 Scope and limitations

The initial scope of work is defined in the first pages of the report. The ship collision part of the task has been completed according to the initial plan, while the scope of the environmental load considerations has been reduced. The computational costs when simulating wind and waves have proven to very high, and the number of time domain simulations that have been conducted is therefore limited. As a consequence, there has not been enough data to predict the 100-year response. In agreement with Supervisor Professor Jørgen Amdahl, it has been decided to do a qualitative assessment of environmental loads instead.

The initial scope of work suggests to employ a simplified model without the cable-stayed section. Since the simplified models do not capture added mass and drag, this has not been prioritized.

The scope of work for this thesis is structural analysis of global bridge response in the ultimate and accidental limit state. Thus, the serviceability and fatigue limit states are not considered. Since global response is the topic of interest, local deformations are only considered qualitatively. This is done by comparing the results to strength assessments obtained from the NPRA. Further, the thesis relies on existing risk assessments and metocean data. It has not been a priority to conduct sensitivity studies with respect to environmental loads.

The details of the cable tower are not available, and it has therefore been decided to model the tower with a very high stiffness and yield strength. Similarly, the yield strength of the stay-cables is also unknown. As a consequence, the utilization of the tower and cables cannot be assessed. This thesis mainly addresses load levels in the bridge girder and the columns.

# Chapter 2

# Literature Review

## 2.1 Single degree of freedom modelling of ship collision

A ship collision can be modelled in USFOS by a single degree of freedom system. A literature search for possible modelling techniques has been carried out. In this section, the findings will be described briefly.

W. Fan et. al. have tested simplified models of vessel-bridge collisions in two different publications. The two single degree of motion models will be considered next.

The first publication is “Dynamic Demand of Bridge Structure Subjected to Vessel Impact Using Simplified Interaction Model”(Fan et al., 2011). Consistent with the NORSOK standard, it states that the majority of the kinetic energy dissipation is due to local plastic deformations(Fan et al., 2011). Thus, the local damping forces in the impact may be neglected. The collision is described by the remaining terms of the equation of motion; the inertia term, the stiffness term and the external force.

The vessel is modelled as a point mass with magnitude equal to the ship mass plus the hydrodynamic added mass. Further, the point mass is defined with a translatory velocity corresponding to the impact velocity of the ship. The mass is connected to the bridge by a nonlinear spring, which aims to model the behavior of the ship bow during the impact. Thus, the compression stiffness of the spring can be retrieved from the ship’s force-displacement curve. Fan et. al. uses a force-deformation curve for the ship colliding with a fixed, rigid wall(Fan et al., 2011). When in tension, the spring stiffness is zero in order to model the disconnection between the ship and the bridge (Fan et al., 2011). An illustration of the model is shown if figure 2.1.

In the other publication, “Dynamic ship-impact load on bridge structures emphasizing shock-spectrum approximation”, the local deformation of the bridge is included as a nonlinear spring in series with the first spring(Fan et al., 2016). From spring mechanics, it is known that an equivalent spring stiffness may be found for springs in series. Another option could therefore be to combine the resistance towards local deformation from both components in one single spring.

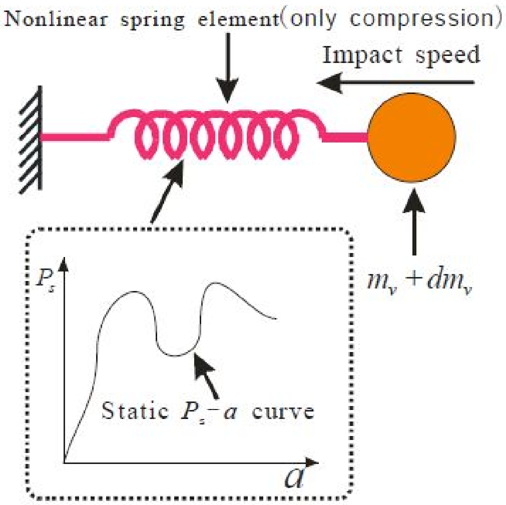

Figure 2.1: Illustration of the simplified interaction model described by W. Fan. $P_s$ is the load level, $a$ is the deformation, $m_v$ is the vessel mass and $dm_v$ is the hydrodynamic added mass. From: (Fan et al., 2011)

Aleksander Aalberg has used USFOS to model ship collisions in his master thesis “Analysis and Design Bjørnefjorden - Floating Cable-Stayed Bridge subjected to Large Ship Collisions and Extreme Environmental Loads”(Aalberg, 2017). Here, two springs in series are used to connect the mass to the bridge. The first spring represents the force-deformation curve of the vessel. The second spring is given a very high stiffness in compression, and almost no stiffness in tension. This is to model the disconnection between the vessel and the bridge after the impact. Aalberg found that the compression stiffness of the second spring should not be too large, as this will cause abnormally large axial forces in the spring(Aalberg, 2017).

## 2.2 Impact on long beams

One of the aims of this master thesis is to study the response of the bridge when subjected to ship collision. Since dynamic effects are expected to be important, it is not straight forward to predict the response. A literature search has therefore been conducted in order to find theory related to bending waves in beams subjected to impulsive loading.

### 2.2.1 Reflection of elastic flexural waves in simply supported beam

In “Dynamic Behaviour of Elastic-Plastic Free-Free Beams Subjected to Impulsive Loading”, Yu et al. study the bending waves in a simply supported beam subjected to impulse. A beam with uniform rectangular cross-section and elastic-perfectly plastic material is assumed. In one of the examples, a numerical procedure is applied in order to predict the beam response when subjected to impact at midspan. Since the the response is symmetric about $x = 0$, only the positive part of the x-axis is considered (Yu et al., 1996). The early stages of the response is divided into four phases. Only the first two phases will be addressed in this literature review.

In the first phase of motion, the oscillations of the flexural wave can be observed as it propagates away from the impact area, see figure 2.2a. It is seen that smaller, high frequency components move faster than the main oscillation, i.e. the peak of the bending wave. This is inline with dispersion of the flexural wave(Yu et al., 1996). If the results of this elastic analysis is compared to plastic analyses, the peak bending moment close to the impact corresponds to a travelling hinge, while the large moment directly under the impact is the stationary hinge(Yu et al., 1996). Plastic hinges will be explained further in section 2.2.3. For simplicity, the large local maximum propagating away from the impact point will be referred to as the travelling hinge.

In phase 2, the first components of the flexural waves reach the free end and are reflected back in the opposite direction(Yu et al., 1996). When the reflected waves interfere with the travelling hinge, the bending moment along the beam is redistributed(Yu et al., 1996). As the phase angles between the travelling hinge and the reflected waves vary, the position of the maximum bending moment will vary. This is analogous to a travelling hinge moving back and forth along the beam(Yu et al., 1996). The feature is evident in figure 2.2b.

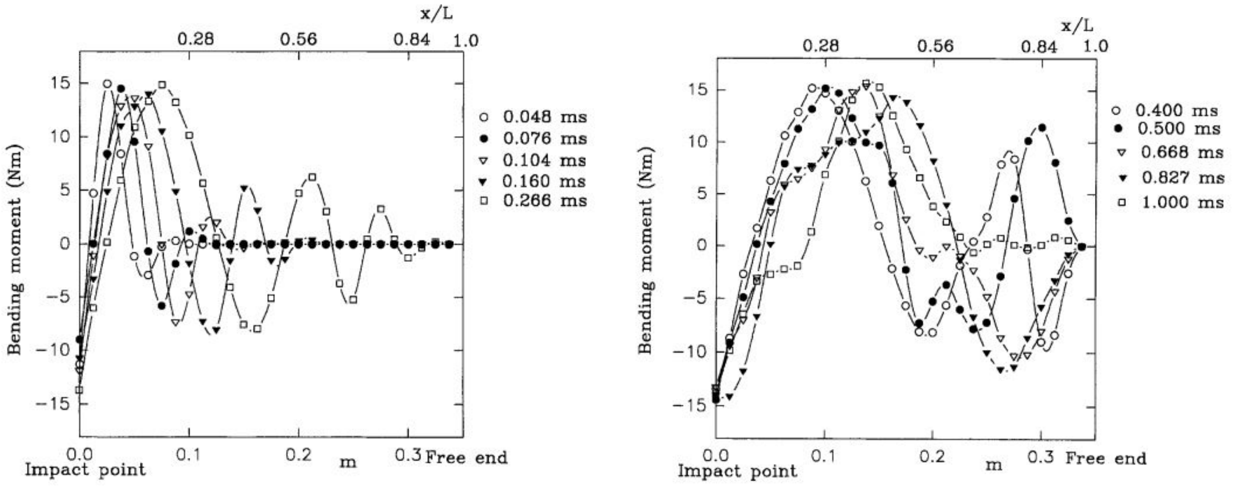

(a) Phase 1

(b) Phase 2

Figure 2.2: Moment diagrams for the first two phases in the transient beam behaviour described by Yu et al. From: (Yu et al., 1996)

### 2.2.2 Flexural waves in thin rods

In the book “Wave Motion in Elastic Solids” by K. F. Graff, there is a chapter on flexural waves in thin rods. Some of the theory discussed in this chapter will be briefely explained in this section.

The theory is discussed by Graff is based on a series of assumptions. The neutral axis of the rod extends in the x-direction, and the transverse deflection is denoted $y$. Euler-Bernoulli beam theory is applied, i.e. plane sections normal to the neutral axis remain plane and perpendicular to the neutral axis after deformations(Graff, 1975). Secondly, small deformations are assumed, such that the curvature of the rod can be expressed as $\frac{\partial^2 y}{\partial x^2} = -\frac{M}{EI}$, where $EI$ is constant. Rotational inertia effects are neglected, such that the shear force $V$ is related to the bending moment $M$ by $V = \frac{\partial M}{\partial x}$. By enforcing zero distributed loading, the differential equation of the system is then as following:(Graff, 1975)

$$\frac{\partial^4 y}{\partial x^4} + \frac{1}{a^2}\frac{\partial^2 y}{\partial t^2}, \qquad a^2 = \frac{EI}{\rho A} \tag{2.1}$$

In equation 2.1, $\rho$ is the material density and $A$ is the cross-sectional area. Further, the bending waves in an infinitely long beam are modelled as harmonic waves. The phase velocity of the flexural wave is then given by equation 2.2, where $k$ is the wave number and $a$ is the parameter from equation 2.1(Graff, 1975). The wave number is given by $k = \frac{2\pi}{\lambda}$, where $\lambda$ is the wave length.

$$c = \pm ak \tag{2.2}$$

What else may be of interest, is that the chapter provides an illustration of the propagating bending waves in an infinite beam. The deformation is given by the solid line in figure 2.3. The illustration is based on the analytic solution of the initial value problem for a beam with an initial disturbance(Graff, 1975).

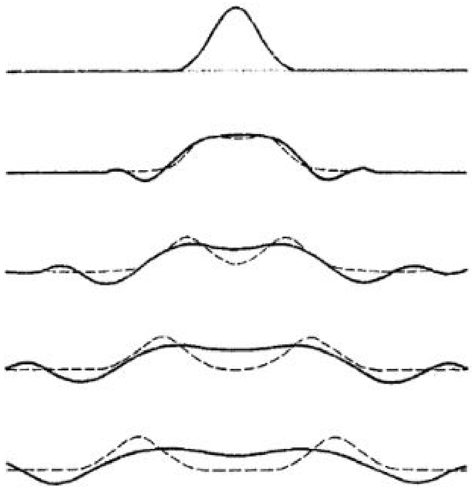

Figure 2.3: Propagation of bending waves in infinite beam subjected to initial disturbance. Results given by the solid line. From: (Graff, 1975)

### 2.2.3 Travelling plastic hinges

The behavior of the Bjørnafjorden bridge is primarily expected to be elastic for the relevant impact scenarios. However, it might be interesting to compare the results obtained in USFOS to theory for travelling plastic hinges in long beams subjected to centralized impacts. The main source of information for this section is “Structural Impacts” by Norman Jones, where load cases that produce inelastic response are studied.

The theory presented by Jones assumes a perfectly plastic material, i.e. strain hardening of the material is neglected. The yield criterion for the material is given in figure 2.4, where the combination of bending moment and shear force required for plasticity is given. A plastic hinge is a section of a beam where the plasticity is reached over the entire cross-section. When the stress distribution is fully plastic, the capacity of the cross-section collapses(Jones, 2011), and it cannot carry any additional loading.

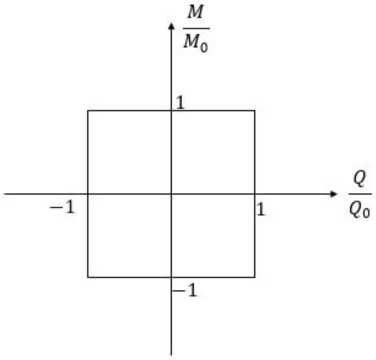

Figure 2.4: Yield criterion applied in the theory presented by Jones.

Jones studies the impact of a mass $G$ on the mid-span of a long beam, see figure 2.5($a$). The mass strikes the beam at $x = 0$ with an initial velocity $V_0$. The response of the beam is divided into two phases. In the first phase of motion, i.e. the time period $0 \leq t \leq T_1$, shear effects are important. It is shown that the transverse shear force at the position of the impact is infinitely large at the moment after the mass strikes the beam(Jones, 2011). See figure 2.5($b$) for the velocity profile of the beam in the first phase. In the figure, $\xi$ denotes the location of the plastic hinge relative to the position struck by $G$. The plastic bending hinges are stationary in the first phase.(Jones, 2011)

The position of the stationary plastic hinges can be found according to equation 2.3, where $\xi_0$ is the position relative to $x = 0$, $M_0$ is the plastic bending moment and $Q_0$ is the shear capacity. The duration of the first phase of motion is expresses by equation 2.4, where $V_0$ is the initial velocity of the mass $G$ and $m$ is the mass per unit length of the beam.(Jones, 2011)

$$\xi_0 = \frac{6M_0}{Q_0} \tag{2.3}$$

$$T_1 = \frac{GV_0}{2Q_0(1 + \frac{G}{m\xi_0})} \tag{2.4}$$

In the second phase of motion, the plastic bending hinges travel away from the impacted area, while shear effects are negligible compared to the bending effects(Jones, 2011). See figure 2.5($c$) for an illustration of the transverse velocity profile in the second phase. The relation between the time and the position of the plastic hinge is expressed in equation 2.5. In the equation, $t$ is the time after the impact, m is the mass per unit length of the beam,

$\xi$ is the position of the hinge, $V_0$ is the initial velocity of the mass $G$ and $M_0$ is the bending capacity of the beam.(Jones, 2011)

$$t = \frac{m\xi^2 V_0}{12M_0(1+\frac{m\xi}{G})} \tag{2.5}$$

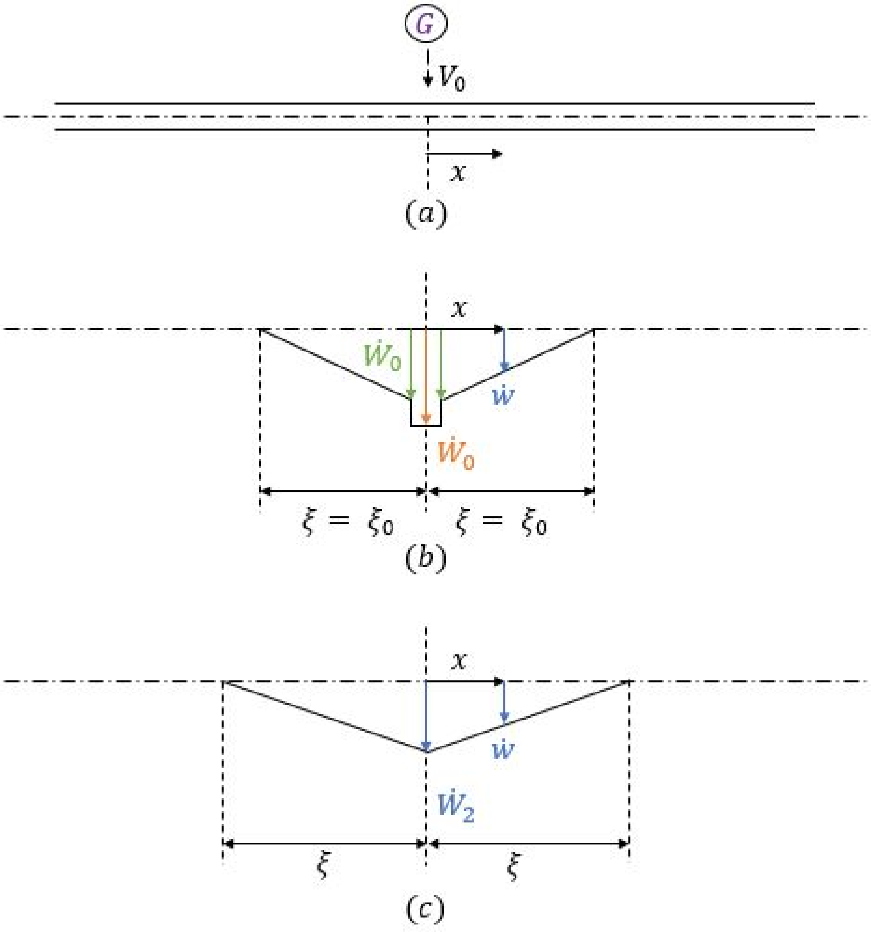
G
$V_0$
$x$
(a)
$x$
$\dot{W}_0$
$\dot{w}$
$\dot{W}_0$
$\xi = \xi_0$
$\xi = \xi_0$
(b)
$x$
$\dot{w}$
$\dot{W}_2$
$\xi$
$\xi$
(c)

Figure 2.5: (a) Illustration of a mass $G$ with initial velocity $V_0$ hitting a long beam. (b) Illustration of the velocity profile of the beam in the first phase of motion, $0 \leq t \leq T_1$. (c) Illustration of the velocity profile of the beam in the second phase of motion, $t \geq T_1$.

# Chapter 3

# Theory

The aim of this section is to explain basic concepts and equations that will be addressed in sections 6 and 7.

## 3.1 Definition of limit states

The NORSOK standards define a limit state as a “state where a structure or part of a structure no longer meets the requirements laid down for its performance or operation”(NORSOK, 2010). The NORSOK standards operate with four limit states; the ultimate, accidental, serviceability and fatigue limit state. This section will mainly consider the accidental limit state.

The resulting loads from actions like ship collisions, dropped objects, explosions and fires are referred to as *accidental loads*. T. Moan defines the Accidental Limit State control in two steps(Moan, 2001):

i) The structure must be able to withstand abnormal load effects with annual exceedance probability of $10^{-4}$. Local damages are tolerable, but the overall integrity of the structure must not be compromised.

ii) After sustaining the accidental load, the structure must still be capable of resisting environmental loads with annual probabilities of $10^{-2}$.

The requirements may be expressed with equation 3.1(Det Norske Veritas, 2010a).

$$S_c \gamma_f = \frac{R_c}{\gamma_M} \tag{3.1}$$

In the equation, $S_c$ is the characteristic load effect, $\gamma_f$ is the partial safety factor for loads, $R_c$ is the characteristic resistance of the structure and $\gamma_M$ is the material factor. In the standard “Integrity of offshore structures”, resistance is defined as the “capacity of a structure, component or cross-section of a component to withstand action effects without exceeding a limit state"(NORSOK, 2010). In both steps of the ALS control, the safety factors are in general 1.0(Moan, 2001).

When considering environmental loads, several actions must be taken into account at the same time. The NORSOK standard "Actions and action effects" provides guidelines for how the environmental loads should be combined in the modelling of 100-year and 10 000-year environmental conditions(NORSOK, 2007), see figure 3.1. It is stated that the design load case should be the combination corresponding to the "worst case" scenario(NORSOK, 2007).

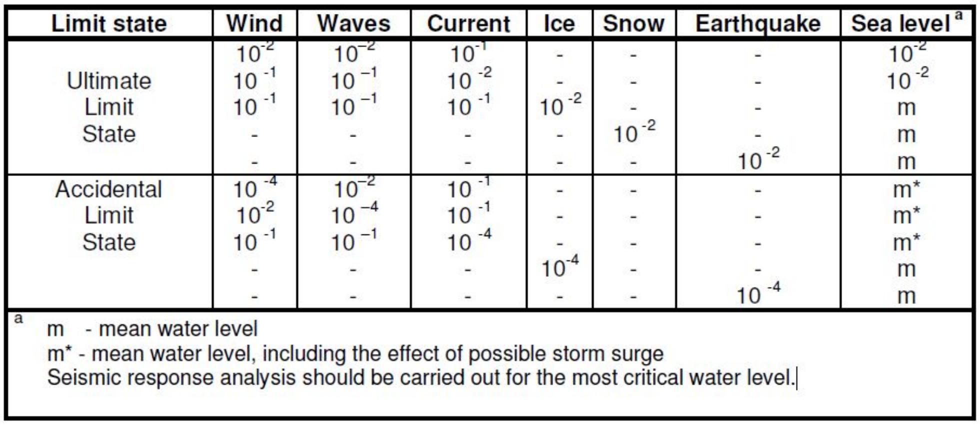

| Limit state | Wind | Waves | Current | Ice | Snow | Earthquake | Sea level[a] |
|---|---|---|---|---|---|---|---|
| Ultimate Limit State | $10^{-2}$ | $10^{-2}$ | $10^{-1}$ | - | - | - | $10^{-2}$ |
| | $10^{-1}$ | $10^{-1}$ | $10^{-2}$ | - | - | - | $10^{-2}$ |
| | $10^{-1}$ | $10^{-1}$ | $10^{-1}$ | $10^{-2}$ | - | - | m |
| | - | - | - | - | $10^{-2}$ | - | m |
| | - | - | - | - | - | $10^{-2}$ | m |
| Accidental Limit State | $10^{-4}$ | $10^{-2}$ | $10^{-1}$ | - | - | - | m* |
| | $10^{-2}$ | $10^{-4}$ | $10^{-1}$ | - | - | - | m* |
| | $10^{-1}$ | $10^{-1}$ | $10^{-4}$ | - | - | - | m* |
| | - | - | - | $10^{-4}$ | - | - | m |
| | - | - | - | - | - | $10^{-4}$ | m |

[a] m - mean water level
m* - mean water level, including the effect of possible storm surge
Seismic response analysis should be carried out for the most critical water level.

Figure 3.1: Combinations of environmental loads in both the ultimate and the accidental limit states. From: (NORSOK, 2007).

## 3.2 Definition of the eigenvalue problem

In order to explain the eigenvalue problem, the dynamic response problem must first be defined. The dynamic equilibrium equation, which can be deduced from Newton's second law, expresses equilibrium between external excitation forces and inertia, damping and stiffness forces, see equation 3.2(Langen and Sigbjörnsson, 1979). Here, $\mathbf{M}$ is the mass matrix, $\mathbf{C}$ is the damping matrix, $\mathbf{K}$ is the stiffness matrix and $\mathbf{r}$(t), $\dot{\mathbf{r}}$(t) and $\ddot{\mathbf{r}}$(t) are the displacement, velocity and acceleration vectors, respectively. In hydrodynamic problems, the mass matrix $\mathbf{M}$ should include added mass. $\mathbf{F}_{exc}(t)$ is the external excitation force. According to Langen and Sigbjörnsson, an arbitrary excitation load can be expressed as an infinite sum of harmonic components(Langen and Sigbjörnsson, 1979). For a harmonic load, the excitation force may be expressed on the form $\mathbf{F}_A sin(\omega t + \epsilon)$. Here, $\mathbf{F}_A$ is the load amplitude, $\omega$ is the angular frequency and $\epsilon$ is a phase angle. Consequently, for a sum of harmonic load components, the excitation force becomes $\Sigma_{j=1}^{N}\mathbf{F}_{A,j} sin(\omega_j t + \epsilon_j)$.

$$\mathbf{M}\ddot{\mathbf{r}}(t) + \mathbf{C}\dot{\mathbf{r}}(t) + \mathbf{K}\mathbf{r}(t) = \mathbf{F}_{exc}(t) \tag{3.2}$$

Forces in the $x$-, $y$- and $z$-direction are denoted $F_1$, $F_2$ and $F_3$, respectively. Similarly, the moments are denoted $F_4$, $F_5$ and $F_6$.

The ratio between the frequency of the excitation force and the eigenfrequency of the structure is referred to as the frequency ratio. If the excitation frequency is close to the natural frequency of a system, the response will become very large due to resonance effects. In problems where this is the case, it can be shown that the damping term will be significant(Larsen, 2014). Without damping, the response would become infinitely large, which is unphysical. If the frequency of the applied force is much larger than the natural frequency, $\frac{\omega}{\omega_n} >> 1$, then the system is inertia dominated. This implies that the first term in equation 3.2 will govern(Larsen, 2014). On the other hand, if $\frac{\omega}{\omega_n} << 1$, the system is stiffness dominated.

The eigenvalue problem will be studied next. For simplicity, the case with a one degree of freedom system subjected to a single harmonic load component will be considered. When the excitation force is on the form $F(t) = F_A sin(\omega t)$, then the response must also be harmonic, i.e. r(t)= $r_A sin(\omega t + \epsilon)$. Consequently, $\ddot{\text{r}}$(t)=-$\omega^2 sin(\omega t + \epsilon)$. If the damping term is zero, the equation of motion for the system can be written as:

$$(-\omega^2 m + k) r_A sin(\omega t) = F_A sin(\omega t) \tag{3.3}$$

In the equation, $m$ is the mass of the system and $k$ is the system stiffness. The eigenfrequency of the system is found by putting the excitation force to zero(Larsen, 2014). The eigenfrequency of the single degree of freedom system is given by(Larsen, 2014):

$$\omega_0 = \sqrt{\frac{k}{m}} \tag{3.4}$$

The underlying principle is the same for the general problem given in equation 3.2. Systems with multiple degrees of freedom may have an infinite number of eigenmodes and corresponding eigenfrequencies(Larsen, 2014). By definition, the first eigenmodes are those that correspond to the lowest eigenfrequencies. The first modes are usually the most interesting, as the energy decreases with increasing mode number(Larsen, 2014). However, higher modes can become important if resonance motions are excited. The eigenmodes and corresponding eigenfrequencies can be found by solving the general eiegenvalue problem, see equation 3.5(Langen and Sigbjörnsson, 1979). In the equation, $\omega_n$ is eigenfrequency $n$ and $\phi_n$ is the eigenvector for mode $n$. The problem may be solved by, for example, vector iteration. Vector iteration methods are suitable when the eigenvalue problem has a banded form and a limited number of eigenvalues are of interest(Langen and Sigbjörnsson, 1979). When these methods are applied, the eigenvalues and eigenvectors are found simultaneously by iteration(Langen and Sigbjörnsson, 1979).

$$(\mathbf{K} - \omega_n^2 \mathbf{M}) \phi_n = 0 \tag{3.5}$$

By considering two eigenfrequencies $\omega_i$ and $\omega_j$, and the corresponding eigenvectors $\phi_i$ and $\phi_j$, it can be shown that the two eigenvectors are orthogonal with respect to **M** and **K**. See chapter 4 of Langen and Sigbjörnsson for the derivation of the orthogonality(Langen and Sigbjörnsson, 1979). The orthogonality is expressed mathematically in equations 3.6 and 3.7.

$$\phi_i^T \mathbf{M} \phi_j = \begin{cases} 1 & \text{if } i = j, \\ 0 & \text{if } i \neq j \end{cases} \tag{3.6}$$

$$\phi_i^T \mathbf{K} \phi_j = \begin{cases} 1 & \text{if } i = j, \\ 0 & \text{if } i \neq j \end{cases} \tag{3.7}$$

As a consequence of the orthogonality, modal analysis can be applied for undamped systems. Modal analysis is explained in chapter 7 of Langen and Sigbjörnsson(Langen and Sigbjörnsson, 1979). In short, modal analysis means that equation 3.2 can be reduced to n decoupled equations that can be solved independently(Langen and Sigbjörnsson, 1979). This will reduce the required computational effort. If there is also damping present in the system, then modal analysis is only possible if the eigenvectors are also proportional with respect to the damping matrix **C**. If Rayleigh-damping is assumed, this is the case. Rayleigh-damping is briefly explained in the following section.

### 3.2.1 Rayleigh-damping

In the physical world, a dynamic system will always be subjected to damping, such that the kinetic energy is dissipated away as other forms of energy(Langen and Sigbjörnsson, 1979). There are several types of damping, for example damping in soil, hydrodynamic and aerodynamic damping and structural damping. Structural damping is due to friction in the material itself and in connections between different components in the structure. When considering damping, the damping ratio $\lambda$ is a commonly applied term. It expresses the ratio between the applied damping and the critical damping, i.e. $\lambda = \frac{c}{c_{cr}} = \frac{c}{2m\omega_0}$(Langen and Sigbjörnsson, 1979). In the expression, c is the damping coefficient, m is the mass and $\omega_0$ is the angular eigenfrequency.

Rayleigh-damping, or proportional damping, is when it is assumed that the damping matrix is linearly dependent on the mass matrix **M** and/or the stiffness matrix **K**. The expression for the damping matrix **C** is given in equation 3.8m where $\alpha_1$ and $\alpha_2$ are weight factors.

$$\mathbf{C} = \alpha_1\mathbf{M} + \alpha_2\mathbf{K} \tag{3.8}$$

In the case of Rayleigh-damping, the damping matrix will display the same orthogonality properties as the two other matrices(Langen and Sigbjörnsson, 1979). As a consequence, modal anlysis can be applied. The derivation of an expression for the damping ratio of mode $i$, $\lambda_i$, is given in chapter 9 of Langen and Sigbjörnsson(Langen and Sigbjörnsson, 1979). The expression for the damping ratio is given in equation 3.9. It is seen that for low frequencies, the damping ratio is proportional to $\frac{1}{\omega_i}$, while for high frequencies, the damping ratio is proportional to $\omega_i$. The relation between the damping ratio and eigenfrequencies is illustrated in figure 3.2. It is seen that for small values of $\omega$, the damping ratio increases rapidly with decreasing frequencies.(Langen and Sigbjörnsson, 1979)

$$\lambda_i = \frac{1}{2}(\frac{\alpha_1}{\omega_i} + \alpha_2\omega_i) \tag{3.9}$$

Say that a given damping level is desired, for example 5% for low frequencies and 10% for high frequencies. By defining two points on the curve, the two constants $\alpha_1$ and $\alpha_2$ can be determined. This is done in figure 3.2, where the damping ratio is defined for two frequencies; $\omega_1$ and $\omega_2$. However, it is seen that the damping ratio will be larger than 10% for frequencies higher than $\omega_2$. It is also seen that the damping ratio will be much higher than 5% for very

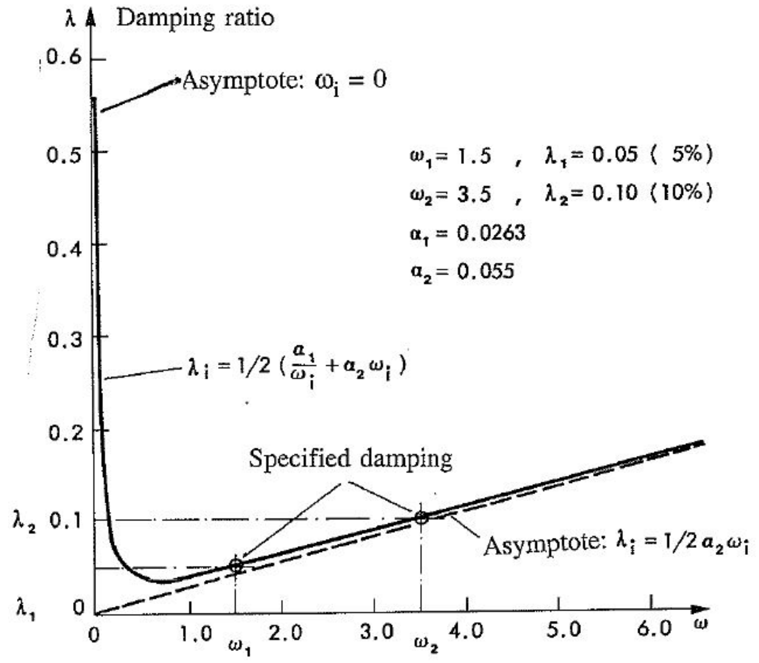

Figure 3.2: Damping ratio as a function of eigenfrequency for Rayleigh-damping. From: (Langen and Sigbjörnsson, 1979)

small frequencies. It is therefore important to identify the most important frequencies in the response problem, such that the damping ratio is close to the desired level at the critical frequencies.(Langen and Sigbjörnsson, 1979)

### 3.2.2 Short impulse model

When an imposed load is of short duration, i.e. shorter or equal to the natural period of the affected system, the action is defined as an impulse(Larsen, 2014). This section presents a simple model for a single degree of freedom system subjected to a short impulse. The model is applicable when $t_d < 0.2T_0$, where $t_d$ is the duration of the impulse and $T_0$ is the natural period of the system(Larsen, 2014).

A single degree of freedom system is subjected to an impulsive load, $F_{exc}(t)$. The equation of motion is then:

$$m\ddot{r}(t) + c\dot{r}(t) + kr(t) = F_{exc}(t) \tag{3.10}$$

The impulse imposed by the load is given by equation 3.11(Larsen, 2014).

$$I = \int_0^{t_d} F_{exc}(t)dt \tag{3.11}$$

C. M. Larsen divides the time history into two phases. In phase 1, when $0 < t < t_d$, the system is subjected to a forced oscillation. In phase 2, when $t > t_d$, the system is oscillating freely(Larsen, 2014).

It is assumed that the system is motionless at $t = 0$, such that $r_0 = 0$ and $\dot{r}_0 = 0$. The acceleration, on the other hand, is dependent on the impulse. As the system is set in motion, a stiffness force and a damping force will develop. However, it is assumed that these two terms are negligible compared to the inertia term when $t$ is very small(Larsen, 2014). Thus, for short impulses, the acceleration of the system can be estimated by equation 3.12.(Larsen, 2014)

$$\ddot{r}(t) \approx \frac{P(t)}{m} \tag{3.12}$$

By integration, the velocity at the end of the impulse can be found:

$$\dot{r}(t_d) = \int_0^{t_d} \ddot{r}(t)dt \approx \frac{P(t)}{m}dt = \frac{I}{m} \tag{3.13}$$

For small $t$, the displacement is proportional to $\dot{r}t$. In phase 1, this term is very small and is assumed negligible(Larsen, 2014). Thus, the oscillation is initiated at $t = t_d$, which is the beginning of phase 2. For simplicity, a time parameter $\bar{t} = t - t_d$ is introduced. The oscillation of an undapmed system with natural frequency $\omega_0$ is given by equation 3.14(Larsen, 2014).

$$r(\bar{t}) = \frac{\dot{r}(t_d)}{\omega_0} sin(\omega_0 \bar{t}) = \frac{I}{m\omega_0} sin(\omega_0 \bar{t}) \tag{3.14}$$

When damping is present, the system oscillates with the damped eigenfrequency, given by $\omega_d = \omega_0\sqrt{1-\lambda^2}$, where $\lambda = \frac{c}{2m\omega_0}$. The displacement of a damped system as a function of time is given by equation 3.15, where $R$ is the amplitude.(Larsen, 2014)

$$r(t) = e^{-\lambda\omega_0 t} R cos(\omega_d t) \tag{3.15}$$

## 3.3 Buckling of curved beams

Buckling of arches subjected to lateral loading is called snap- through. The phenomenon of snap-through can be explained as a “sudden jump between remote configurations”(Abdelgawad et al., 2013). This occurs when the lateral load exceeds the critical buckling load, which results in a sudden curvature reversal. An illustration of the phenomenon is shown in figure 3.3. The dynamic buckling load is in general lower than the static buckling load (Cheung and Babcock, 1970; Kounadis et al., 1989; Pi and Bradford, 2008). Dynamic buckling can occur when an action, for example a suddenly applied load, causes an arch to oscillate. If the oscillation amplitude is sufficiently large, then the arch is in danger of reaching an unstable equilibrium position, i.e. it buckles (Pi and Bradford, 2008). The phenomenon of more than one equilibrium conditions for a simple truss-model is illustrated in figure 3.4. Here, $R$ is the load level and $r$ is the displacement. Figure 3.4a shows how the resistance changes along with the deformation of the truss-model, and figure 3.4b illustrates how the model can have three different equilibrium positions at the same load level.

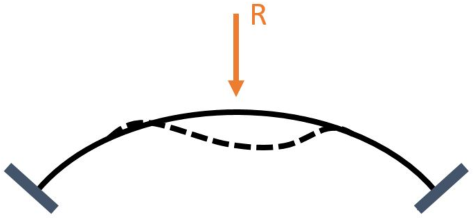

Figure 3.3: Illustration of the snap-through phenomenon.

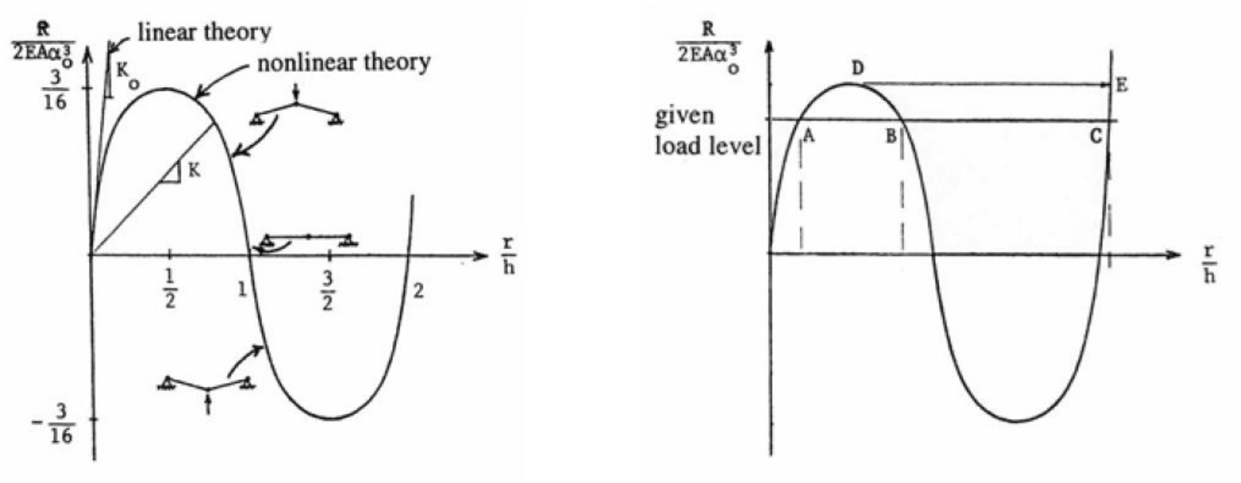

(a) Example of load-deformation curve

(b) Example of load level with three different equilibrium positions.

Figure 3.4: Load-deformation curve for a simple truss-model. From: (Moan, 2003)

## 3.4 Ship collision

This section presents some commonly applied methods and definitions applied when assessing ship collisions. The described principles are closely related to those exercised in the NORSOK-standards.

### 3.4.1 Terms and design principles

The NORSOK-standards distinguish between compliant and fixed structures. An installation is assumed to be compliant when “the duration of impact is small compared to the fundamental period of vibration of the installation”(NORSOK, 2004). On the contrary, if the duration of the impact is long compared to the fundamental eigenperiods, the structure is assumed to be fixed(NORSOK, 2004). By implementing the theory described in section 3.2, it is seen that inertia dominated systems are assumed to be compliant, while stiffness dominated systems are assumed to behave as fixed installations.

The NORSOK-standards operate with three design principles when considering ship collision. A ship collision is characterized by the initial kinetic energy of the ship, given by the mass and impact velocity of the vessel. If the vessel hits a fixed structure, almost all the kinetic energy must be dissipated by local deformations of the ship and installation(NORSOK, 2004). According to NORSOK n-004 “Design of steel structures”, the elastic strain energy is negligible compared to plastic strain energy in these local deformations(NORSOK, 2004). If the installation is compliant, a portion of the energy may remain kinetic after the impact(NORSOK, 2004). Based on how kinetic energy is dissipated by local deformations, it is distinguished between three design principles; strength design, ductile design and shared-energy design. See figure 3.5 for a visualization of the three principles.

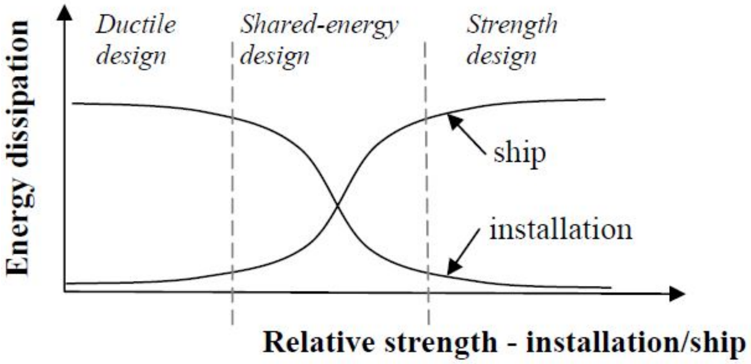

Figure 3.5: Design principles for dissipation of energy in ship collisions. From: (NORSOK, 2004)

In strength design, the installation is capable of withstanding the collision force with only small strain deformations(NORSOK, 2004). In other words, the ship must absorb the majority of the strain energy. In ductile design, on the other hand, the strain energy taken by the installation governs. As the name suggests, the strain energy is shared between the ship and the structure in shared-energy design.(NORSOK, 2004)

In NORSOK n-004 “Design of steel structures”, response problems are divided into three categories based on the duration of the loading relative to the fundamental period of the system. The categorization is aimed at explosions, but it is also of interest when considering other impulsive loads such as ship collision. The first response category is the impulsive domain, i.e. the duration of the load is relatively short. For a impulsive load with duration $t_d$ and an installation with fundamental period $T$, the impulsive domain applies for loads with $t_d/T < 0.3$. In this domain, the structure is capable of resisting large impulses, as long as the duration of the load is short(NORSOK, 2004). Further, the dynamic domain is defined as $0.3 < t_d/T < 3$ and the quasi-static domain as $3 < t_d/T$. In the dynamic domain, the response problem must be solved by integration of the dynamic equation of motion, i.e. equation 3.2(NORSOK, 2004). For quasi-static problems, the load is applied at a slower rate, and the dynamic effects can be accounted for by including a dynamic amplification factor(Haver, 2017).(NORSOK, 2004)

### 3.4.2 Collision mechanics

The NORSOK-standard “Actions and action effects” recommends the decoupled approach for ship collisions within the impulsive domain(NORSOK, 2007). The main feature of the decoupled approach is the disconnection between the external dynamics and the internal mechanics of the collision impact(Yu et al., 2016). This means that the installation is assumed fixed when considering the internal mechanics. The method is applicable in case of a head-on collision between a ship and a stationary structure(Yu et al., 2016).

External dynamics includes the rigid body motions of the colliding objects, and any added mass effects of the water(Pedersen and Zhang, 1998). This indicates that external collision mechanics is governed by the conservation of momentum and the conservation of energy. It is further assumed that the collision is perfectly inelastic, i.e. the ship and the impacted structure are connected to each other after the impact, traveling with a common velocity $v_c$. If the mass and added mass of the ship and the installation are denoted by $m_s$, $a_s$ and $m_i$, $a_i$, respectively, and the velocity of the ship at the time of the impact is $v_s$, then the conservation of momentum can be expressed as:

$$(m_s + a_s)v_s + (m_i + a_i)v_i = (m_s + a_s + m_i + a_i)v_c \tag{3.16}$$

Equation 3.17 can be rearranged to find an expression for the common velocity, see equation 3.17.

$$v_c = \frac{(m_s + a_s)v_s + (m_i + a_i)v_i}{(m_s + a_s + m_i + a_i)} \tag{3.17}$$

The conservation of energy can be expressed as given in 3.18, where $E_s$ is the total amount of energy dissipated by the plastic deformations of both ship and structure.

$$\frac{1}{2}(m_s + a_s)v_s^2 + \frac{1}{2}(m_i + a_i)v_i^2 = \frac{1}{2}(m_s + a_s + m_i + a_i)v_c^2 + E_s \tag{3.18}$$

By inserting the expression for $v_c$ from 3.17 into equation 3.18, an expression for the strain energy dissipation can be found, see equation 3.19. This is the formula given in NORSOK n-004 for ship impacts with compliant structures(NORSOK, 2004).

$$E_s = \frac{1}{2}(m_s + a_s)v_s^2 \frac{(1 - \frac{v_i}{v_s})^2}{1 + \frac{m_s + a_s}{m_i + a_i}} \tag{3.19}$$

When the strain energy is found, the internal mechanics of the collision can be investigated. The internal mechanics of the collision deal with the local plastic deformations and damages of the two colliding objects(Pedersen and Zhang, 1998). NORSOK n-004 recommends the use of force-deformation curves(NORSOK, 2004). A load-deformation curve illustrates a structure’s resistance against deformation. The strain energy dissipated for a given load level is equal to the area below the curve, see figure 3.6. Recalling Newton’s third law, it

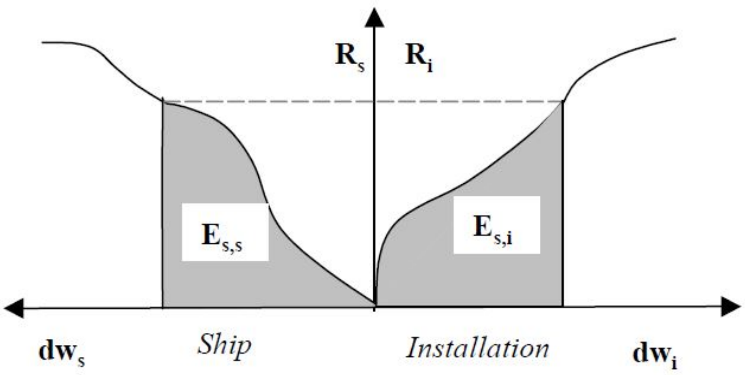

Figure 3.6: Example of a combined load-deformation curve for a ship and an installation. The total dissipated strain energy for the given load level is equal to the grey area below the curves. From: (NORSOK, 2004)

is apparent that the load acting on the ship and installed structure must be the same, i.e. $R_s$=$R_i$. Given that the curves are known, and that the total strain energy, $E_s$, is known from external considerations, equation 3.20 may now be solved.

$$E_s = E_{s,s} + E_{s,i} = \int_0^{w_{s,max}} R_s dw_s + \int_0^{w_{i,max}} R_i dw_i \tag{3.20}$$

This way, the magnitude of the impact load is found. The solution will also reveal which of the components absorbs the most of the strain energy and the corresponding deformations.

### 3.4.3 Current codes and regulations on determining design loads

Standards such as the NORSOK standards, the Eurocodes and the AASHTO standards provide guidelines on design against ship collision. In this section, the recommendations of these codes on determining design loads will be described. While the guidelines in the Eurocodes and AASHTO standards are directly applicable for bridges, the NORSOK standards are mainly aimed at offshore installations.

The design loads should be determined based on risk assessments for the relevant area and arrangement of the installation(NORSOK, 2007; AASHTO, 2014; Norsk Standard, 2008). Firstly, the ship traffic in the region close to the installation should be mapped(AASHTO, 2014). The NORSOK standards also emphasize that the anticipated future traffic should be accounted for(NORSOK, 2007). Based on the risk assessment, one or more design vessels can be decided upon. Ship mass, transit velocity and direction, frequency of transit under the bridge and historical accident statistics of the ship should all be taken into account when assessing the probability and severity of a collision(AASHTO, 2014).

If a design vessel has been decided upon, the impact velocity must also be determined in order to obtain the collision energy. Both the NORSOK and AASHTO standards state that the collision energy should be determined for each bridge component individually(NORSOK, 2007; AASHTO, 2014). The NORSOK standards allow for the assumption of drifting ships, and thus low velocity impacts, for some components(NORSOK, 2007). This is further explained for bridges in the AASHTO standards. Components close to the transit channel will historically be subjected to the largest impact velocities(AASHTO, 2014). This is because ships that hit the bridge far from the channel are drifting, i.e. moving with the current, while ships close to the passage are moving with the transit velocity(AASHTO, 2014). The design impact velocity for components close to the transit channel will therefore be the vessel velocity at normal operating conditions, while reduced velocities may be utilized further away.

The impact load should be applied at the least favorable, yet realistic, location and direction(Norsk Standard, 2008). If relevant, bow, stern and side impacts should all be considered(NORSOK, 2007; AASHTO, 2014; Norsk Standard, 2008). The added mass of the ship can be assumed to be 10% for bow and stern collisions, while for side collisions the added mass can be taken to be 40%(NORSOK, 2007).

## 3.5 Environmental loads

### 3.5.1 Wave theory

In this section, methods for estimating wave loads based on the surface elevation will be reviewed. Faltinsen's "Sea Loads on Ships and Offshore Structures" will serve as the main source of information.

Say that the surface elevation is a representation of an underlying probabilistic model. If this underlying model can be said to be constant within a period of time, then the surface process may be said to be completely described by a wave spectrum(Haver, 2017). When the spectrum is known, it can be used to generate series of surface elevations with the same underlying probabilistic model. Once that a representative surface process is established, the corresponding wave loads can be determined.(Haver, 2017)

Some assumptions are made in the description of ocean waves. Firstly, sea water is assumed to be incompressible, inviscid and irrotational(Faltinsen, 1990). As a consequence of this, the velocity vector $\mathbf{V}$ can be completely described by a scalar function; the velocity potential $\varphi$. See equation 3.21.

$$\mathbf{V} = \nabla\varphi \tag{3.21}$$

If this relation is implemented in the Bernoulli equation, an expression for the pressure $p$ as a function of the velocity potential is obtained, see equation 3.22. Here, $C(t)$ is an arbitrary function of time and $\rho$ is the water density. It is assumed that gravity is the only external force field and that the $z$-axis is vertical with positive direction upwards(Faltinsen, 1990).

$$p = C(t) - \rho g z - \rho\frac{\partial\varphi}{\partial t} - \frac{\rho}{2}\nabla\varphi\cdot\nabla\varphi \tag{3.22}$$

The velocity potential must capture the physical behaviour of the fluid. The behaviour at the free surface is described by two boundary conditions; the kinematic and the dynamic free-surface conditions. Physically, the kinematic condition requires that a fluid particle situated at the free surface remains at the free surface, while the dynamic boundary condition demands that the pressure at the surface is equal to the atmospheric pressure(Faltinsen, 1990). The kinematic and dynamic free surface conditions can be expressed mathematically and solved for $\varphi$.

### 3.5.2 Linear wave theory

If the wave steepness is small, linear wave theory may be applied. Linear implies that higher order terms of the wave amplitude are neglected. A consequence of this is that the free surface conditions are enforced at the mean free surface, z = 0, instead of the exact surface. A differential equation can then be deduced by combining the kinematic and dynamic boundary conditions, see equation 3.23. The velocity potential for a regular wave oscillating with frequency $\omega$ can be found by solving this expression.(Faltinsen, 1990)

$$-\omega^2\varphi + g\frac{\partial\varphi}{\partial z} = 0|_{z=0} \tag{3.23}$$

An irregular wave can be expressed as a sum of regular wave components, see equation 3.24(Faltinsen, 1990). $A_j$, $\omega_j$ and $k_j$ are the amplitude, frequency and wavenumber of component j, while $\beta$ is the angle between the global x-axis and the direction of the wave. The amplitudes corresponding to the various frequencies can be estimated based on the wave spectrum, see equation 3.25(Faltinsen, 1990). The value obtained by this equation is the deterministic amplitude(Haver, 2017).

$$\zeta = \Sigma_{j=1}^{N} A_j sin(\omega_j t - k_j x cos\beta - k_j y sin\beta + \epsilon_j) \tag{3.24}$$

$$A_j = \sqrt{2S_{\zeta\zeta}(\omega_j)\Delta\omega} \tag{3.25}$$

In linear theory, the response caused by a regular wave is proportional to the wave amplitude, and oscillates with the same frequency as the incoming wave. As a consequence, the reaction caused by an irregular wave can be found by adding the response from each wave component. The expression for the response of a given body subjected to an irregular wave is given in equation 3.26(Faltinsen, 1990). In the equation, $\eta$ is the response, $|H(\omega_j)|$ is the transfer function and $\delta(\omega_j)$ is the phase angle between the load and wave component j. The transfer function is the response amplitude per unit wave amplitude.(Faltinsen, 1990)

$$\eta = \Sigma_{j=1}^{N} A_j |H(\omega_j)| sin(\omega_j t - k_j x cos\beta - k_j y sin\beta + \delta(\omega_j) + \epsilon_j) \tag{3.26}$$

In theory, the number of frequency components $N$ should approach infinity, and with $\omega_{min} \to 0$ and $\omega_{max} \to \infty$. If $N$ is finite, the process will repeat itself after $\frac{2\pi N}{\omega_{max}-\omega_{min}}$(Faltinsen, 1990). However, this repetition can be avoided by choosing $\omega_j$ at a random position within each subinterval $\Delta\omega_j$(Faltinsen, 1990). Although this will reduce the demand for frequency resolution,

$N$ must still be chosen such that $(\omega_{max} - \omega_{min}/N$ is a small fraction of the frequency that is to be captured(Faltinsen, 1990). To capture a sinusoidal wave component, at least three sample points are needed within the period of the wave. For that reason, the time step $\Delta t$ defines the highest frequency that can be captured by $\omega_0 \leq \frac{2\pi}{4\Delta t}$(Haver, 2017). When the sampling frequency is $\Delta t$, the cut-off frequency, also called the Nyquist frequency, is given by $f_N = \frac{1}{2\Delta t}$(Haver, 2017). This is half the sampling frequency. Wave components with frequencies higher than the Nyquist frequency will be perceived as if they have frequencies below the Nyquist frequency, see figure 3.7(Lehn, 2009). For more thorough description of the *folding* phenomenon, see "Tidsserier" by Lehn(Lehn, 2009).

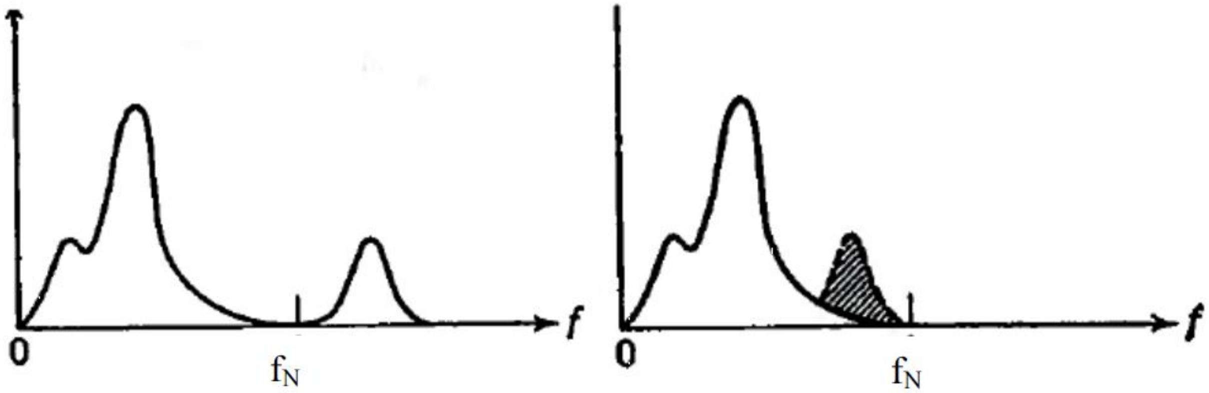

(a) True spectrum

(b) Spectrum with folded signal

Figure 3.7: Illustration of folding about the Nyquist frequency. From: (Lehn, 2009)

It has now been determined that irregular waves can be written as a sum of regular waves and that the response of wave components can be studied individually. Faltinsen distinguishes between two types of loads on a structure in regular incident waves(Faltinsen, 1990). The first category of forces are those that take place when a structure is held fixed in regular incident waves. The resulting load is the excitation force, i.e. the right hand side of equation 3.2. In the other category, there are no incident waves, but the structure is forced to oscillate with the same frequency as the incident waves. The loads caused by the motion are added mass, damping and restoring forces and moments. The last category will not be reviewed any further.

The excitation load is the resultant of fluid pressure on the surface of the body(Greco, 2016). The pressure field can be subdivided into two components. The first component is the pressure in the undisturbed wave, as if the structure were not there. This pressure results in Froude-Kriloff forces and moments. The other pressure component results from the disturbance of the wave. Physically, this means that the presence of the structure causes diffraction waves. These waves can be modelled by a velocity potential $\varphi_D$, which due to linearity can be added to the velocity potential of the incident wave(Greco, 2016). The total velocity potential, $\varphi_{tot} = \varphi_0 + \varphi_D$, is found such that the boundary conditions at the surface of the body are satisfied. Subsequently, the total pressure can be derived. The loads are linearized, which means that the pressure is integrated to the mean free surface, z=0.(Greco, 2016)

### 3.5.3 Difference-frequency effects

In the previous section, linear theory was touched upon. The load was shown to oscillate with the same frequency as the incident wave. In general, structures will also experience nonlinear effects. In nonlinear theory, higher order terms of the wave amplitude are included, and boundary conditions are satisfied at the true surface. In addition, the pressure integration accounts for the instantaneous position of the body(Faltinsen, 1990). By solving the nonlinear problem, it is found that the structure is subjected to mean drift, sum-frequency and difference-frequency effects(Faltinsen, 1990). This section will elaborate upon difference-frequency effects, as these may excite resonance motions in structures with long eigenperiods. For more information on nonlinear effects, see Faltinsen page 131-170.(Faltinsen, 1990)

Difference-frequency effects are slowly varying wave loads, oscillating with a frequency equal to the difference between two wave frequencies(Faltinsen, 1990). Accordingly, the effect is only relevant in irregular waves with at least two different frequency components. If the structure has eigenmodes with high eigehperiods, difference-frequency effects may become of equal importance as first order effects(Faltinsen, 1990). The reason for this is that the linear damping due to wave radiation will be small when the oscillation frequency is low(Greco, 2016).

The presence of difference-frequency effects in a two-component wave can be proven by including second-order terms from the $\frac{\rho}{2}\nabla\varphi \cdot \nabla\varphi$-term in equation 3.22(Faltinsen (1990), p.133). This can also be generalized for a $N$-component wave. The second-order potential $\varphi_2$ will also contribute to slow-drift excitation(Faltinsen, 1990). A general formula for the slowly varying excitation force, $F_i^{SV}$, is given in “Sea loads on ship and offshor structures” as(Faltinsen, 1990):

$$F_i^{SV} = \Sigma_{j=1}^{N}\Sigma_{k=1}^{N} A_j A_k [T_{jk}^{ic} cos\{(\omega_k - \omega_j)t + (\epsilon_k - \epsilon_j)\} + T_{jk}^{is} sin\{(\omega_k - \omega_j)t + (\epsilon_k - \epsilon_j)\}] \quad (3.27)$$

In equation 3.27, $F_i^{SV}$ is the slow-drift force in direction $i$. $A_j$ and $A_k$ are the amplitudes of wave components $j$ and $k$, while $\epsilon_k$ and $\epsilon_j$ are their phase angles. $T_{jk}^{ic}$ and $T_{jk}^{is}$ are constants corresponding to the cosine and sine term, respectively. These can be regarded as second-order transfer functions, which implies that they functions of the $\omega_k$ and $\omega_j$, but are independent of the amplitudes.(Faltinsen, 1990)

Newman's approximation can used to simplify the expression for the slowly varying drift force. Basically, the idea of this approximation is to express $T_{jk}^{ic}$,$T_{kj}^{ic}$, $T_{kj}^{is}$ and $T_{jk}^{is}$ as functions of $T_{jj}^{ic}$, $T_{kk}^{ic}$, $T_{jj}^{is}$ and $T_{kk}^{is}$, see equation 3.28 and 3.29.

$$T_{jk}^{ic} = T_{kj}^{ic} = 0.5(T_{jj}^{ic} + T_{kk}^{ic}) \quad (3.28)$$

$$T_{jk}^{is} = T_{kj}^{is} = 0 \quad (3.29)$$

By implementing equations 3.28 and 3.29 in equation 3.27, and further approximating the double summation by the square of one single series, equation 3.30 is obtained(Faltinsen, 1990).

$$F_i^{SV} = 2[\Sigma_{j=1}^{N} A_j (T_{jj}^{ic})^{1/2} cos(\omega_j t + \epsilon_j)]^2 \quad (3.30)$$

The advantages of the Newman's approximation are that the computational time is reduced and that the second-order velocity potential is not needed. The approximation yields good results when $\omega_j$ and $\omega_k$ are close(Faltinsen, 1990). The reason for this is that the transfer functions $T^{ic}_{jk}$ and $T^{is}_{jk}$ do not change that much with the frequency, as long as there are no maxima or minima in the area of the line $\omega_j = \omega_k$. When $\omega_j$ and $\omega_k$ are not close, i.e. when $\omega_j - \omega_k$ is large, the oscillation period will be low. For structures with high eigenperiods, these components will be of secondary importance.(Faltinsen, 1990)

The Newman's approximation also has some disadvantages. Firstly, equation 3.30 will include high-frequency effects, which are unwarranted due to the approximations in equations 3.28 and 3.29(Faltinsen, 1990). Also, the coefficient $T^{ic}_{jj}$ has to be positive(Faltinsen, 1990). According to the recommended practice by DNV, Newman's approximation yields adequate results for slow drift forces in the horizontal plane, but vertical motions may be underestimated(Det Norske Veritas, 2010c).

Faltinsen shows that the slowly varying drift force has a non-zero mean value when $j = k$. The mean value is given in equation 3.31(Faltinsen, 1990). Here, $A^2_j T^{ic}_{jj}$ is the mean wave load in direction $i$ caused by a regular incident wave with amplitude $A_j$(Faltinsen, 1990). Thus, $T^{ic}_{jj}$ can be expressed as shown in equation 3.32(Greco, 2016). This is the mean drift coefficient, which is independent of the wave amplitude(Faltinsen, 1990). As far as there is no current and the structure has no forward speed, the coefficient will only depend on the first-order solution in regular waves(Faltinsen (1990),p.134). This is because the pressure caused by the second-order potential has zero mean value when integrated over one period of oscillation. Thus, the response caused by an irregular wave can be found by adding the response of the regular wave components.(Faltinsen, 1990)

$$\bar{F}^{SV}_i = \Sigma^N_{j=1} A^2_j T^{ic}_{jj} \tag{3.31}$$

$$T^{ic}_{jj} = \frac{\bar{F}_i(\omega_j, \beta)}{\zeta^2_a} \tag{3.32}$$

Mean drift forces are related to the structure's ability to cause waves by reflection(Faltinsen, 1990). The mean wave forces can be found either by applying the principle of conservation of momentum, also called far field integration, or by the direct pressure integration method. The latter method might experience issues when a body has sharp corners.(Faltinsen, 1990)

### 3.5.4 JONSWAP spectrum

During the design phase of a project, the exact wave spectrum for the relevant area is usually unknown(Myrhaug, 2007). As a consequence, there is a need for generalized wave spectra to describe wave conditions. Examples of such generalized spectra are the Pierson-Moskowitz spectrum and the JONSWAP spectrum. The spectrum selected to represent the wave condition must be regarded as an approximation, and cannot be expected to be accurate for all frequencies(Myrhaug, 2007). A sensitivity study with respect to the input parameters should therefore be conducted. In this section, the JONSWAP spectrum will be addressed.

The JONSWAP spectrum is based on measurements from the southeast part of the North Sea, at an area close to shore with shallow water depths(Myrhaug, 2007). It is applicable for wind waves in developing sea. As a result, the spectrum has a narrow peak, indicating that the majority of the energy is distributed over a short range of frequencies(Myrhaug, 2007). In the recommended practice by DNV, the following expression for the JONSWAP spectrum is applied(Det Norske Veritas, 2010b).

$$S_{\zeta\zeta}(\omega) = (1 - 0.287ln(\gamma))\frac{5}{16}H_s^2\omega_p^4\omega^{-5}exp(-\frac{5}{4}(\frac{\omega}{\omega_p})^{-4})\gamma^{exp(-0.5(\frac{\omega-\omega_p}{\sigma\omega_p})^2)} \tag{3.33}$$

In the equation, $H_s$ is the significant wave height for the wave condition, $\omega_p$ is the angular spectral peak frequency, $\gamma$ is the non-dimensional peak shape parameter and $\sigma$ is the spectral width parameter(Det Norske Veritas, 2010b). The latter is defined accordingly:

$$\sigma = \begin{cases} \sigma_a & \text{if } \omega \leq \omega_p \\ \sigma_b & \text{if } \omega > \omega_p \end{cases} \tag{3.34}$$

In the JONSWAP experimental data, the average values for the parameters are $\gamma = 3.3$, $\sigma_a = 0.07$ and $\sigma_b = 0.09$(Det Norske Veritas, 2010b).

### 3.5.5 Predicting extreme wave loads

In this section, methods for predicting extreme wave loads and extreme wave responses will be reviewed. First, some of the basic principles in stochastic modelling of ocean waves are explained.

The wave process can be subdivided into time-intervals, within which the underlying statistical model of the wave process is assumed constant. In other words, the significant wave height and peak period is constant within the interval(Haver, 2017). In the North Sea, it is common practice to consider 3-hour intervals. The maximum response within a given 3-hour interval is denoted $X_{3h}$, and is a function of the significant wave height, $H_s$, and the spectral peak period, $T_p$. The conditional cumulative distribution of $X_{3h}$ is denoted $F_{X_{3h}|H_sT_p}(x|h,t)$. The joint distribution of $H_s$ and $T_p$, $f_{H_sT_p}(h,t)$, can be considered the long term distribution of the sea states. From this, the marginal distribution of $X_{3h}$, $F_{X_{3h}}(x)$, can be determined according to equation 3.35(Haver, 2017). This is the long term distribution of the maximum response within an arbitrary 3-hour sea state.(Haver, 2017)

$$F_{X_{3h}}(x) = \int_h\int_t F_{X_{3h}|H_sT_p}(x|h,t)f_{H_sT_p}(h,t)dhdt \tag{3.35}$$

The response corresponding to an annual exceedance probability of q, $X_q$, can then be estimated based on equation 3.36(Haver, 2017). Here, $m_{3h}$ is the number of 3-hour sea states per year. If all sea states are included, $m_{3h}$=2920. When considering the accidental limit state, q=$10^{-4}$.

$$1 - F_{X_{3h}}(x) = \frac{q}{m_{3h}} \tag{3.36}$$

The nature of the response problem should be taken into account in order to determine a suitable method for predicting extreme responses. When considering quasi-static structures, where the response is governed by the instantaneous wave load, the design wave method is applicable(Haver, 2017). When applying this method, the response of a structure subjected to the q-probability wave is determined as a function of time. The maximum response in the time history is the q-probability response. When dynamic effects, i.e. previous load history, become important, this method is not suitable. In this case, the preferred method is to carry out a full long term analysis(Haver, 2017), where equations 3.35 and 3.36 are solved. However, if the relation between the sea state and the response magnitude is complex, it can be time consuming and expensive to establish $F_{X_{3h}|H_sT_p}(x|h,t)$, for example if model tests are required. For complex problems, the contour line method is a good option. This method will be described next.(Haver, 2017)

### 3.5.6 The contour line method

The metocean contour line method is well suited for non-linear response problems, for example problems where low-frequency effects are of importance(Haver, 2017). The advantage of this method, compared to a full long term analysis, is that only a few sea states need to be examined. The first step is to establish the contour line for sea states with q-probability of exceedance annually. A set of typical contour lines are illustrated in figure 3.8, where the 1-year, 100-year and 10 000-year contour lines are indicated. The idea is that a small number of sea states situated on the contour are identified as the most critical with respect to response. Typically, these are the sea states with the largest significant wave heights. Further, a number of time domain analyses, or model tests, are carried out with each of the selected sea states. Based on these simulations, the most critical sea state along the q-probability contour line is determined.(Haver, 2017)

When the most critical sea state is identified, a larger number of 3-hour simulations are run, such that a sample of values for $X_{3h}$ is obtained. If the 100-year contour is considered, it is preferable that the sample size exceeds 20(Haver, 2017). A probabilistic model is then fitted to the sample of 3-hour maximums. Haver recommends to fit a Gumbel-model to the sample by using the method of moments(Haver, 2017). The fitted distribution is denoted $F_{X_{3h}|H_sT_p}(x|h_s^*,t_p^*)$, where $h_s^*$ and $t_p^*$ are the parameters of the worst sea state along the contour. The q-probability response is estimated by solving equation 3.37. In the equation, $\alpha$ is an empirical percentile used to identify the q-probability response, $x_\alpha$.(Haver, 2017)

$$F_{X_{3h}|H_sT_p}(x_\alpha|h_s^*,t_p^*) = \alpha \tag{3.37}$$

If the short term variability is negligible, then the mean value of $X_{3h}$ can be used as the q-probability response. This corresponds to $\alpha$=0.5. However, this is generally not the case(Haver, 2017). Therefore, a value corresponding to a higher percentile is used. NORSOK recommends $\alpha$=0.85-0.95 in the ultimate limit state and $\alpha$=0.9-0.95 in the accidental limit state(NORSOK, 2007). In order to ensure conservatism, Haver recommends to use $\alpha$=0.90 when identifying the $10^{-2}$-probability response, and $\alpha$=0.95 for the $10^{-4}$-probability response(Haver, 2017).

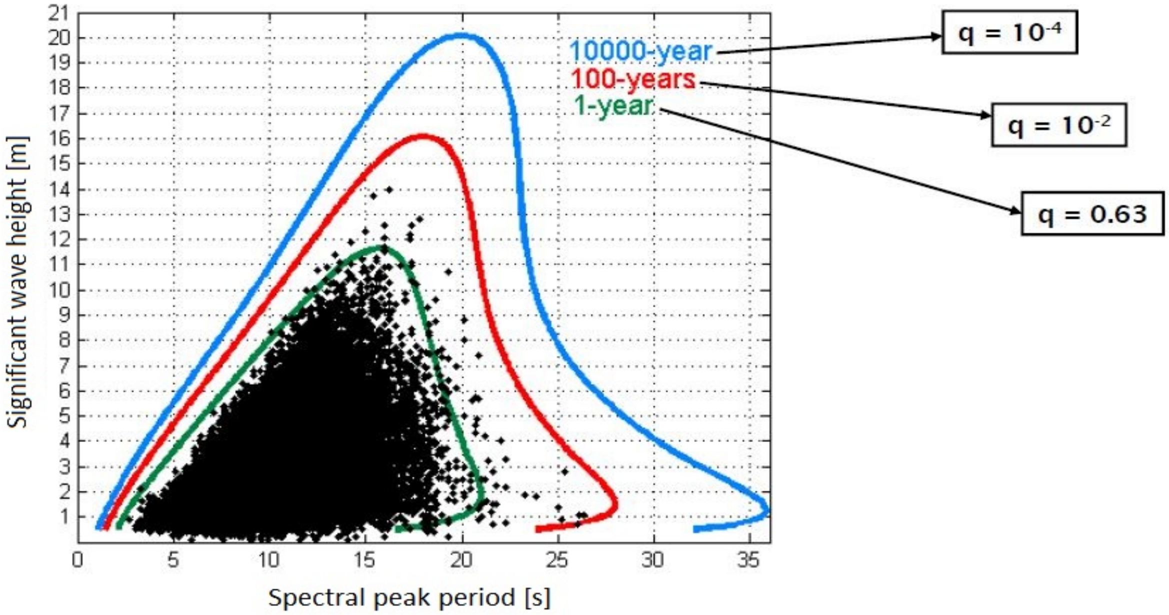

Figure 3.8: Example of contour lines. From: (Haver, 2017)

### 3.5.7 Distribution of the largest wave height and response

The aim of this section is to provide a simple method of estimating the characteristic largest wave height. Consider a time interval with $N$ waves, for example a three hour interval. The characteristic largest wave height is then the wave height that is exceeded by only one of the $N$ wave heights(Myrhaug, 2007).

Say that the wave heights are denoted $H_1, H_2, ..., H_N$, and that $H_{max}$ is the largest out of these. Further, it is assumed that all the wave heights are identically Rayleigh distributed and that they are all statistically independent. Based on these assumptions, it can be shown that the distribution of the maximum wave height is given by equation 3.38, where $F_H(h)$ is the distribution of individual wave heights(Myrhaug, 2007).

$$F_{H_{max}}(h) = [F_H(h)]^N \tag{3.38}$$

The most probable largest wave height, $H_M$ is given by the maximum of $f_{H_{max}}(h)$, which is given by:

$$[\frac{d}{dh}f_{H_{max}}(h)]_{h=H_M} = 0 \tag{3.39}$$

When $N$ becomes large, it can be shown that the characteristic largest wave height can be approximated by equation 3.40(Myrhaug, 2007).

$$H_M = 2\sqrt{2m_{0,\zeta\zeta}lnN} \tag{3.40}$$

In the equation, $m_0$ is the variance of the surface elevation, which is given by:

$$m_{0,\zeta\zeta} = \int_0^\infty S_{\zeta\zeta}(\omega)d\omega \tag{3.41}$$

The derivation is also applicable for the characteristic largest response, $X_M$(Myrhaug, 2005). Since it is the amplitude of the response that is of interest, the expression becomes:

$$X_M = \sqrt{2m_{0,XX} lnN} \tag{3.42}$$

The response spectrum can be established based on the wave spectrum and the transfer function:

$$S_{XX} = |H_{\zeta X}(\omega)|^2 S_{\zeta\zeta}(\omega) \tag{3.43}$$

### 3.5.8 Wind theory

According to NORSOK, wind loads must be accounted for when modelling extreme environmental loads, see figure 3.1. Wind is comparable to current, and can induce drag, lift and torsional loads(Faltinsen, 1990). This section will review some basic principles for local description of wind. In addition, the theory implemented in WindSim will be briefly explained. WindSim is a computational tool for simulating of wind.

Wind velocity may be considered the sum of a slowly varying mean wind and a fluctuating part, i.e. a higher-frequency wind gust. The mean wind decreases with decreasing elevation above the ground, while the gust component is fairly independent of the altitude(Myrhaug, 2014). If the mean wind is aligned with the x-axis, wind velocity can be expressed as:

$$U(x,y,z,t) = [U(z) + u(x,y,z,t)]\mathbf{i} + v(x,y,z,t)\mathbf{j} + w(x,y,z,t)\mathbf{k} \tag{3.44}$$

In equation 3.44, $U(z)$ is the mean wind velocity profile and $u$, $v$ and $w$ are the wind gust components. The mean wind velocity profile is given by the $\alpha$-profile in WindSim(Aas-Jakobsen), see equation 3.45. In the equation, $z_{ref}$ is the reference height, $U_{ref}$ is the mean wind velocity at $z_{ref}$ and $\alpha$ is the shape parameter of the profile.

$$U(z) = U_{ref}(\frac{z}{z_{ref}})^{\alpha} \tag{3.45}$$

The remaining part of this section will focus on the theory applied in WindSim. The wind gust is described by the one point wind spectra(Aas-Jakobsen). The spectrum for the gust component in direction $i$ is given by the Kaimal spectrum in equation 3.46. $I_i$ is the turbulence intensity, defined as the standard deviation of the wind gust divided by the mean wind velocity. $U_{10min}$ is the mean wind taken as the average over 10 minutes. $L_i$ is the length of the area over which the wind is considered and $f$ is the frequency.(Aas-Jakobsen)

$$S_i(f) = \frac{I_i^2 U_{10min} L_i}{(1 + 1.5\frac{f \cdot L_i}{U_{10min}})^{5/3}} \tag{3.46}$$

WindSim also offers a variation of the Kaimal spectrum, where the input parameters are taken as those specified in DNV-OS-J101(Aas-Jakobsen, 2015). The spectrum is given in equation 3.47. Here, the standard deviation is taken as $\sigma(z) = I_u U(z)$, $L_k(z) = 5.67z$ for $z < 60\ m$ and $L_k = 340.2$ for $z > 60\ m$.

$$S_i(f) = \sigma_u^2 \frac{4 \cdot \frac{L_k(z)}{U(z)}}{(1 + 6.0\frac{f \cdot L_k}{U(z)})^{5/3}} \tag{3.47}$$

Say that we have two arbitrary points, $s_i$ and $s_j$, separated by a distance s=$|s_i - s_j|$. The cross-spectrum can then be expressed as a function of the two single-point spectra(Aas-Jakobsen and Strømmen, 2001):

$$S_{ij}(s,f) = \sqrt{S_i(f)S_j(f)}\sqrt{coh_{ij}(s,f)}\exp\left[i\Phi_{ij}(f)\right] \tag{3.48}$$

In equation 3.48, $i$ is the imaginary unit and $\Phi_{ij}(f)$ is the phase spectrum. The coherence function $coh_{ij}(s,f)$ is calculated according to equation 3.49, where $c_i$ is a decay constant(Aas-Jakobsen). It is seen that the coherence approaches zero when the distance $s \rightarrow \infty$. When $s \rightarrow 0$, the coherence approaches 1.

$$\sqrt{coh_{ij}(f,s)} = exp(-\frac{c_i \cdot f \cdot s}{U_{10min}}) \tag{3.49}$$

It is assumed that the cross-variance between $u$, $v$ and $w$ can be neglected, such that $u$, $v$ and $w$ can be determined independently. The frequency range is divided into N sections, while the flow is field is divided into M points. For each of the N frequencies, a MxM matrix, S, containing the cross spectra $S_{ij}(s,f_n)$ is determined. A lower triangular matrix G is found by Cholesky decomposition, such that $S = GxG^T$(Aas-Jakobsen). For $f_m$=$u$, $v$ or $w$ at point m, a time domain simulation of the process is found with equation 3.50(Aas-Jakobsen and Strømmen, 2001). Here, the angular frequency $\omega_n$=$2\pi f_n$ is used. The phase angle $\varphi_{mk}(\omega_n)$ is a random value, evenly distributed between 0 and $2\pi$.

$$f_m(t) = \Sigma_{k=1}^{m}\Sigma_{n=1}^{N-1}|G_{mk}(\omega_n)|\sqrt{2\cdot\Delta\omega}cos[\omega_n t + \varphi_{mk}(\omega_n)] \tag{3.50}$$

For more detailed explanations, see Aas-Jakobsen and Strømmen(Aas-Jakobsen and Strømmen, 2001).

# Chapter 4

# Modelling of the Bridge in USFOS

## 4.1 Description of bridge design

This section will provide a brief description of the end-anchored floating bridge.

The end-anchored floating bridge is a single girder, curved bridge with one cable-stayed part and one part supported by pontoons. An illustration of the model is given in figure 4.1. The orientation of the bridge is given in figure 4.2. The arrow indicates the northward direction. As indicated in the figure, the curvature in the horizontal plane is 5 km.

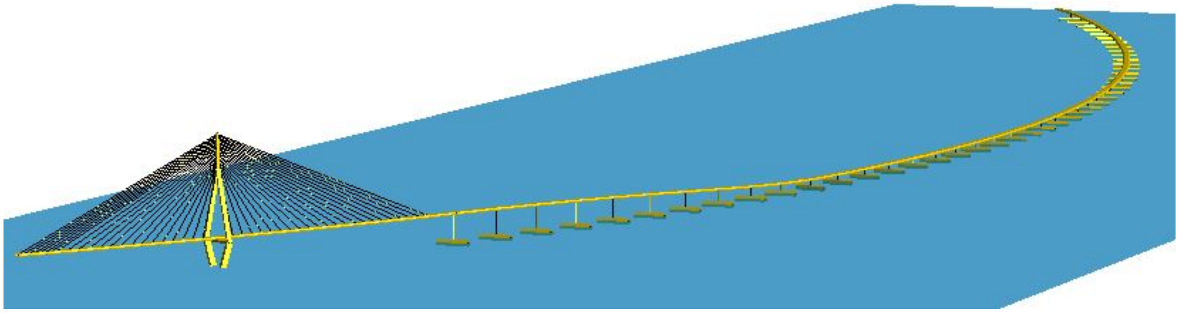

Figure 4.1: USFOS-model of the bridge seen from the south end.

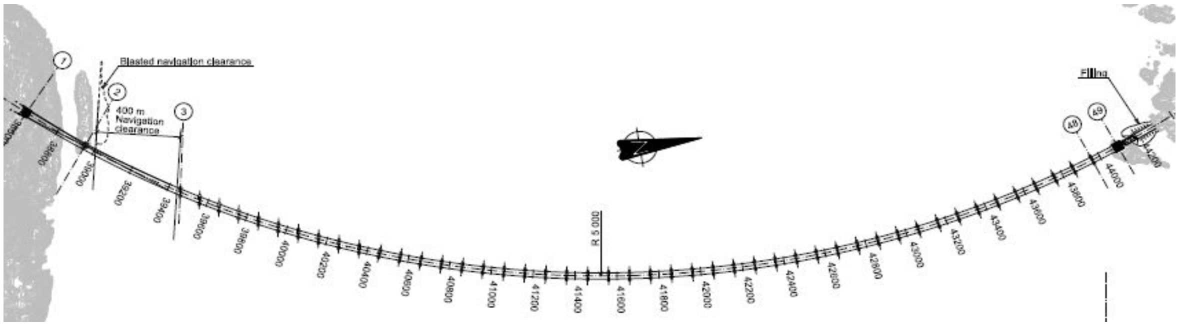

Figure 4.2: Orientation of the bridge as seen from above. The arrow indicates geographic north. From: (Norconsult AS, 2017a)

The cable-stayed part of the bridge is at the south end, which will simply be referred to as the south end of the bridge. In this region, the bridge girder is supported by a 232 $m$ tall tower. The tower and bridge girder are connected by tension cables at both sides of the tower. The cables occur in pairs, with one connection at each side of the girder. In total, there are 44 of these cable-pairs, 22 at each side of the tower. To be exact, 7 of the south cable-pairs are anchored to the ground. The purpose of the cable-stayed section is to serve as a passage for ships, and the south end is therefore elevated compared to the remaining part of the bridge. The maximum girder elevation is about 55 $m$.

The main part of the bridge is a floating bridge configuration, where the weight of the bridge girder is supported by a total of 46 pontoons. The span between pontoons is approximately 100 $m$. Each pontoon is connected to the bridge by a single column. In the region after the cable-stayed part, the elevation of the girder decreases until it reaches approximately 14.4 $m$ at the tenth pontoon. After this, the heights of the columns are constant. Columns are numbered from the south end, such that the first column after the cable-stayed bridge is column 1 and the last column at the north end is column 46.

The report “K7 Bjørnafjorden end-anchored floating bridge - Appendix 1 - Model” by Norconsult describes the modelling approach applied when modelling the bridge in the software 3DFloat(Norconsult AS, 2017f). This report is used in order to obtain the properties of the bridge, along with the structural drawings in the document “K7 Bjørnafjorden End-anchored floating bridge Appendix A – Drawings binder”(Norconsult AS, 2017a). These two documents will be referred to as the model description and the drawings, respectively.

In the drawings of the bridge, the bridge is divided into three parts; the cable-stayed bridge, the floating high bridge and the floating low bridge. The cable-stayed bridge starts at the south end and ends at the connection between the bridge girder and the $40^{th}$ cable-pair. The floating high bridge includes the last four cable-pairs and ends after column 12. The floating low bridge is the remaining part of the bridge. These terms will be used when describing of the modelling steps.

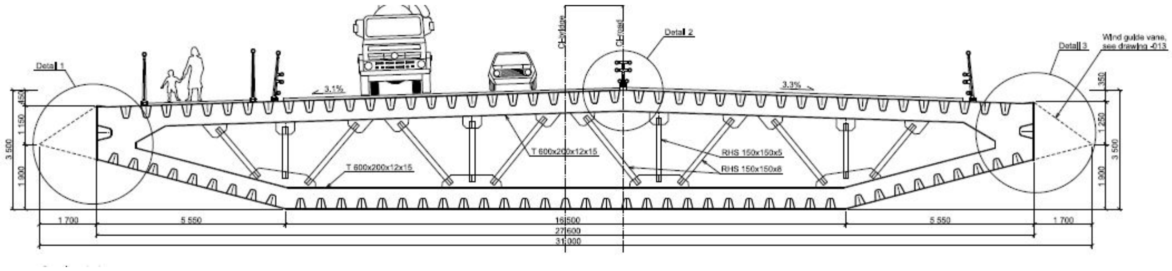

Figure 4.3: General cross section of the bridge girder. From: (Norconsult AS, 2017a)

## 4.2 Modelling of the bridge girder

Two-node beam elements are used to model the bridge girder. The general cross section of the girder is shown in figure 4.3. The diaphragms, i.e. the bracing and transverse girders shown in the figure, are repeated every $4^{th}$ meter(Norconsult AS, 2017c). Between these, only the stiffeners and plates carry the weight. Due to the complexity of the cross section, the general beam element in USFOS is used to model the bridge girder. A single beam element with constant cross section is applied between each column. Only the stiffeners and plates are considered in the calculation of the cross section parameters, i.e. area, moment of inertia, plastic section modulus and shear area. When estimating the mass, however, the diaphragms are also taken into account. The constant cross section simplification should be justifiable since the girder elements are slender, thus the weight will mainly be carried by bending stresses. The transverse girders will not affect the bending capacity.

The girder has three main types of cross sections. Type 1 is found in the cable-stayed part of the bridge and the floating-low bridge, type 2 is applied in the floating high bridge and type 3 is at the ends of the bridge. For simplicity, the girder type is changed at nodes and not at the exact transition locations. This is believed to be of minor importance, but since it will affect the mass and strength in the transitional areas, these locations are checked. In static analyses, it is found that the plastic utilization is high in the northern end-support. The yield strength of girder type 3 is therefore increased. As long as the stresses at the ends are monitored, this should be an acceptable adjustment; local stress distribution is not the topic of interest in this thesis, and the exact girder design at the ends is unknown. The properties of the girder cross sections, as implemented in the USFOS-model, are shown in table 4.1. The values for the second moments of area are obtained from the model description(Norconsult AS, 2017f).

Simplified hand-calculations are carried out to confirm the second moments of area and to estimate the remaining input values required. In the calculations, the cross section is estimated by a rectangular box with height 3.5 $m$ and width 24 $m$. An equivalent plate thickness is used, where the stiffener area is "smeared out" and added to the original plate thickness. The torsional moment of area for the simplified cross section is found according to equation 4.1(Leira, 2015), where $A_0$ is the enclosed area. The equivalent thickness is used. The second moments of area about the y- and z-axes are calculated according to the standard formula for hollow rectangular box-sections.

Table 4.1: Properties of the main girder cross sections.

| **Girder cross-section type** | **Postion along arch**[m] | **Area** $[m^2]$ | $\mathbf{I}_t$ $[m^4]$ | $\mathbf{I}_y$ $[m^4]$ | $\mathbf{I}_z$ $[m^4]$ | $\mathbf{W}_{px}$ $[m^3]$ | $\mathbf{W}_{py}$ $[m^3]$ | $\mathbf{W}_{pz}$ $[m^3]$ | $\mathbf{Sh}_y$ $[m^2]$ | $\mathbf{Sh}_z$ $[m^2]$ |
|---|---|---|---|---|---|---|---|---|---|---|
| **1** | 110-750<br>1827.5-5475 | 1.43 | 6.10 | 2.68 | 115.62 | 2.3 | 1.65 | 7.81 | 0.624 | 0.245 |
| **2** | 750-1827.5 | 1.68 | 7.32 | 3.2 | 132.47 | 2.76 | 1.94 | 8.82 | 0.624 | 0.245 |
| **3** | 0-110<br>5475-5515 | 1.68 | 10.86 | 5.049 | 181.1 | 3.61 | 1.94 | 8.82 | 0.624 | 0.245 |

$$I_t = \frac{4A_0^2}{\int \frac{ds}{t}} \tag{4.1}$$

The plastic section moduli about the y- and z-axes are calculated according to equation 4.2(Amdahl, 2010). The plastic torsional section modulus, $W_{px}$, is approximated by using the elastic torsion modulus obtained from the model description(Norconsult AS, 2017f). The shear area in the $y$-direction can be taken as the cross-sectional area of the horizontal plates, while the shear area in the $z$-direction can be taken as the cross-sectional area of the vertical plates(Amdahl, 2014). The original plate thickness is used when estimating the shear area, not the equivalent thickness.

$$W_p \approx 1.125(\frac{b_{ext}h_{ext}^2}{6} - \frac{b_{int}h_{int}^2}{6}) \tag{4.2}$$

In the accessed design drawings, there are no figures of girder cross section type 3(Norconsult AS, 2017a). The section moduli and shear areas for section-type 2 are therefore used, as cross section 2 and 3 have the same areas.

The second moments of area obtained from the model description are within the same order of magnitude as those obtained by simple hand calculations, and are therefore considered accurate. The simplified rectangular cross section is also used to estimate the plastic section moduli about the $y$- and $z$-axis. The deviation is therefore expected to be within the same range, i.e. about 15%. The elastic torsional modulus that is used is probably a bit on the low side compared to the plastic modulus, which is the property required by USFOS. If the torsion modulus is comparable to the bending moduli, the elastic modulus is about 10-20% too low. Consequently if the plastic capacity in torsion becomes a topic of interest, the values can be revised.

The shear areas are approximate. However, since the bridge girder is slender and bending stresses will govern, the shear stresses should be of secondary importance. On the other hand, when considering loading from the side, such as wind, shear forces might be somewhat important. The girder's width to length ratio is about 0.28 if considering the element length as the distance between two columns. Until further, it is assumed that the shear areas assigned to the girder are sufficiently accurate.

The steel quality in the girder is S420, for which the properties are given in table 4.2(Norconsult AS, 2017a). However, the bridge girder will mainly be modelled as elastic. This is done by increasing the yield strength of the material by a factor of 1000. The main reason for this is that the accuracy of the USFOS plasticity model is uncertain when it comes to general beam elements, which are used to model the bridge girder. Plasticity is modelled by plastic hinges at ends and the midspan of elements(Marintek, 2001). Buckling of the cross section, however, is not predicted when general beam elements are employed. Therefore, the capacity of the bridge girder may be overestimated in the analyses. It has therefore been decided to increase the yielding capacity of the material, such that plasticity is not reached. Thus, since the material does not yield, the forces and moments in the bridge girder are not limited by yielding. Instead, potentially very high load levels are reached. The maximum load levels obtained in the bridge girder may be compared to the ultimate strength predictions from the NPRA.

Table 4.2: Steel properties for the bridge girder.

| **Yield strength** $[MPa]$ | **Elastic modulus** $[MPa]$ | **Poisson ratio [-]** |
|---|---|---|
| 420(*1000) | 210 000 | 0.3 |

There will be several other contributors to the girder self-weight than the plates and stiffeners. Some of these masses are evenly distributed, such as asphalt, which is believed to be significant, and railings. These are therefore included as increased material density. It is also assumed that the mass of the diaphragms can be taken into account by increasing the material density. This should be acceptable, since the girder length between columns is much larger than the spacing between transverse girders. The mass per unit length for the three bridge girder cross sections are given in the model description(Norconsult AS, 2017f). The equivalent density is calculated based on this, see table 4.3.

Table 4.3: Equivalent density for the three bridge girder cross sections.

| **Girder cross section type** | **1** | **2** | **3** |
|---|---|---|---|
| **Unit mass** [kg/m] | 17 836 | 19 798 | 27 287 |
| **cross-sectional area** $[m^2]$ | 1.43 | 1.68 | 1.68 |
| **Equivalent density** [kg/$m^3$] | 12 472.7 | 11 784.5 | 16 242.3 |

The anchor weights must also be taken into account. However, these act at discrete locations, i.e. the connection points between stay cables and the bridge girder. Since the bridge girder is discretized such that there is a node at the connection point for each cable-pair, the cable anchor weights are simply applied as point masses in the model. The masses of the cable anchor-pairs are given in table 4.4.

Table 4.4: Masses of cable anchors.

| | **Cable-stayed bridge** | **Floating high bridge** |
|---|---|---|
| **Total mass** $[kg]$ | 60 000 | 8000 |
| **Number of anchor couples** | 33 | 4 |
| **Mass of anchor couple** $[kg]$ | 1818.18 | 2000 |

Above columns, the cross section of the bridge girder is strengthened. These strengthened sections are also included as a point masses at the top of the columns, as an addition to the weight of the girder. The additional steel masses at column tops are given in table 4.5.

Table 4.5: Additional steel mass at column tops.

| **Column number** | **1** | **2-4** | **5-10** | **11-45** | **46** |
|---|---|---|---|---|---|
| **Additional steel mass** $[kg]$ | 101 000 | 71 400 | 59 000 | 55 000 | 71 400 |

The point masses are defined in the $x$-, $y$- and $z$-directions.

## 4.3 Modelling of the cable tower

The tower structure is made out of concrete. It consist of two legs, one at each side of the bridge girder, that are connected at about 168 $m$ above water level, see figure 4.4a. Above the contact point, a vertical member extends 59 $m$ upwards, serving as a connection point for the stay-cables. The cross section of the tower legs varies with the elevation. In the model, the legs are simplified using constant cross sections, see figure 4.4b. The height and width used in the box-sections are approximately the mean values for the respective components. General beam elements are used at the tower top, since the area and moments of area are known from the model description(Norconsult AS, 2017f). The properties of the cross section are unknown, as the geometry of the tower top is not clear from the drawings. Therefore, the section moduli and shear areas are given very high values, i.e. 1000 times higher than the expected values. The properties assigned to the tower components are given in table 4.6 and table 4.7.

Table 4.6: Geometry of tower components.

| **Tower component** | **i** | **ii** | **iii** |
|---|---|---|---|
| **External height** $[m]$ | 4.5 | 4 | 3 |
| **Thickness of side** $[m]$ | 1.2 | 1.5 | 1.2 |
| **Thickness of bottom flange** $[m]$ | 1 | 0.7 | 1 |
| **Thickness of top flange** $[m]$ | 1 | 0.7 | 1 |
| **External height** $[m]$ | 11 | 9.5 | 8.5 |

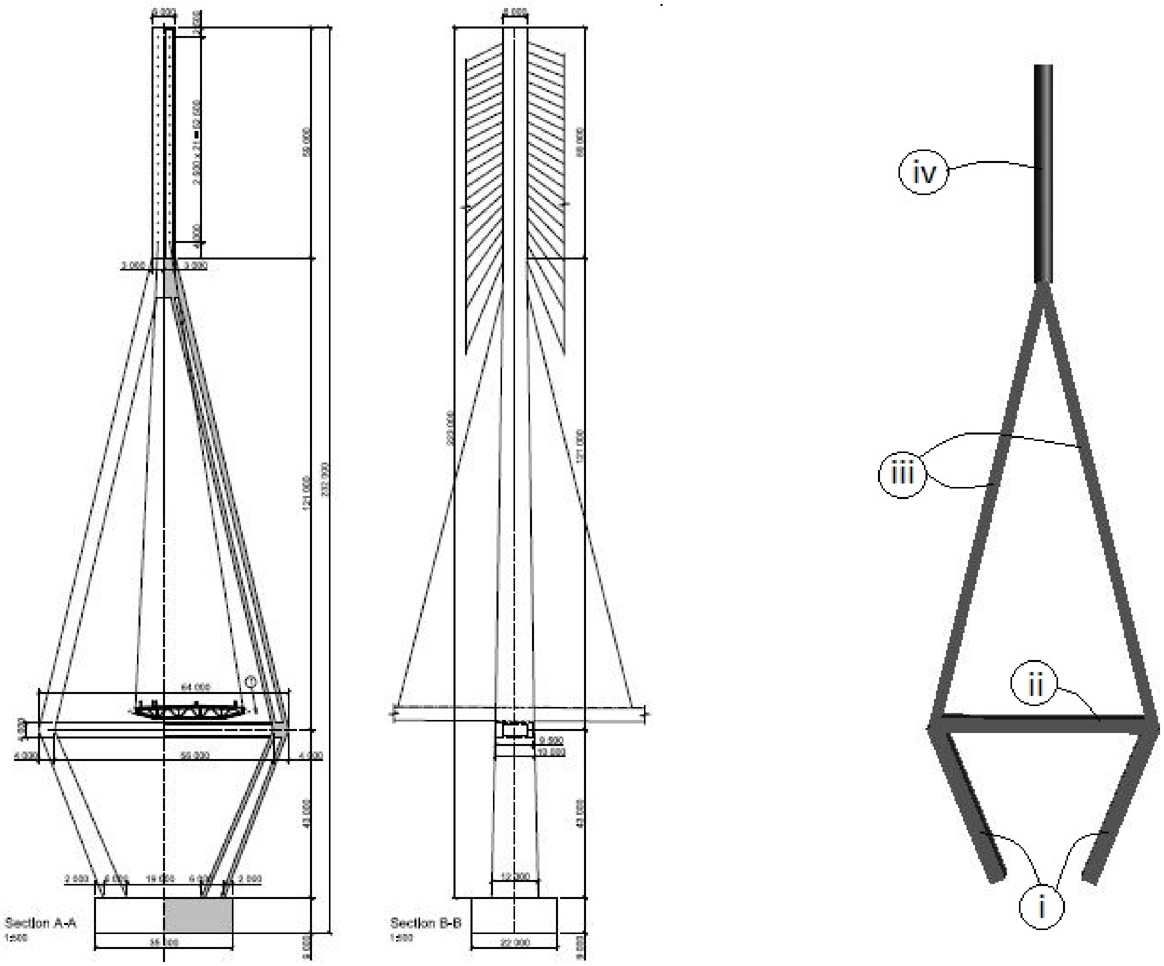

(a) Structural drawings of the tower as seen from the south-end of the bridge and from the side. From: (Norconsult AS, 2017a)

(b) USFOS-model of the tower with numbering.

Figure 4.4: Figures of the cable-tower.

Table 4.7: Input parameters for tower top.

| **Tower component** | **Area** $[m]$ | $\mathbf{I}_t$ $[m^4]$ | $\mathbf{I}_y$ $[m^4]$ | $\mathbf{I}_z$ $[m^4]$ | $\mathbf{W}_{px}$ $[m^3]$ | $\mathbf{W}_{py}$ $[m^3]$ | $\mathbf{W}_{pz}$ $[m^3]$ | $\mathbf{Sh}_y$ $[m^2]$ | $\mathbf{Sh}_z$ $[m^2]$ |
|---|---|---|---|---|---|---|---|---|---|
| iv | 21.6 | 181.2 | 92.4 | 88.8 | 10e+03 | 10e+03 | 10e+03 | 10e+03 | 10e+03 |

The material properties implemented are given in table 4.8. The Young's modulus and Poisson ratio are obtained from the model description(Norconsult AS, 2017f). The density is taken as the density of regular concrete, i.e. 2500 $kg/m^3$(Sørensen, 2010). In other words, the contribution from the steel is neglected, as the rebaring is unknown. For the same reason, the yield strength must be assumed. Since stresses in the tower are not expected to reach the yield capacity, a very high value is chosen, i.e. 55 $MPa$*1000. 55 $MPa$ is the characteristic compressive strength of the concrete.

Table 4.8: Properties of tower material.

| **Yield strength** $[MPa]$ | **Elastic modulus** $[MPa]$ | **Poisson ratio** [-] | **Density** $[kg/m^3]$ |
|---|---|---|---|
| 55*1000 | 36 000 | 0.2 | 2 500 |

The properties of the tower are rough estimates, as an accurate tower description has not been found. The density should not gravely influence the results, since the mass should be transferred directly to the ground on which the tower stands. The Young's modulus will be underestimated when disregarding rebaring. If it is seen that the tower deflections are large, the elastic modulus should be revised. However, according to the report describing the model, the tower stiffness is not important with regard to the global response(Norconsult AS, 2017f). The tower is not expected to be subjected to yielding, and it has therefore been assumed that it is tolerable to use a very high yield strength. If the yield capacity of the tower proves to be important, for example in extreme wind, a more appropriate value should be implemented. Since the tower is expected to be rigid and have high capacity, the simplification of legs with constant cross section should be acceptable.

## 4.4 Modelling of the stay-cables

The stay-cables are connected to the top of the tower in one end and to the bridge girder in the other. As mentioned earlier, the cables occur in pairs, such that there is one cable connected to each side of the girder. Since the USFOS-model only has nodes at the center-line of the girder, it has been decided to use eccentricities when modelling the cable-bridge connection. This way, the cables are connected to a location relative to the center-line node.

The stay-cables are formed by bunts of strands, i.e. the cross section is compact and fairly circular. The effective Young's modulus and cross-sectional area for each cable is known from the modelling report from the NPRA(Norconsult AS, 2017f). Since the cables will function as tensile members, $EA$ will be the most important parameter. It is also of interest to model the cables with the correct external diameter, such that the drag properties will be captured. In the USFOS-model, the stay-cables are modelled as pipe elements with very small internal diameters, i.e. 0.0002 $m$. The external diameter is calculated based on the area, i.e. D=$\sqrt{\frac{4A}{\pi}}$. A material density of 7850 $kg/m^3$ is applied, as specified in the model description(Norconsult AS, 2017f). The yield strength is not known, but it is expected to be about 500 MPa. Since this value is uncertain, and the cables are not expected to yield, a very high value is used; 500 $MPa$*1000. The unrealistically large yield strength must be kept in mind when assessing structural response. If the response in the cable stayed bridge is the topic of interest, then it might be necessary to revise the yield strength. The properties of each cable-pair are attached in appendix A.1.

A special kind of USFOS element, namely the riser element, is used to model the cables. This is in order to avoid numerical issues due to high slenderness. Since the stay-cables are very slender structures, they will not have any strength in compression. The cables are therefore

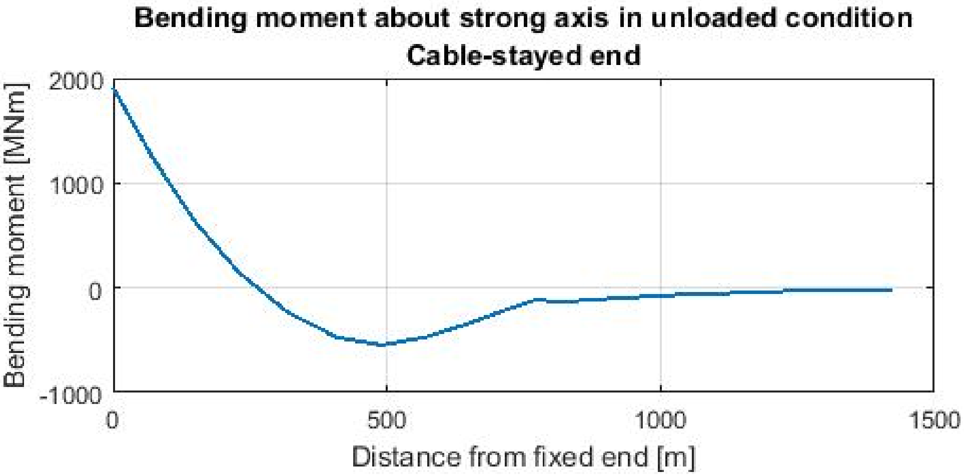

Figure 4.5: Bending moment about the strong axis of the bridge girder at the south end of the bridge due to pretension in the stay-cables.

designed with a pretension of 520.8 MPa, which can be introduced in the USFOS-model by imposing a temperature field that affects only the cable elements. When the temperature is reduced, the material will strive to contract, causing tensile stresses in the cables. The USFOS-model was initially created with temperatures causing stresses close to 500 $MPa$. However, this resulted in torsion of the bridge girder in the cable stayed section, which again caused the model to be unstable. Therefore, the temperature was increased in the cables on the east side of the bridge. The distribution of temperatures over the various cables are described in table A.1 in appendix A.1. It is seen that the cables on the west side of the bridge have temperatures in the order of $-200°C$, while temperatures in the cables on the east side are about $-70°C$. This increase in temperature in the eastern cables means that the pretension is slightly off. The cables close to the tower have stresses in the order of 1000 $MPa$, while the stresses in the remaining cables are at about 400 $MPa$. It is difficult to investigate whether this softens or stiffens the behaviour of the bridge, since the bridge is unstable with other temperature fields.

A major problem with the pretension, is that it causes large bending moments in the bridge girder. Figure 4.5 shows the bending moment about the strong axis as a function of the distance from the fixed end. In the report "K7 Bjørnafjorden End-anchored floating bridge; Appendix J – Ultimate resistance of bridge girder", the NPRA assesses the capacity of the bridge girder. It is found that the bending capacity about the strong axis is 3069 $MNm$, while the capacity about the weak axis is 574 $MNm$(Norconsult AS, 2017e). When comparing this with the results in figure 4.5, it is seen that the utilization in bending about the strong axis is up to 62%. Since the only load is self-weight, there should not actually be any bending about the vertical axis. The high utilization is therefore troublesome.

The high utilization of the bridge girder indicates that plastic analyses of the model are inaccurate, at least in the cable-stayed section of the bridge. Yielding will be reached at unrealistically low load levels. Since plasticity leads to redistribution of the loading, the results will not be accurate. If the analysis is run elastically, however, it is believed that the initial stresses will not affect the behaviour of the bridge. Thus, spurious load levels can be filtered out. For bending moments about the strong axis, this means that the initial bending moment is subtracted from the results. For bending moments about the weak axis, on the other hand, it might be best to leave the results unchanged. When this is done, the load levels can be compared to the girder resistance found by the NPRA.

## 4.5 Modelling of the columns

The columns are connected to the bottom-side of the bridge girder and the top of the pontoons. In the USFOS-model, there are only nodes at the center-line of the main girder, not at the bottom side. In order to account for this, such that the column mass is not exaggerated, eccentricities are introduced at the top of the columns. The eccentricities are set to -1.75 m, which is half the girder height. These eccentricities are large, and the model should therefore be checked for instabilities. However, this does not appear to be a problem. The bottom of the columns are attached to nodes on the topside of the pontoons.

There are four different column cross sections, see table 4.9. cross sections 1 and 2 are circular cylinders with stiffeners and transverse frames. Column types 3 and 4 are designed in a similar manner, but the cross sections are elongated in the transverse direction of the bridge girder. In the model, these columns are modelled as circular with equivalent diameters, in the same manner as what is done in the model description(Norconsult AS, 2017f). The columns are modelled with constant cross sections, i.e. the transverse frames will only be included as additional weight. Also, the change in geometry close to the ends is neglected. Since the utilization of the columns is expected to be low in the considered loading scenarios, the simplifications should be acceptable.

General beam elements are implemented in USFOS instead of pipe-elements, such that the stiffeners can be accounted for. As with the bridge girder, the second moments of area for the columns are obtained from the model description(Norconsult AS, 2017f). The thicknesses of the column walls and stiffener dimensions are unknown, and an equivalent thickness is therefore found based on the area and diameter obtained from the modelling report(Norconsult AS, 2017f). Further, the plastic section moduli about the $y$- and $z$-axes are estimated according to equation 4.3, while the torsional section modulus is assumed to be twice of this. In the calculations, the mid-radius is used for $r$. The shear area is set to half the cross-sectional area(Amdahl, 2014). Since the plate thickness is unknown, it is assumed to be 70% of the equivalent thickness in the estimations of shear area. Since the columns are short relative to the cross-sectional area, shear stresses may be important. There might therefore be a need to revise these values if large shear deformations proves to be a problem. However, it is believed that the estimated shear areas are sufficiently accurate.

$$W_p = 4r^2t \tag{4.3}$$

The material properties of the columns are the same as given in table 4.2(Norconsult AS, 2017f).

Table 4.9: Properties of the columns as implemented in USFOS.

| **Columns** | **1** | **2-4** | **5-10** | **11-46** |
|---|---|---|---|---|
| **External diameter** $[m]$ | 12 | 10 | 9.185 | 7.16 |
| **Area** $[m^2]$ | 2.101 | 1.158 | 0.977 | 0.872 |
| **Mass per unit length** [kg/m] | 17 317 | 9 429 | 7 956 | 7 200 |
| **Equivalent density** [kg/$m^3$] | 8 242.3 | 8 142.5 | 8 143.3 | 8 256.9 |
| $\mathbf{I}_t$ $[m^4]$ | 74.94 | 28.738 | 20.46 | 11.06 |
| $\mathbf{I}_y$ $[m^4]$ | 37.47 | 14.369 | 10.23 | 5.53 |
| $\mathbf{I}_z$ $[m^4]$ | 37.47 | 14.369 | 10.23 | 5.53 |
| $\mathbf{W}_{px}$ $[m^3]$ | 15.984 | 7.348 | 5.695 | 3.955 |
| $\mathbf{W}_{py}$ $[m^3]$ | 7.992 | 3.674 | 2.847 | 1.978 |
| $\mathbf{W}_{pz}$ $[m^3]$ | 7.992 | 3.674 | 2.847 | 1.978 |
| $\mathbf{Sh}_y$ $[m^2]$ | 0.736 | 0.406 | 0.342 | 0.306 |
| $\mathbf{Sh}_z$ $[m^2]$ | 0.736 | 0.406 | 0.342 | 0.306 |

## 4.6 Modelling of the pontoons

The general geometry of the pontoons is shown in figure 4.6. The bridge has four types of pontoons; one for each type of column, where the width is the only varying parameter. The initial plan was to model the pontoons with a special kind of buoyancy element that is available in USFOS. However, according to Professor Jørgen Amdahl, this element is deficient. In agreement with Professor Amdahl it has been decided that the properties of the pontoons are to be modelled with springs and beam elements.

Beam elements are used to model the geometry of the pontoons. This way, the mass is distributed in a realistic manner. For simplicity, the pontoons are modelled as rectangular beam elements with sharp corners. The height and width of the box cross sections are taken as the same as specified in the design drawings(Norconsult AS, 2017a). The pontoon length is chosen such that the waterplane area is correct. See table 4.11 for the dimensions. An arbitrary wall thickness of 1 $cm$ is chosen. It is assumed that the pontoons will not be subjected to large deformations and yielding. Therefore, a material with very high Young's modulus and yield strength is specified. See table 4.10 for the applied values. The density of the material is found such that the correct pontoon mass is obtained. The density shall account for both the steel mass and the ballast. The method for finding the correct mass is described later in this section.

Table 4.10: Material properties applied for the pontoons.

| **Young's modulus** $[GPa]$ | **Poisson's ratio** [-] | **Yield strength** $[MPa]$ |
|---|---|---|
| 210*1000 | 0.3 | 420*1000 |

The waterplane stiffness is a function of the geometry of the pontoon. The stiffness in heave, roll and pitch can be determined according to equations 4.4, 4.5 and 4.6. It has been assumed

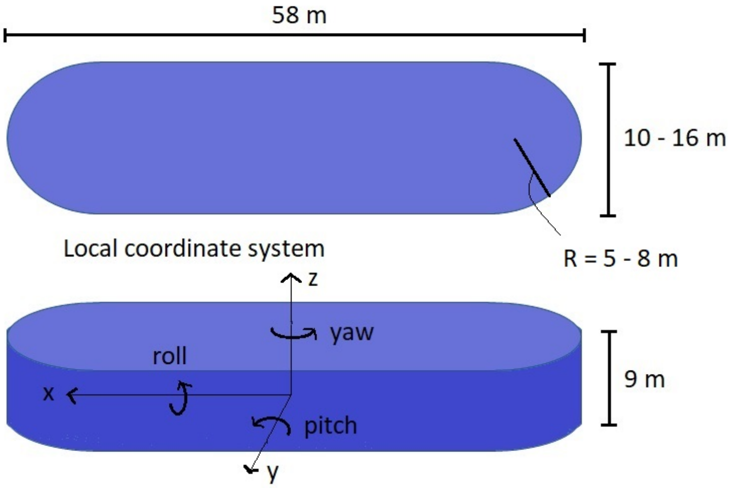

Figure 4.6: Geometry and local coordinate system for the pontoons.

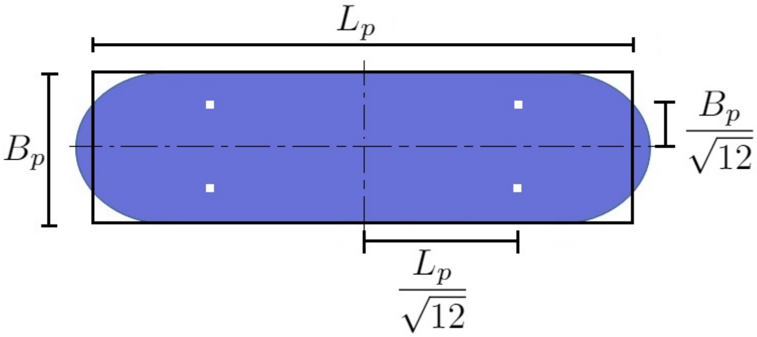

Figure 4.7: Connection points for the spring to ground elements attached to the pontoons.

that the center of gravity and the center of buoyancy coincide, such that $GM = BM = \frac{I}{\nabla}$. In the equations, $A_{WP}$ is the waterplane area, $\nabla$ is the displaced volume, while $GM_T$ and $GM_L$ are the metacentric height in the transverse and longitudinal direction, respectively. $L_p$ is the length of the pontoon and $B_p$ is the width, see figure 4.7. The resulting waterplane stiffness for the pontoons is shown in table 4.11.

$$C_{33} = \rho g A_{WP} \tag{4.4}$$

$$C_{44} = \rho g \nabla GM_T = \rho g \frac{L_P B_P^3}{12} \tag{4.5}$$

$$C_{55} = \rho g \nabla GM_L = \rho g \frac{B_P L_P^3}{12} \tag{4.6}$$

Several options for modelling the pontoons have been considered. It is decided to use four spring to ground elements on each pontoon. Each spring is defined with 25% of the total waterplane stiffness in heave. Further, the spring stiffness in roll and pitch is set to zero. The springs are connected to four nodes that are rigidly connected to the pontoon. For the

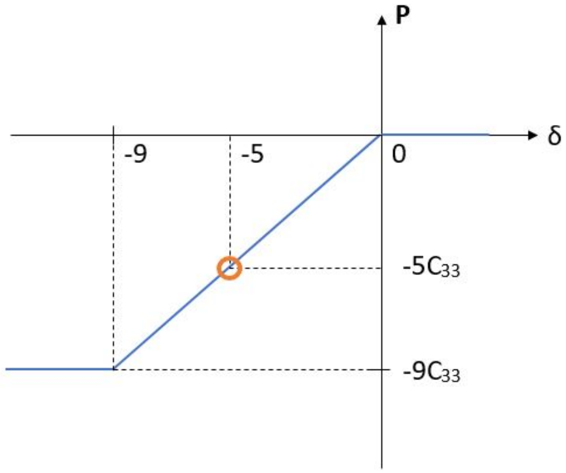

Figure 4.8: Nonlinear spring applied for modelling buoyancy. Equilibrium position indicated with orange circle.

Table 4.11: Geometry and spring stiffness of the four pontoon types.

| **Pontoon type** | **Symbol** | **1** | **2-4** | **5-10** | **11-46** |
|---|---|---|---|---|---|
| **Length** $[m]$ | $L_p$ | 54.57 | 55.00 | 55.43 | 55.86 |
| **Width** $[m]$ | $B_p$ | 16.00 | 14.00 | 12.00 | 14.00 |
| **Height** $[m]$ | $H_p$ | 9.00 | 9.00 | 9.00 | 9.00 |
| **Thickness of flanges and webs** $[m]$ | t | 0.01 | 0.01 | 0.01 | 0.01 |
| **Total pontoon stiffness in heave** $[MN/m]$ | $C_{33}$ | 8.78 | 7.74 | 6.69 | 5.62 |
| **Total pontoon stiffness in roll** $[MNm]$ | $C_{44}$ | 187.3 | 126.4 | 80.3 | 46.8 |
| **Total pontoon stiffness in pitch** $[MNm]$ | $C_{55}$ | 2179 | 1951 | 1712 | 1460 |

location of the spring connection points, see figure 4.7. $\frac{L_p}{\sqrt{12}}$ is the radius of gyration in the longitudinal direction, while $\frac{B_p}{\sqrt{12}}$ is the radius in gyration in the transverse direction. This way, the rotational stiffness of the pontoon in pitch due to the spring stiffness in heave will correspond to $C_{55}$. Similarly, the roll stiffness will be identical to that found in equation 4.5. With this method, the pontoon properties will be updated as the bridge deforms. More exactly, the roll and pitch stiffness will account for yaw motions of the pontoon.

The springs that are used to model the pontoon properties are linear, which implies that the buoyancy force will increase indefinitely. This is of course nonphysical, since the maximum buoyancy will be reached once the pontoon is fully submerged. This should be kept in mind if large vertical motions of the pontoons occur. In that case, nonlinear spring elements with the characteristics displayed in figure 4.8 should be applied. In the equilibrium condition, after gravity has been applied, the springs are at the point indicated with the orange circle in the figure. However, since the nonlinear spring elements have some stability issues, the linear springs are preferred as long as the deformations are not too large.

In order to determine the mass of the various pontoons, the density of the pontoon materials are scaled such that the weight of the bridge causes a 5 $m$ vertical displacement of each pontoon. This way, the spring force is equal to the buoyancy for a given pontoon, since the pontoons have a draft of 5 $m$ in the design drawings. However, it is desirable to maintain the initial configuration of the bridge when gravity is applied. Therefore, the HJHANSEN command is utilized, such that the deformations caused by gravity are disregarded. See table 4.12 for the various densities. It is seen that most pontoons have densities of about 6 times the density of steel, which seems reasonable. The additional weight for pontoons 12-42 corresponds to roughly 1.5 $m$ of ballast water.

Table 4.12: Material density for the pontoons

| **Pontoon number** | **1-11** | **12-42** | **43-44** | **45** | **46** |
|---|---|---|---|---|---|
| **Density** $[kg/m]$ | 7850*7.00 | 7850*6.00 | 7850*6.20 | 7850*4.40 | 7850*1.30 |

The added mass on the pontoons should be accounted for in the model. Added mass is a term for hydrodynamic forces and moments resulting from oscillating pressure fields on the body surface, which are caused by harmonic rigid body motions(Faltinsen, 1990). The added mass coefficient is a function of both the oscillation frequency and the oscillation modes(Faltinsen, 1990). In the model description, added mass is given as a function of oscillation period for surge, sway and heave motions. The values are found in WAMIT(Norconsult AS, 2017f). Plots are attached in appendix A.2. It is seen that the masses seem to approach asymptotic values as the period exceeds 20 $s$. For shorter periods, the added mass is strongly frequency dependent.

With the command HYDMASS, the magnitude of the hydrodynamic added mass can be specified in surge, sway and heave in USFOS. The masses can be defined in the local coordinate system of the pontoons. This is beneficial, since the properties will be updated along with the rotations of the pontoon. In order to capture inertia effects, the added mass is distributed over the four nodes used for spring connections. The nodes are placed 2.5 $m$ below the free surface, i.e. the mid-level of the submerged part. However, added mass cannot be defined as frequency dependent. Therefore, constant values must be chosen. When performing eigenvalue analyses where the fundamental periods are of interest, the asymptotic values for large oscillation periods are applicable. For higher order eigenmodes, periods in the range of 5 to 15 $s$ might be more relevant. See table 4.13 for a selection of added mass values.

Table 4.13: Added mass in surge, sway and yaw relative to the local pontoon coordinate system.

| Oscillation period | Motion | 1 | 2-4 | 5-10 | 11-46 | Unit |
|---|---|---|---|---|---|---|
| | Surge | $5.6e+5$ | $4.7e+5$ | $3.7e+5$ | $2.9e+5$ | |
| t > 40 $s$ | Sway | $3.1e+6$ | $3.1e+6$ | $3.1e+6$ | $3.0e+6$ | $[kg]$ |
| | Heave | $10.6e+6$ | $8.6e+6$ | $6.7e+6$ | $4.9e+6$ | |
| | Surge | $7.1e+5$ | $5.8e+5$ | $4.6e+5$ | $3.5e+5$ | |
| 5 $s$ < t < 10 $s$ | Sway | $4.6e+6$ | $4.6e+6$ | $4.6e+6$ | $4.6e+6$ | $[kg]$ |
| | Heave | $5.0e+6$ | $4.0e+6$ | $3.1e+6$ | $2.2e+6$ | |

In order to validate the added mass values, simple estimations are carried out for the smallest pontoon. The mass of the displaced volume for one pontoon is about $2.8e+6$ $kg$. Thus, the added mass in sway and heave is in the same order as the mass, while the added mass in surge is reduced by a factor of 0.1. This is inline with what is expected. In heave, the added mass coefficient is often taken to be 1.0. For ships, which have similar geometry as the pontoons, NORSOK applies an added mass of 10% in surge, see section 3.4.3. Further, the added mass is compared to theory given in the compendium "Hydrodynamikk" by Pettersen. Figure 3-20 in the compendium indicates added mass in heave for a rectangular cross section(Pettersen, 2004). For oscillation periods of about 8 $s$, the added mass in heave is estimated to about 0.8 of the displaced mass, i.e. $2.2e+6$ $kg$. For periods of about 40 s, the figure indicates an added mass of about $7e+6$ $kg$. These values are fairly consistent with the values displayed in table 4.13. According to table 6 page 3.66 in the compendium, the added mass in sway is lower than 1.21 times the displaced mass for low oscillation frequencies(Pettersen, 2004). This indicates that the added mass is lower than $3.4e+6$ $kg$, which is consistent with the added mass in sway for periods larger than 40 $s$.

The final step is to include drag forces on the pontoons. The drag term in the Morison equation is given in equation 4.7(Faltinsen, 1990); d$F_D$ is the drag force per unit length of the cylinder, $\rho$ is the water density, $C_D$ is the drag coefficient, D is the characteristic diameter, and u is the water particle velocity. Drag forces are only defined for pipe elements in USFOS, where the diameter of the pipe and the drag coefficient are the parameters that must be defined. The draft of the pontoons will vary when the bridge is subjected to waves and other loads, which should be accounted for in the calculations of the drag force. However, in USFOS, the draft is only updated for vertical cylinders. It has therefore been decided to define vertical pipe elements in the center of the pontoons. The pipe elements extend from the topside to the bottom of the pontoons. The pipe element is defined with a diameter of 1 $m$ and a material with high stiffness and low density. The value of the drag coefficient is then defined as a function of the direction, with a value corresponding to the product of the drag coefficient and the characteristic diameter. The drag coefficients are obtained from the model description(Norconsult AS, 2017f). See table 4.14. The drag coefficient is defined as a function of the orientation for each pontoon.

$$dF_D = \frac{1}{2}\rho C_D D|u|u \tag{4.7}$$

Table 4.14: Drag coefficients and characteristic diameters for the pontoons.

| **Pontoon number** | **1** | **2-4** | **5-10** | **11-46** |
|---|---|---|---|---|
| **Characteristic diameter in surge** [m] | 16 | 14 | 12 | 10 |
| **Drag coefficient in surge** [-] | 0.8 | 0.8 | 0.8 | 0.8 |
| $C_D * D$ in surge [m] | 12.8 | 11.2 | 9.6 | 8.0 |
| **Characteristic diameter in sway** [m] | 58 | 58 | 58 | 58 |
| **Drag coefficient in sway** [-] | 1.0 | 1.0 | 1.0 | 1.0 |
| $C_D * D$ in sway [m] | 58 | 58 | 58 | 58 |

## 4.7 Modelling of wind parameters

Equation 4.7 is also valid for wind drag. Consequently, drag coefficients must be assigned to the various bridge components. The height and width of the cross section is also required when considering components defined by general beam elements. For simplicity, the equivalent diameters described in section 4.5 are used as drag diameters for the columns. Since the drag area of the columns is small compared to the area of the bridge girder, this should be a reasonable simplification.

In addition to the drag coefficient, the bridge girder is also defined with lift and moment coefficients. See table 4.15 for drag, lift and moment coefficients for the various parts.

Table 4.15: Drag, lift and moment coefficients for wind drag.

| **Bridge component** | **Main girder** | **Tower** | **Stay cables** | **Columns** | **Pontoons** |
|---|---|---|---|---|---|
| **Drag coefficient** $C_D$ [-] | 0.529 | 2.0 | 0.8 | 1.05 | 0.8/1.0[1] |
| **Lift coefficient** $C_L$ [-] | 0.133 | [-] | [-] | [-] | [-] |
| **Moment coefficient** $C_T$ [-] | 0.042 | [-] | [-] | [-] | [-] |

[1] $C_D = 0.8$ in pontoon surge, 1.0 in pontoon sway.

## 4.8 Eigenvalue analysis

The eigenmodes of the bridge give an indication of how it will behave when subjected to external loading. To put it differently, it is crucial to determine the eigenperiods in order to ensure that large resonance motions are avoided. In addition, it will be interesting to compare the eigenmodes obtained in USFOS to eigenmodes obtained by alternative software. If the deviations are large, there might be a need to revise the model.

### 4.8.1 Method

The Lanczos algorithm is implemented in the eigenvalue analysis. The self-weight of the bridge and the pre-tension in the stay cables are applied as static loading over a period of 1 $s$. The bridge is then subjected to a wave with height 0.0001 $m$. Since the WAVEDATA command is switched on, the automatically generated added mass must be set to zero. The eigenvalues are calculated at 4.50 $s$, but this is arbitrary, as the time does not affect the results.

A challenge with regards to the eigenvalue analysis, is that USFOS cannot model frequency dependent added mass. For eigenperiods larger than 20 $s$, the first values in 4.13 should be sufficiently accurate. However, for periods lower than 20 $s$, the added mass is gravely influenced by the oscillation period. A solution could be to carry out series of iterations, such that the eigenperiod for each mode is found with the correct added mass. This would be tedious. Instead, the estimated added mass for 5 $s$<t<10 $s$ is used, see table 4.13. An additional eigenvalue analysis with added mass corresponding to a 5 $s$ oscillation period was carried out. It showed that for eigenmodes 21 to 40, the eigenperiods are only changed with about 2%. Since the uncertainties related to the model and the eigenvalue calculations are believed to be larger than this, this simplification should not govern the analysis.

### 4.8.2 Results

The first 20 eigenmodes obtained in the eigenvalue analysis are described in table 4.16. The valid range for the added mass applied in the calculations are given in the table. In the description of the mode motions, the terms horizontal, vertical and torsional are used. These refer to the motion of the bridge girder. The number of half waves is only specified when the wave motion is distinctive. For the first 40 modes, see appendix B.2.

The first four eigenmodes are pure horizontal modes. After the fourth mode, torsion seems to more or less take place in all modes, and will therefore only be commented upon when especially noticeable. Mode 5 to 11 are also horizontal modes, but there are torsional motions in the floating high bridge. In mode 12 to 20, the torsional motions are evident over the entire span of the bridge. From mode 13, vertical motions in the high bridge start to occur, while the horizontal motions are less and less detectable. Mode 17 to 22 are dominated by vertical motions in the high bridge. In mode 23 to 31, vertical movements in the floating low bridge govern. Contradictory to what is expected, the first of the almost pure heave modes does not have one single half wave, but a more disorganized motion pattern. The number of half waves does not increase with mode number either. However, since the periods for these heave modes are very close, it is not a large concern that the order is not quite as expected. Mode 34 through 50 are mainly dominated by vertical motions over the entire span of the bridge. Nevertheless, there are some almost pure torsional modes, namely 42 and 47. Modes 2 and 13 are illustrated in figures 4.9 and 4.10. See appendix B.1 for more eigenmodes.

Table 4.16: The first 20 eigenmodes of the USFOS model. The valid range for the applied added mass is given in the last column.

| **Eigenmode** | **Eigenperiod** $[s]$ | **Description of motion** | **Valid period range for the added mass** |
|---|---|---|---|
| 1 | 119.61 | Horizontal, 2 half waves | t $>$ 40 $s$ |
| 2 | 62.29 | Horizontal, 3 half waves | t $>$ 40 $s$ |
| 3 | 36.30 | Horizontal, 4 half waves | t $>$ 40 $s$ |
| 4 | 25.24 | Horizontal, 5 half waves | t $>$ 40 $s$ |
| 5 | 17.74 | Horizontal<br>Torsional in high bridge | t $>$ 40 $s$ |
| 6 | 16.66 | Horizontal<br>Torsional in high bridge | t $>$ 40 $s$ |
| 7 | 13.65 | Horizontal<br>Torsional in high bridge | t>40 $s$ |
| 8 | 11.15 | Horizontal and Torsional | 5 $s$<t<10 $s$ |
| 9 | 10.68 | Horizontal and Torsional | 5 $s$<t<10 $s$ |
| 10 | 9.10 | Horizontal and Torsional | 5 $s$<t<10 $s$ |
| 11 | 8.31 | Horizontal and Torsional | 5 $s$<t<10 $s$ |
| 12 | 7.74 | Torsional (and Horizontal) | 5 $s$<t<10 $s$ |
| 13 | 6.99 | Torsional (and Horizontal)<br>Vertical in high bridge | 5 $s$<t<10 $s$ |
| 14 | 6.82 | Torsional (and Horizontal)<br>Vertical in high bridge | 5 $s$<t<10 $s$ |
| 15 | 6.69 | Vertical in high bridge<br>(Torsional and Horizontal) | 5 $s$<t<10 $s$ |
| 16 | 6.60 | Vertical in high bridge<br>(Torsional and Horizontal) | 5 $s$<t<10 $s$ |
| 17 | 6.40 | Vertical in high bridge | 5 $s$<t<10 $s$ |
| 18 | 6.37 | Vertical in high bridge | 5 $s$<t<10 $s$ |
| 19 | 6.32 | Vertical in high bridge | 5 $s$<t<10 $s$ |
| 20 | 6.22 | Vertical in high bridge | 5 $s$<t<10 $s$ |

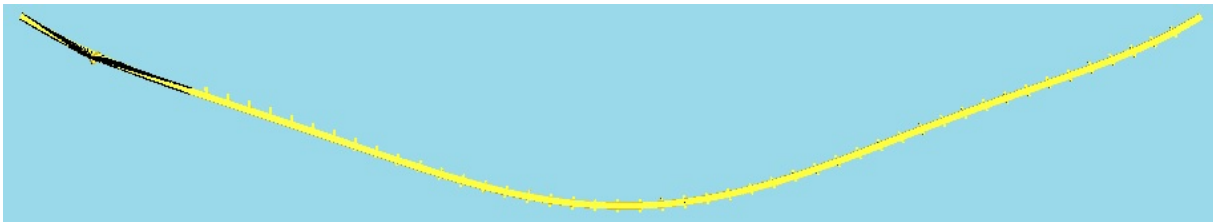

Figure 4.9: Illustration of eigenmode 2.

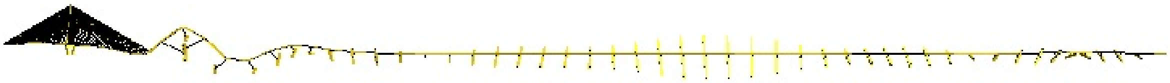

Figure 4.10: Illustration of eigenmode 13.

The first five eigenperiods are larger than 25 seconds. These eigenmodes are therefore most vulnerable with respect to wind, slowly varying drift forces and maybe ship collision. When considering eigenperiods lower than 10 $s$, i.e. eigenmode 10 and up, wind sea must also be taken into account.

### 4.8.3 Comparison to eigenperiods obtained in alternative software

Norconsult has carried out eigenvalue analyses of the bridge on behalf of the NPRA. The computational tool used is 3DFloat. The results obtained are described in the model descriptio(Norconsult AS, 2017f). In appendix B.3, the results obtained in 3DFloat are compared to the eigenmodes found in USFOS.

The motion patterns for the eigenmodes obtained in USFOS coincide fairly well with the ones found in 3DFloat. Fist, there are four purely horizontal modes. In 3DFloat, a fifth purely horizontal mode is identified. This difference might be a matter of interpretation, i.e. how the motion is defined. Then, the horizontal modes continue, but with torsion in the high bridge. The first vertical modes have heave motions in the low bridge, before there is a large number of heave modes where the entire length of the bridge is excited.

The eigenperiods obtained in USFOS also seem to fit the ones from Norconsult well. The fundamental eigenperiod obtained in 3DFloat is 119.9 $s$, which is less than 1% higher than the fundamental period found in USFOS. Taking into account the simplifications related to the USFOS model, and that the eigenvalues are calculated in two different softwares, this level of agreement is surprisingly high. When comparing the eigenperiods of the first seven modes, it is seen that the deviation increases slightly. One reason for this might be that the the added mass is assumed constant in USFOS. The motion patterns of the modes might also slightly deviate. Since the cable-stayed section is excited in these modes, the inaccuracy of the USFOS model in this region might reduce the preciseness of the results. The modes with coupled torsional and horizontal motions, as well as the modes with vertical motions in the high bridge, are difficult to compare between the two programs. Since the motion patterns from 3DFloat are described in only a few words, any attempt of identifying corresponding eigenperiods would be speculative. The modes with vertical motions in the low bridge, however, are easier to compare. Vertical motions in the low bridge start to appear for periods lower than six seconds with both types of software. All in all, the eigenperiods obtained in USFOS are supported by the ones found in 3DFloat.

### 4.8.4 Discussion of eigenvalue analysis

There are several uncertainties in the model that might influence the eigenperiods. It is known from equation 3.5 that the eigenperiods depend on the stiffness term and mass term of the system's equilibrium equation.

The uncertainty related to structural mass is believed to be small compared to the uncertainty related to neglecting frequency dependent added mass. The plots in appendix A.2 shows that the added mass is fairly constant for periods larger than 20 $s$. Therefore, the applied added mass should be sufficiently accurate for the first six modes. For modes 7 to 25, periods are within the time interval where the variation in added mass is large. These eigenperiods are therefore of questionable accuracy. The eigenmodes with vertical motions in the floating low bridge have periods of about 6 $s$. The applied added mass is applicable for this range, and the accuracy of these eigenperiods should therefore be satisfactory. The same can be said for the first modes with vertical motions over the entire span of the bridge. The uncertainty related to estimating the added mass of the pontoons in WAMIT is believed to be small.

The credibility of the stiffness term is likely to be affected by the cable-stayed section of the bridge. This will affect modes with motions in the floating high bridge and in the cable-stayed section. Since the pretension of the cables deviates from the design stress, this might either soften or stiffen the behaviour of the bridge. Since the bridge is unstable when other pretensions are applied, it is difficult to determine exactly how this affects the eigenperiods. In addition to this, the yield strength is unrealistically high in the stay cables, which might have a stiffening effect.

In addition to the modelling uncertainties, there will also be numerical uncertainties related to USFOS, and to the Lanczos algorithm used to estimate the eigenmodes.

### 4.8.5 Simple control of modes with vertical motions in the floating low bridge

The vertical modes in the floating low bridge can easily be controlled by simple hand calculations. This is done by determining the upper and lower limit for the eigenperiods.

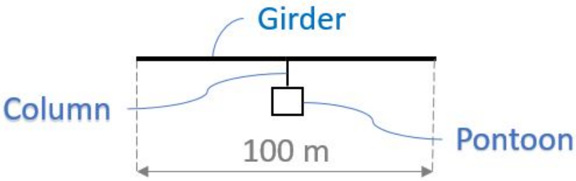

Figure 4.11: Repetitive component in the floating low bridge.

Equation 3.4 shows that the eigenfrequency is uniquely defined by the stiffness and by the mass and added mass. Theoretically, the highest eigenperiod corresponds to the softest heave mode; i.e. when the contribution to the restoring term from the bridge girder is zero. Physically, this is understood as if there is no bending moment in the bridge girder. This is the case for the motion illustrated in figure 4.12, where all the pontoons oscillate with the same phase angle. For this motion, the waterplane stiffness $C_{33}$ is the only acting stiffness. Since the floating low bridge can be divided into identical repetitive components, see figure 4.11, it is sufficient to study one of these individually. By rearranging equation 3.4, the following expression for the upper limit can be derived:

$$T_{max} = 2\pi\sqrt{\frac{M + A_{33}}{C_{33}}} \tag{4.8}$$

In the equation, $C_{33}$ is the waterplane stiffness of pontoon type 4, M is the mass of the displaced water and $A_{33}$ is the added mass of pontoon type 4 in heave. The added mass is taken as $2.2 * 10^6\ kg$, which is the added mass implemented in USFOS for lower eigenperiods between 5 and 10 $s$.

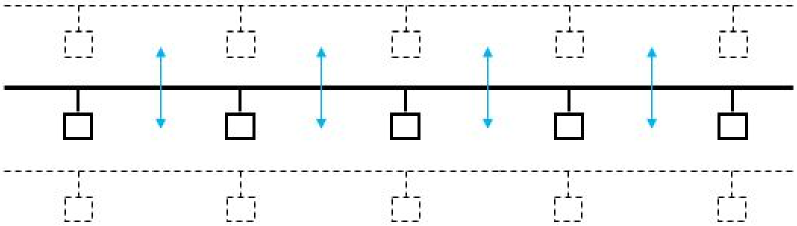

Figure 4.12: Illustration of the mode applied when determining the maximum eigenperiod in heave. The bridge is seen from the side.

The lower boundary is obtained by considering the case illustrated in figure 4.13. This is the mode where the curvature of the bridge girder is the largest. Here, the bending stiffness about the weak axis of the bridge girder will provide stiffness. The deflection of a free-free beam at midspan is given by $\delta = \frac{1}{48}\frac{PL^3}{EI}$(Irgens, 1999). Thus, the stiffness contribution from the bridge girder is $\frac{48EI}{L^3}$. When this is added to the waterplane stiffness, the lower boundary is obtained:

$$T_{min} = 2\pi\sqrt{\frac{M + A_{33}}{C_{33} + \frac{48EI}{L^3}}} \tag{4.9}$$

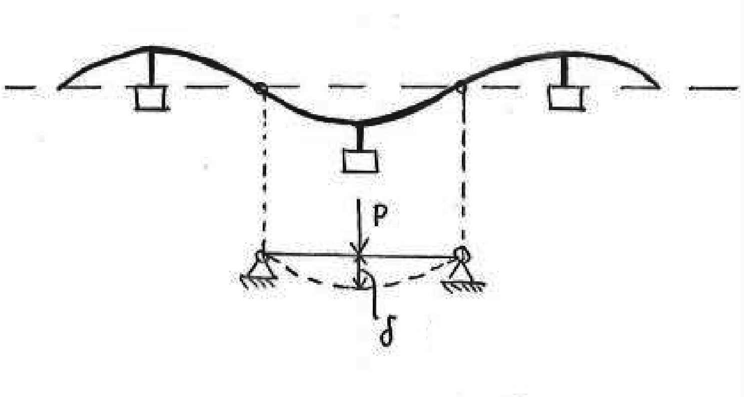

Figure 4.13: Illustration of the mode applied when determining the minimum eigenperiod in heave. The bridge is seen from the side.

Table 4.17: Applied values in the control calculations of eigenperiods in heave.

| **M**<br>[$kg$] | **A**$_{33}$<br>[$kg$] | **C**$_{33}$<br>[$N/m$] | **E**<br>[$GPa$] | **I**<br>[$m^4$] | **L**<br>[$m$] |
|---|---|---|---|---|---|
| $2.9*10^6$ | $2.2*10^6$ | $5.6*10^6$ | 210 | 2.68 | 100 |

Table 4.18: Theoretical upper and lower limit for the eigenperiods in heave in the floating low bridge.

| **T**$_{min}$ | **T**$_{max}$ |
|---|---|
| 2.5 $s$ | 6.0 $s$ |

The limits fit well with the eigenperiods from USFOS. The first modes with vertical motions in the low bridge have eigenperiods of 6.00 $s$. From a physical assessment, the mode closest to the upper limit is expected to be a mode with one half wave. However, there is no such mode. There are, on the other hand, nine modes with relatively few half waves, namely mode 23 to 31. These have eigenperiods between 5.94 $s$ and 6.0 $s$. Since the number of half waves is low, the stiffness contribution from the bridge girder is small. Thus, it seems reasonable that their eigenperiods are close to the upper limit obtained by equation 4.8.

Mode 97 is close to what is shown in figure 4.13, see figure 4.14. The eigenperiod is 2.51 $s$, which is close to what is predicted by the hand-calculations. Of course, the applied added mass is not accurate for oscillations with periods in this range, which means that the model is not representative for the physical world. Nevertheless, the results indicate that the model behaves the way it is expected to when it comes to heave motions in the low bridge.

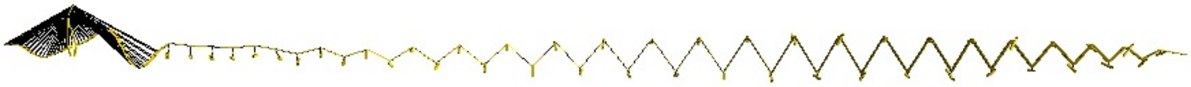

Figure 4.14: Illustration of eigenmode 97.

## 4.9 Structural damping

In order to obtain as conservative results as possible, it is preferable to neglect structural damping. However, some analyses will then become unstable. Structural damping is therefore applied in the following manner.

Structural damping is modelled by Rayleigh-damping in USFOS. It is known from section 3.2.1 that the damping ratio is defined by a curve characterized by two constants $\alpha_1$ and $\alpha_2$. It is desirable that the structural damping is reasonable in the frequency range of the most important eigenmodes. In other words, the damping should not be too high for oscillation periods in the range from 5 $s$ to 120 $s$. It has proven difficult to find values of $\alpha_1$ and $\alpha_2$ such that the model behaviour is stable. The most favorable, yet stable, solution that has been found is plotted in figure 4.15. The curve has the parameters $\alpha_1$=0.006 and $\alpha_2$=0.0039.

It is seen that the damping ratio is lower than 6% for periods between 1 $s$ and 120 $s$. Thus, the damping model should be acceptable for the most important eigenmodes of the bridge. For the fundamental eigenperiod of the bridge, the curve gives a damping ratio of about 6%. This is on the non-conservative side, since high energies might be damped out at a too high rate. In analyses where the fundamental mode is believed to be important, it is therefore preferable to neglect structural damping. Figure 4.15 shows that the damping ratio increases rapidly for decreasing periods lower than 2 $s$. Thus, high frequency oscillations will be damped out immediately. However, the eigenvalue analyses shows that the first 50 eigenmodes have periods higher than 2 $s$. The modes that are affected by this damping should therefore not be high energy modes.

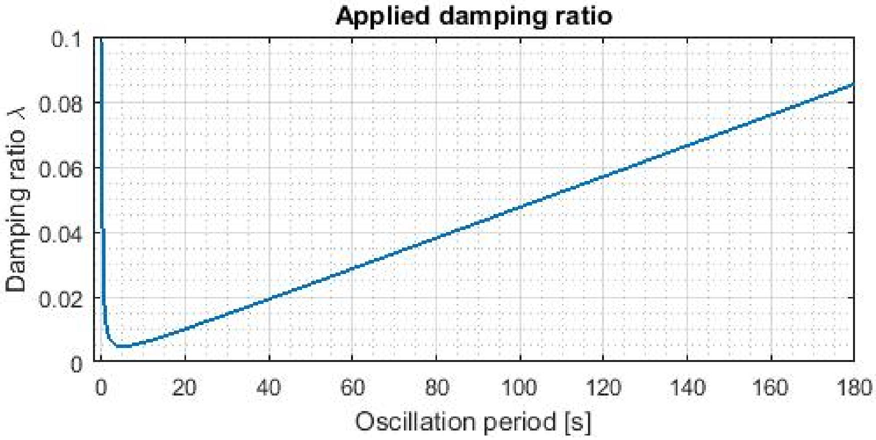

Figure 4.15: Applied damping ratio for structural damping.

# Chapter 5

# Applicability of Plastic Hinge Theory on Ship Collision

One of the ambitions for this thesis has been to find a simple theoretical model for how impact forces are balanced by reaction forces in the bridge. In this chapter, the relevance of the plastic hinge theory by Jones, which is presented in section 2.2.3, will be assessed. The theory will be compared to the results obtained in USFOS when a simplified model is subjected to high energy impacts.

In short, Jones presents a model for how plastic hinges form at the impact location and then travel away towards the end-supports. A plastic hinge is a section of a beam where the plasticity is reached over the entire cross-section. Yu et al. also study travelling hinges, but for elastic materials, see section 2.2.1. The travelling hinge is then defined as the position of the largest bending moment(Yu et al., 1996). In addition to plastic analyses, the theory by Jones will be tested on an elastic model with this definition for travelling hinges.

## 5.1 Method for comparing theory to results from USFOS-analysis

In this chapter, a simplified model of the bridge is studied. The bridge has the same length as the end-anchored floating bridge, but it is straight and has no cable-stayed section. The properties are the same as those applied in the floating low bridge, i.e. the same girder properties, pontoons and columns.

The impact is modelled as a mass travelling with an initial velocity in the transverse direction of the bridge. In order for the collision model to be comparable to the scenario addressed by Jones, drag forces on the bridge are not included. Also, energy dissipation due to local deformations is neglected. First, a 1000 $MJ$ collision is tested. The results show that plasticity is not fully reached in this collision. It is therefore tested both how an increase in the striking mass and an increase in the initial velocity will affect the results. The input

Table 5.1: Characteristics of the impact scenarios applied in the comparison to the theory presented by Jones.

| **Impact scenario** | **Symbol** | **1** | **2** | **3** | **4** | **Unit** |
|---|---|---|---|---|---|---|
| **Mass** | $G$ | 34.8 | 174 | 34.8 | 34.8 | $[Mkg]$ |
| **Velocity** | $V_0$ | 7.58 | 7.58 | 15 | 20 | $[m/s]$ |
| **Impact energy** | $E_{kin}$ | 1000 | 5000 | 3915 | 6960 | $[MJ]$ |

parameters for the impact scenarios are displayed in table 5.1.

The position of a plastic hinge is simply read manually from the results. When plasticity is not fully reached, which is the case both with impact scenario 1 and 2, the position of the largest plastic utilization is used. Impact scenario 1 is also tested elastically, i.e. with very high yield strength. The position of the largest bending moment is then used, i.e. the definition of a travelling hinge by Yu et al.(Yu et al., 1996).

The parameters required by equations 2.3 to 2.5 are given in table 5.2. The mass per unit length of the bridge girder, the mass of the pontoons and the added mass in global sway is accounted for in the unit mass of the bridge. The bending capacity is taken as the yield strength times the plastic section modulus. For simplicity, the shear capacity is taken as the yield strength times the shear area of the girder in the global y-direction, which means that the shear stress is assumed to be uniformly distributed.

Table 5.2: Input parameters implemented in the equations by Jones.

| $\mathbf{M}_0$ | $\mathbf{Q}_0$ | **m** |
|---|---|---|
| 3282 $MNm$ | 262 $MN$ | 31650 $kg$ |

## 5.2 Results and discussion

The duration of the first phase of motion, $T_1$, is very short, ranging between 0.03 $s$ for the lowest velocity and 0.08 $s$ for the highest. Compared to the duration of the impact, this is a very short period of time. It is also shorter than the time step in the USFOS analysis, which means that it cannot be captured. The location of the stationary hinge, $\xi_0$ is estimated to be about 75 $m$. This is fairly consistent with the position of where the plastic hinges first occur, which is at a distance of 50 $m$ from the impact point at both sides. It should be kept in mind that USFOS only models plastic hinges at element ends and midspan. All in all, due to the short duration of the first phase of motion, it is difficult to assess the applicability of the theoretic model on the results obtained in USFOS.

The second phase starts at the end of the first phase, when the plastic hinges start to travel. Since a long beam is considered in the theory, the influence from the supports is not accounted for. As a consequence of this, the formulas are only applicable up to the point of which the plastic hinges reach the supports. In the results obtained in USFOS, it is seen that there are some small wave components propagating faster than the hinges, something that is also noted by Yu et al.(Yu et al., 1996). These start to reach the ends of the bridge after about 6 to 8 $s$. A conservative interpretation of this is that the theory by Jones is only applicable the first 6 $s$ after the impact.

In the USFOS analysis, the positions of the plastic hinges are taken as the position of largest plastic utilization. Figure 5.1 shows how bending waves propagate away from the struck area. At the areas with large curvature, it is seen that the plastic utilization is high. As expected, a large bending moment is observed at the struck point. In addition, it is seen that the utilization is high at two points on each side of the impact location. This is the travelling hinge described by Yu et al., see section 2.2.1.

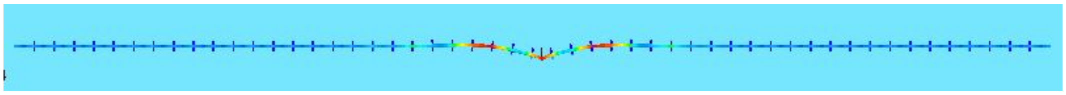

(a) At 1.0 $s$ after impact.

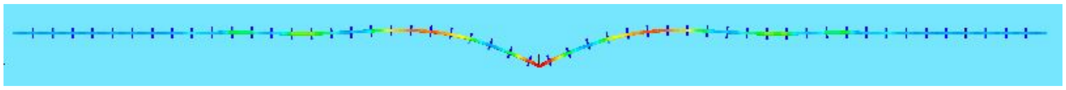

(b) At 3.0 $s$ after impact.

Figure 5.1: Illustration of the deformations and plastic utilization of the straight bridge model after impact. The deformations are scaled by a factor of 5.

The theoretical positions of the plastic hinges are plotted as a function of time for the four impact scenarios, see figure 5.2. The position obtained in USFOS is plotted along with the theoretical solution by Jones. For the first scenario, the position of the elastic maximum bending moment is also plotted. The bridge is symmetric about the impact point, which means that the response is also symmetric. Therefore, only the position of the plastic hinge along the positive x-axis is plotted.

Figure 5.2a shows the results from the first impact scenario with the lowest collision energy. It is seen that the position of the maximum elastic bending moment and the plastic hinge are fairly identical, the deviation is probably a consequence of how the results are interpreted. Compared to the theoretical position, the plastic hinges appear to travel at a slower rate in the USFOS results. In other words, it appears that the model is not suited to estimate the position of the maximum elastic bending moment, nor the plastic hinge, when the collision energy is lower than 1000 $MJ$.

Figure 5.2b shows the results for scenario 2, where the mass is increased such that the collision energy is 5000 $MJ$. In scenario 3, the collision energy is increased to about 4000 $MJ$ by increasing the velocity, see figure 5.2c. It is seen that the results for collision scenario 3, where the velocity is increased, coincide very well with the theoretical solution. When the mass is increased, on the other hand, the hinge propagates more slowly away from the impact than what is predicted by the theory. By studying the results in USFOS more closely, it is seen that the level of plasticity is lower in the second scenario than in the third scenario. This is somewhat unexpected, since the collision energy is about 1000 $MJ$ higher. One reason

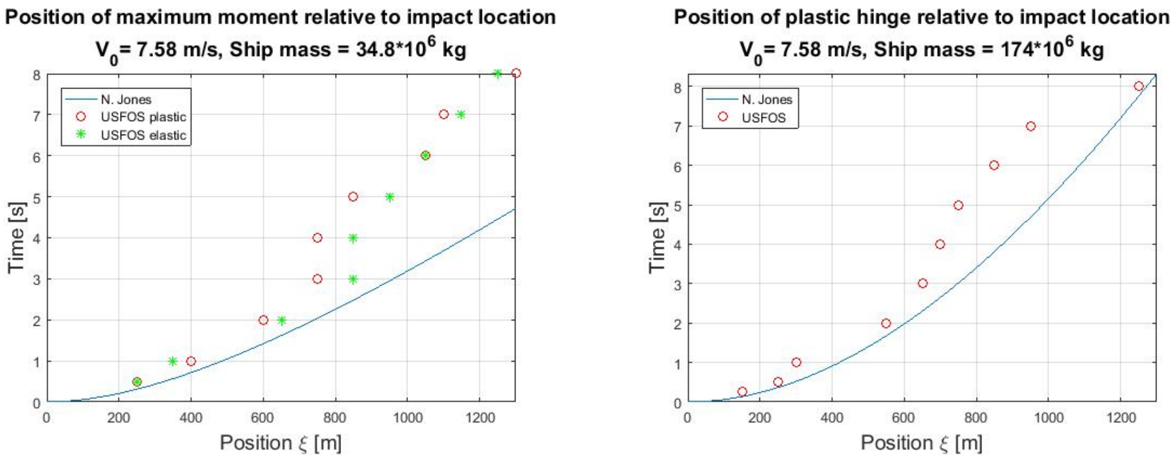

(a) Impact scenario 1, 1000 $MJ$

(b) Impact scenario 2, 5000 $MJ$

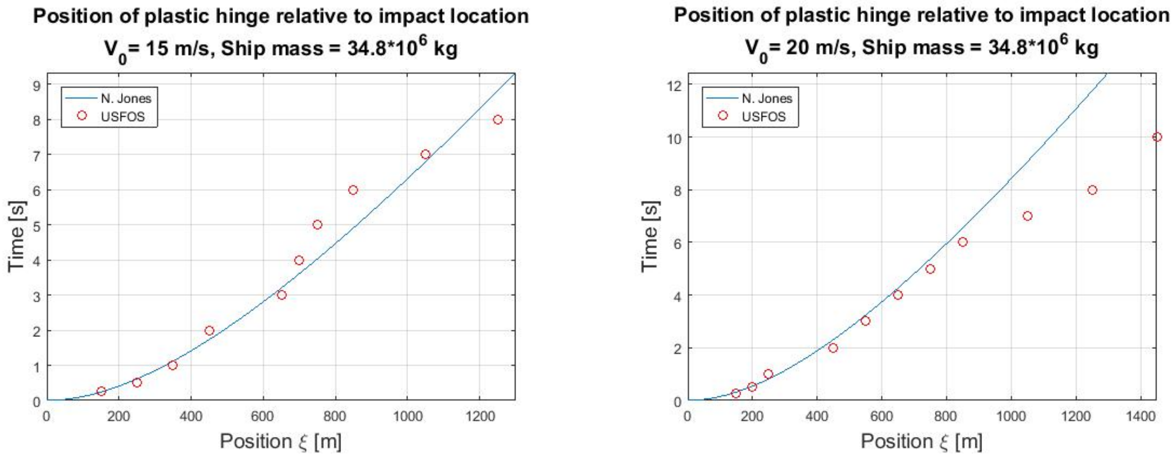

(c) Impact scenario 3, 3900 $MJ$

(d) Impact scenario 4, 7000 $MJ$

Figure 5.2: Position of travelling hinge found in USFOS compared to theoretical solution by Jones. Position given by distance from impact point.

might be that the dynamic effects are less important when the impact velocity is lower, since the acceleration of the bridge girder is smaller.

Based on the results from the first three impact scenarios, one might expect that the relevance of the theoretical model will increase with increasing impact velocities. However, from figure 5.2d it is seen that model is only satisfactory for the first six seconds for an impact velocity of 20 $m/s$. After this, the plastic hinge travels faster than what is predicted. As mentioned earlier, the theoretical model is strictly only applicable up to about 6 $s$ after the impact. This might be one explanation for the deviation in the results. However, this cannot be concluded with certainty.

## 5.3 Relevance of model with respect to ship collision analysis

Phase 1, i.e. the time interval after the impact when shear forces balance the impact force, is less than 0.1 $s$. Thus, this phase can be disregarded.

In phase 2, travelling hinges can be observed propagating away from the impact area, consistent with what is described by both Yu et al. and Jones. However, the model by Jones is only applicable for very high impact energies, i.e. larger than 4000 $MJ$. For lower impact energies, the phase velocity of the bending waves is overestimated. The design impact energies for the end-anchored floating bridge are in the order of 660 $MJ$ and lower. For this reason, the model presented by Jones will not be considered further in this thesis.

# Chapter 6

# Analysis of Ship Collision

## 6.1 Design Ship

As addressed in section 3.4.3, the design vessel should be decided based on the local traffic and the design collision energy should be determined for each bridge component individually. A risk analysis related to ship collision is therefore required before carrying out the ship collision analyses. The NPRA, i.e. Statens Vegvesen, has conducted such an analysis for pontoon collision, and it was decided on three different design ships. For the three pontoons closest to the transit channel, a large container ship is to be implemented. For the next two pontoons, the recommended design ship is a smaller cargo ship. The design ship for the remaining pontoons is a slightly smaller cargo or bulk ship. See table 6.1 for an overview of the design ships. As before, the pontoons are numbered from the south end of the bridge.

Table 6.1: Overview of the design ships recommended by the NPRA for pontoon collision.

| **Design ship** | **1** | **2** | **3** |
|---|---|---|---|
| **Related pontoons** | 1-3 | 4-5 | 6-46 |
| **Ship type** | Container | Cargo | Cargo or Bulk |
| **Collision energy** | 660 $MJ$ | 360 $MJ$ | 250 $MJ$ |
| **Example ship** | MAERSK Flensburg<br> <br>DWT: 11 135 $t$<br>LOA: 134 $m$<br>(Marine Traffic, 2018a) | WILSON Saga<br> <br>DWT: 6489 $t$<br>LOA: 113 $m$<br>(Marine Traffic, 2018c) | WILSON Ross<br> <br>DWT: 6258 $t$<br>LOA: 104 $m$<br>(Marine Traffic, 2018b) |

The force-deformation curve of the bow is needed for the three design ships. The forecastle and bulb characteristics can be determined in local analyses carried out in LSDYNA. However, this requires a highly detailed FEM-model, which is tedious and time-consuming to create. Therefore, the bow characteristics of already existing LSDYNA-models will be used instead. For design ship 1, the characteristics of a slightly larger container vessel will be used, while a 7500 ton supply vessel will be used for both design ship 2 and 3. As an indication of the ship size, the largest ship has the same mass as about 500 $m$ of the bridge, including pontoons and columns.

As of March 2018, the NPRA has not decided on a design ship and collision energies for the impacts with the bridge girder. Energies of 600 $MJ$, 360 $MJ$ and 250 $MJ$ have been suggested. An existing LSDYNA-model for a 20 000 DWT ship is used to generate the combined force-deformation curves for the bridge girder and deckhouse.

## 6.2 Modelling of ship collision in USFOS

The ship is modelled by a point mass with an initial velocity. An added mass of 10% is included in the ship mass, inline with the NORSOK recommendations for bow collision(NORSOK, 2007). In order to account for the local deformation energy, the mass is connected to the bridge through a nonlinear spring. The shared energy principle is applied in the collision model, i.e. the strain energy in both the bridge and the ship bow is taken into account. In practice, this means that the nonlinear spring reflects the combined force-deformation curve for the bridge and ship hull. Postdoc Yanyan Sha has found the force-deformation curves for a series of collision scenarios in the nonlinear FEA-tool LS-DYNA. Further, it is desirable that the ship disconnects from the bridge after the impact. This is achieved by putting a compression spring in series with the the first spring. This spring is given a very high stiffness in compression, i.e. 5E+10 $N/m$, and a very low stiffness in tension, i.e. 10 $N/m$. As a result, the spring force will be close to zero after the ship has been pushed back by the resistance in the bridge. The high compression stiffness ensures that no energy is dissipated in this spring.

The collision analyses are run elastically. As discussed in section 4.2, the reason for this is that the accuracy of the USFOS plasticity model is uncertain when it comes to general beam elements, which are used to model the bridge girder. The yield strength of the materials of both the bridge girder and the columns are increased by a factor of 1000, such that the yield limit is not reached. The maximum load levels obtained in the bridge girder will be compared to the ultimate strength predictions from the NPRA. Another reason for running the collision analyses elastically, is the initial stress state of the bridge girder in the cable-stayed section. Due to the difficulties with pretension in the cables, the utilization of the bridge girder is high in this region, even when the only applied load is self-weight. For this reason, plasticity will be reached at much lower load levels than what is realistic. Consequently, it is preferable to not include plasticity.

Several spring configurations for modelling ship collision have been tested. For a stable solution, the compression spring must be placed between the nonlinear spring and the bridge. Another stability criterion is that the nonlinear spring must be restrained from moving in the transverse directions at both ends. Further, it is found that connecting the compression spring directly to the bridge is not a good solution, since the disconnection between ship and bridge is not captured. This is because the bridge girder or pontoon in most cases will experience some sideways and vertical motions. When the compression spring is no longer parallel to the impact velocity, and the node at the other end of the spring is restrained from lateral displacements, the ship mass is “locked” to the bridge.

The applied spring configuration will be described in this paragraph. See figure 6.1 for an illustration. It is seen that the compression spring is connected to the bridge through a light pipe element with high yield strength. The idea of this set-up is that the two springs can be restrained from moving in the transverse directions, without having to prevent transverse motions of the bridge. Boundary conditions are introduced such that the springs are fixed from lateral movements, but the node between the compression spring and connection element is allowed to rotate. The connection element is made long, i.e. 150 $m$, such that the sideways motion of the bridge is not artificially resisted. Due to the slender nature of the connection element, the Young’s modulus must be higher than for structural steel. However, it is desirable that the element transfer the collision load as an axial force, and that the shear forces are limited. The Young’s modulus should therefore not be too high. A value corresponding to a thousand times higher than that of structural steel is applied, i.e. $1000*210$ $GPa$. For both springs, the stiffness in transverse directions is set to low values, such that rotation of the connection element is not prevented.

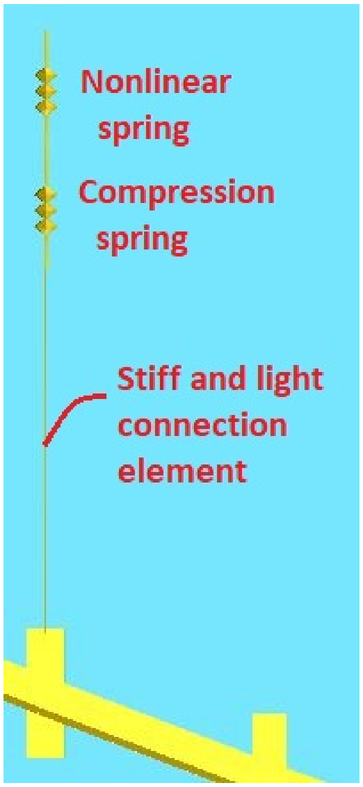

Figure 6.1: Illustration of the general spring configuration for modelling ship collision.

### 6.2.1 Added mass and structural damping

The horizontal and torsional eigenmodes of the bridge are believed to be the most important for collision analyses, while the vertical modes are not believed to be decisive. Therefore, the added mass corresponding to eigenperiods larger than 40 $s$ is implemented. Consequently, the eigenperiods in heave are slightly overestimated.

To ensure conservatism, it is preferable to run the analyses without structural damping. This way, as much of the collision energy as possible is transferred to the bridge. However, it is found that without structural damping, some of the collision analyses become unstable. Therefore, structural damping is applied inline with what was described in section 4.9. As a consequence, some of the collision energy will be dissipated by structural damping in the collision springs. This is on the non-conservative side.

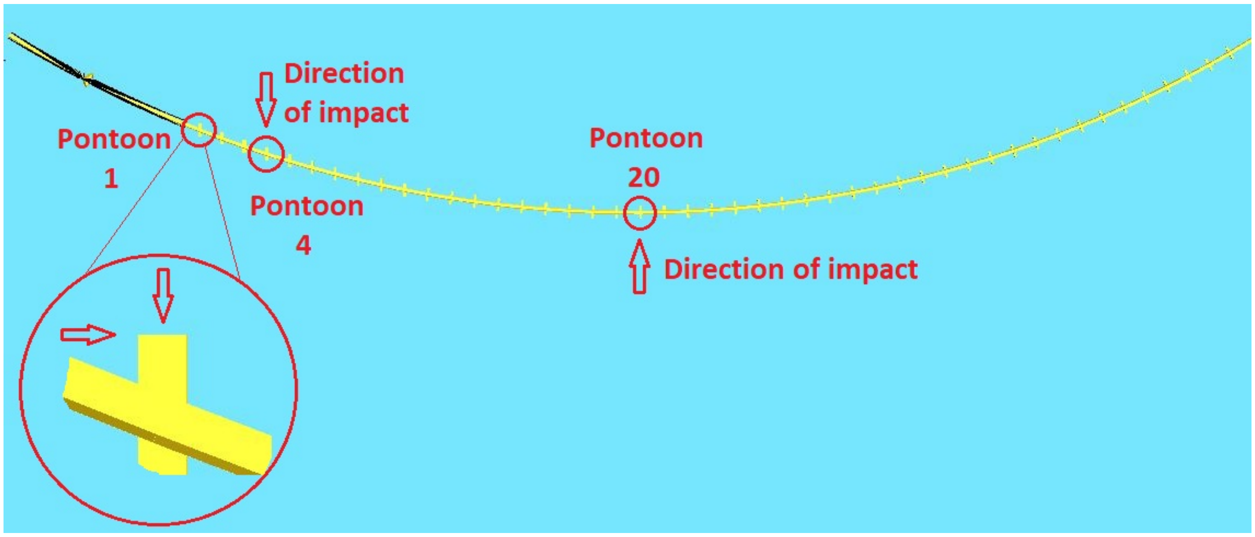

Figure 6.2: Position of the three pontoons subjected to ship collision, and the direction of the impacts.

### 6.2.2 Pontoon collision

Five scenarios of pontoon collision will be studied. Firstly, three different impacts with pontoon 1 are considered. The same way as earlier in the report, the pontoons are numbered from the south end of the bridge, such that pontoon 1 is the pontoon closest to the transit channel. Pontoon 1 will be impacted both head-on and at a 90 degree angle. In this context, head-on indicates that the initial velocity of the ship is parallel to the longitudinal axis of the pontoon, see figure 6.4. When referring to the collision at a 90 degree angle, the ship strikes the pontoon in the transverse direction, 3 $m$ from the tip. In the latter case, a reduced collision energy will be applied. Further, head-on collisions with pontoon 4 and 20 will also be studied, see figure 6.2 for the position of these pontoons. In addition to considering the design collision energies decided by the NPRA, a 1000 $MJ$ head-on collision with pontoon 1 will also be considered. The aim is to provoke an extreme response, such that the characteristics are easier to identify. See table 6.2 for an overview of the considered collision scenarios.

Figure 6.3 illustrates the impact between ship and pontoon. It is seen that the bulb and forecastle hit the pontoon at different locations. For this reason, the bulb and forecastle are modelled by two parallel springs. The configuration is displayed in figure 6.4. A node is defined at each of the impact locations, with rigid connections to the center of the pontoon. Figure 6.3 shows that the forecastle crashes into the pontoon at a later stage than the bulb. To model this, the forecastle-spring should be defined with zero stiffness in the region before contact is reached. However, the spring stiffness must be of a certain magnitude in order for the USFOS-model to function. As a consequence, some of the collision energy will be wrongfully dissipated. Nevertheless, this energy is in the order of 5% of the total energy in the forecastle-spring, which should be acceptable.

The number of points that the nonlinear collision springs can be defined with is limited, and the curves must therefore be simplified. See figure 6.5 for the comparison between the applied

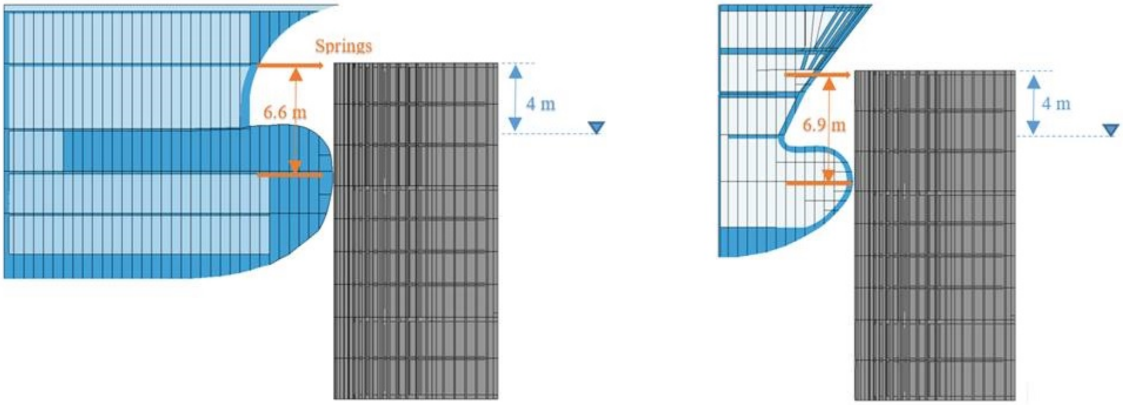

(a) Container vessel (b) Supply vessel

Figure 6.3: Impact points between ship bow and pontoon. The illustrations are screenshots from LSDYNA, obtained from Postdoc Yanyan Sha.

spring stiffness and the force-deformation curve found in LSDYNA for the head-on collision between pontoon 1 and the container vessel. The curves are extrapolated in USFOS based on the last two data points. Therefore, a point is added at the end of the data file, such that the extrapolation looks somewhat reasonable.

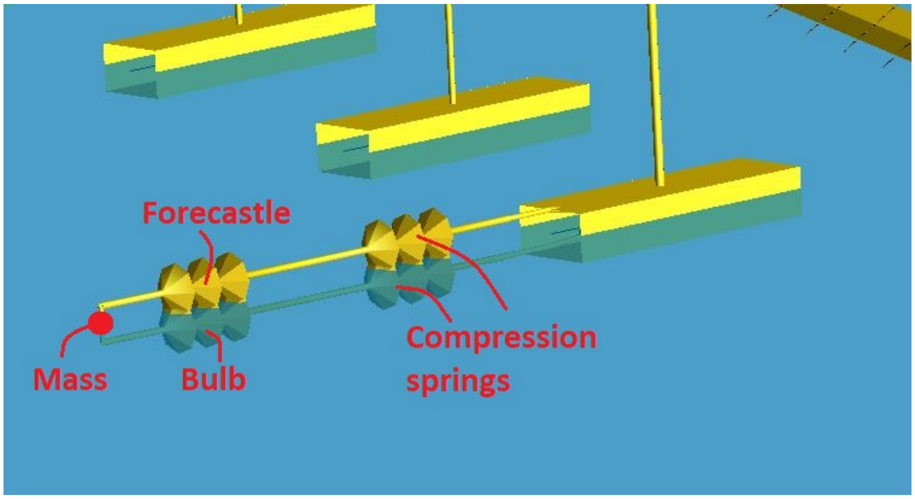

Figure 6.4: Spring configuration for the ship-pontoon impact, here for a head-on collision. For illustrative purposes, the connection element is shortened.

The local collision analysis carried out in LSDYNA by Postdoc Yanyan Sha shows that the pontoon suffers the largest damages in the collision. As a consequence, the pontoon will lose some of its buoyancy in large energy collisions, either due to flooding of pontoon compartments or loss of waterplane area. It is decided not to include the loss of buoyancy in the collision model.

During the work with the master thesis, a new pontoon design has been decided on. Therefore, new collision analyses with updated force-deformation curves are carried out for the collisions with pontoon 1. In addition, the head-on collision is run with a slightly reduced energy.

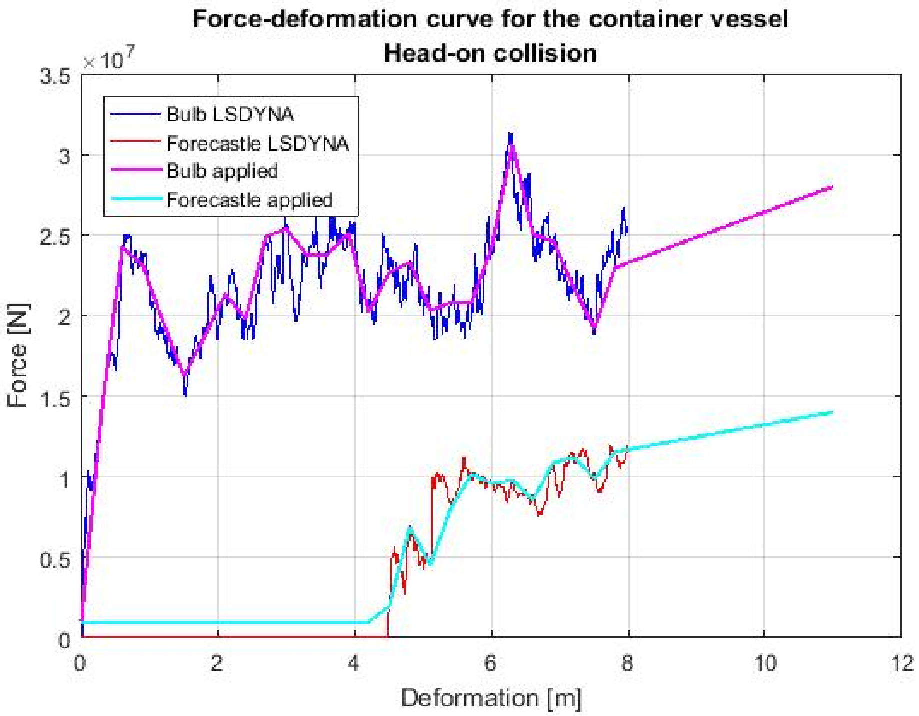

Figure 6.5: Applied force-deformation curve versus the curve found in LSDYNA for the head-on collision between the container vessel and pontoon 1.

### 6.2.3 Girder collision

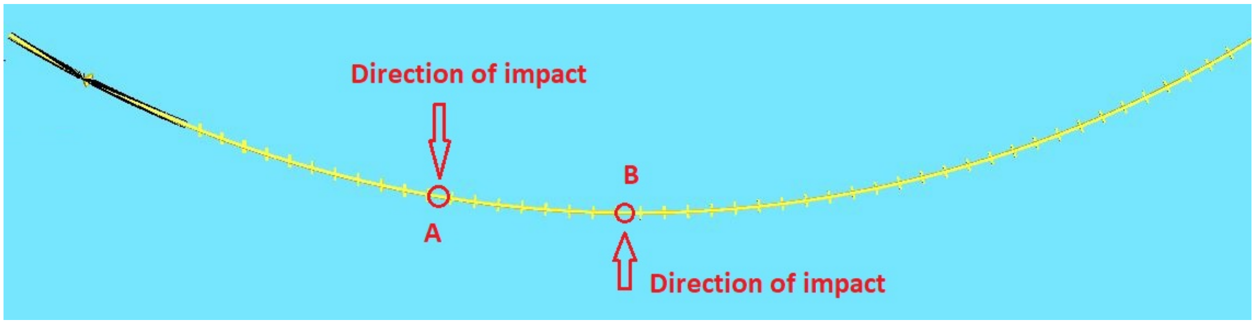

Figure 6.6: Position of the two areas subjected to girder impact, and the direction of the impacts.

In the floating low bridge, the bridge girder is situated only about 14 *m* above the water surface. Impacts between the deckhouse of a ship and the bridge girder is therefore a risk that must be accounted for. Three impact scenarios between deckhouse and bridge girder will

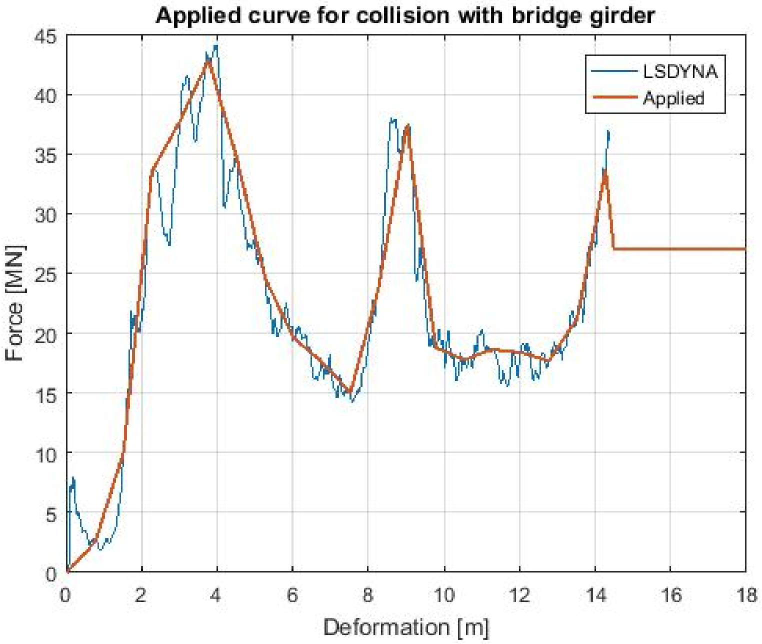

Figure 6.7: Force-deformation curve for deckhouse-girder collision.

be analyzed; one at position $A$ in figure 6.6, and two at position $B$. Position $A$ is the position closest to the transit channel where the bridge girder is low enough for a deckhouse collision. Here, a 360 $MJ$ collision will be applied. A 250 $MJ$ collision at position $B$ is studied in order to compare the deckhouse collision with pontoon collision scenario 5. During the spring semester, the NPRA has suggested a design energy of 600 $MJ$ for position $B$, i.e. at midspan. This collsion energy will therefore also be applied. The force-deformation curve for a 20 $Mkg$ ship is applied in all three analyses. The curve is established by FEM analysis in LSDYNA by Postdoc Yanyan Sha.

For the girder collisions, there is only one contact point between the ship and bridge, and therefore only one force-deformation curve. Thus, there is no need for the parallel spring connection shown in figure 6.4. Besides from this, the spring configuration for the girder collisions is the same as for the pontoon collision. The force-deformation curve for the deckhouse collision is given in figure 6.7. The fitted curve applied in USFOS is also indicated.

The bridge girder has a higher resistance towards local deformations than the pontoons do. When considering the cross section of the girder, it is seen that there is a thin wind-flange at the side. In figure 6.7, the small peak at the beginning corresponds to the crushing of this wind-flange. After this, the deckhouse will collide with the 35 $mm$ thick side-plate of the cross section. Due to the high thickness of this plate, the deckhouse of the ship takes the majority of the deformations from this stage. The peaks in the curve corresponds to crushing of bulkheads in the deckhouse. Although the deckhouse suffers the largest deformations, the girder will also suffer damages during the collision. According to Postdoc Yanyan Sha, the cross section of the bridge is compressed in the vertical direction. This will most likely cause a deterioration of the girder capacity. Since local deformation is not the topic of interest in this thesis, this will not be assessed any further.

## 6.3 Results and discussion of pontoon collision analyses

Table 6.2: Overview and results of the ship-pontoon collision analyses.

| **Collision scenario** | **1** | **2** | **3** | **4** | **5** |
|---|---|---|---|---|---|
| **Collision energy** | 1000 $MJ$ | 660 $MJ$ | 400 $MJ$ | 360 $MJ$ | 250 $MJ$ |
| **Pontoon** | 1 | 1 | 1 | 4 | 20 |
| **Direction** | Head-on | Head-on | 90 degree | Head-on | Head-on |
| **Design ship** | Container vessel | Container vessel | Container vessel | Supply vessel | Supply vessel |
| **Local deformation energy** | 512.3 $MJ$ (51.2%) | 326.2 $MJ$ (49.4%) | 306.2 $MJ$ (76.6%) | 218.5 $MJ$ (60.7%) | 135.6 $MJ$ (54.2%) |
| Energy in bulb-spring | 372.6 $MJ$ (37.3%) | 250.2 $MJ$ (37.9%) | 195.5 $MJ$ (49.9%) | 139.6 $MJ$ (38.8%) | 92.8 $MJ$ (37.1%) |
| Energy in forecastle-spring | 139.7 $MJ$ (14.0%) | 76.0 $MJ$ (11.5%) | 110.7 $MJ$ (27.7%) | 78.9 $MJ$ (21.9%) | 42.8 $MJ$ (17.1) |
| **Maximum impact force** | 51.8 $MN$ | 42.7 $MN$ | 42.7$MN$ | 36.5 $MN$ | 33.6 $MN$ |
| Force in bulb-spring | 34.5 $MN$ | 28.7 $MN$ | 23.1 $MN$ | 21.5 $MN$ | 21.8 $MN$ |
| Force in forecastle-spring | 17.3 $MN$ | 14.3 $MN$ | 19.6 $MN$ | 15.3 $MN$ | 13.5 $MN$ |
| **Maximum local deformation** | 15.2 $m$ | 11.3 $m$ | 13.8 $m$ | 8.4 $m$ | 5.8 $m$ |
| Larger than pontoon width? | N/A | N/A | No, 86% | N/A | N/A |
| **Remaining energy** | 487.7 $MJ$ | 333.8 $MJ$ | 93.8 $MJ$ | 141.5 $MJ$ | 114.4 $MJ$ |
| Kinetic energy in ship after impact | 1.8 $MJ$ | 1.3 $MJ$ | 8.2 $MJ$ | 1.4 $MJ$ | 4.2 $MJ$ |
| Energy transferred to bridge[1] | 485.9 $MJ$ | 332.5 $MJ$ | 85.6 $MJ$ | 140.1 $MJ$ | 110.2 $MJ$ |
| **Maximum bending moment[2]** | | | | | |
| Bridge girder at the south anchoring | 3800 $MNm$ | 3100 $MNm$ | 1600 $MNm$ | 2400 $MNm$ | 1900 $MNm$ |
| Bridge girder above struck pontoon | 4700 $MNm$ | 3900 $MNm$ | 1200 $MNm$ | 2800 $MNm$ | 2500 $MNm$ |
| Bridge girder at the north anchoring | 3400 $MNm$ | 3000 $MNm$ | 1100 $MNm$ | 2100 $MNm$ | 2000 $MNm$ |
| **Maximum shear force** | | | | | |
| Bridge girder at the south anchoring | 14 $MN$ | 12 $MN$ | 9 $MN$ | 14 $MN$ | 10 $MN$ |
| Bridge girder above struck pontoon[3] | 27 $MN$ | 23 $MN$ | 7 $MN$ | 16 $MN$ | 16 $MN$ |
| Bridge girder at the north anchoring | 14 $MN$ | 13 $MN$ | 5 $MN$ | 11 $MN$ | 11 $MN$ |

[1] Without respect to energy damped out by structural damping
[2] About the strong axis of the bridge girder
[3] In the bridge girder at the north side of the column

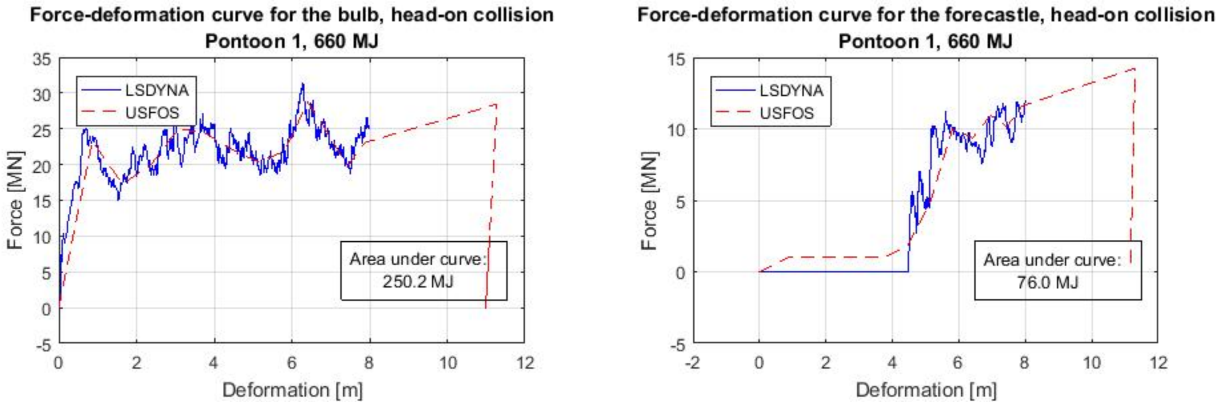

(a) Bulb

(b) Forecastle

Figure 6.8: Measured force-deformation relationship in collision springs compared to curve from LSDYNA. Collision scenario 2.

### 6.3.1 Local deformations caused by pontoon collision

The kinetic energy dissipated by local deformations is given for the five collision scenarios in table 6.2.

An important criterion for the collision springs, is that energy dissipation due to local deformations must be captured correctly. Figure 6.8 shows the force-deformation relationship measured in the collision springs in collision scenario 2, plotted along with the force-deformation curve for the container ship from LSDYNA. It is seen that the springs behave according to what is expected. Similar plots for the other collision scenarios are attached in appendix C.1. These plots also show good agreement. Thus, the springs should transfer the collision force and dissipate kinetic energy in a satisfactory manner. The accuracy is limited by the simplifications made to the curve from LSDYNA when implemented in USFOS, and of course by the modelling assumptions applied in the LSDYNA analysis. Keeping in mind the assumptions and simplifications in the collision modelling in USFOS, the uncertainties related to the force-deformation curve are small. However, for the large energy collisions, where the curve has been extrapolated, the accuracy is far less certain.

The extrapolation of the curve is intended to be conservative, i.e.the slope of the curve is believed to be steeper than what is actually the case. This way, the impact force is overestimated. By studying the force-deformation curves obtained in LSDYNA, it is seen that the load level seems to be stabilizing at a constant level when the deformation approaches 8 $m$. The sudden jumps are due to the ship bow hitting bulkheads. Since the bulkheads and stiffeners are regular in the pontoon, the resistance of the pontoon is not expected to continue to increase after the first stages of impact. At the same time, the impact area will increase during the collision, due to the shape of the ship bow. Thus, the maximum load level that the pontoon may withstand might increase. Nevertheless, since the maximum possible contact area is limited, the extrapolation is considered conservative.

Another criterion for the nonlinear springs is that they should model the behaviour of the deformed ship and bridge after the impact. The nonlinear spring element is unloaded at a very steep slope. Physically, this is consistent with large plastic deformations of the ship and the bridge component subjected to impact. Further, the spring is reloaded along the same steep slope. This can be understood as though the spring "remembers" the damage. In other words, the nonlinear spring element appears to be well suited to model local deformations caused by the collision.

It is seen that about 50% of the kinetic energy is dissipated in local deformations for the head-on collisions with pontoon 1, i.e. scenario 1 and 2. The bulb-pontoon collision takes the majority of the energy, which is expected, since the forecastle hits the pontoon at a later stage of the collision. For the 360 $MJ$ head-on collision with pontoon 4, i.e. scenario 4, the portion of the collision energy absorbed by local deformations is about 60%. In other words, the local deformation energy is slightly higher in this collision scenario. The main reason for this is probably that the collision energy is lower. Since the force increases with increasing deformation, see figure 6.8, the first portion of the collision energy will cause a relatively small impact load. Thus, lower impact energies will not generate as severe reactions in the bridge globally. Table 6.2 confirms that the maximum impact force is lower in collision scenario 4 than in the first two. Another factor is that a different design ship is assigned to these pontoons, and the force-deformation curve is therefore not the same.

In load scenario 5, where a pontoon at the midspan of the bridge is struck by a 250 $MJ$ collision, 54.2% of the kinetic energy is dissipated by local deformations. Based on the reasoning in the previous paragraph, it would be expected that the percentage of energy absorbed locally is larger than for collision scenario 4, since the energy level is lower. The applied design ship is the same for these two collisions, and cannot be used to explain the difference. The results therefore indicate that the bridge is more compliant in the central region than in the high bridge. This will be addressed in the next paragraph. On the other hand, since the deviation is only 5%, there might also be other explanations. It is thinkable that the percentage of energy dissipated by structural damping is higher for the low energy collision. However, when running the simulations without structural damping, the results show the same trend.

The results indicate that the bridge is slightly more sensitive towards pontoon collisions at the midspan than in the high bridge. This is somewhat unexpected, since the columns in the floating high bridge are much taller than columns in the floating low bridge. The column between the girder and pontoon 4 is about 50 $m$ long, while the column connecting pontoon 20 to the bridge girder is about 14 $m$. Combining this knowledge with the load levels in table 6.2, it is found that the maximum bending moment in the bridge girder is almost four times higher in collision scenario 4. It would therefore be reasonable to believe that rotation of the bridge girder could be an issue. By studying the response, it is seen that the rotation of the bridge girder is small at the time of impact, and that translation of the bridge girder in the lateral direction seems to be more important. A possible explanation for this is the large mass of the pontoons, which indicates a large restoring moment. Due to the relatively small rotations, it is evident that the bridge girder absorbs energy by lateral translations. Based on this knowledge, it seems reasonable that the bridge is more compliant in the central region than in the high bridge. When a ship strikes a pontoon at the midspan, the collision velocity is perpendicular to the bridge girder. Since the horizontal radius of the bridge is fairly large, the impact load must mainly be carried by bending moments. At pontoon 4, on the other hand, the horizontal slope of the bridge girder is larger. Thus, a part of the impact load can be carried by axial forces. Nevertheless, it must be stressed that the variation in local energy dissipation is small, and that it should not be weighed too heavily.

In the 90 degree angle collision with pontoon 1, i.e. scenario 3, local deformations dissipate 85.7% of the collision energy. Compared to the head-on collisions, this is a very high ratio. At the same time, it seems credible that the bridge has a high global resistance to this action, since a major part of the load is carried by axial forces in the bridge girder. Another reason for the high amount of energy dissipated locally might be the force deformation curve, which is different for 90-degree angle collisions. It is seen from table 6.2 that the total amount of energy dissipated locally and the maximum load level is similar for the 660 $MJ$ head-on collision and the 400 $MJ$ perpendicular collision. In figure 6.9, the force-deformation curves for the two collision scenarios are displayed. It is seen that the pontoon is slightly softer in the 90 degree collision. However, the difference is not substantial, so the curve is not the governing reason for the high portion of energy absorbed locally.

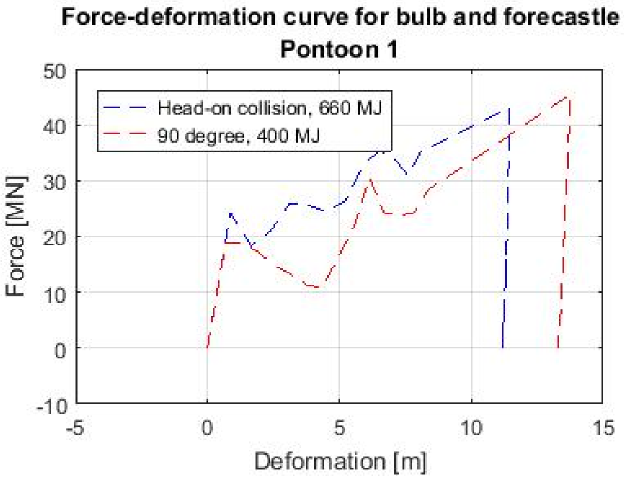

Figure 6.9: Force-deformation curves obtained in the 660 $MJ$ head-on collision and the 400 $MJ$ perpendicular collision. The forces in the bulb-spring and forecastle-spring are added together in the figure.

Table 6.2 shows that the local deformation is 13.8 $m$ in the sideways collision. Since it is known that the pontoon suffers the majority of the damage, and that the width of the pontoon is 16 $m$, this implies substantial deformations of the pontoon. Figure 6.10 shows that the deformation is far into the extrapolated region of the force-deformation curve, which means that the behaviour is highly uncertain. It is not unthinkable that the resistance of the pontoon is reduced when the damages are large. A possible scenario is that the pontoon is weakened so much that it cannot stop the ship altogether, only slow it down. If this is the case, then only a portion of the kinetic energy in the ship is transferred to the bridge. In conclusion, the collision model is believed to be conservative, since the collision force is high, and since all the energy is transferred to the bridge.

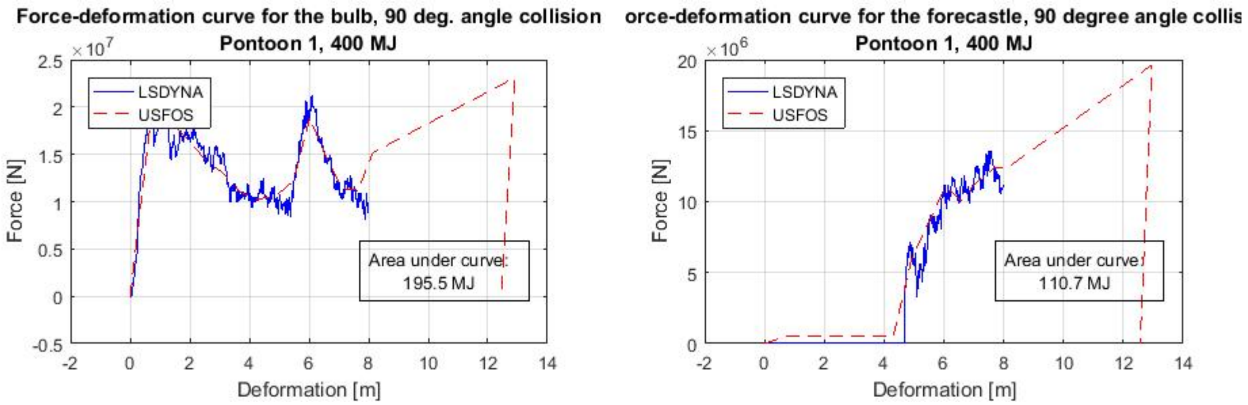

(a) Bulb

(b) Forecastle

Figure 6.10: Measured force-deformation relationship in collision springs compared to curve from LSDYNA. Collision scenario 3.

### 6.3.2 Description of impact load as a function of time

The force histories for the collision springs are shown for collision scenario 2 and 5 in figure 6.11. The history plots for the remaining collision scenarios are attached in appendix C.2. It is seen that the duration of the load is between 3 to 8 *s* for all the collision scenarios. Compared to the fundamental eigenperiod of the bridge, the duration is very short, less than 6%. Thus, the impacts are in the impulsive domain according to the definition applied in the NORSOK standards. This is consistent with what is expected.

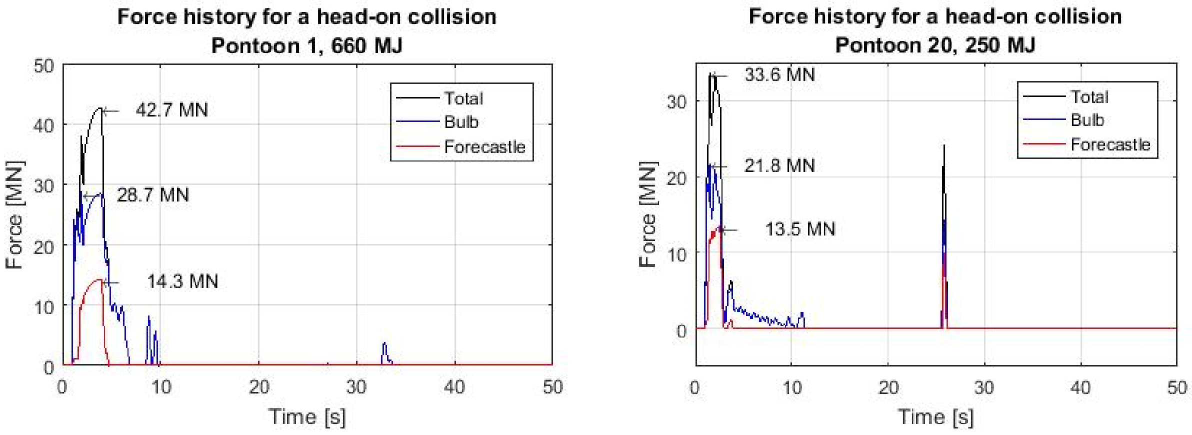

(a) Collision scenario 2

(b) Collision scenario 5

Figure 6.11: Axial force in the collision springs as a function of time.

Figure 6.11a shows a small force in the bulb-spring after about 10 *s*. This small peak occurs in both head-on collisions with pontoon 1, and also in the head-on collision with pontoon 4. Physically, the load can be explained by a second impact between the ship and pontoon. In collision scenario 2, the ship is close to stationary after the first impact, while the pontoon starts to move back towards its initial position. This is also evident by the velocity of the ship mass, which is shown for collision scenario 2 in figure 6.12. The ship mass is given the velocity corresponding to the impact energy at 1.0 $s$. During the next 6 seconds or so, the ship is decelerated. This coincides with the duration of the impact force shown in figure 6.11a. Then, at about 8 and 9 $s$, the mass is accelerated in the opposite direction of the initial velocity. This is consistent with the two spikes in the force history.

The force in the forecastle spring is zero at the time of the second impact, i.e. only the bulb-spring is compressed. It is believed that this can be explained by a pendulum motion of the pontoon. During the main impact, the pontoon and column rotate about the bridge girder. In the reversed pendulum motion, a compressive force is induced in the bulb spring. In the 250 $MJ$ collision at midspan, there is also a second peak close to the main impulse. In figure 6.11b, it is seen that this second peak is much closer to the first impulse than what is the case for collision scenario 2. This also seems to coincide with the theory of a pendulum motion of the pontoon, since the column is much shorter in this collision. The natural period of a pendulum is proportional to $\sqrt{L}$, where $L$ is the height of the column in this case. It is also seen that the bulb spring is subjected to compression over a 6 second period of time after the second impact. The reason for this can be that a certain amount of energy is required in order to push the ship away.

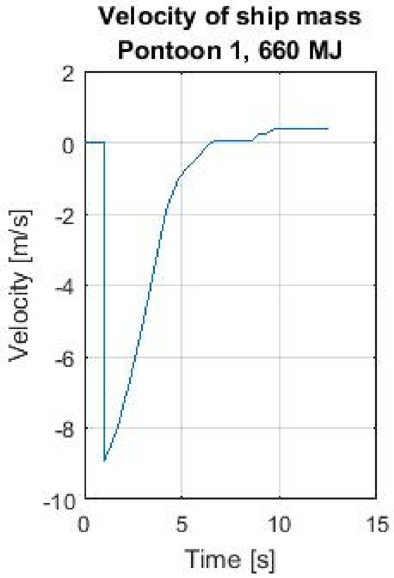

Figure 6.12: Velocity of the ship mass as a function of time. Collision scenario 2.

Figure 6.11b shows a third peak in the force history for collision scenario 5, i.e. the head-on collision with the pontoon at midspan. In this collision between ship and pontoon, there is force both in the bulb and in the forecastle. By studying the animation of the collision, it is seen that this impact occurs when the bridge girder is traveling back towards its initial position. Figure 6.13 shows that the struck pontoon is traveling back when the third peak occurs. The third impulse is large enough to reverse the direction of the pontoon.

In collision scenario 2, there is a third impact between the ship and bridge after about 33 $s$. The impact is detected in figure 6.11a as a small spike in the collision load. This third impact is an undesirable side effect of the structural damping, and does not have a physical explanation such as the third impulse in collision scenario 5. Due to structural damping, the velocity of the ship mass is slowly damped out. As a consequence, the oscillating bridge collides with the stationary ship mass, while in reality, the ship would have drifted away at this stage. Since the load level is small, it is not believed that the action should affect the results.

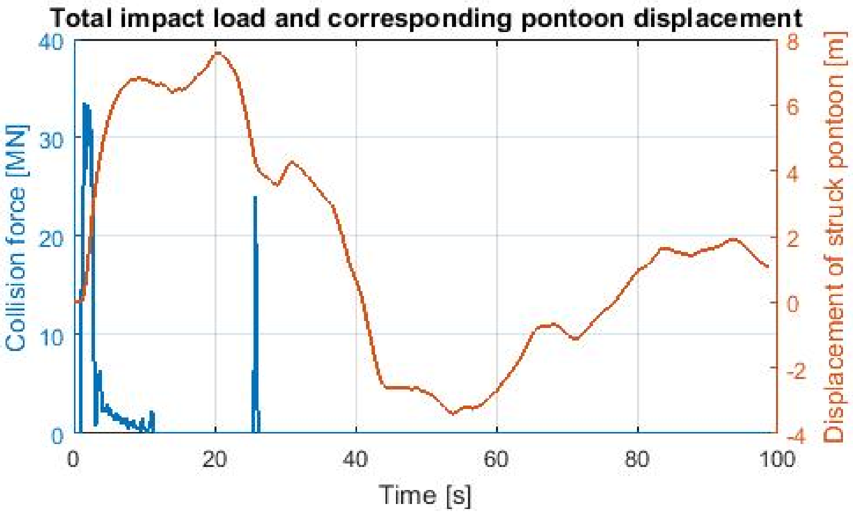

Figure 6.13: Position of the struck pontoon in the direction of the impact, i.e. in the global y-direction, plotted along with the impact force. Collision scenario 5.

### 6.3.3 Critical bridge regions in case of pontoon collision

The ALS design criterion states that the bridge can endure small local damages, as long as the integrity of the structure is not compromised(Moan, 2001). In this context, this implies that some damage on the struck pontoon is allowed. In a global perspective, it is desirable that the pontoon is easily deformed, such that a large portion of energy is dissipated locally. At the same time, the deformations should not be so large that the ship hits the column, which would require more extensive repairs. It is of course also desirable that the pontoon preserves its buoyancy properties. According to the NPRA, the bridge can withstand flooding of two pontoon compartments. However, it is found that in all collisions except for scenario 5, the local deformations are so large that there is a risk of penetrating more than two compartments. As a consequence, the structural integrity of the bridge might be threatened. Flooding of compartments will be studied more closely in section 6.5. In this section, the load levels in the bridge girder and columns will be assessed.

The most critical regions in a ship collision appear to be in the bridge girder above the struck pontoon and at the fixed ends. The maximum bending moments about the strong axis and the largest shear forces are given for these locations in table 6.2.

From the ultimate resistance assessment by the NPRA, it is known that the critical bending moment is 3069 $MNm$(Norconsult AS, 2017e). It is seen that this maximum allowable value is exceeded in collision scenario 1 and 2. Since scenario 1 is analyzed mainly as an experiment, the reaction forces in this collision are not that interesting. Collision scenario 2, on the other hand, is a design collision determined in risk analyses carried out by the NPRA. According to load levels found in the USFOS analysis, the bridge girder will suffer plastic deformations above the pontoon and at the south end-anchoring. At the north end-anchoring, 98% of the capacity is utilized. This means that there is a high risk of permanent deformations at the north end of the bridge as well, given the uncertainties related to the analysis. In conclusion, there is a high risk of permanent damage to the bridge when subjected to the 660 $MJ$ design collision. This collision scenario should therefore be assessed more thoroughly, in order to determine if modifications must be made to the design. Damages to the bridge girder will reduce the capacity of the bridge, and expensive repairs might be necessary.

For the 660 $MJ$ collision with pontoon 1, shear and torsion stresses appear to be of secondary importance. The largest torsional moment in the bridge girder occurs above the struck pontoon, and has a value of about 240 $MNm$. Assuming that the torsional section modulus of 2.76 $m^3$ is correct, this corresponds to a maximum torsional stress of 87 $MPa$. Thus, torsional loads are fairly small compared to bending about the strong axis. The largest shear force in the column that can be caused by the collision load is 51.8 $MN$. If the shear stress is assumed to have a parabolic distribution, with a maximum value $\sqrt{3}\frac{V_y}{Sh_y}$, then the highest shear stress in the column is 122 $MPa$. Here, $V_y$ is the shear force and $Sh_y$ is the shear area, which is 0.736 $m$ for column 1. Thus, the column should have sufficient shear capacity to carry the collision load.

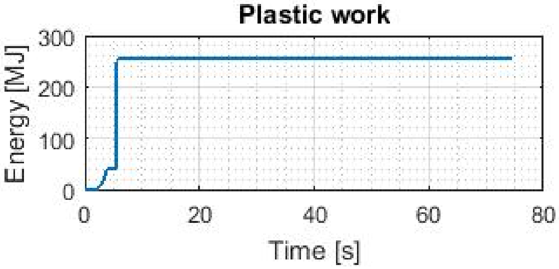

Figure 6.14: Accumulated plastic work as a function of time. Collision scenario 2.

A plastic analysis is carried out for the 660 $MJ$ collision. As mentioned earlier in the report, USFOS does not capture local buckling of the cross section, which means that the plastic model does not accurately describe the bridge behaviour. Still, a plastic analysis may give an idea of how the plasticity will manifest itself. Another issue with including plasticity, is that the initial stress level in the cable-stayed bridge is unnatural high. This is a consequence of the pretension in the cables, which is not precise. In the region closest to the anchoring, the initial bending stress about the strong axis is approximately 120 $MPa$. This should be zero. To avoid reaching plasticity at too low load levels, the yield strength is increased to 540 $MPa$ in the first 100 $m$ of the bridge girder. This must also done for the north side anchoring, in order for the analysis to be stable. The results show, not unexpectedly, high plastic utilization at the end supports and above the struck pontoon. Also, a high utilization is reached close to the impact area, before it travels away towards the ends. This is consistent with the travelling hinge theory by Norman Jones. The accumulated plastic work in the bridge as a function of time is shown in figure 6.14. A large jump is seen at about 6 $s$. This is the time instant where a plastic hinge forms at the south end-anchoring. It is seen that the plastic work reaches 255 $MJ$, which means that 39% of the collision energy is absorbed by plastic deformations in the bridge. Given that 50% of the energy has already been dissipated by spring compression, the plasticity is unexpectedly high; structural and hydrodynamic damping will also dissipate some energy. It is believed that the jump in plastic work at 6 $s$ caused by an instability, and that the results are not trustworthy. When the analysis is run with a different time step, the results change, which supports the theory of an instability. The plastic work should maybe be in the range of 40 $MJ$, i.e. the plastic work before 6 $s$. This corresponds to 6% of the collision energy. All in all, the plastic analysis is too unstable to draw any conclusions.

The bending moment capacity of the bridge girder is not exceeded in the last three collision scenarios. However, structural damping might dissipate some of the collision energy during the impact. This means that the analyses are non-conservative. For the 360 $MJ$ collision with pontoon 4, the bending moment in the bridge girder above the struck pontoon is 91% of the capacity. When structural damping is not imposed, the analysis is stable for about 70 $s$, which is sufficient for identifying the maximum bending moments. The bending moment in the bridge girder above pontoon 4 is found to be 2900 $MNm$. This is high, yet still within the capacity of the girder. In other words, the bridge appears to have sufficient capacity to withstand the 360 $MJ$ collision without plastic damages. However, since the utilization is very high, it may be wise to perform further analyses. A short analysis with no structural damping is also carried out for the 250 $MJ$ collision. The maximum bending moment above the struck pontoon is found to be 2600 $MJ$, which is 85% of the capacity. Thus, it should be safe to say that the bridge girder can resist this collision without plastic utilization.

The shear forces in the bridge girder appear reasonable; approximately half the impact load is carried at each side of the column. The largest measured shear force is 27 $MN$, and occurs above the struck pontoon in the 1000 $MJ$ collision with pontoon 1. The applied shear area in the horizontal direction is 0.624 $m$. If it is assumed that the shear stress in the girder is parabolically distributed, with a maximum value $\sqrt{3}\frac{V_y}{Sh_y}$, then the maximum stress is 75 $MPa$. $V_y$ is the shear force in the horizontal plane, while $Sh_y$ is the corresponding shear area. Though the shear area applied in this estimation is approximate, it is seen that the shear stress will be far below the yield strength of 420 $MPa$. This is consistent with the hypothesis of long beam behaviour, as the load is mainly carried by bending moments.

The response of the bridge is different when subjected to collision scenario 3, than in the head-on collision scenarios. In this collision, the torsional moment in the column is perhaps the most critical response. Figure 6.15 shows the torsional moment in the column as a function of time. It is seen that there is some torsion present before the collision load is applied, about 200 $MNm$ to be exact. Ideally, this should not be the case, since the pontoon should be completely free to move. However, due to the fact that there are two collision springs placed in parallel, the pontoon will be somewhat restrained from rotating. In the 90 degree collision, the roll motion of the pontoon is resisted. It is believed that the initial torsion moment emerges when the pretension and gravity is applied. Naturally, this is undesirable. However, since the explanation has been identified, it is believed that the results of the analysis can be trusted with some confidence. If the initial load level is subtracted from the results in figure 6.15, it is found that the maximum torsion moment, $T_{max}$, is 1144 $MNm$. The credibility of this value is easily checked by hand calculations; the maximum impact load is 42.7 $MN$ and acts at a distance of 26 $m$ from the column center. This implies a bending moment of 1370.2 $MNm$, which supports the measured torsional moment.

The large torsional moment might be critical for the connection between the column and bridge girder. The capacity of this joint to take bending moment is not known, but it

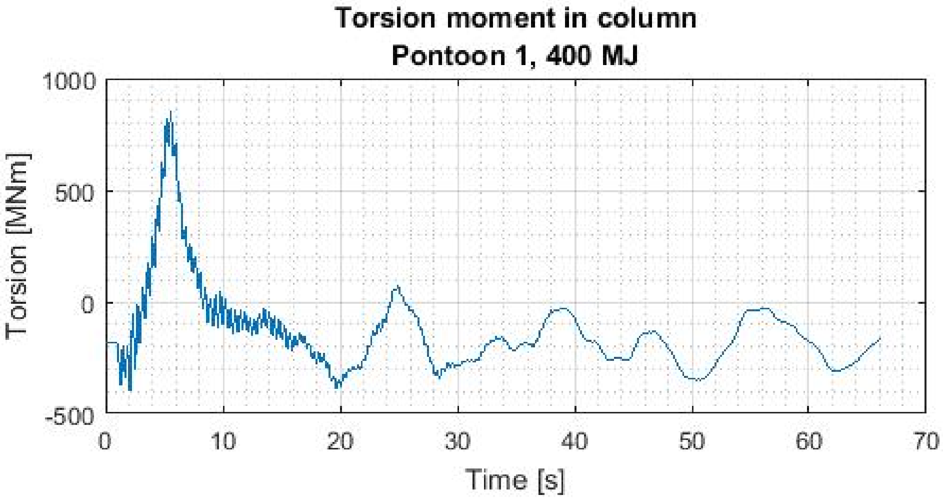

Figure 6.15: Torsional moment in column between pontoon 1 and bridge girder. Collision scenario 3.

might be interesting to compare the results to a local finite element analysis carried out by Norconsult. The results are described in the report “Appendix E - Pontoon and column structural sizing and design”(Norconsult AS, 2017d). A 350 $MJ$ ship collision at a 30 degree angle is considered. The resulting force in the transverse direction of the pontoon is 30 $MN$, which is 70% of the maximum collision force obtained in the USFOS analysis. In the report, it is stated that the 30 degree collision will be survived by the bridge, but that it will sustain plastic deformations in the joint itself, and in the bottom plate of the bridge girder(Norconsult AS, 2017d). In other words, plastic deformations in the connection between the column and the girder are highly probable in collision scenario 3. More thorough analyses are therefore required to assess whether or not the bridge will fulfill the design criteria when subjected to this collision. It should be noted that a 90-degree collision angle with the pontoon is highly conservative, and that a 30-degree angle might be more realistic. This would reduce the torsional moment by 50%.

The torsional capacity of the column itself should be sufficient. The column has a circular cross section with an external radius $R$=6 $m$. In the modelling process, the torsional moment of area, $I_t$, was found to be 74.9 $m^4$. The maximum shear stress in the outer surface is given by $\tau = \frac{T_{max}}{I_t}R$, which gives 91.6 $MPa$. This is only about 22% of the assumed yield capacity of 420 $MPa$, and the torsion of the column should therefore be well within the acceptable range.

Since the collision load in scenario 3 to a large extent is carried by axial forces in the bridge girder, it is also interesting to control this. When the axial force caused by pretension in the cables is subtracted, it is seen that the maximum axial force is 32 $MN$. Since the girder has a cross-sectional area of 1.68 $m$ in this region, the axial stress is about 19 $MPa$. This is less than 5% of the yield strength, which means that the axial load is not critical.

### 6.3.4 Global motions of bridge after impact

The motions in the bridge after the 1000 $MJ$ collision with pontoon 1 are given in figure 6.16. The motion pattern for the 660 $MJ$ collision is very similar, just not as pronounced. For illustrative purposes, plasticity is included, and plastic utilization is indicated by color. It is seen that large bending waves propagate away from the impacted pontoon. The position of the largest plastic utilization is also seen travelling away from the impacted area and towards the north end-anchoring. This is comparable to the theory for travelling plastic hinges by Jones. The plasticity is reduced with increasing distance travelled, which can perhaps partly be explained by energy absorption in plastic hinges.

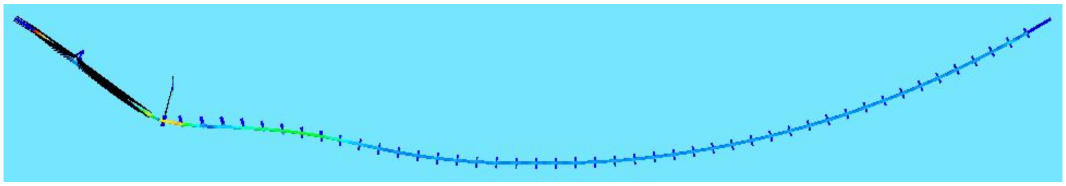

(a) At 6.0 $s$ in the time history.

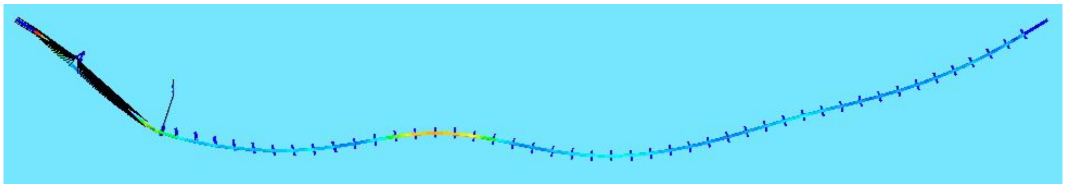

(b) At 15.2 $s$ in the time history.

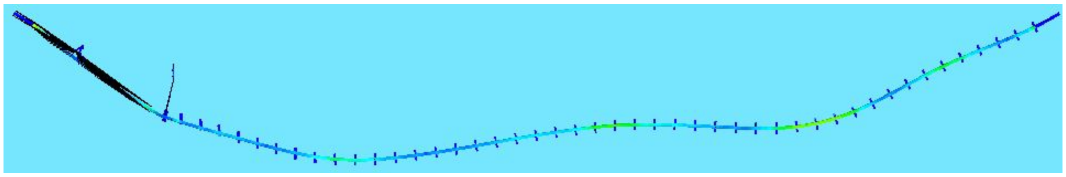

(c) At 25.0 $s$ in the time history.

Figure 6.16: Bridge deformations caused by collision scenario 1. The deformations are scaled by a factor of 10. The disturbance at the struck pontoon are the collision springs and connection elements, and can be ignored.

The motions in figure 6.16 are scaled by a factor of 10 for illustrative purposes. The actual displacement of the struck pontoon is given for the 660 $MJ$ collision in figure 6.17. The bridge girder above the pontoon follows the same displacement pattern. It is seen that the maximum displacement is 8 $m$. To get a physical understanding of how large the displacement is, it can be compared to the pontoon width, which is 16 $m$.

The impact causes torsion of the bridge girder in the high bridge, see figure 6.18. This is not unexpected; the columns are tall, which indicates that the torsional moment is large. For the 1000 $MJ$ collision, the torsional moment will be in the order of 2600 $MNm$. During the first 100 $s$ of the analysis, the torsion motion of the bridge girder in the high bridge oscillates with a period of approximately 10 $s$. From the eigenvalue analysis, it is known that the bridge

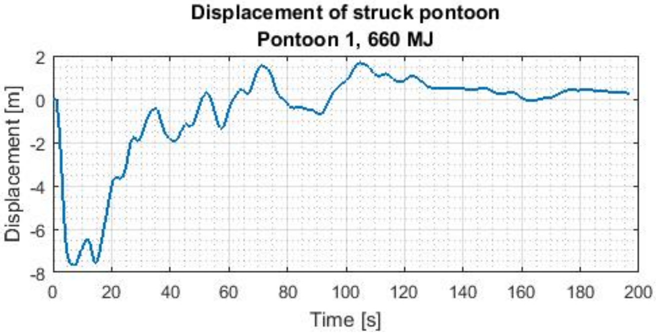

Figure 6.17: Displacement of the struck pontoon in the global y-direction caused by collision scenario 2.

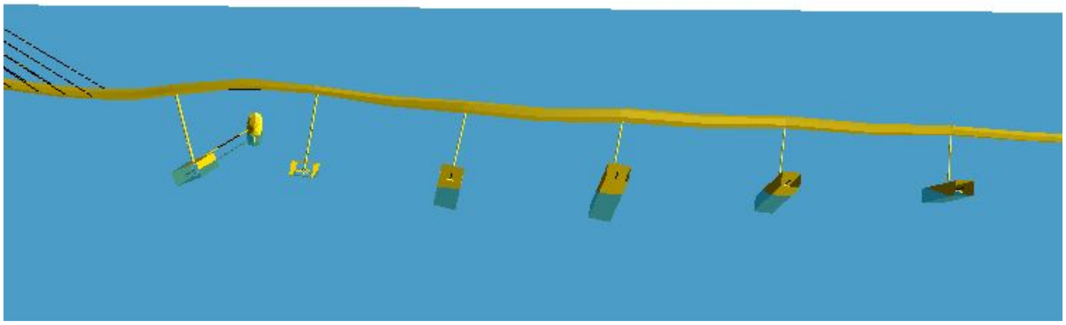

Figure 6.18: Torsion in high bridge caused by collision scenario 1 at time 9.3 $s$. The deformations are scaled by a factor of 10.

has several torsional modes with periods in this range, namely modes 7 to 12.

The deformation of the bridge after impact is shown for collision scenario 3 in figure 6.19. It is found that the largest motions occur in the cable-stayed bridge and the high bridge. Figure 6.19a shows the bridge girder directly after the impact. It is seen that the struck pontoon is pushed in the direction of the impact velocity, which also leads to a sideways motion due to the slope of the girder. The yaw motion of the pontoon is small relative to the motion of the bridge girder, which at first seems unexpected. However, since the column connection is stiff, yaw motion of the pontoon implies bending about the strong axis for the bridge girder. Thus, the resistance against yaw is high. Roll motions, on the other hand, appear to be significant. Figure 6.19b illustrates how the pontoon and column rotate and cause bending about the weak axis of the bridge girder.

The bridge deformations caused by the 250 $MJ$ collision are shown for a selection of time instants in figure 6.20. Horizontal motions dominate the bridge response, while torsional and vertical motions are small. As the column between the pontoon and bridge girder is short, the torsional moment that the impact imposes on the bridge girder will be moderate. Therefore, it seems reasonable that the torsion of the bridge girder is small. Bending waves can be observed propagating away from the impacted area, similar to what was described in

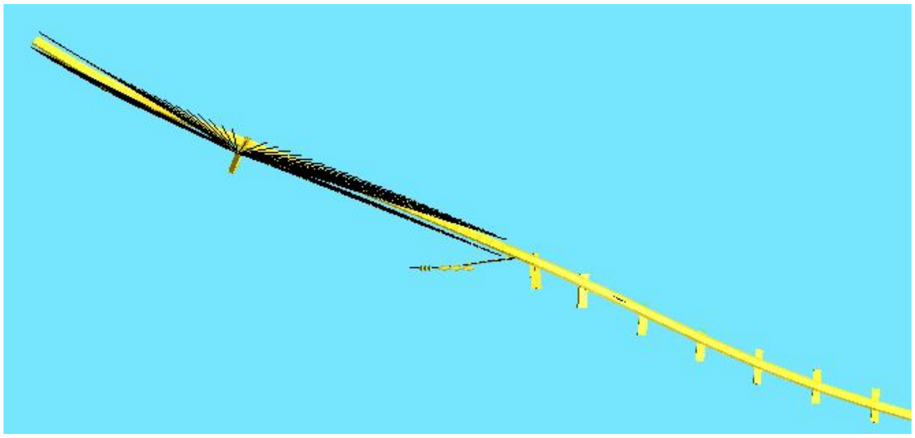

(a) At 5.6 *s* in the time history, from above.

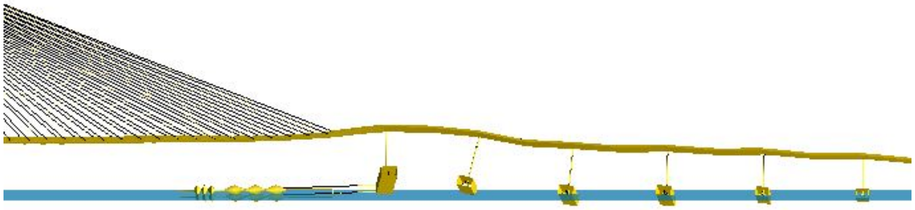

(b) At 5.6 *s* in the time history, from the side.

Figure 6.19: Bridge deformations caused by collision scenario 3. The deformations are scaled by a factor of 15.

chapter 5. Further, the girder appears to be oscillating with three half waves. Although the motion pattern is modest, the three half waves can be detected in figures 6.20b and 6.20c.

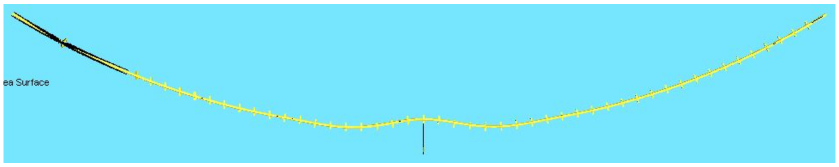

(a) At 3.0 *s* in the time history.

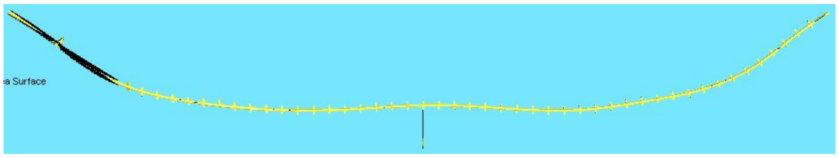

(b) At 20.7 *s* in the time history.

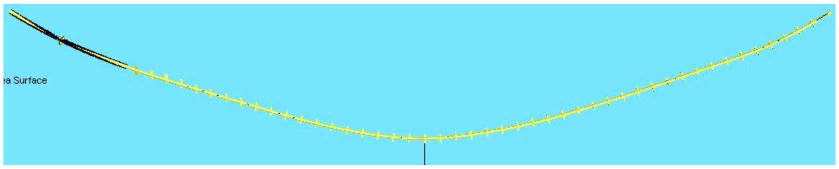

(c) At 52.0 *s* in the time history.

Figure 6.20: Bridge deformations caused by collision scenario 5. The deformations are scaled by a factor of 15.

From the eigenvalue analysis, it is known that the second eigenmode of the bridge is a horizontal mode with three half waves. It is therefore interesting to see if this mode is excited in the collision. Figure 6.21 shows that the position of the pontoon oscillates with a period of about 60 to 70 seconds. This is consistent with the second eigenmode of the bridge, which has a period of 62.3 *s*. Thus, it appears as though the bridge oscillates with the second eigenperiod after the central impact.

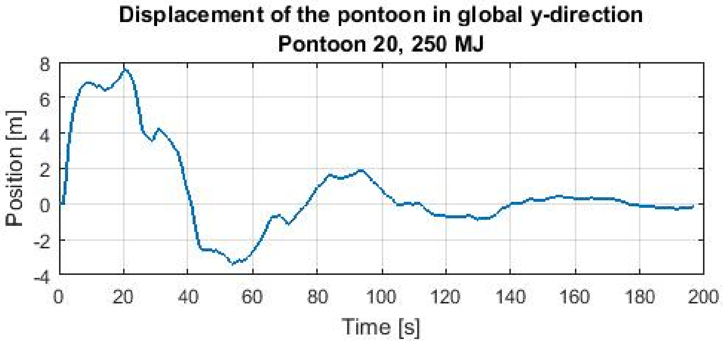

Figure 6.21: Position of the struck pontoon in the direction of the impact, i.e. in the global y-direction. Collision scenario 5.

### 6.3.5 Single degree of freedom model for ship impact at midspan

In the previous section, it was noted that the bridge appears to oscillate with eigenmode 2 when impacted at pontoon 20. It is therefore interesting to see if a simple single degree of freedom model can describe the behaviour of the bridge. The single degree of freedom system is represented by the displacement of pontoon 20 in the transverse direction of the bridge girder.

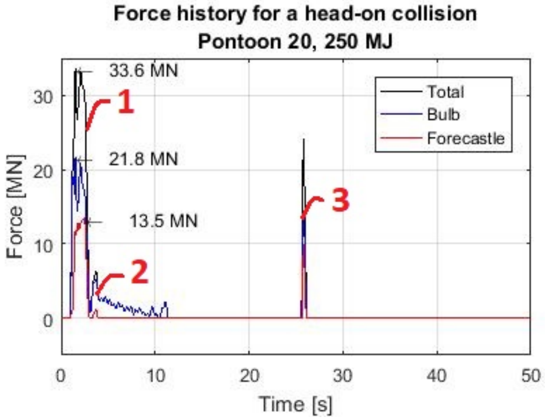

Figure 6.22: Axial force in the collision springs as a function of time, collision scenario 5.

The collision force is given as a function of time in figure 6.22. Three different peaks are detectable, indicated with numbers 1,2 and 3. The duration of the main impact, i.e. impulse 1, is about 3 $s$. Eigenmode 2 oscillates with a period of 62.3 $s$. Thus, the impact duration is 4.8% of the eigenperiod, which means that the collision is in the short impulse domain. In section 3.2.2, a simple oscillation model was presented for short impulses. According to the model, the pontoon will oscillate freely with an amplitude of $I/m\omega_0$ after the impact. In this case, $\omega_0$ corresponds to eigenfrequency 2. At first, only the first peak in the force history is accounted for in the calculations. The impulse $I$ is given by the area below the curve, which is found by integration. The mass per unit length of the bridge is taken as the mass of the bridge girder and the mass of the pontoons divided by the spacing of 100 $m$. Added mass in pontoon surge is also included. The length of the bridge girder that is accelerated is chosen such that the oscillation amplitude is about the same as the maximum deformation found in USFOS. Damping is included by the $e^{-\lambda\omega_0 t}$-term in equation 3.15, where the damping ratio is taken as 3%. This is the imposed structural damping for eigenperiod 2. It is found that the difference between the eigenfrequency and the damped eigenfrequency is very small. The resulting oscillation model is indicated in yellow in figure 6.23a.

As mentioned, two small impacts are detectable in figure 6.22 after the first impact. These impulses are accounted for in a second model, $u_3(t)$. Here, the superposition principle is applied. The three impulses are treated as three separate incidents, where the bridge oscillates with eigenfrequency 2. The displacement histories for the three impulses are presented individually in figure 6.23b. When the three responses are added together, the displacement history indicated in red in figure 6.23a is obtained. The damping and bridge mass is the same as before.

The length $L$ that yields the best fit is 2100 $m$, which is about one third of the bridge length. The model can be interpreted as though this is the accelerated region of the bridge in the initial stages of the response. The impact action is in the inertia dominated domain, which means that the impact is resisted by inertia forces. Since the bridge is long, it will take

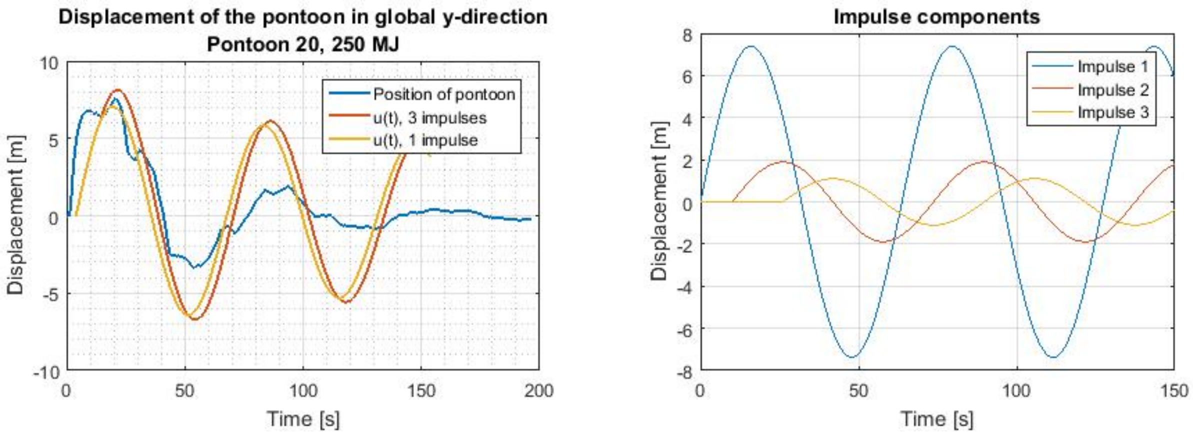

(a) Position of struck pontoon along with model

(b) Impulse components

Figure 6.23: Fitted impulse model for the transverse displacement of pontoon 20 after the central pontoon collision.

time before the action reaches the end supports. At first, only the region close to the struck pontoon will "feel" the impact. It is the mass of this region that decides the inertia forces directly after the impact. According to this simple impact model, the "surrounding region" extends 1050 $m$ from the impact point in each direction.

It is seen in figure 6.23a that the pontoon motion is damped out much faster than what is predicted by the short impulse model. The difference is too large to be explained by hydrodynamic damping, which is expected to be low. Since the model is elastic, plasticity will not cause any damping either. In the impulse model, it is seen that the oscillation amplitude is proportional to $1/m$, where $m$ is the mass. It is therefore thinkable that the apparently large damping may actually be a "decrease in amplitude". The length of the bridge girder that is accelerated will increase as a function of time, which implies that the excited mass will also increase. It is therefore an oversimplification to implement a constant mass in the model. Thus, the simple SDOF-model is not very good when considering longer periods of time.

### 6.3.6 Study of flexural wave propagation after impact

The results show that head-on collisions close to the transit channel impose fairly large maximum bending moments at the north end-anchoring. For collision scenario 1 and 2, the bending moment at the north end reaches 90% of the maximum bending moment at the south end. This seems surprisingly high, and it is therefore interesting to see if the flexural wave theory presented in section 2.2 can substantiate any of the findings. The 1000 $MJ$ collision in impact scenario 1 is studied, as this collision yields the most extreme response.

In order to get an idea of how dynamic effects influence the results, it can be convenient to have a simplified, static model as a reference. A clamped beam subjected to a single point load is illustrated in figure 6.24. Here, the point load is located at a distance $x$ from end

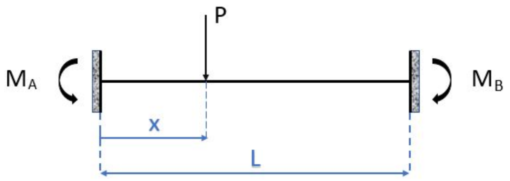

Figure 6.24: Clamped beam subjected to a point load $P$.

$A$, where $x < L/2$. The bending moment at end $A$ is $M_A = \frac{Px(L-x)^2}{L^2}$, while the bending moment at end $B$ is $M_B = \frac{Px^2(L-x)}{L^2}$(Engineering ToolBox, 2018). The ratio between $M_B/M_A$ is accordingly $\frac{x}{L-x}$. If this simple model is applied for the head-on collisions with pontoon 1, the bending moment at the north end should be only about 22% of the bending moment at the south end. This indicates that dynamic effects must have a substantial influence on the maximum bending moment at the north end of the bridge.

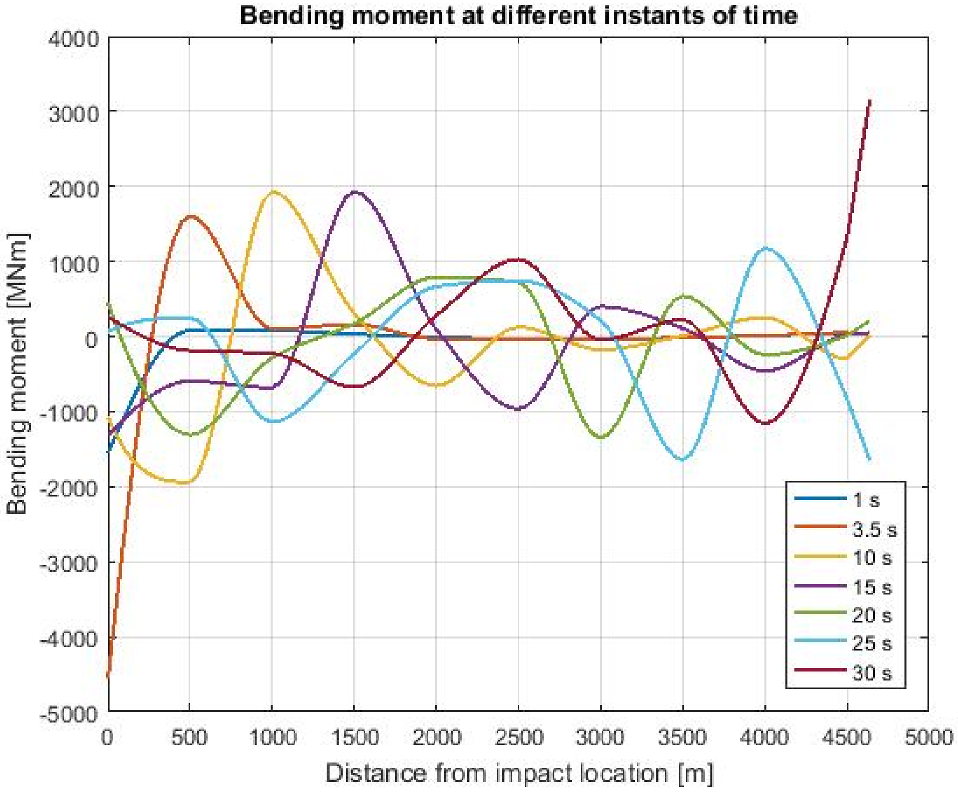

Figure 6.25: Bending moment in the bridge girder north of pontoon 1. Collision scenario 1, structural damping included.

The bending moment at element ends can be plotted as a function of time in USFOS, and the data can be exported. The bending moment about the strong axis of the bridge girder is retrieved for a series of locations at the north side of pontoon 1, i.e. at the longest side. Based on this data, the distribution of bending moment along the girder can be found. In figure 6.25, the moment diagram for the north side of the impacted pontoon is plotted for a selection of time instants. The distance between each data point is 500 *m*. In order to obtain a more realistic diagram, a rounded curve has been fitted to the data points. For a larger figure, see appendix C.3, figure C.15.

The moment diagram is consistent with what is described in the theory by Yu et al., see section 2.2.1. After 1 second, i.e. during the impact, a bending moment forms at the point of impact. At distances greater than 1500 *m*, the bridge is not affected by the collision at all. At 3.5 *s*, the bending moment at the impact point reaches it maximum value. See appendix C.3, figure C.18 for the time history at a selection of locations. The moment diagram for 3.5 *s* also shows a local maximum in the opposite direction, situated close to the impact area. In the theory by Yu et al., this peak was compared to the travelling hinge in elastic-plastic materials. The moment diagram for 10 and 15 *s* shows how this “hinge” propagates away from the impact site. Figure 6.25 also shows how smaller wave components propagate away in front of the main peak at a higher velocity, consistent with dispersion wave behaviour.

The theory by Yu et al. on reflection of flexural waves from the supports is not applicable for the bridge. Yu et al. considers a simply supported beam, i.e. the hinge cannot reach the ends. For the bridge, on the other hand, the end-supports can take high bending moments. However, figure 6.25 shows that the bending waves become irregular after the first wave components reach the end-supports. This indicates that bending waves are reflected and interfere with the incoming waves. The local maximum, which is compared to a travelling hinge by Yu et al., can also be observed travelling back and forth in the period between 25 and 40 seconds. The moment diagrams for a selection of time instants between 25 and 60 seconds are attached in appendix C.3, figure C.16.

Even though the theory on flexural waves by Yu et al. is not directly applicable for the bridge, it might still help explain the high bending moment at the north side anchoring. In the paper, it is shown how incoming and reflected bending waves interfere. Thus, interference can reinforce the load level.

The moment diagrams show that it takes 30 *s* before the maximum moment is reached at the north end. In this time, the imposed structural damping will have dissipated an unknown amount of energy. It is therefore interesting to see how the bridge behaves without structural damping. The moment diagrams for this analysis is attached in appendix C.3, figure C.17. In the figure, it is seen that the maximum bending moment at the north end now has an even higher value than what is reached at the impact point. In other words, dynamic effects cause the north end to be the most critical region. Since the structural damping in the system is unknown, there is a theoretical possibility for this to be the case.

The theory by Graff might also shed some light over the dynamic effects in the floating low bridge. First of all, the deformation of the bridge can easily be compared to the analytic solution illustrated in figure 2.3. The deformation of the bridge girder at the north side of the collision site is shown in figure 6.26. The deformation pattern at 1 and 3.5 seconds resembles the first and second phase, respectively. After the impact, a bending wave starts to form, which is also in agreement with the analytic solution. However, what differs from the theory presented by Graff, is that the bridge girder does not oscillate about the initial configuration.

One possible explanation can be reflection effects, since the bridge girder is not infinitely long. Other factors might be that the bridge girder is curved and that the bridge is not symmetric about the impact point.

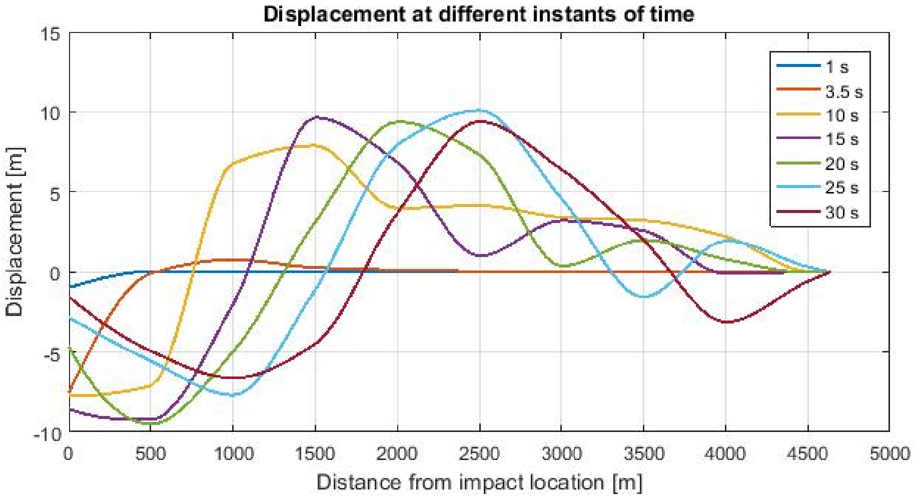

Figure 6.26: Horizontal displacement of the bridge girder in the transverse direction. Collision scenario 1, structural damping included.

Graff also presents a formula for the phase velocity of the flexural wave, if harmonic waves are assumed. In the bending wave in figure 6.25, the positions of the local maxima are easily identified, and it is therefore simple to estimate the velocity of the wave. The curves for 10 $s$ and 15 $s$ are used, since this is after the impulse and before reflected waves interfere with the “hinge”. The peak travels 500 $m$ during a period of 5 $s$, which implies a phase velocity of 100 $m/s$. It should be mentioned that the accuracy of the position is limited by the distance between sample points, but it has been controlled that the deviation is small. The wave length of the bending wave is taken as twice the distance between zero-crossings, i.e. about 1600 $m$. By imposing the properties of cross section type 1 in equation 2.2, a phase velocity of 145 $m/s$ is found. This is in fairly good agreement with the measured results, taken into account the validity range of the equation. The assumption of small displacements is probably applicable. However, the cross section is assumed constant. Since the pontoons impose disturbances, this assumption is not valid. Also, the bridge curvature might influence the wave propagation.

### 6.3.7 Collision analysis with new pontoon design

A new pontoon design has been developed by the NPRA. The design collisions with pontoon 1, i.e. collision scenario 2 and 3, are revisited with the new pontoon design. During the project, the NPRA has decided on a new design energy for the head-on collision. Therefore, a 400 $MJ$ head-on collision with pontoon 1 is also analyzed. The results are presented in table 6.3, along with the results for the old pontoon design.

Table 6.3: Overview and results of the collision analyses with the new pontoon design.

| **Collision scenario** | **2** | | **2a** | **3** | |
|---|---|---|---|---|---|
| **Collision energy** | 660 $MJ$ | | 400 $MJ$ | 400 $MJ$ | |
| **Pontoon** | 1 | | 1 | 1 | |
| **Direction** | Head-on | | Head-on | 90 degree | |
| **Design ship** | Container vessel | | Container vessel | Container vessel | |
| | **New design** | **Old design** | **New design** | **New design** | **Old design** |
| **Local deformation energy** | 53.7% | 49.4% | 52.5% | 76.8% | 76.6% |
| Energy in bulb-spring | 34.8% | 37.9% | 36.6% | 50.0% | 49.9% |
| Energy in forecastle-spring | 18.8% | 11.5% | 16.0% | 26.8% | 27.7% |
| **Maximum impact force** | 36.3 $MN$ | 42.7 $MN$ | 32.6 $MN$ | 38.3 $MN$ | 42.7$MN$ |
| Force in bulb | 22.2 $MN$ | 28.7 $MN$ | 20.0 $MN$ | 21.8 $MN$ | 23.1 $MN$ |
| Force in forecastle | 15.0 $MN$ | 14.3 $MN$ | 14.9 $MN$ | 16.5 $MN$ | 19.6 $MN$ |
| **Maximum local deformation** | 15.0 $m$ | 11.3 $m$ | 10.3 $m$ | 13.3 $m$ | 13.8 $m$ |
| **Remaining energy** | 305.9 $MJ$ | 274.0 $MJ$ | 189.9 $MJ$ | 92.9 $MJ$ | 92.2 $MJ$ |
| Kinetic energy in ship after impact | 1.2 $MJ$ | 1.3 $MJ$ | 0.9 $MJ$ | 8.1 $MJ$ | 8.2 $MJ$ |
| Energy transferred to bridge[1] | 304.7 $MJ$ | 332.5 $MJ$ | 189.0 $MJ$ | 84.1 $MJ$ | 85.6 $MJ$ |
| **Maximum bending moment[2]** | | | | | |
| Bridge girder at the south anchoring | 3000 $MNm$ | 3100 $MNm$ | 2500 $MNm$ | 1300 $MNm$ | 1600 $MNm$ |
| Bridge girder above struck pontoon | 3600 $MNm$ | 3900 $MNm$ | 2800 $MNm$ | 1200 $MNm$ | 1200 $MNm$ |
| Bridge girder at the north anchoring | 2700 $MNm$ | 3000 $MNm$ | 2300 $MNm$ | 1000 $MNm$ | 1100 $MNm$ |
| **Maximum shear force** | | | | | |
| Bridge girder at the south anchoring | 11 $MN$ | 12 $MN$ | 13 $MN$ | 7 $MN$ | 9 $MN$ |
| Bridge girder above struck pontoon[3] | 19 $MN$ | 23 $MN$ | 19 $MN$ | 10 $MN$ | 7 $MN$ |
| Bridge girder at the north anchoring | 11 $MN$ | 13 $MN$ | 9 $MN$ | 4 $MN$ | 5 $MN$ |

[1] Without respect to energy damped out by structural damping

[2] About the strong axis of the bridge girder

[3] In the bridge girder at the north side of the column

The force-deformation curves and the force histories are attached in appendix C.1.2 and C.2.2, respectively. The force-deformation curves for collision scenario 2 and 3 reach the extrapolated region. Thus, the force-deformation curve imposes an additional uncertainty for these two collision scenarios.

When considering the collision scenario 2, the new pontoon appears to be softer than the old design. The amount of energy dissipated by local deformations is about 4% higher, and the maximum load level is decreased by 7.9 $MN$. As a result, the bending moments in the bridge girder at the end supports and at the impact area are lower. However, the maximum bending moment above the struck pontoon is still larger than the estimated capacity of 3069 $MNm$.

It should be noted that the differences in results between the new and old results are too small to draw any conclusions. Although it appears as though the maximum load levels decrease with the new pontoon design, this will to a large extent depend on how the force-deformation curve is extrapolated. Figure 6.27 shows that the extrapolated region of the force-deformation curve is reached in collision scenario 2, and that the maximum force is decided by the extrapolated line. Thus, a different extrapolation will yield a different maximum force. The analysis is rerun with an extrapolation which is considered to be as steep as reasonably possible. It is found that the maximum force is increased to 42.8 $MN$, while the local deformation energy is decreased to 51.1%. This indicates that the load levels may actually be as high as with the old pontoon, although the extrapolation is believed to be highly conservative. In a similar matter, the flattest extrapolation that is considered possible is implemented. In this case, the maximum force is reduced to 32.6 $MN$, and 55% of the collision energy is dissipated by local deformations. The alternative extrapolations are attached in appendix C.1.3.

Based on the findings in the previous paragraph, it appears as though the analysis is not that sensitive with respect to extrapolation of the force-deformation curve. The variation in amount of energy absorbed by local deformations is only about 5%, while the variation in maximum load level is a bit higher, about ±15%. Since the chosen extrapolation is believed to be on the conservative side, it is believed that the applied force-deformation curve should be sufficiently accurate.

The results obtained with the new, reduced design energy is given in table 6.3 as load case 2a. It is seen that the maximum bending moments in the girder are lower than the capacity, which means that the bridge design is sufficiently strong to withstand the new design energy. However, it should be kept in mind that loss of buoyancy is not accounted for. The ability of the bridge to survive pontoon flooding will be assessed in section 6.5.

For the 90 degree angle collision in scenario 3, it is seen that the difference in results is small. The amount of energy absorbed by local deformations is the same, and the maximum force is also in the same order of magnitude. In this collision scenario, the torsional moment in the column between the pontoon and girder is believed to be a critical factor. Table 6.4 shows that the torsion in the column is reduced by about 17% with the new pontoon design. As mentioned earlier, it is the capacities of the connection points at the column ends that are governing, not the torsional capacity of the column itself. From the section 6.3.3, it

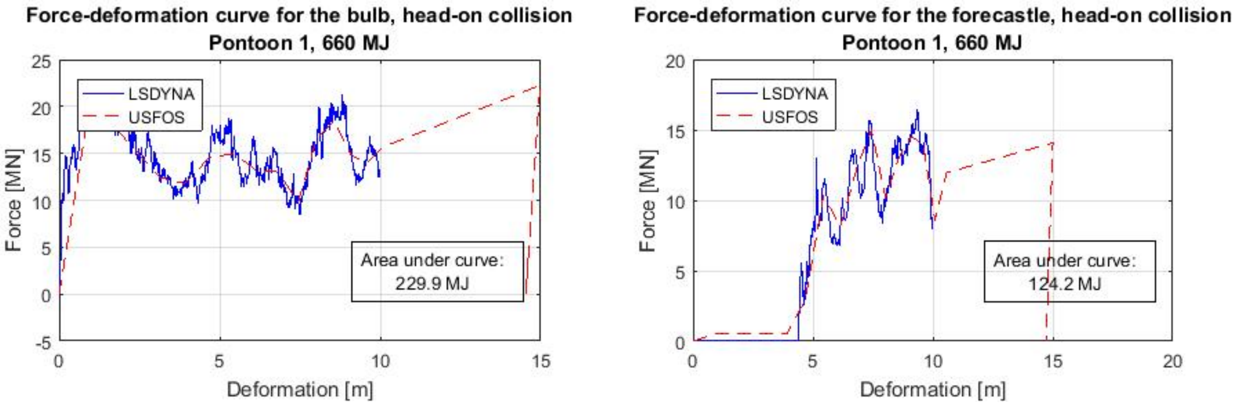

Force-deformation curve for the bulb, head-on collision Pontoon 1, 660 MJ

Force-deformation curve for the forecastle, head-on collision Pontoon 1, 660 MJ

(a) Bulb

(b) Forecastle

Figure 6.27: Measured force-deformation relationship in collision springs compared to curve from LSDYNA. Collision scenario 2, new pontoon design.

is known that the torsional moment must be reduced by more than 30% in order to avoid plastic deformations. This is based on detailed analyses carried out by Norconsult(Norconsult AS, 2017d). Thus, it is believed that yielding will occur in the connection between column and girder, even though the new pontoon is somewhat softer. It should be mentioned that the extrapolation of the force-deformation curve imposes an uncertainty, especially as the maximum force occurs in the extrapolated region.

Table 6.4: Maximum torsion in the column between the struck pontoon and the bridge girder.

| **Collision scenario** | **3** | |
|---|---|---|
| **Collision energy** | 400 $MJ$ | |
| **Pontoon** | 1 | |
| **Direction** | 90 degree | |
| **Design ship** | Container vessel | |
| | **New Design** | **Old design** |
| **Maximum torsion in column** | 947 $MNm$ | 1144 $MNm$ |

## 6.4 Results and discussion of deckhouse-girder collision analyses

Table 6.5: Overview and results of the ship-girder collision analyses.

| **Collision scenario** | **1** | **2** | **3** |
|---|---|---|---|
| **Collision energy** | 360 $MJ$ | 250 $MJ$ | 600 $MJ$ |
| **Point of impact** | A | B | B |
| **Impact with:** | Deckhouse | Deckhouse | Deckhouse |
| **Local deformation energy** | 132.4 $MJ$ (36.8%) | 50.9 $MJ$ (20.4%) | 256.6 $MJ$ (42.8%) |
| **Maximum impact force** | 42.2 $MN$ | 41.8 $MN$ | 42.2 $MN$ |
| **Maximum local deformation** | 5.8 $m$ | 3.6 $m$ | 11.4 $m$ |
| **Remaining energy** | 227.6 $MJ$ | 199.1 $MJ$ | 343.4 $MJ$ |
| Kinetic energy in ship after impact | 10.8 $MJ$ | 7.6 $MJ$ | 1.7 $MJ$ |
| Energy transferred to bridge[1] | 216.8 $MJ$ | 191.5 $MJ$ | 341.7 $MJ$ |
| **Maximum bending moment[2]** | | | |
| Bridge girder at the south anchoring | 1800 $MNm$ | 2200 $MNm$ | 2600 $MNm$ |
| Bridge girder above struck pontoon | 2600 $MNm$ | 3100 $MNm$ | 3000 $MNm$ |
| Bridge girder at the north anchoring | 2300 $MNm$ | 2400 $MNm$ | 2900 $MNm$ |
| **Maximum shear force** | | | |
| Bridge girder at the south anchoring | 9 $MN$ | 10 $MN$ | 11 $MN$ |
| Bridge girder at point of impact | 21 $MN$ | 21 $MN$ | 19 $MN$ |
| Bridge girder at the north anchoring | 10 $MN$ | 13 $MN$ | 11 $MN$ |

[1] Without respect to energy damped out by structural damping

[2] About the strong axis of the bridge girder

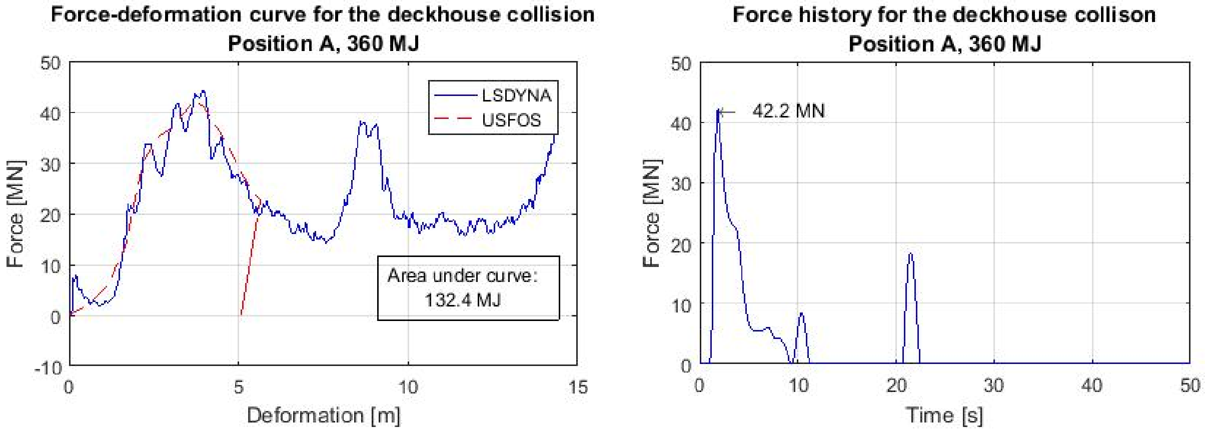

(a) Force-deformation curve

(b) Force history

Figure 6.28: Impact-force characteristics for collision between deckhouse and girder at location $A$.

The main findings are presented in table 6.5. Firstly, it is interesting to compare the first two collision scenarios to the pontoon collisions with identical collision energies. It is seen that the percentage of energy dissipated by local deformations is much lower in girder collisions than in pontoon collisions. This is as expected, since the girder has a higher resistance towards local deformations than the pontoons do. In figure 6.28a, the force-deformation curve for the collision spring is shown for the deckhouse collision at location $A$. A large collision force of 42.2 $MN$ is reached when the local deformation is only about 4 $m$, when a bulkhead in the deckhouse is penetrated. In other words, only a small amount of energy has been dissipated by local deformations when the global motions are excited. Thus, a larger amount of the collision energy is absorbed by global motions in the girder collisions than in the pontoon collisions.

The time history of the impact load is given in figure 6.28b. The plot is taken from the 360 $MJ$ collision between deckhouse and girder at location A. It is seen that the unloading process is slower than the pontoon collision, and that there is contact for about 10 $s$. One reason for the longer unloading period might be that the mass of the design ship is higher, such that more energy is required in order to push the ship away. The third peak in the force history is caused by a collision between the almost stationary ship and the bridge girder travelling back towards the equilibrium position.

It is seen from table 6.5 that the 250 $MJ$ collision at location $B$ causes larger bending moments at critical regions than the 360 $MJ$ collision at location $A$. This is unexpected, as it is seen that the transferred energy is lower, and that the maximum force is approximately the same. The explanation might be that the bridge is stronger when subjected to collisions from the west side. The bridge girder can carry the impact load by axial tensile forces for the collision at location $A$. For the 250 $MJ$ collision at point $B$, on the other hand, it is seen that the curvature of the bridge girder is reversed at the impact location. This can be compared to snap-trough buckling. In this case, the collision load is carried by bending moments, not axial forces.

The 250 $MJ$ and 360 $MJ$ collisions will both cause damages at the impacted location, while at the end-supports, less than 80% of the bending capacity is utilized. The 250 $MJ$ collision causes a maximum bending moment of 3100 $MNm$ at the impact point, which is higher than the girder capacity estimated by the NPRA. For the 360 $MJ$ collision at $A$, the bending moment reaches 2600 $MNm$ at the impact point, i.e. 85% of the capacity. However, the collision will cause local deformations of the girder, which might gravely reduce the ability of the cross-section to carry loads. Thus, collapse may occur at the impact point, even though the initial capacity is not reached. In addition, local deformations will cause a redistribution of forces that is not accounted for in the USFOS analysis. As a consequence, it will be necessary to conduct more thorough collision analyses where the local deformation is accounted for. The local deformations cannot be too extensive to survive the 100-year storm in damaged condition, which is the second criterion in the ALS-control.

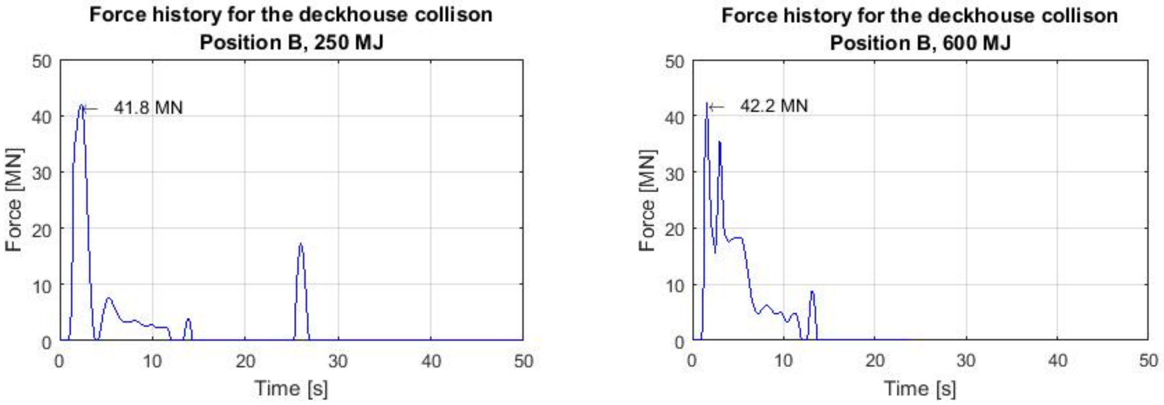

(a) Location B, 250 $MJ$

(b) Location B, 600 $MJ$

Figure 6.29: Force histories for the collision springs in deckhouse-girder collision scenarios 2 and 3.

Table 6.5 also shows the characteristics of a 600 $MJ$ collision at midspan. It is seen that the maximum collision force is not much affected when increasing the collision energy from 250 $MJ$ to 600 MJ. Though this seems counter intuitive, it is explained by the force-deformation curve for the deckhouse-girder impact. It is also found that the maximum bending moment in the bridge girder at the impact area is decreased, which is highly unexpected. However, since the difference is small, it could simply be explained by numerical uncertainty. Dynamic effects due to impact velocity might also contribute; it is seen in the force histories in figure 6.29 that the peaks are narrower for the 600 $MJ$ collision. All in all, both the 250 $MJ$ collision and the 600 $MJ$ collision will cause significant local damages at the impacted area, while the remaining part of the bridge should be undamaged.

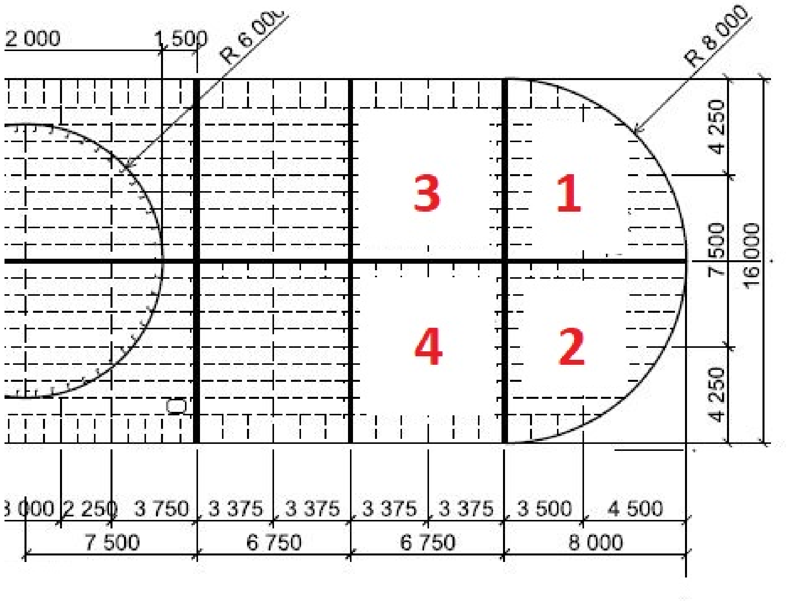

Figure 6.30: Drawing of pontoon 1 with numbering of pontoon compartments. From: (Norconsult AS, 2017a)

## 6.5 Analysis of bridge with flooded pontoon compartments

The NPRA has assessed the capacity of the bridge to withstand flooding of two compartments in pontoon 1, and it was found that the bridge can resist this action. However, table 6.3 shows that even for the new reduced design energy, the local deformation is 10.3 $m$. Since the pontoon takes the majority of the local deformations, there is a significant risk of the ship penetrating into the third and fourth pontoon compartment, see figure 6.30. In this section, the ability of the bridge to withstand flooding of the four numbered compartments will be studied.

### 6.5.1 Method for modelling flooding of compartments

It is assumed that the flooding is very slow, such that dynamic effects are negligible. Thus, the action can be modelled by applying a mass statically. It is desirable to apply the mass after the self-weight of the bridge, i.e. not at the same time. Therefore, the load is applied as a nodal load in the negative global z-direction. The load is given a magnitude equal to the mass time the gravitational acceleration $g = 9.81\ m/s$.

The mass should correspond to the 5 $m$ of water in compartment 1 to 4. The waterplane area of compartment 1 and 2 combined is given by $\pi R^2/2 = 100.5\ m^2$. Compartment 3 and 4 have a joint waterplane area of 108.0 $m^2$. When all four compartments are filled with 5 $m$ of sea water with density $\rho$ =1025 $kg/m^3$, the mass of the fluid is 1.07 $Mkg$. This can be applied as a point mass located approximately at the midpoint between the four compartments, i.e. 21 $m$ from the center of the column. However, to avoid having to create an additional node at this location, it is chosen to use the existing nodes. There is one node at the pontoon end, 27.3 $m$ from the center of the column, and one node at the radius of gyration, which is 15.8 $m$ from the center of the column. If 55% of the mass is placed at the radius of gyration, and the remaining mass at the pontoon end, the bending moment will be close to correct. The analysis is run elastically by increasing the yield strength.

### 6.5.2 Results and discussion of analysis with flooded compartments

The results in table 6.6 are obtained by flooding the pontoon end at the west side of the bridge. When the opposite end is flooded, the results are fairly identical.

Table 6.6: Results from static analysis of the bridge when four compartments of pontoon 1 are flooded.

| | **Flooding of pontoon 1** |
|---|---|
| **Vertical displacement of pontoon 1, flooded end** | -2.2 $m$ |
| **Vertical displacement of pontoon 1, opposite end** | -0.6 $m$ |
| **Vertical displacement of girder above pontoon 1** | -0.9 $m$ |
| **Rotation of bridge girder above pontoon 1** | 1.6° |
| **Torsional moment in bridge girder above pontoon 1** | 120 $MNm$ |
| **Torsional stress in bridge girder above pontoon 1** | 44 $MPa$ |
| **Total bending moment about weak axis above pontoon 1**[1] | 200 $MNm$ |
| Increase in bending moment due to flooding | 50 $MNm$ |
| **Total bending stress about weak axis above pontoon 1**[1] | 100 $MPa$ |
| Increase in bending stress due to flooding | 25 $MPa$ |

[1] Including contribution from self-weight

The deflections seems reasonable. The increased buoyancy of the pontoon is estimated to 1.3 $Mkg$, which is close to the applied mass of 1.07 $Mkg$. It should be kept in mind that the displacements are rounded off to one decimal place.

The deflection of the bridge girder is the largest above the flooded pontoon. Since the deflection is less than 1% of the span between pontoons, a steel bridge should be more than capable of handling the deformations. The rotation of the bridge girder is small enough that it should not be in conflict with the serviceability limit state. By comparison, the driving lane at the bridge is designed with a 3.1% slope for water drainage. It is also seen from table 6.6 that the maximum torsional stress is only about 10% of the material yield strength. In addition, the bending moment about the weak axis of the bridge girder is well below the capacity of 574 $MNm$ that the NPRA has estimated(Norconsult AS, 2017e). All in all, even though the girder will suffer some damages in the collision, it is believed that the bridge has sufficient capacity to survive flooding of four pontoon compartments. It should, however, be checked if the bridge will survive the 100-year storm in damaged condition.

## 6.6 Limitations of ship collision modelling

There are several limitations in the study on ship collision carried out in this report. Firstly, there are the uncertainties and errors due to the way ship collision is modelled. In addition, there are the possibly important collision scenarios that are not considered. These limitaitons will be briefly discussed in this section.

Ship collision is modelled by a point mass with an initial velocity, connected to the bridge through a nonlinear spring that represent the local deformations. Since the shared energy principle is applied, the uncertainties related to load transfer in the nonlinear spring should be small. What is less certain, is how suitable the configuration of springs shown in figure 6.4 is. The collision springs are connected to the bridge through a long connection element, such that the disconnection between the ship and the bridge can be captured. The issue is that the far end of this connection element is fixed from lateral motions. After the initial stages of the impact, when the bridge girder starts to return towards its initial position, the connection element causes an artificially large resistance. As a consequence, the kinetic energy in the bridge is possibly underestimated. Another issue with the configuration, is that the impacted point on the bridge is allowed to move sideways while the ship continues to move straight forward. This, on the other hand, should be conservative, since the behaviour is overly soft.

It is observed that the spring configuration causes a rotational constraint on the struck pontoon, which is not physical. For head-on collisions, pitch motion is resisted, while for the transverse collision, roll motion is withheld. The rotational motion is not completely refused, but based on the rotation of surrounding pontoons, it is believed that the struck pontoon is not entirely free to rotate. The reason for this is that there are two connection elements placed parallel; one below the surface and one at the pontoon top. As a consequence of this, the bridge resistance is overestimated in the analyses. However, since rotational motions appear to be less important than translation, the results should not be entirely unwarranted.

In order to maintain stability, structural damping is included in the analyses. As a consequence, a portion of the collision energy is dissipated by structural damping in the collision springs, which is on the non-conservative side. However, the error is not believed to be unacceptably large. For the 660 $MJ$ collision with pontoon 1, structural damping reduces the maximum bending moment in the girder above the struck pontoon by 7%.

The gravitational load on the ship is not included in the analysis. A possible effect that is disregarded by this, is that the ship can be lifted up in the collision, such that the mass of the ship pushes the bridge down. Alternatively, the ship can be pushed down in the collision. If either of these scenarios take place, the disconnection between the ship and bridge can be viewed as an additional impulse load in the vertical direction. This could for example be modelled by gradually applying a mass during the impact, and then removing it when the ship disconnects.

Local damages are not accounted for in the collision analyses. It has been assumed that pontoon flooding is a slow process, such that it does not affect the instantaneous response. However, if this is not the case, then the loss of buoyancy can enhance the torsional moment in the bridge girder. It was found in section 6.5 that the static torsional moment due to flooding of four compartments is 120 $MNm$, which is about half the torsional moment caused by the 660 $MJ$ collision. Thus, the flooding might not be negligible when dynamic effects are accounted for. Nevertheless, since the torsion moment in the 660 $MJ$ collision is only 20% of the capacity, it is believed that the simplification is acceptable.

# Chapter 7

# Analysis of the Bridge Exposed to Extreme Environmental Loads

## 7.1 Description of environmental conditions at the Bjørnafjord

Information about the environmental conditions in the Bjørnafjord is obtained from the report “K7 Bjørnafjorden End-anchored floating bridge; Appendix B – Global analyses” (Norconsult AS, 2017b).

### 7.1.1 Combination of load cases in the ultimate limit state

For ultimate limit state considerations, the combination of environmental loads given in table 7.1 should be applied(Norconsult AS, 2017b).

Table 7.1: Load cases applied in ultimate limit state considerations.

| | **Wind** | **Wind sea** | **Swell** | **Current** | **Sea level** |
|---|---|---|---|---|---|
| **Return period** | 100 years | 100 years | 10 years | 100 years | 100 years |

According to the NORSOK standards, the design load case should be the most unfavorable combination of actions with an annual exceedance probability of $10^{-2}$(NORSOK, 2007). Since wind generated waves and wind are directly correlated, the design sea state should be combined with a wind condition with the same annual probability(Norconsult AS, 2017b). The waves should propagate in the worst possible direction within ±30° of the wind(Norconsult AS, 2017b). While wind generated waves are generated locally, swell is generated at a distance and then travels to the area in question. Therefore, the direction of swell is governed by topography, not by local winds. The swell condition with a 10-year return period should be applied(Norconsult AS, 2017b).

According to the design basis described in the report by Norconsult, both swell conditions and wind sea conditions should be considered constant across the Bjørnafjord(Norconsult AS, 2017b). Mean wind should be applied in two ways; constant across the fjord and linearly increasing from $0.6U$ at one end to $U$ at the other end. The most unfavorable should be applied(Norconsult AS, 2017b).

### 7.1.2 Wind generated waves

The significant wave height and peak spectral period depend on the heading angle of the incoming waves. In figure 7.1, sea states with $10^{-2}$ annual probability of exceedance are given for the various wave directions. Here, the angles are given relative to north(Norconsult AS, 2017b). The coordinate system is defined such that a wave propagating from east to west is at 90°. The orientation of the bridge is indicated by the black line in the figure. The characteristics of the sea states are also given in table 7.2

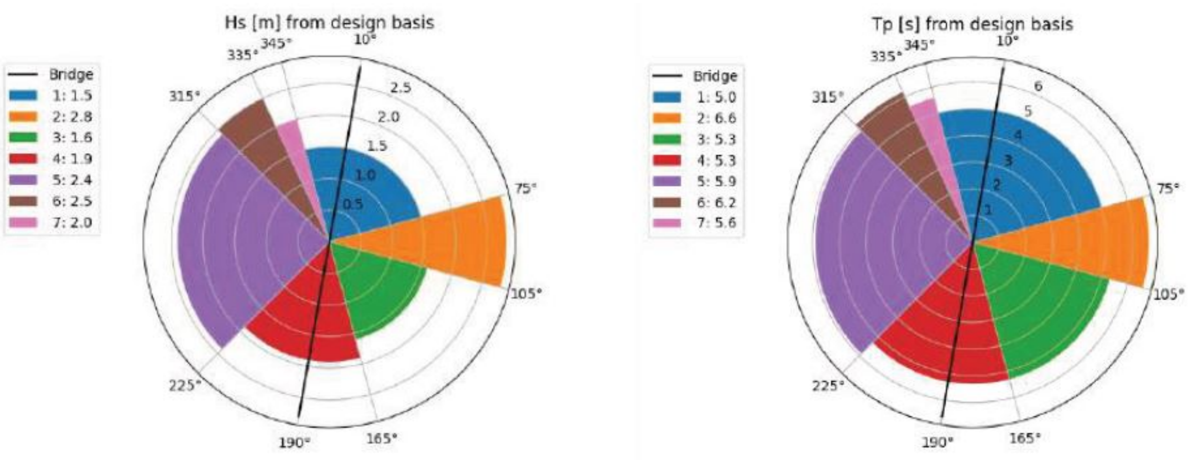

Figure 7.1: Sea states corresponding to a 100 year return period. From: (Norconsult AS, 2017b)

Table 7.2: Significant wave height and maximum spectral peak period for the 100-year sea states.

| | **1** | **2** | **3** | **4** | **5** | **6** | **7** |
|---|---|---|---|---|---|---|---|
| **Direction [Deg]** | 345-75 | 75-105 | 105-165 | 165-225 | 225-315 | 315-335 | 334-345 |
| $\mathbf{H}_{s,3h}$ **[m]** | 1.5 | 2.8 | 1.6 | 1.9 | 2.4 | 2.5 | 2.0 |
| $\mathbf{T}_{p,max}$ **[s]** | 5.0 | 6.6 | 5.3 | 5.3 | 5.9 | 6.2 | 5.6 |

### 7.1.3 Swell

The response due to swell is expected to be much less important than the response caused by wind and wind sea(Norconsult AS, 2017b). Since swell is generated in the ocean, the bridge is only subjected to swell from the west. In the Bjørnafjord, swell consists of two components; one from the southwest and one from the northwest(Norconsult AS, 2017b). According to Norconsult, swell from the northwest dominates(Norconsult AS, 2017b), and for that reason, only waves with directions between 300° and 330° will be considered. The directions are given relative to the same coordinate system as that in figure 7.1. The swell characteristics that correspond to a 10-year return period are given in table 7.3.

Table 7.3: Significant wave height and spectral peak periods for the 10-year sea state.

| **Direction** [Deg] | **300-330** | **300-330** | **300-330** |
|---|---|---|---|
| $\mathbf{H}_{s,3h}$ [m] | 0.34 | 0.34 | 0.34 |
| $\mathbf{T}_p$ [s] | 12 | 18 | 20 |

### 7.1.4 Wind

The 100-year mean wind speed at 10 $m$ is given as 29.5 $m/s$ times a reduction factor $n^2$(Norconsult AS, 2017b). The reduction factor is a function of the wind direction, see table 7.4. The shape factor $\alpha$ is taken to be 0.127, and the turbulence intensity is 14% for angles between 210° and 150°(Norconsult AS, 2017b). The decay factor $c_i$ in the direction of the wind can be taken as 10, while the decay factors in the transverse directions are 6.5(Norconsult AS, 2017b).

Table 7.4: Mean wind reduction factor $n^2$ as a function of wind direction.

| **Direction** [Deg] | **75-225** | **225-255** | **255-285** | **285-345** | **345-75** |
|---|---|---|---|---|---|
| $\boldsymbol{n}^2$ | 0.7 | 0.8 | 1.0 | 0.8 | 0.5 |

## 7.2 Modelling of wave loads

With the command WAVEDATA, irregular waves can be modelled in USFOS based on the wave spectrum. Among the input parameters are spectrum type, e.g. JONSWAP, significant wave height, spectral peak period and the direction of the waves(Marintek, 2015). Further, the wave loads are calculated with the Morison equation for small volume structures or with the Mac-Camy and Fuchs solution for large volume structures(Marintek, 2010). Thus, the forces will depend on the mass coefficient $C_M$ and the drag coefficient $C_D$. In the bridge model, USFOS will calculate wave forces at the vertical pipe elements inside the pontoons. However, since the accuracy of the applied drag properties is believed to be limited, it has been decided to calculate the wave loads externally, and then to implement them as force histories in USFOS. An additional reason for this is that nonlinear wave loads cannot be modelled by USFOS. This is because linear wave theory is implemented(Marintek, 2010), and as discussed in section 3.5.3, the second-order velocity potential will in general contribute to difference-frequency effects(Greco, 2016).

The wave loads are calculated according to the principles described in section 3.5.1 to 3.5.3. The transfer functions of the pontoons are found by WADAM-analyses in HydroD, and MATLAB is used to calculate the loads and generate load files. The load files include load levels as a function of time and unit nodal loads that assign direction and position to the time histories. The modelling principles will be described more thoroughly in the following sections.

The coordinate system in figure 7.2 will be referred to when describing the wave loads, unless specified otherwise. In other words, surge is in the longitudinal axis of the pontoon and sway is in the transverse direction. The local z-axis is oriented in the same direction as the global z-axis. When referring head-on waves or waves at a 0 degree angle, it is the wave direction illustrated in figure 7.2 that is implied.

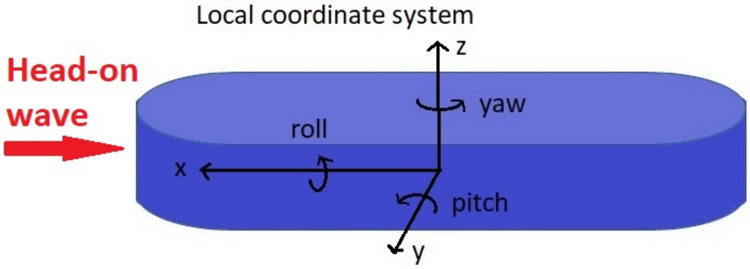

Figure 7.2: Applied coordinate system when describing wave loads.

### 7.2.1 Wave spectrum

The JONSWAP spectrum is applied in the modelling of waves in the Bjørnafjord. The spectrum is applicable for wind waves in developing sea, which is believed to be a reasonable assumption for the area. Norconsult has also used the JONSWAP spectrum(Norconsult AS, 2017b). The spectrum is given by equation 3.33 in section 3.5.4. For wind sea, the peak shape parameter and spectral width parameters recommended by DNV should be fair, see table 7.5 for the applied values. For swell in the Bjørnafjord, Norconsult recommends to use the Jonswap spectrum with $3 < \gamma < 5$(Norconsult AS, 2017b). Therefore, the same spectral properties are applied as for the wind sea. However, since the directions of swell and wind waves are not the same, the forces are calculated individually and added together at the end.

Table 7.5: Applied JONSWAP-parameters for wind sea and swell.

| $\gamma$ | $\sigma_a$ | $\sigma_b$ |
|---|---|---|
| 3.3 | 0.07 | 0.09 |

When the spectrum has been established, the deterministic amplitude for frequency component $j$ can be determined by $A_j = \sqrt{2S(\omega_j)\Delta\omega}$(Faltinsen, 1990). As discussed in section 3.5.2, the frequency step length should in theory approach zero. However, since this would require a very high computational effort, the largest step length that can be allowed is chosen. It is assumed that waves with periods lower than 1 second and higher than 30 seconds will have very low energy. The corresponding angular frequencies are therefore applied as $\omega_{max}$ and $\omega_{min}$, respectively. It is chosen to use identical frequency step lengths, such that $\Delta\omega = \frac{\omega_{max}-\omega_{min}}{N}$, where $N$ is the number of frequency components. The signal will repeat itself after a period equal to $\frac{2\pi N}{\omega_{max}-\omega_{min}}$(Faltinsen, 1990). Therefore, the first option is to choose $N$ such that the force surface elevation repeats itself after three hours. The choice of frequency resolution will be discussed further in section 7.2.3.

### 7.2.2 Linear transfer functions

In order to calculate the linear wave forces, the linear transfer functions must first be established. This is done by first creating panel models of the four pontoon types in Genie, and then performing WADAM analyses in HydroD. It is only necessary to model a quarter of the pontoon in Genie, as the model can be mirrored about the x- and y-axis in HydroD. The center of gravity is assumed to be located at the same position as the center of buoyancy, such that there is no additional restoring moment or overturning moment.

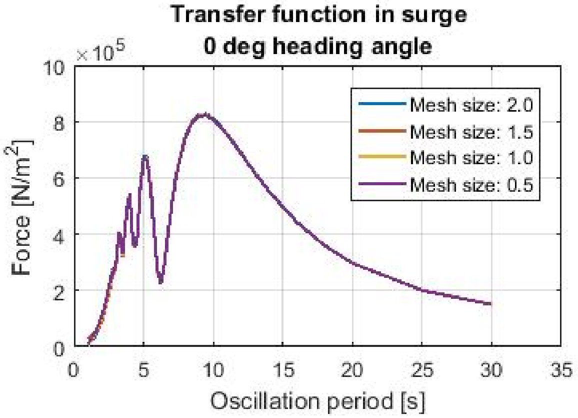

Figure 7.3: Transfer function on surge with four different mesh sizes for a head-on wave, pontoon 4.

First of all, a simple convergence test with respect to mesh size is carried out. The transfer functions for pontoon type 4 are calculated with four different mesh sizes; 0.5 $m$, 1.0 $m$, 1.5 $m$ and 2.0 $m$. The non-zero transfer functions for a head on-wave are attached in appendix D.1. The transfer function in surge is also shown in figure 7.3. It is seen that the difference is very small. This is probably due to the box-like geometry, which results in a fairly regular mesh. Since the results appear to converge, a mesh size of 0.5 $m$ is applied in further calculations.

The transfer functions when the pontoons are subjected to a head-on wave are given for heave and pitch in figure 7.4.

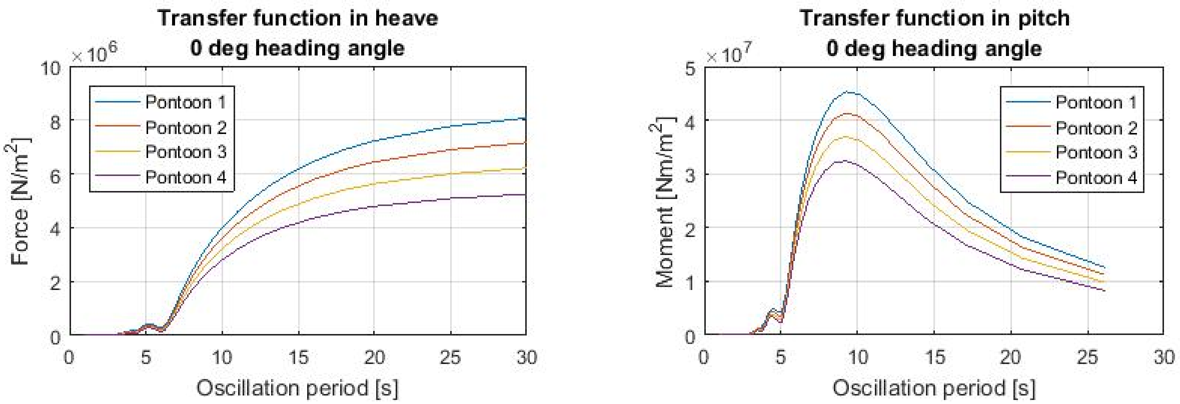

(a) Heave

(b) Pitch

Figure 7.4: Linear transfer functions in heave and pitch for all four pontoon types, head-on wave.

The transfer functions are established for every tenth heading angle between 0 and 80 degrees. When calculating wave forces, the angle between the incoming wave and the longitudinal axis of the pontoon is rounded to the nearest tenth when selecting transfer function. See appendix D.2 for the transfer functions for a selection of a heading angles.

The linear transfer functions coincide very well with those that Norconsult has obtained in WADAM analyses. The results are presented in “Appendix B - Global analyses”(Norconsult AS, 2017b). Seemingly, the only differences are those caused by choice of frequency domain.

### 7.2.3 Linear wave forces

When the linear transfer functions have been established, the linear wave forces can be calculated. The following steps are repeated for each pontoon. Firstly, the angle between the incident wave and the longitudinal axis is determined. From this, the appropriate transfer functions are determined. Then, equation 3.26 is applied in each degree of freedom in order to calculate the forces and moments in the local coordinate system of the pontoon. From this, a force history is obtained in each degree of freedom. These steps are carried out both for wind sea and swell, and the force histories for each pontoon are added together at the end, in line with the superposition principle. If only linear forces are to be accounted for, the force histories can be implemented directly with the command TIMEHIST in USFOS. The time histories are then related to the correct pontoon by applying nodal loads. Each nodal load is a unit vector, where the direction of the load has been transferred to the global coordinate system.

Initially, the wave loads are generated with a frequency resolution given by $N = \frac{1}{2\pi}(\omega_{max} - \omega_{min})T_{3h}$. The number of frequency components is then in the order of 10 000, which indicates very high computational costs. Therefore, a different approach is tested. According to Faltinsen, one can avoid repetition of the signal by calculating the amplitude for an arbitrary frequency $\omega_j$ within each interval $\Delta\omega_j$(Faltinsen, 1990). Thus, the number of sub-intervals can be reduced. Nevertheless, the number of steps $N$ must still be sufficiently high, such that $(\omega_{max} - \omega_{min})/N$ is a small fraction of relevant response frequencies(Faltinsen, 1990). For the bridge, the highest eigenperiod is 2 minutes. If $N$ is chosen to be 250, the frequency step will be 46% of the first eigenfrequency. It is found that this approach reduces the computational time with 90%. In order to make sure that the signal is not repeated, a one hour simulation of wave forces due to wind sea is carried out. In figure 7.5a, the wave amplitude is calculated at the middle of each sub-interval $\Delta\omega_j$, while the amplitude is calculated at an arbitrary location within the sub-interval in figure 7.5b. The figures show that repetition is avoided by the method described by Faltinsen. Another possibility would have been to model the wave amplitude of each frequency component as Rayleigh distributed with $E[A_i^2] = 2S(\omega_j)\Delta\omega$(Haver, 2017).

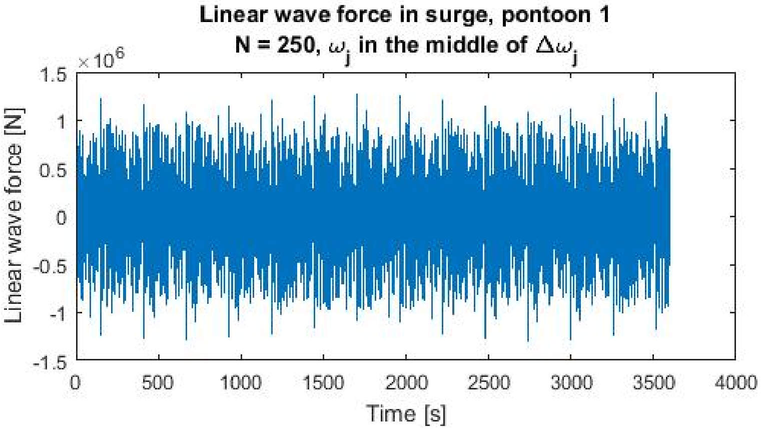

(a) Amplitude calculated at the midpoint of each sub-interval $\Delta\omega_j$

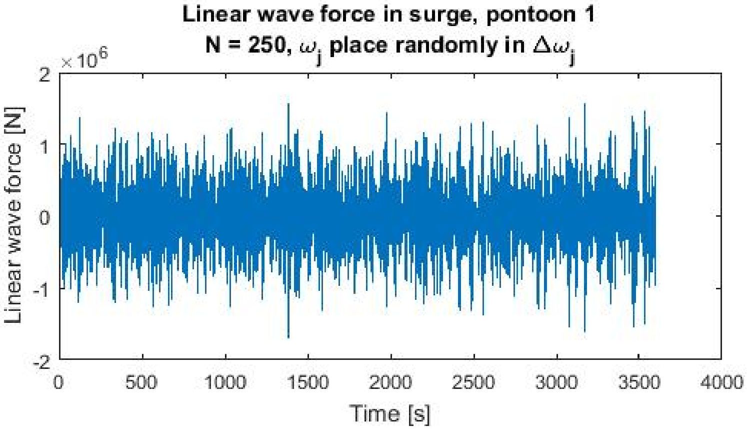

(b) Amplitude calculated at an arbitrary location within each sub-interval $\Delta\omega_j$

Figure 7.5: Linear wave force due to wind sea calculated with $N$=250.

The importance of swell wave forces compared to forces from wind sea is illustrated in all six degrees of freedom in appendix E. It is seen that wind sea causes much larger loads, although there is one exception. In figure E.3, it is seen that swell causes heave forces in the same order of magnitude as those generated by wind sea. This can be explained by the transfer function in heave, see figure 7.4a. In the case illustrated in figure E.3, the spectral peak period for the swell sea is 12 *s*, while wind sea has a spectral peak period of 5.9 *s*. The transfer function in heave is much larger for periods in the range of 12 *s* than in for 6 *s*. Thus, swell sea can cause equally large wave forces in heave as wind sea, even though swell has a much smaller significant wave height.

### 7.2.4 Mean drift coefficients

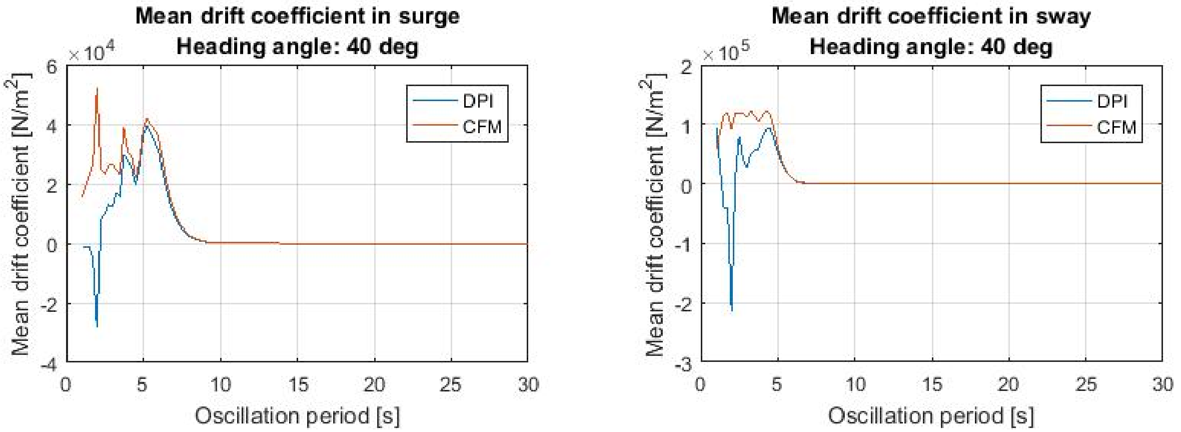

(a) Surge, heading angle of 40 degrees

(b) Sway, heading angle of 40 degrees

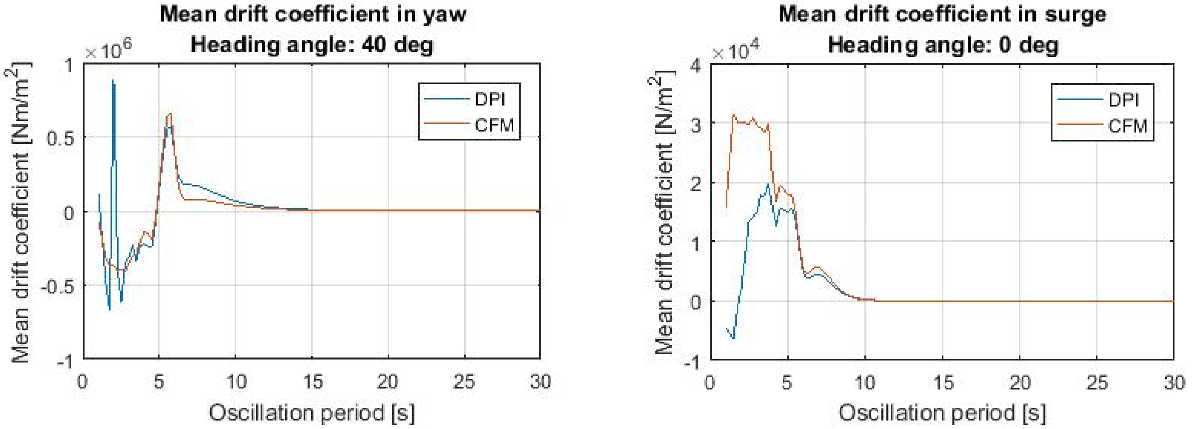

(c) Yaw, heading angle of 40 degrees

(d) Surge, heading angle of 0 degrees

Figure 7.6: Selection of mean drift coefficients for pontoon type 4.

As discussed in section 3.5.3, the mean drift coefficient can be found both by direct pressure integration (DPI) and by conservation of fluid momentum (CFM). Both methods are available in HydroD. In this section, both methods are applied in order to compare the results. However, it should be noted that only horizontal coefficients are found with CFM(Faltinsen, 1990).

At first, the mean drift coefficients are found by both methods for pontoon 4 with a mesh size of 0.5 *m*. A selection of the results are given in figure 7.6.

The results obtained with direct pressure integration show some unexpected features. Firstly, it is seen that the drift coefficients in surge and sway are negative for high frequencies. This is not physical, since the drift force should be in the same direction as the incoming wave(Faltinsen (1990), p. 139). A convergence test with respect to mesh size is carried out with DPI, and it is found that the results do not converge. This is consistent with the findings of Pan, Vada and Hanssen, who have shown that it is numerically challenging to determine horizontal mean drift coefficients with direct pressure integration(Pan et al., 2013). Since the results obtained with direct pressure integration are less than satisfactory, it has been decided to reject this method, and instead apply the results obtained with conservation of fluid momentum.

A convergence test with respect to mesh size is carried out for pontoon 4 with the CFM method. The results in surge for a 30 degree heading angle are given in figure 7.7. It is seen that the results are somewhat unstable for high frequencies, and that there is no clear trend of convergence. However, the results obtained with the finest mesh size have the smallest spikes, i.e. the coefficient seems to be stabilizing about 30 $N/m^2$ for high frequencies. Therefore, it is decided to use this mesh size. In theory, the mesh size should be decreased further, such that proper convergence is obtained. However, the computational cost of this is very high, and it has therefore not been prioritized. This should be acceptable, since second order effects are not expected to be a governing environmental load.

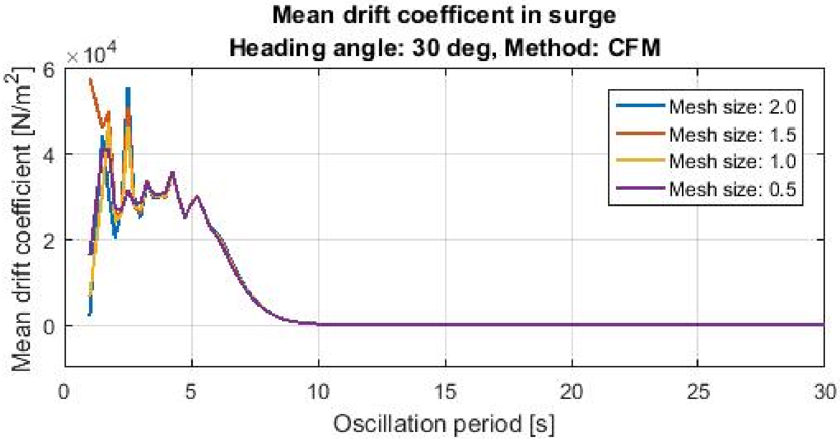

Figure 7.7: Mean drift coefficient in surge for four different mesh sizes. The heading angle is 30 degrees.

Figure 7.6 shows that the mean drift coefficients have the highest values for the smallest oscillation periods. This is as expected, since drift forces are important for large volume structures, where the incident waves are altered by the structure(Faltinsen, 1990). It is seen in figures 7.6a, 7.6c and 7.6d that there is a peak in the load level at about 6 seconds. As discussed in section 4.8.5, this is the eigenperiod in heave for the pontoon. Since the motions of the pontoon will be large at resonance, the amplitude of the reflected waves will be large as well, which implies large drift forces(Faltinsen, 1990). Thus, the peak in the drift force is expected at regions close to the natural period. These findings indicate that the mean drift coefficients behave inline with what is expected.

In an example, Faltinsen studies mean drift forces on a straight walled body with very similar geometry as the pontoons. The geometry of the body is given in figure 7.8, where it is seen that it has length $2L$ and the ends have curvature radii $R$. The mean drift coefficients when the frequency becomes very high are given by equations 7.1, 7.2 and 7.3, for surge, sway and yaw respectively(Faltinsen, 1990). Here, $\beta$ is the angle between the incoming wave and the longitudinal axis of the pontoon. The results obtained when implementing the dimensions of pontoon type 4, and a heading angle of 40 degrees, are given in table 7.6. This is the case considered in the first three plots in figure 7.6. The average level for high frequencies is compared to the theoretical solution in table 7.6. It is seen that the results coincide well, which implies that the WADAM analysis has functioned the way it was intended to.

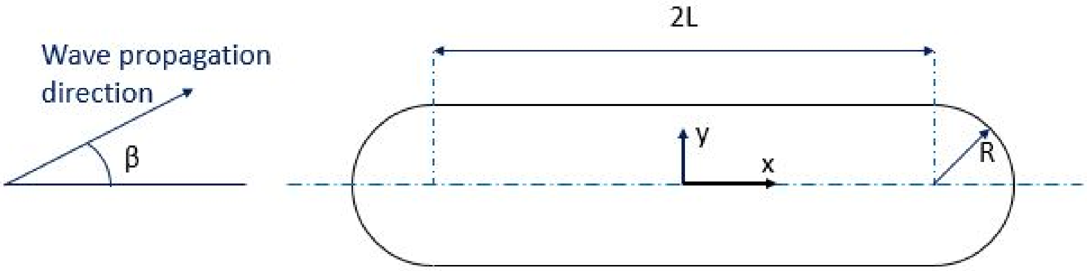

Figure 7.8: Geometry of body in Faltinsen's example.

$$\frac{\bar{F}_1}{\zeta_a^2} = \frac{2}{3}\rho g R cos\beta \tag{7.1}$$

$$\frac{\bar{F}_2}{\zeta_a^2} = \rho g(\frac{2}{3}Rsin\beta + Lsin\beta|sin\beta|) \tag{7.2}$$

$$\frac{\bar{F}_3}{\zeta_a^2} = -\frac{\rho g}{3}LRsin2\beta \tag{7.3}$$

Table 7.6: Mean drift coefficients for high frequencies in the case of $\beta = 40°$, $R = 5$ $m$ and $L = 24$ $m$.

| **Mean drift coefficient** | **Surge** | **Sway** | **Yaw** |
|---|---|---|---|
| **According to formulas by Faltinsen** | 25.7 $kN/m^2$ | 121.3 $kN/m^2$ | -396.1 $kNm/m^2$ |
| **According to WADAM analysis** | 30 $kN/m^2$ | 120 $kN/m^2$ | -350 $kNm/m^2$ |

In figure 7.6, it is seen that the mean drift coefficients obtained by WADAM analysis are fairly constant for low oscillation periods, before they display a sudden drop in magnitude at about 1 $s$. This is unexpected, as the drift coefficients are expected to approach the asymptotic limits in table 7.6. The behaviour is also observed by Aalberg(Aalberg, 2017), and it is suggested that it might be caused by irregular frequencies, such as studied by Pan, Vada and Hanssen(Pan et al., 2013). Here it is noted that high frequency response calculations require a very fine mesh. In other words, the mesh might not be fine enough for the highest frequencies in the considered domain. Since high frequency incident waves are associated with low energy levels, it is decided to not pursue the matter any further, and to employ the mean drift coefficients as they are.

The mean drift coefficients in surge and sway appear to coincide well with those obtained by Norconsult with the same software. See appendix D.3 for a selection of the drift coefficients. There is a slight difference in the load levels at the peaks, but this is believed to be caused by difference in mesh and in choice of frequency domain. In yaw, it appears as though Norconsult has plotted absolute value of the drift coefficient. Equation 7.3 indicates that the asymptotic limit for small frequencies should be negative, while it is positive in the report by Norconsult(Norconsult AS, 2017b). When comparing absolute values, the mean drift coefficients in yaw also coincide well.

### 7.2.5 Nonlinear wave loads

There are three types of nonlinear wave loads; sum-frequency, difference-frequency and mean drift forces. For the bridge, which has high eigenperiods, it is the difference-frequency effects that can potentially be important. Sum-frequency effects will not excite resonance motions, and are therefore neglected. Since nonlinear forces are proportional to the wave amplitude squared, it is decided to neglect the second order forces from swell. This should be an acceptable simplification, since $H_{s,Swell}/H_{s,WindSea}$ is in the order of $10^{-2}$.

As discussed in section 3.5.3, difference-frequency effects can be estimated with Newman's approximation. The idea of the approximation is to estimate the cosine coefficients in equation 3.27 as $T_{jk}^{ic} = 0.5(T_{jj}^{ic} + T_{kk}^{ic}) \cong \sqrt{T_{jj}^{ic} T_{kk}^{ic}}$(Greco, 2016). By further assuming that $\omega_j$ and $\omega_k$ are close, such that $T_{jj}^{ic}$ and $T_{kk}^{ic}$ are close, equation 3.27 can be reformulated as equation 7.4. Here, $T_{jj}^{ic}$ is the mean drift coefficient, which can be established without the nonlinear velocity potential(Faltinsen, 1990). Another advantage is that the computational costs will be reduced, since the number of summations is reduced from $N^2$ to $N$(Greco, 2016).

$$F_i^{SV} = 2[\Sigma_{j=1}^{N} A_j (T_{jj}^{ic})^{1/2} cos(\omega_j t + \epsilon_j)]^2 \tag{7.4}$$

In the previous section, it was found that only horizontal mean drift coefficients are found with the CFM method. Pan, Vada and Hanssen suggest to use DPI to establish vertical mean drift coefficients, and CFM to establish the horizontal coefficients(Pan et al., 2013). However, since slow-drift is not expected to be important for vertical motions, only the horizontal slowly varying drift forces are accounted for in this thesis. Thus, only the horizontal drift coefficients found by CFM will be necessary. This simplification should be acceptable. Firstly, the magnitude of second order forces are less than 1/100 of linear forces for the relevant wave amplitudes(Faltinsen, 1990). Secondly the bridge has no vertical modes that can be excited by slowly varying drift forces. As mentioned in section 3.5.3, Newman's approximation should provide satisfactory results for horizontal difference-frequency effects.

The underlying assumption in Newman's approximation is valid when $\omega_j$ and $\omega_k$ are close, i.e. when the difference frequency forces oscillate with low frequencies(Faltinsen, 1990). This implies that the slow drift forces will at least be satisfactory for the first two eigenperiods, which are in the range of 1-2 minutes. However, it also implies that the force-history will be corrupted by high-frequency components(Faltinsen, 1990). It is therefore decided to use a low-pass filter to remove the high-frequency components of the signal. As mentioned, Newman's approximation is valid for slow drift oscillations with periods in the range of 1-2 minutes, and it might therefore be reasonable to filter out force components with periods lower than 60 $s$. However, in order to ensure conservatism, only components with periods below 30 $s$ are filtered out. Figure 7.9 shows an example of how the filter influences the signal. It is seen that the filter reduces the peak load levels with about 75%.

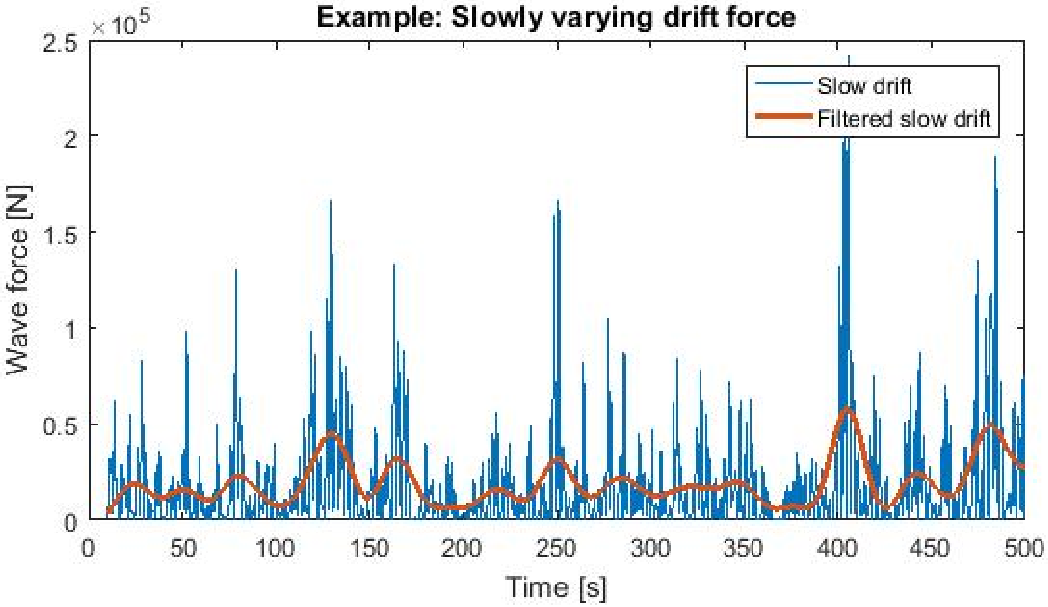

Figure 7.9: Example of slowly varying drift force before and after low-pass filtering.

A challenge with Newman's approximation is that the mean drift coefficients are required to be positive. While this requirement is fulfilled for the coefficients in surge and sway, it is seen that the drift coefficient in yaw is negative for some frequencies, see figure 7.6c. Aalberg employs a method that is similar to Newman's approximation, but where the sign of the drift coefficient is accounted for(Aalberg, 2017). The solution was presented by Standing, Brendling and Wilson in "Recent developments in the analysis of wave drift forces, low-frequency damping and response"(Standing et al., 1987). However, the accuracy of this method has proven to be highly dependent on the incident waves(Standing et al., 1987). For this reason, it is chosen to use Newman's approximation in all three degrees of freedom. In yaw, the mean drift coefficients are treated as if they are all positive.

Figure 7.10 provides a visualization of the relative importance between linear forces and nonlinear forces in surge. It is seen that the nonlinear forces are very small compared to the linear forces. The estimated slow drift forces in yaw are even smaller compared to the linear forces, see figure E.6 in appendix E.

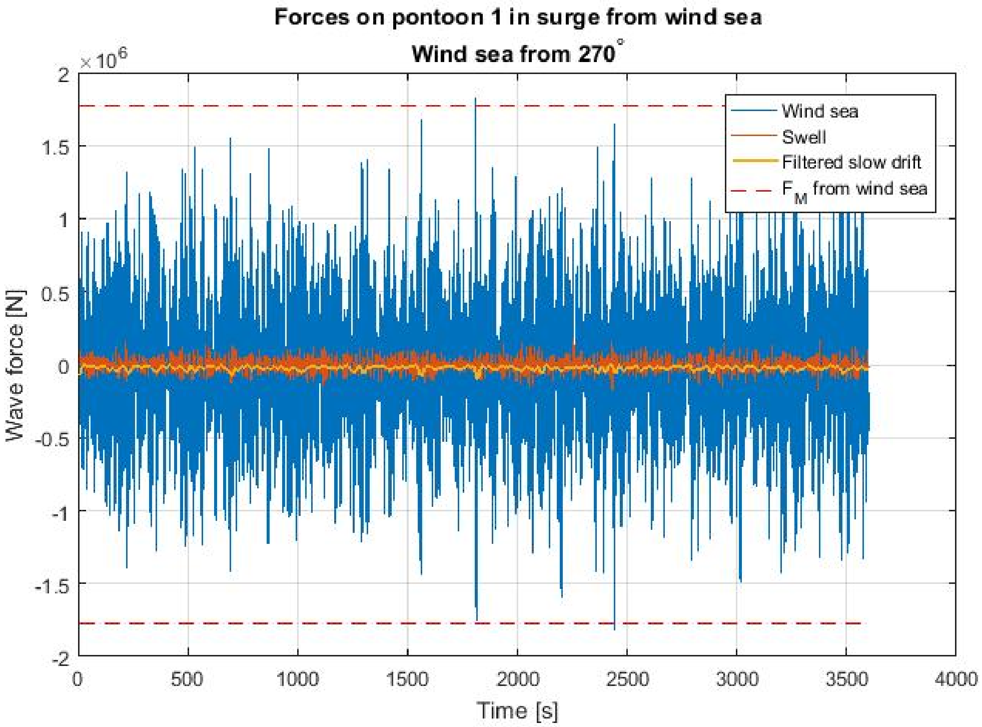

Figure 7.10: Example of wave force in 100-year sea state with wind sea from 270° and swell from 330°. Direction of incoming waves defined in figure 7.1. Force history in surge for pontoon 1. Characteristic 1-hour wave load from wind sea indicated by the dashed line.

## 7.3 Modelling of wind loads

Wind loads are believed to be the governing physical process in the 100-year storm condition. Because of the slender nature of the bridge, there is a risk of snap-through buckling of the bridge girder due to large wind loads. As discussed in section 3.3, the dynamic buckling load might be lower than the static buckling load, and it is therefore necessary to include the dynamic aspect of the wind, i.e. the wind gusts. Therefore, wind will be applied as a time varying load.

Wind loads on an element are calculated in USFOS based on the local wind speed and the drag properties of the element. The drag force per unit length is given by the drag term in the Morison equation, see equation 7.5. The drag properties of the elements are described in section 4.7. In addition to drag forces, the wind may also induce lift and torsion. Therefore, lift and moment coefficients are also assigned to the bridge girder.

$$dF_D = \frac{1}{2}\rho C_D D|u|u \tag{7.5}$$

The wind speed should be defined as a function of both time and space. USFOS is compatible with the nonlinear time domain tool WindSim, which simulates the wind based on mean wind speed, turbulence intensity and the coherence of the turbulence intensity. The applied properties are summed up in table 7.7. Here $n^2$ is the reduction factor for mean wind speed, see section 7.1. The mean wind speed as a function of the elevation is modelled by the power-law profile, which is given by equation 3.45 in section 3.5.8. The power exponent is taken as $\alpha = 0.127$, as discussed in section 7.1. This is inline with the suggestion of $\alpha = 0.12$ for open sea in the recommended practice by DNV(Det Norske Veritas, 2010b). Turbulence intensity is modelled with the Kaimal spectrum, with the parameters recommended in DnV-OS-J10(Aas-Jakobsen, 2015), see equation 3.47. The spectrum for wind gusts at the elevation of the bridge girder in the floating low-bridge is shown in figure 7.11. The decay factors $c_i$ in the transverse directions of the wind are taken as 6.5, as described in section 7.1. By implementing this in equation 3.49, the coherence for oscillations with period 120 $s$ is as shown in figure 7.12.

Table 7.7: Wind properties applied when modelling wind in WindSim.

| **Mean wind speed** $\bar{U}_{10m,1h}$ $[m/s]$ | **Reference height** $Z_{ref}$ $[m]$ | **Zero level** $Z_{ref}$ $[m]$ | **Power exponent** $\alpha$ $[-]$ | **Turbulence intensity** $I_u$ $[-]$ | **Decay factor** $c_i$ $[-]$ | **Air density** $\rho$ $[kg/m^3]$ |
|---|---|---|---|---|---|---|
| $29.5 \cdot n^2$ | 10 | 0 | 0.127 | 0.14 | (10, 6.5, 6.5) | 1.293 |

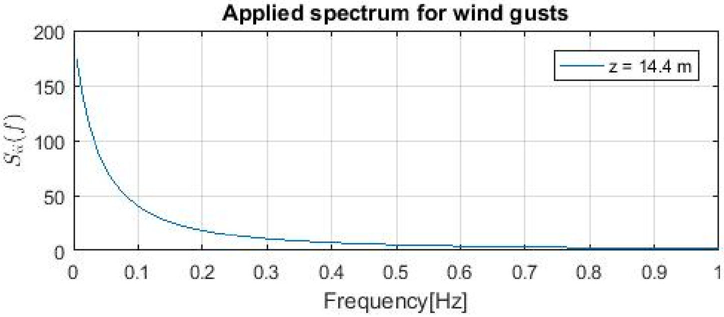

Figure 7.11: Kaimal wind spectrum with parameters according to DnV-OS-J10 recommended practice.

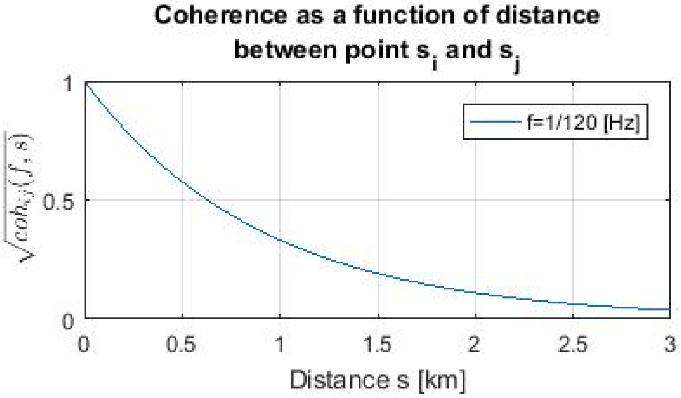

Figure 7.12: Coherence as a function of distance when f = 1/120 $Hz$.

WindSim calculates the wind speed at grid points that are defined by the user. The number of points allowed by the working memory is limited, and the grid must therefore be chosen with care. Since the bridge girder is believed to take the majority of the wind loads, it is prioritized to have a large number of grid points along the longitudinal axis of the bridge. The grid is chosen such that there are 52 points in the x-direction, i.e. 100 $m$ between each point. The velocity is calculated at 14.4 $m$, i.e. at the elevation of the floating low bridge, and at 55 $m$, which is the elevation of the bridge girder in the cable-stayed bridge. Outside the grid, USFOS will apply the wind velocity at the closest point. The simplified 2-point wind profile is plotted along with the true power-law profile in figure 7.13.

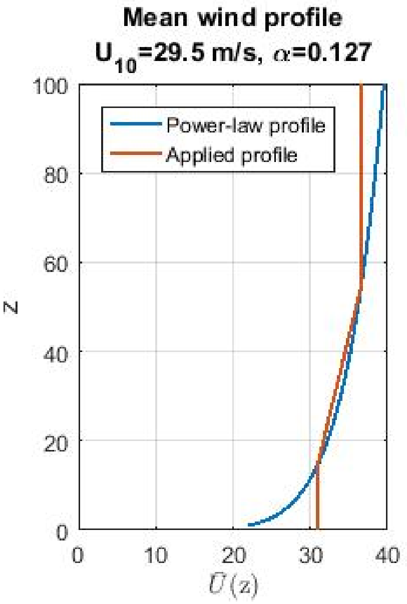

Figure 7.13: Mean wind profile for the 100-year storm.

Figure 7.13 shows that the mean wind speed will be overestimated at the pontoons and columns. The wind speed is about 10% too high at the midpoint of the columns, while it is about 30% too high at the pontoons. Since the drag force is proportional to the wind speed squared, the drag is overestimated by 20% and 65%, respectively. The elevation of the bridge girder ranges between 14.5 $m$ and 55 $m$. Thus, the wind speed should be fairly accurate along the girder. The drag on the tower, which extends 230 $m$ up into the air, will be underestimated. Since the tower is situated on land, the drag forces will be transferred to the ground. Consequently, the wind load on the tower should not be that important. The drag forces on the stay-cables, on the other hand, will reach the bridge girder. The drag forces at 130 $m$ elevation will be underestimated by approximately 40%. However, in agreement with Professor Jørgen Amdahl, it has been decided to apply the simplified wind profile anyway. Since the total area of the stay cables is in the range of 10% of the area of the bridge girder, the girder will take the majority of the wind forces. Also, it is the floating low-bridge that is of interest when considering snap-through buckling.

USFOS has difficulties reading the wind file if it is too large, and the time step must therefore be 1.0 $s$ or more with the chosen grid. This is believed to be okay, since the wind gust spectrum has low energy for small oscillation periods, see figure 7.11. In figure 7.14, the wind gust speed is calculated with a time step of 0.1 $s$. It is seen that the sign of the wind gust velocity changes every third second or so. Consequently, if the time step is 1.0 $s$, there will be about three sample points between every time the wind gust changes sign. This should be sufficiently accurate, since wind gusts with low periods will not excite any important eigenperiods in the bridge.

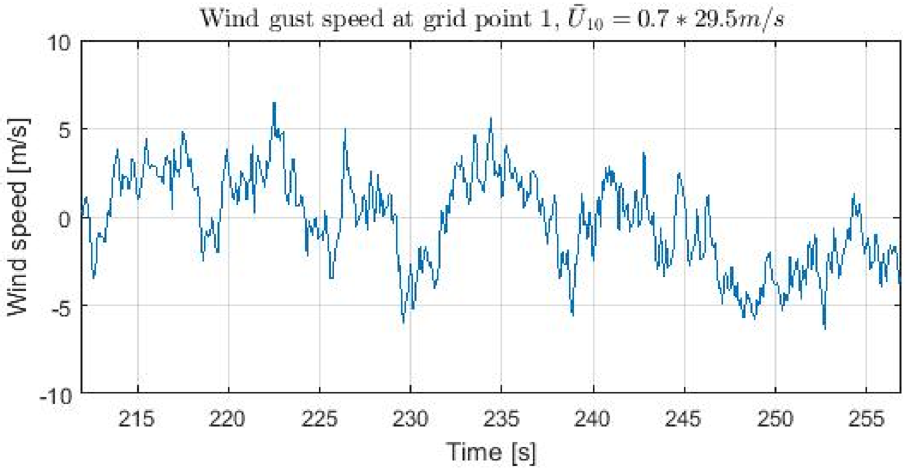

Figure 7.14: Wind gust speed at a random grid point calculated with a time step of 0.1 $s$.

## 7.4 Studied combinations of environmental loads

The incoming waves and wind can be combined in several ways. The aim is to find the worst case scenario along the 100-year contour line. The wind and wave loads will be considered individually when determining the most severe wind direction and sea state. Then, the aim is to employ the loads simultaneously in order to estimate the 100-year response of the bridge.

The reference period for the mean wind speed is 1 hour, while the reference period for the significant wave height is 3 hours. When performing an analysis, the reference period must be equal to the simulation period. In “DNV-OS-J101 Design of Offshore Wind Turbine Structures”, the recommended practice for solving this issue is to apply inflation and deflation factors(Det Norske Veritas (2014), p. 76). For a simulation period of 1 hour, the 3-hour significant wave height can be multiplied by a factor of 1.09(Det Norske Veritas (2014), p. 76), see equation 7.6. By applying this inflation factor to both wind sea and swell, 1-hour simulations where wind and waves are combined can be carried out. It should be mentioned that this factor is based on a sea state with 1000 waves per 3 hours, while the 100-year wind sea in the Bjørnafjord will have 1800 waves per 3 hours. Thus, the factor might be on the non-conservative side for wind sea.

$$H_{s,1h} \approx 1.09 \cdot H_{s,3h} \tag{7.6}$$

The 100-year current should be included when considering extreme storm conditions, but since a good description of current in the Bjørnafjord has not been accessed, only wind and waves will be applied.

In section 7.1, it was stated that the 100-year sea level should be applied in the ultimate limit state. However, since the bridge is mainly supported by floating pontoons, the sea level will only matter close to the end-supports. It is therefore decided to enforce the default water level.

## 7.5 Wave analyses considering 100-year sea states

The significant wave heights in the 100-year sea states are not very high, and it is therefore expected that wave loads will be less important than wind. At the same time, the peak spectral periods in the design sea states are about 6 $s$, which means that linear wave loads may excite resonance motions. From the eigenvalue analysis, it is known that the bridge has several vertical eigenmodes with periods in this range. Also, since the two highest eigenperiods of the bridge are in the range of 1-2 minutes, it is believed that difference-frequency effects may become of importance.

### 7.5.1 Determining worst sea state based on static analysis

When time domain analyses of wave loads are carried out, a very small incremental time step is required in USFOS, i.e. in the order of 0.005 $s$. Due to the small time step, the computational costs are very high, and the number of time domain simulations must therefore be limited. Thus, it is necessary to identify the most important sea states by other means. It has therefore been decided to carry out static analyses in order to determine the worst sea states. After the static analyses, time domain analyses are carried out for the wave direction that is believed to be the worst case scenario.

Since the wave force is proportional to the wave amplitude, it is assumed that the worst wind generated sea state must be one of the sea states presented in table 7.8.

Table 7.8: Most severe wind generated sea states corresponding to a 100-year return period.

| | **2** | **5** | **6** |
|---|---|---|---|
| **Direction**[1] | $75° - 105°$ | $225° - 315°$ | $315° - 335°$ |
| **Significant wave height** $\mathbf{H}_{s,3h}$ | 2.8 $m$ | 2.4 $m$ | 2.5 $m$ |
| **Spectral peak period** $\mathbf{T}_p$ | 6.6 $s$ | 5.9 $s$ | 6.2 $s$ |

[1] Relative to the north, measured clockwise. See figure 7.1.

The force spectrum is given by equation 7.7. Here $H_{\zeta F}(\omega)$ is the transfer function found in section 7.2.2, and $S_{\zeta\zeta}(\omega)$ is the JONSWAP spectrum for wind sea. The resulting force spectra in surge, sway and yaw are given in figure D.7 in appendix D.4 for a selection of heading angles.

$$S_{FF} = |H_{\zeta F}(\omega)|^2 S_{\zeta\zeta}(\omega) \tag{7.7}$$

The characteristic wave load is the wave load that is exceeded by only one of $N$ occurrences. From section 3.5.7, it is known that the characteristic wave load on a pontoon in direction $i$ can be estimated by $F_{M,i} = \sqrt{2m_{0,FF} lnN}$(Myrhaug, 2005). Here, $m_{0,FF}$ is the variance given by integrating the spectrum $S_{FF}$ over $0 \rightarrow \omega \rightarrow \infty$. In the static analyses, the characteristic wave loads in all degrees of freedom are applied simultaneously. The characteristic wave loads of pontoon 15 to 24 are applied, as if these were hit by a very large, long crested wave, see figure 7.15. The $y$-component of the wave load is applied in the positive $y$-direction, since the bridge girder is vulnerable to snap-through buckling in this direction. Wave loads on remaining pontoons are set to zero. Heading angles of 90°, 270° and 330° are tested, see table 7.8. The characteristic wave loads from wind sea are given in table 7.9 for pontoon number 22.

Table 7.9: Characteristic wave loads for pontoon 22 when subjected the sea states in table 7.8. Loads are given according to the global coordinate system.

| | | **Force component** | | | | | |
|---|---|---|---|---|---|---|---|
| | | $F_1$ | $F_2$ | $F_3$ | $F_4$ | $F_5$ | $F_6$ |
| **Sea state** | **Direction** | | $[MN]$ | | | $[MNm]$ | |
| **2** | 90° | 0.63 | 1.34 | 2.03 | 55.64 | 1.48 | 22.73 |
| **5** | 270° | 0.50 | 1.04 | 1.01 | 35.22 | 0.90 | 17.84 |
| **6** | 330° | 4.26 | 1.30 | 2.79 | 46.09 | 4.05 | 98.12 |

The most critical response caused by the static wave loads appears to be the bending moment about the strong axis of the bridge girder. Since the vertical wave force is applied with the same sign at each pontoon, the increase in bending moment about the weak axis is very small. Bending moments about the strong axis and axial forces in the girder are given in table 7.10. The directions of the applied loads and the deformation of the bridge when subjected to wave condition number 6 are given in figure 7.15.

Table 7.10: Main findings in static wave load analysis.

| | **Wave direction** | | | | |
|---|---|---|---|---|---|
| | **90°** | **270°** | **330°** | **Capacity** | **Unit** |
| **Bending moment about strong axis** | | | | | |
| South anchoring | 1900 | 1400 | 1400 | 3069 | $[MNm]$ |
| Maximum along girder | 2500 | 1800 | 4800 | 3069 | $[MNm]$ |
| North anchoring | 2100 | 1700 | 9500 | 3069 | $[MNm]$ |
| **Maximum axial force**[1] | 27 | 18 | 48 | 418 | $[MN]$ |
| **Maximum lateral displacement** | 30 | 25 | 100 | | $[m]$ |
| **Maximum vertical displacement** | 0.3 | 0.2 | 0.4 | | $[m]$ |

[1] Disregard cable-stayed section

Figure 7.15 shows that the deformations are very large. The lateral displacement of the girder is in the order of 100 $m$ at central regions. Of course, since the loads are applied statically, the deformations will have more time to accumulate than what is realistic for a wave load. Therefore, the displacements are not expected to be this large in dynamic analyses.

Table 7.10 shows that the bending moments in the bridge are substantially higher for sea

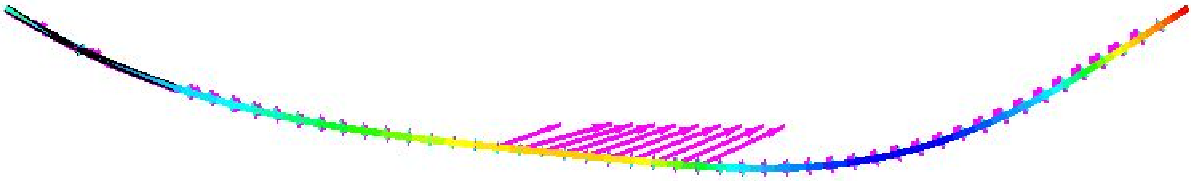

Figure 7.15: Deformation of bridge when the characteristic load from wave condition 6 is applied to pontoons 15 to 24. Direction of applied load indicated by the arrows.

state 6 than for the other two. Therefore, this appears to be the worst sea state. On the other hand, only the maximum load level is considered in the static analyses. Interaction between pontoons and possible excitation of eigenmodes are not accounted for. For this reason, full simulations are preferable in order to assess the worst sea state along the the 100-year contour line. However, since the computational costs are so high, this is not practicably possible due to time limitations. Since sea state 6 yields the worst response, it is prioritized to study this sea state in a full time domain analysis. See figure 7.16 for an overview of the considered sea states.

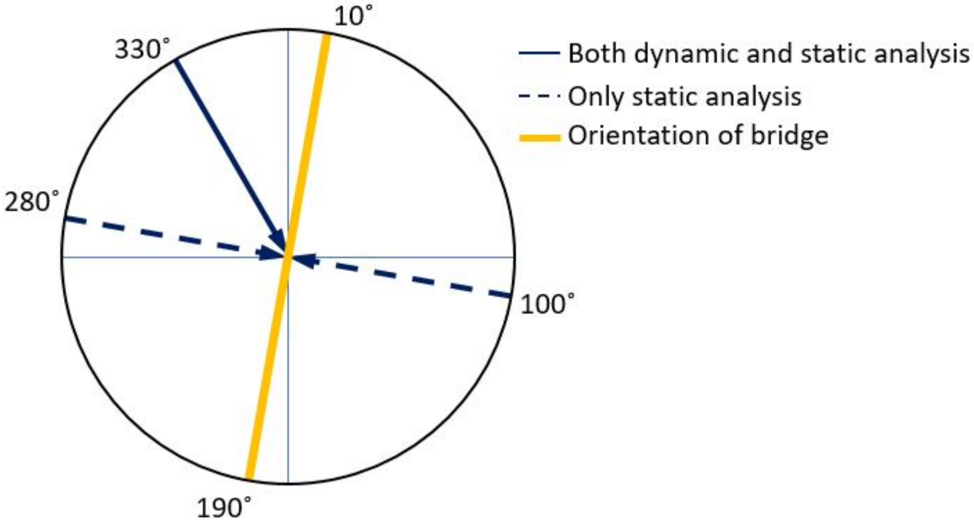

Figure 7.16: Considered directions of wind sea in static and dynamic analyses.

It has been shown earlier that swell forces are small compared to forces from wind sea. The exception is heave forces, which are in the same order of magnitude for wind sea and swell. Since the characteristic wave loads in heave are not much affected by the choice of peak period, nor by the choice of wave direction, it is chosen to only study swell sea with peak period 12 $s$ and direction 330°. This combination have the largest horizontal characteristic loads.

### 7.5.2 Mean drift in time domain analyses caused by numerical issues

When studying the results from wave load analyses, a drift motion of the bridge is observed, also when slow-drift forces are not applied. This is not physical, since the applied forces have zero mean value. In figure 7.17, the displacement of a point on the bridge girder is shown for the case of only swell sea. It is seen that the drift motion is about 1 $m$ over a period of 3600 $s$, which is much larger than the oscillation induced by the waves. The drift motion is also observed by Aalberg, who notes that the problem may be reduced be decreasing the time step(Aalberg, 2017). However, since the time step is already as low as 5 $ms$, this is not an option.

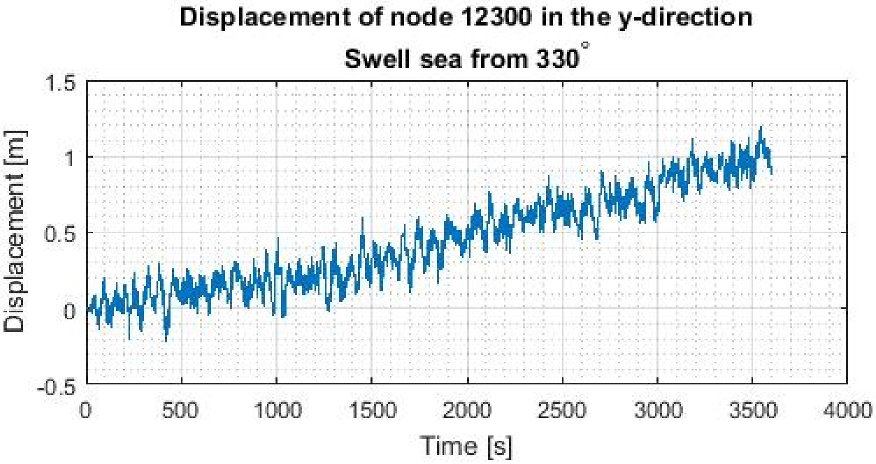

Figure 7.17: Displacement of the midpoint on the bridge girder in the global y-direction when the bridge is subjected to swell sea.

The drift motion is illustrated in figure 7.18. Since the drift motion is very small compared to the dimensions of the bridge, the displacement is scaled by a factor of 40. The drift pattern is different from analysis to analysis.

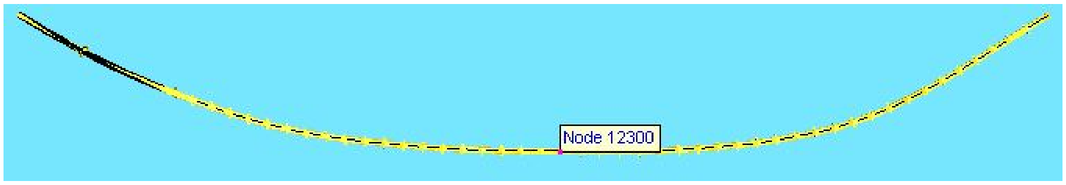

Figure 7.18: Drift motion of bridge girder when only subjected to swell. Displacement scaled by a factor of 40.

As a consequence of the drift motion, there will also be a constant increase in the mean value of the reaction forces. This will for example be evident in the bending moment about the strong axis of the girder at the end-supports, see figure 7.19. It is seen that the mean value is changed by about 300 $MNm$ over a period of 3600 $s$. In comparison, the oscillation amplitude appears to be in the range of 200 $MNm$.

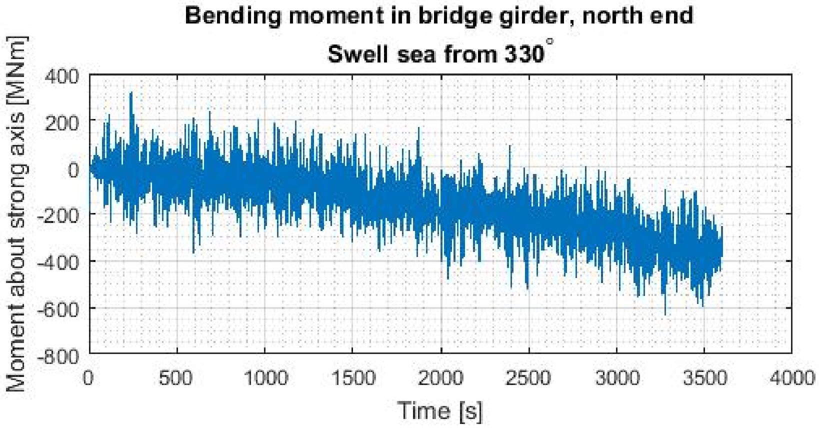

Figure 7.19: Moment about strong axis of bridge girder at the north anchoring. The bridge is subjected to long-crested swell.

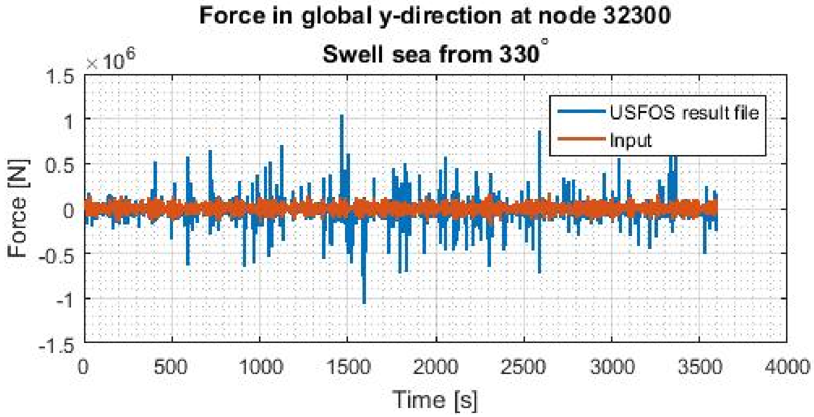

(a)

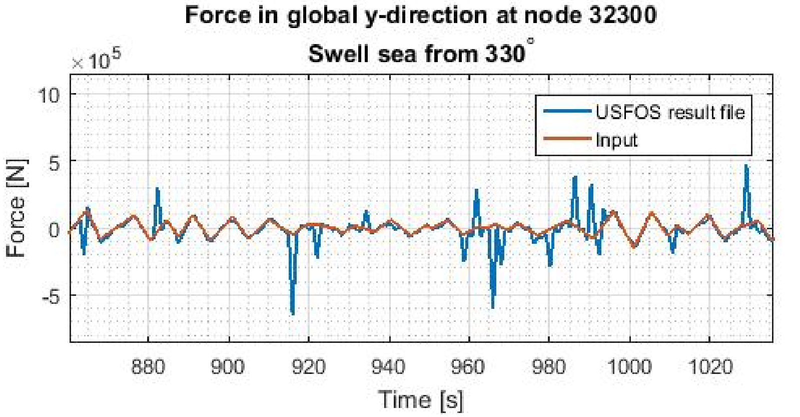

(b)

Figure 7.20: Force at pontoon 21 as a function of time in the case of swell sea from 330°.

In order to ensure that the drift is not caused by errors in the input, the nodal loads in the result file are plotted along with the values from the load file. The results are shown for the surge force on pontoon 23 in figure 7.20. It is seen that the force has zero mean value, which means that the applied force cannot explain the drift. What is also seen, is that the nodal loads in the result file do not coincide with the loads in the input file. Figure 7.20b shows that the forces coincide at some time instants, but that there are also some unexpected large spikes. The largest load levels in the result file are up to 6 times higher than the largest load levels in the input file. According to Professor Jørgen Amdahl, it is not entirely clear what is actually plotted, which means that the deviation might not be a problem. However, as it will be seen in the next section, the reaction forces in the bridge indicate that the wave loads are unphysically high.

### 7.5.3 Dynamic analysis of long crested wind sea and swell from northwest

In this section, the case of long-crested swell and long-crested wind sea from 330° is considered. Both linear forces and difference frequency forces are included. The drift motion is even more pronounced in the analysis of combined sea, making it difficult to assess the results. The drift after a 2500 $s$ period is given in figure 7.21, where the displacement of the girder is about 80 $m$ at node 10900. The bending moment at the north end-anchoring is given as a function of time in figure 7.22. In table 7.11, the main findings in the analysis are summed up. It should be noted that values are only rough estimates, since there is no exact way of filtering out the drift motion from the results.

Table 7.11: Main findings in dynamic analysis of long-crested swell and wind sea from 330°. Drift motions have been roughly filtered out of the results.

| | **Wave direction** | | |
|---|---|---|---|
| | **330°** | **Capacity** | **Unit** |
| **Maximum bending moment**[1] | | | |
| South anchoring | 2000 | 3069 | $[MNm]$ |
| North anchoring | 1800 | 3069 | $[MNm]$ |
| **Maximum axial force**[2] | 30 | 418 | $[MN]$ |
| **Max. displ. of node 10900**[3] | | | |
| In global y-direction | 10 | | $[m]$ |
| In global z-direction | 0.4 | | $[m]$ |

[1] About strong axis

[2] Disregard cable-stayed section

[3] See position of node in figure 7.21

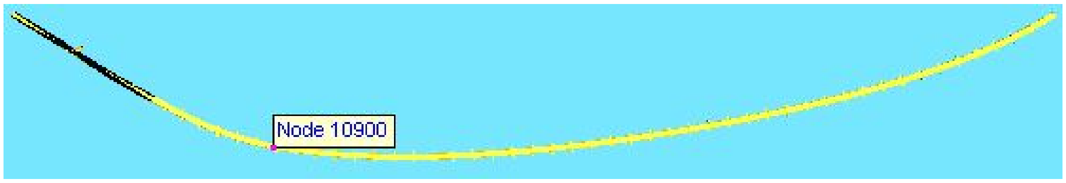

Figure 7.21: Drift motion over a period of 2500 $s$ when the bridge is subjected to linear and nonlinear wave forces from wind sea and swell. The results are scaled by a factor of 1.0.

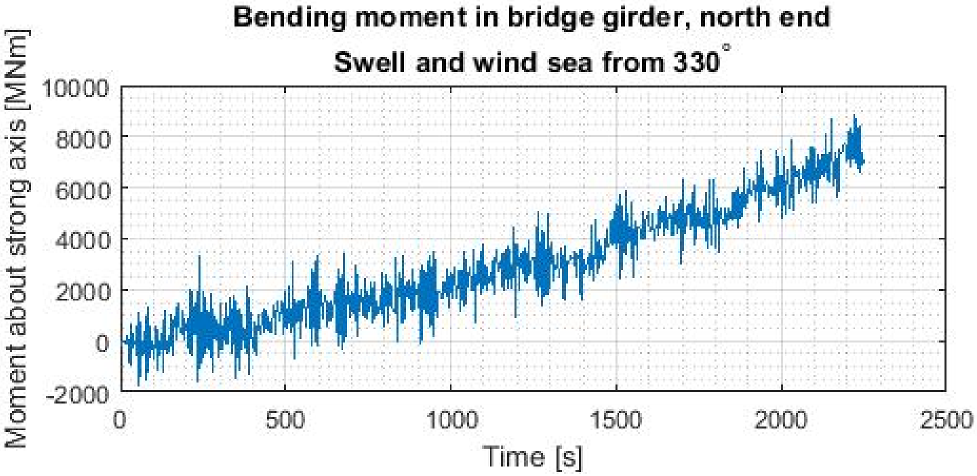

Figure 7.22: Bending moment at the north end-anchoring when subjected to long-crested wind sea and swell from 330°.

The results in table 7.11 show that the bending moments in the bridge girder are very high; about 65% of the capacity. Taking into account that wind is expected to be the governing process in the 100-year storm, this does not seem likely. The issues with spurious spikes in the force history that were discussed in section 7.5.2, are also evident in this analysis. Figure 7.23a shows that the forces in the global $y$-direction are overestimated up to 10 times. The issue is only a problem in the horizontal plane; figure 7.23b shows that the vertical forces fit well.

The peak period of the wind sea spectrum is in the same range as the bridge's eigenperiods in heave, which means that there is a risk of resonance motions. Figure 7.24 shows the vertical displacement plotted in the frequency domain. It is seen that the energy is concentrated at frequencies close to the eigenfrequencies in heave. Even though the heave modes appear to be excited, the motions are small. Also, the acceleration amplitude is less than 1 $m/s^2$, which means that there should be no risk of structural damage. Since the bridge will be closed in the 100-year storm, the serviceability limit state is not an issue. Thus, vertical motions induced by wave loads should not be critical.

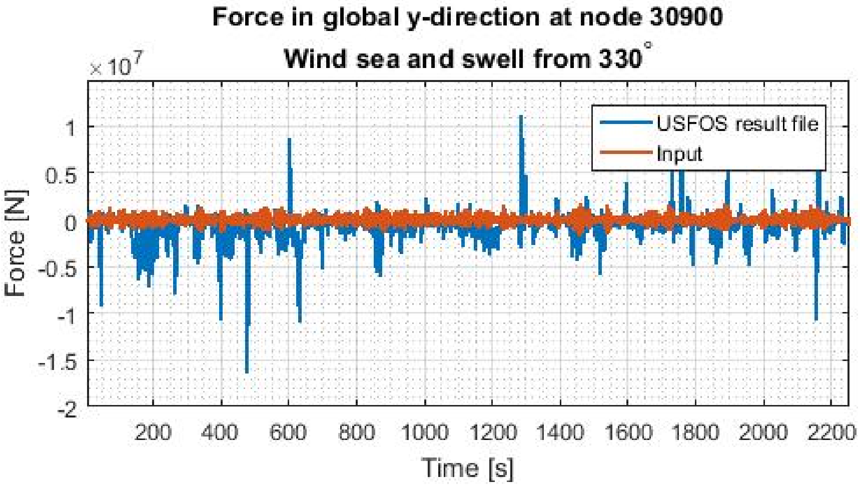

(a) Wave force in global y-direction

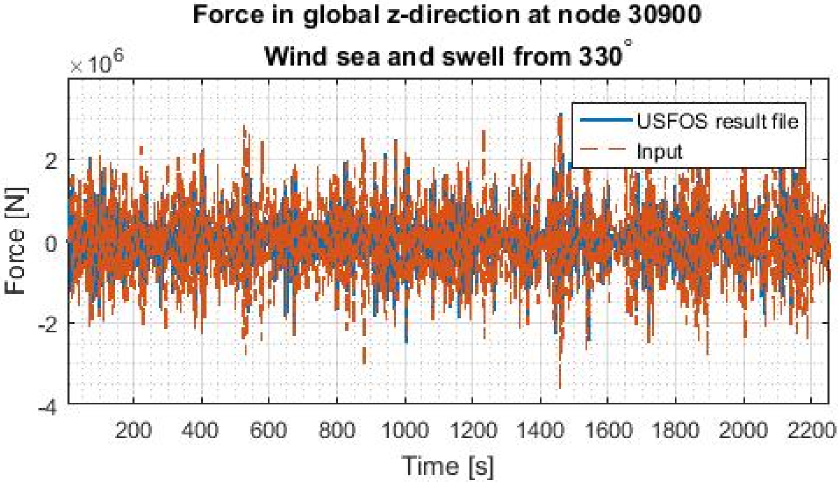

(b) Wave force in global z-direction

Figure 7.23: Force at pontoon 7 as a function of time in the case of long-crested wind sea and swell from 330°.

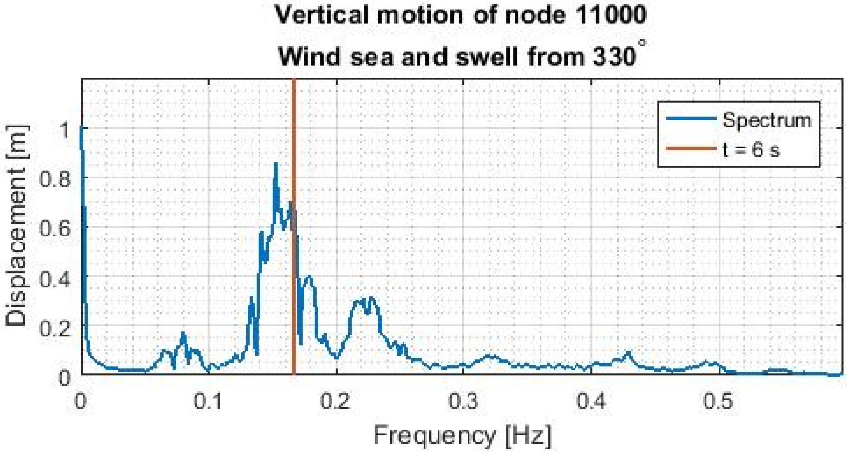

Figure 7.24: Vertical displacement of bridge girder plotted as a function of frequency.

### 7.5.4 Relative importance of swell

In this section, the wave forces from swell are studied separately in a 1-hour simulation. The case of long-crested swell from 330° is considered. This is the same sea state that is considered in section 7.5.2, which means that there is a nonphysical drift motion. The main findings are summed up in table 7.12, where it has been attempted to filter out the drift motion. It is seen that the response from swell is approximately 10% of the response in combined sea.

Table 7.12: Main findings in dynamic analysis of long-crested swell from 330°. Drift motions have been roughly filtered out of the results.

| | **Wave direction 330°** | **Relative to full sea[1]** | **Capacity** | **Unit** |
|---|---|---|---|---|
| **Maximum bending moment[2]** | | | | |
| South anchoring | 250 | 13% | 3069 | $[MNm]$ |
| North anchoring | 300 | 17% | 3069 | $[MNm]$ |
| **Maximum axial force[3]** | 8 | 27% | 418 | $[MN]$ |
| **Max. displ. of node 10900[4]** | | | | |
| In global y-direction | 0.5 | 5% | | $[m]$ |
| In global z-direction | 0.1 | 25% | | $[m]$ |

[1] Relative to maximum value found in analysis of combined wind and swell sea
[2] About strong axis
[3] Disregard cable-stayed section
[4] See position of node in figure 7.21

### 7.5.5 Relative importance of difference-frequency forces

In this section, difference frequency forces are studied in a 1-hour simulation. The case of long-crested waves from 330° is considered. It is believed that numerical drift is present in this analysis as well; the largest vertical displacement caused by slowly varying drift forces is 3.6 $m$, which is larger than the vertical motions caused by linear wave forces. Since only horizontal slow-drift forces are modelled, it is evident that this cannot be correct. However, since the horizontal slow-drift force has a non-zero mean value, it is difficult to filter out the drift from the results. Therefore, the values in table 7.13 are taken directly from the result files.

Table 7.13 shows that the bending moments at the supports are in the same order of magnitude as when the bridge is subjected to linear swell forces, while the horizontal displacements are much larger. One reason for this might be that the difference-frequency forces have a non-zero mean value, which will give a mean drift. Further, the slowly varying drift force oscillates with periods that are much closer to the horizontal eigenperiods of the bridge. Thus, it appears logical that the displacements caused by slow-drift forces are larger, even though the linear forces from swell have larger amplitudes. It should be noted the displacements are still very small compared to the dimensions of the bridge, and that the utilization of the bending capacity of the girder is only in the order of 10%. In addition, it must be kept in mind that the numerical drift of the bridge has not been filtered out from the results from the slow-drift analysis. At the same time, based on the displacement as a function of time, see figure 7.25, there is no clear indication of numerical drift horizontally.

Table 7.13: Main findings in dynamic analysis of difference-frequency forces when long-crested wind sea from 330° is considered.

| | **Wave direction 330°** | **Relative to full sea**[1] | **Capacity** | **Unit** |
|---|---|---|---|---|
| **Maximum bending moment**[2] | | | | |
| South anchoring | 240 | 12% | 3069 | $[MNm]$ |
| North anchoring | 330 | 18% | 3069 | $[MNm]$ |
| **Maximum axial force**[3] | | | | |
| Compression | 5 | 17% | 418 | $[MN]$ |
| **Max. displ. of node 10900**[4] | | | | |
| In global y-direction | 3.4 | 34% | | $[m]$ |
| In global z-direction | 3.6 | 900% | | $[m]$ |

[1] Relative to maximum value found in analysis of combined wind and swell sea

[2] About strong axis

[3] Disregard cable-stayed section

[4] See position of node in figure 7.21

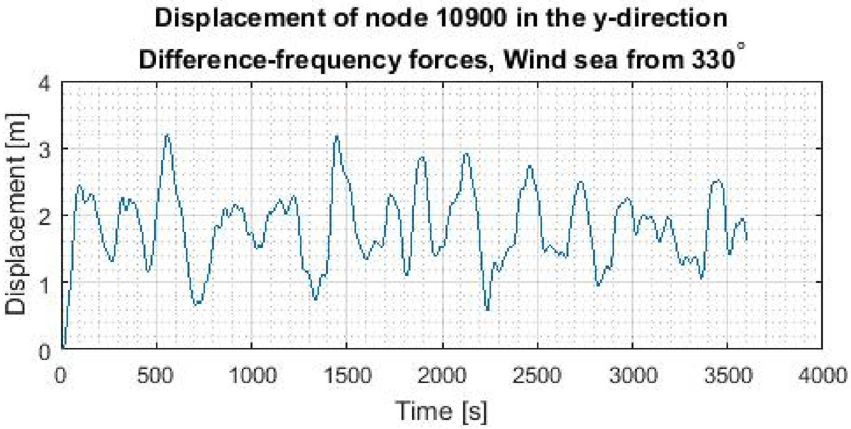

Figure 7.25: Displacement in the global y-direction when the bridge is subjected to slowly varying drift forces from 330°. See figure 7.21 for position of node.

# 7.6 Wind analyses considering 100-year storms

In this section, the response of the bridge when subjected to the 100-year wind will be studied. The modelling principles described in section 7.3 will be applied. Further, the mean wind speed and turbulence intensity are taken to be constant along the span of the bridge.

## 7.6.1 Static analysis of wind loads

The strongest wind in the ultimate limit state travels from west to east, see table 7.4. West winds are therefore believed to be important. In addition, one of the main concerns for the bridge is that strong east winds might trigger snap-through buckling of the bridge girder. Therefore, the wind conditions given in table 7.14 are tested statically. To be exact, the the mean wind speed of the wind condition is applied dynamically over a long period. See figure 7.26 for an illustration of the wind directions.

Table 7.14: Wind conditions applied statically to the bridge. The direction is relative to the north, measured clockwise.

| **Load case number** | **1** | **2** | **3** | **4** |
|---|---|---|---|---|
| **Direction** | 100° | 130° | 280° | 330° |
| **$U_{10}$** $[m/s]$ | 20.65 | 20.65 | 29.5 | 23.6 |

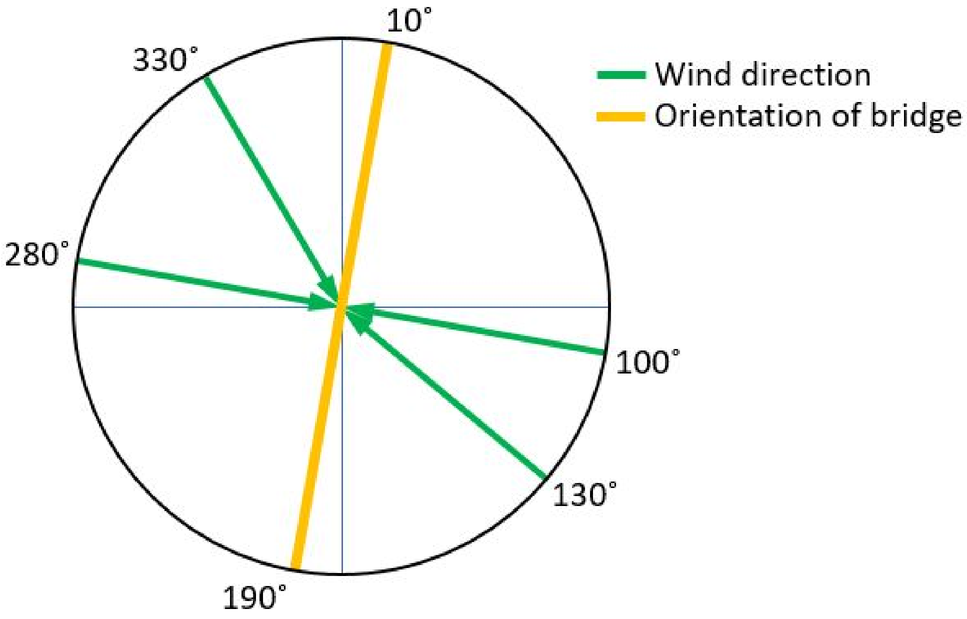

Figure 7.26: Considered wind directions in static and dynamic analyses.

The most important findings in the static analyses are presented in table 7.15.

Table 7.15: Main findings in static wind load analysis.

| | **Wind direction** | | | | | |
|---|---|---|---|---|---|---|
| | **100°** | **130°** | **280°** | **330°** | **Capacity** | **Unit** |
| **Bending moment about strong axis** | | | | | | |
| South anchoring | 320 | 580 | 430 | 600 | 3069 | $[MNm]$ |
| Maximum along girder | 100 | 350 | 500 | 350 | 3069 | $[MNm]$ |
| North anchoring | 50 | 300 | 550 | 900 | 3069 | $[MNm]$ |
| **Maximum axial force**[1] | 1 | 1 | 15 | 10 | 418 | $[MN]$ |
| **Maximum displacement in y-direction** | 3.5 | 6.5 | 5 | 7 | | $[m]$ |

[1] Disregard cable-stayed section

### 7.6.2 Time domain analysis of wind loads

A single 1-hour analysis has been carried out for the each of the four wind directions given in figure 7.26, except for the wind from west, i.e. 280°. Due to trouble with running this analysis, four separate simulations with a total duration of 1300 $s$ are run instead. Since the analysis of wind from 280° only has a duration of 1300 $s$, the characteristic response will be smaller than the 1-hour maximum. However, since the aim is only to get an understanding of how large the wind loads are, and how dynamic effects will affect the results, the simplification should be acceptable. In all of the analyses, wind is applied three seconds after gravity and pretension.

The main findings are given in table 7.16. The results indicate that reaction forces caused by the four 100-year wind scenarios are fairly similar in magnitude. The maximum bending moments about the strong axis of the girder are reached at the end-supports, where about 30% of the capacity is utilized. Further, it is seen that the maximum vertical displacements induced by wind are small, only about 30 $cm$. The maximum deformation in the global $y$-direction is 9 $m$, which is about one third of the width of the girder. Considering how long the bridge is, and that the material is steel, this displacement is not terribly large. At the other hand, the analysis does not consider wave loads or any safety factors. This will be discussed in section 7.8.

Table 7.16: Main findings in dynamic wind load analyses.

| | Wind direction | | | | | |
|---|---|---|---|---|---|---|
| | **100°** | **130°** | **280°** | **330°** | **Capacity** | **Unit** |
| **Maximum bending moment[1]** | | | | | | |
| South anchoring | 600 | 900 | 900[2] | 900 | 3069 | $[MNm]$ |
| Along girder | 400 | 600 | 300[2] | 600 | 3069 | $[MNm]$ |
| North anchoring | 500 | 800 | 800[2] | 900 | 3069 | $[MNm]$ |
| **Maximum torsional moment** | 14 | 21 | 14[2] | 15 | 966[3] | $[MNm]$ |
| **Maximum axial force[4]** | | | | | | |
| Compression | 5 | 4 | N/A | N/A | 418 | $[MN]$ |
| Tension | N/A | N/A | 13[2] | 8 | 705 | $[MN]$ |
| **Max. displ. of node 10900[5]** | | | | | | |
| In global y-direction | 6 | 9 | 8[2] | 9 | | $[m]$ |
| In global z-direction | 0.2 | 0.3 | 0.1[2] | 0.2 | | $[m]$ |

[1] About strong axis

[2] Taken from four different simulations with a combined duration of 1300 $s$

[3] Determined based on elastic section modulus

[4] Disregard cable-stayed section

[5] See position of node in figure 7.18

A snapshot of the deformation is given for two of the wind scenarios in figure 7.27.

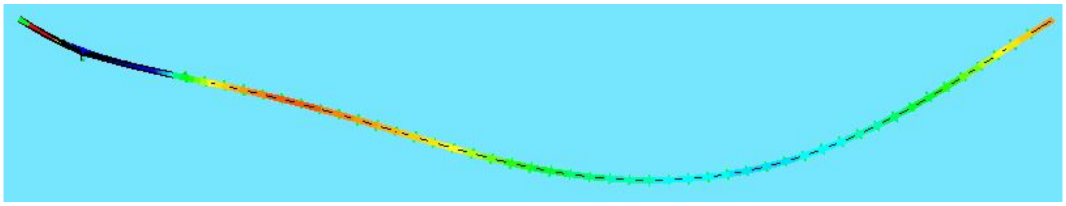

(a) Wind from 130°

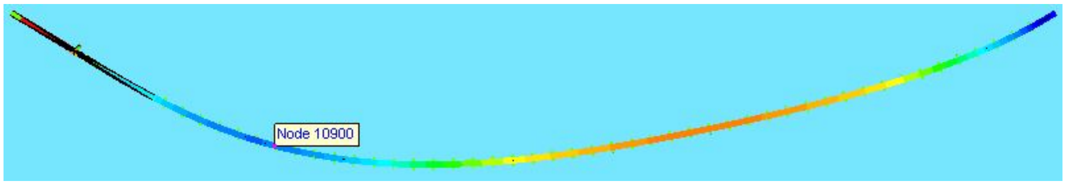

(b) Wind from 330°

Figure 7.27: Snapshots of bridge deformation due to stochastic wind. Deformations are scaled by a factor of 20. Bending moment about strong axis is indicated by color.

It is seen that the axial force in the girder is very low compared to the capacity, i.e. about 1%. The maximum axial force is reached in the initial stages after wind is applied, before the bending deformations are initiated, see figure 7.28. This is observed both for east winds and west winds, i.e. both when the girder is in tension and in compression. One explanation might be that bending moments are not formed immediately, and in the mean time, axial forces carry the external loads. Since the wind is applied over a period of only one second, the maximum axial force is probably overestimated. In the physical world, the wind would build up over a longer period of time. In other words, axial forces are of lower importance than bending moments in balancing wind loads.

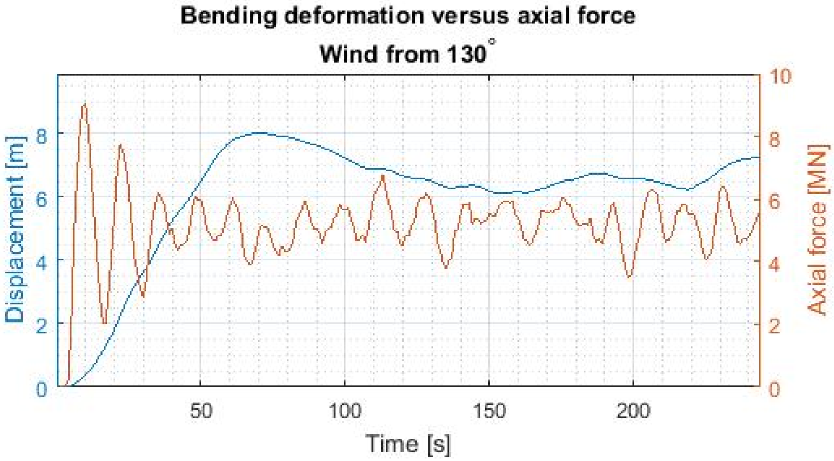

Figure 7.28: Displacement of node 10900 in the global y-direction along with the axial force in the bridge girder.

### 7.6.3 Utilization of bridge girder at locations damaged by ship collision

In the environmental load analyses, the undamaged bridge has been considered. However, the results may still indicate how the damaged bridge will be affected by the extreme storm. In this section, the utilization of the bridge girder will be studied at locations that were found to be critical in the considered ship collision scenarios. Since the plastic deformations are believed to reduce the capacity of the girder, the reaction forces induced by wind loads must be well below the initial capacity at these regions. Wind from 330° is applied. Further, since the accidental limit state is considered, material and load factors of 1.0 can be applied(NORSOK, 2010).

It was shown in section 6.5 that flooding of four pontoon compartments in pontoon 1 will not have severe consequences for the bridge. The estimated torsional stress in the girder above the flooded pontoon is only about 10% of the yield stress. For this reason, it has been decided not to prioritize environmental analyses with the bridge in flooded condition. This should be acceptable, since the torsional moment caused by wind is low.

Areas in the bridge girder that might be damaged by ship collision will be studied next. In the deckhouse-girder collisions, the bridge will suffer large local damages, which will reduce the capacity at the impacted areas. The 660 $MJ$ head-on collision with pontoon 1 also results in plastic deformations of the bridge girder, both at the end-supports and above the struck pontoon. Based on findings earlier in this section, bending moment about the strong axis of the bridge girder is believed to be the most important response parameter when considering wind. Therefore, this property is given for the critical areas in table 7.17.

Table 7.17: Bending moment about strong axis at areas damaged by ship collision.

| | **South end** | **Above pontoon 1** | **Position** $A^1$ | **Position** $B^1$ | **North end** | **Unit** |
|---|---|---|---|---|---|---|
| **Max. bending moment**$^{\mathbf{2}}$ | 900 | 400 | 400 | 150 | 900 | $[MNm]$ |
| Relative to initial capacity | 29% | 13% | 13% | 5% | 29% | |

$^1$ See figure 6.6

The table shows that the highest utilization is at the end-supports. At these positions, the bending moment reaches 29% of the initial capacity. At the impacted areas, the bending moment is in the range of $5 - 15\%$ of the initial capacity. Since local damages have not been studied in this thesis, it is not known how large the damages will be. In case of the 660 $MJ$ impact with pontoon 1, the bending moment above the pontoon will exceed the capacity with about 30%. Thus, buckling of stiffeners and perhaps diaphragms is expected, based on the findings by Norconsult(Norconsult AS, 2017d). Further, local collision analyses carried out by Postdoc Yanyan Sha show that the bridge girder will be compressed in the impact with a ship deckhouse.

Wave loads, self weight and possibly traffic loads will come in addition to the wind loads. The von Mises stress at the ends due to self-weight is approximately 100 $MPa$. For simplicity, say that 25% of the capacity is utilized by permanent loads. If the wave loads are in the order of 20% of the wind loads, the highest utilization in the storm is about 60% of the initial capacity. This means that the integrity of the bridge is threatened if the collision damages have reduced the girder capacity by more than 40%.

In this thesis, one single 1-hour simulation has been conducted. In order to determine the 100-year response, several simulations are required. Based on the maximum response of these simulations, the response corresponding to the 90-percentile can be determined. This will be assessed more thoroughly in section 7.8.

### 7.6.4 Comparison of static and stochastic wind analyses

The 100-year wind conditions have now been considered both dynamically in section 7.6.2, and statically in section 7.6.1. It is therefore interesting to compare the results, in order to estimate the importance of the fluctuating wind component. Dynamic effects may also contribute to increase responses. A simple overview is given in table 7.18 of the increase in response when including the stochastic component.

Table 7.18: Increase in reaction forces and displacements when including wind gusts compared to results obtained in the static analysis.

| | **Wind direction** | | | |
|---|---|---|---|---|
| | **100°** | **130°** | **280°** | **330°** |
| **Bending moment about strong axis** | | | | |
| South anchoring | 88% | 55% | 109% | 50% |
| North anchoring | 900%[1] | 167% | 45% | 0% |
| **Maximum displacement in y-direction** | 70% | 38% | 60% | 29% |

[1] Large increase in percentage due to low value in static analysis

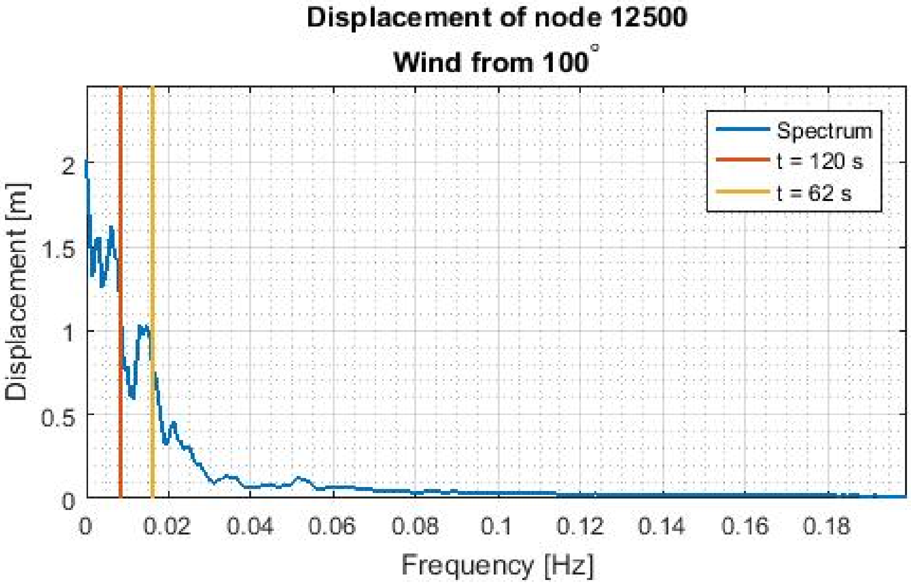

Figure 7.29: Displacement of the bridge girder at midspan in the global y-direction. The results are based on a 5000 $s$ simulation of wind from 100°.

It is seen that both the deformations and reaction forces are increased substantially. This is as expected. Firstly, the maximum loads are larger than the static loads. For the largest wind gusts, the wind speed reaches values of about 125% of the mean speed at the elevation of the bridge girder. Since drag forces are proportional to $U^2_{wind}$, dynamic loads are expected to be about 55% higher than static loads. However, for some of the response quantities, the increase is even higher than this. This is believed to be due to dynamic amplification. Figure 7.29 shows the displacement in the global $y$-direction plotted in the frequency domain. It is seen that there are peaks close to the first and second eigenperiod. This indicates that these modes might be excited by the wind. The peaks in the plot occur for frequencies slightly lower than the estimated eigenfrequencies. This is believed to be because of structural and hydrodynamic damping, since the damped eigenfrequency is given by $\omega_d = \omega_0\sqrt{1-\xi^2}$, i.e. it is lower than the undamped eigenfrequency(Larsen, 2014). In addition to dynamic amplification, the distribution of wind along the girder may also contribute to amplify the response.

## 7.7 Combined environmental load analysis

It has been decided not to carry out combined wind and wave analyses. The reasoning for this is that the results of such an analysis would be unreliable, due to the numerical issues in the wave loads. Firstly, the drift motion would be difficult to filter out. Secondly, since the wave loads are not represented correctly in USFOS, the response would be severely miscalculated.

## 7.8 Discussion of environmental load analyses

The characteristic response of the 100-year storm has not been determined. For this, a high number of 1-hour simulations are required. This has not been practicably possible due to high computational costs. In addition, due to numerical instabilities in the wave load analysis, a combined wind and wave analysis has not been conducted.

If simulation time had not been an issue, it would have been interesting to conduct several sensitivity studies. In this thesis, only long-crested sea has been studied, which might not be conservative. In a complete analysis, several analyses with short-crested sea should be carried out, such that unfavorable interference can be detected. The applied assumptions in modelling of wind should also be studied. According to Norconsult, wind should be applied both with constant mean wind across the fjord and with linearly increasing mean wind speed. In this thesis, only constant mean wind has been considered. Since the asymmetry might trigger buckling, linearly increasing wind should also be studied. Also, the results by Moe indicate that fully correlated wind yields the worst response(Moe, 2016). Therefore, the wind analysis may be made more conservative by increasing the correlation.

In this thesis, only a few 1-hour simulations have been conducted. In order to determine the 100-year response, a much higher number of simulations are required. Firstly, several combinations of wind and waves must be tested. For each combination, different random seeds should be implemented. Further, when the most unfavorable combination of wind and waves has been determined, numerous simulations must be conducted for the worst case scenario. Haver recommends 20 for ULS considerations(Haver, 2017). Based on the maximum response of these simulations, the response corresponding to the $90^{th}$ percentile can be determined. However, the few 1-hour simulations that have been carried out can give an indication of the order of magnitude of the 100-year response. In the design basis for the Bjørnafjorden suspension bridge, the NPRA estimates the $95^{th}$ percentile as the worst out of 10 simulations, multiplied by a factor of 1.25(Statens Vegvesen, 2016). In the next paragraph, it will be assumed that the worst response in the 1-hour simulation multiplied by a factor of 1.3 will give an acceptable approximation.

The simple environmental load analyses in this thesis are not sufficient to determine the 100-year response, but the results give an indication of how high the utilization will be. The highest bending moment about the strong axis found in the wind analyses is 900 $MNm$, which is about 30% of the capacity. If the wave load is assumed to be 20% of the wind load, and the combined response is multiplied by 1.3, the 100-year response is estimated to 1400 $MNm$. For ULS considerations, safety factors must be included. The material factor is taken as 1.15, inline with NORSOK recommendations for steel structures(NORSOK, 2010), while the load factor for environmental loads is taken as 1.6(Statens Vegvesen, 2016). The bending moment then reaches 2600 $MNm$, which is 70% of the capacity. Self-weight, and possibly traffic loads, will come in addition to this. In section 7.6.3, the utilization of the girder due to self-weight is taken as 25%. Assuming that these assumptions are valid, the 100-year response will cause very high utilization of the bridge girder.

In advance, snap-through buckling of the bridge girder was one of the concerns. It is not an issue in the few wind analyses that have been carried out. Still, buckling might have been observed if a high number of combined wind and wave simulations had been conducted.

# Chapter 8

# Conclusions

The fundamental eigenmode of the bridge oscillates with two half waves in the horizontal plane and has a period of 119.6 $s$. The second eigenperiod is 62.3 $s$, and corresponds to a horizontal mode with 3 half waves. Further, the vertical modes in the floating low bridge have periods close to 6 $s$. The results of the eigenvalue analysis coincide well with the results obtained in 3DFloat by Norconsult on behalf of the NPRA.

A literature search has been performed to find a simple model for how impact forces are balanced by shear forces and bending moments in a long beam. High energy impacts on a simplified, straight model of the bridge has been studied in USFOS, and compared to theory on travelling plastic hinges. However, the results indicate that the model is not applicable for collision energies in the range relevant for this thesis.

For the 660 $MJ$ design collision with the pontoon closest to the transit channel, the bridge will suffer large damages in both the pontoon and in the bridge girder. The ship penetrates 11 $m$ into the pontoon and local deformations dissipate 50% of the collision energy. At the impact area, the lateral displacement of the bridge girder is about 8 $m$. The analysis shows that the impact force is balanced by bending moments in the bridge girder. By considering the bending capacity estimated by the NPRA, it is seen that plastic deformations will occur in the girder above the struck pontoon and at the end-supports. The high utilization at the north end of the bridge appears to be the result of interference between incoming and reflected bending waves. For the new pontoon design, a slightly larger portion of the collision energy is absorbed by local damages, but the difference is small. The pontoon collisions with lower energies do not cause as severe responses in the bridge. However, in the impact where the ship strikes the pontoon perpendicularly, yielding is likely to occur in the connection point between the column and the bridge girder.

The majority of the pontoon collisions result in flooding of four pontoon compartments. If the four compartments at the end of pontoon 1 are flooded, the rotation of the bridge girder will be in the order of 1°. This corresponds to a torsional stress of 44 $MPa$, which is far below the yield strength.

In the collision between a ship deckhouse and the bridge girder, the deckhouse will suffer the largest damages. Still, the girder will take some deformations at the impact location, which will cause a deterioration in strength. Since the maximum bending moment in this area is large, it might be necessary to conduct more thorough analyses. Local deformations dissipate between 20-40% of the collision energy in impacts with the bridge girder.

Waves from the northwest cause the largest characteristic wave loads on the bridge. Winds from east and west cause loads of similar magnitude, and cause lateral displacements in the order of 10 $m$. Wind loads are carried by bending about the strong axis of the bridge girder. The utilization at critical areas is about one third of the bending capacity. If wave loads, self weight and safety factors are also accounted for, the 100-year response is believed to be close to the capacity, which means that plastic deformations might occur. In advance, snap-through buckling of the bridge girder was one of the concerns. However, for the few simulations that have been conducted, buckling is not an issue.

# Chapter 9

# Recommendations for Further Work

The number of ship collision analyses that have been carried out is limited. As a consequence, some of the potentially critical scenarios are not considered. For example, one could consider the collision between the forecastle of a large ship and the bridge girder. Since the deckhouse is the weaker component in the girder collisions, it is thinkable that the impact force could be higher for a high-strength forecastle. Similarly, the collision between an ice-strengthened vessel and a pontoon could be considered. However, since the pontoon is the weaker component, the results should not be much affected by the strength of the bow.

Local damages have not been the topic of interest in this thesis. The conducted collision analyses indicate that the bending capacity is exceeded in several of the collision scenarios. More detailed finite element analyses are required in order to determine the extent of the damages, and if the damaged bridge has sufficient integrity to survive a 100-year storm. Further, the costs of the necessary repairs must be evaluated. In addition to this, the cable tower and the stay-cables should be studied more closely; ship impacts with the pontoon closest to the transit channel can induce yielding in the stay-cables, while the 100-year storm will cause large wind loads on the tower.

In order to assess if the bridge fulfills the ultimate limit state criterion, the 100-year response must be determined. Firstly, the worst combination of wind, waves and current along the 100-year contour line must be determined. This is done by conducting numerous 1-hour simulations. Further, at least 20 1-hour simulations of the worst load combination should be carried out. The worst response in each each 1-hour simulation can then be identified, and a Gumbel-model can be fitted to the sample by the method of moments. From this, the response corresponding to the $90^{th}$ percentile can be identified, and applied as an estimate for the 100-year response. As a part of the accidental limit state control, the damaged bridge should also survive the 100-year storm. However, safety factors equal to 1.0 can be applied in this limit state.

# Bibliography

Aalberg, A. (2017). Analysis and design bjørnefjorden floating cable-stayed bridge subjected to large ship collisions and extreme environmental loads. Master's thesis, Norwegian University of Science and Technology.

Aas-Jakobsen, K. Wind simulation by windsim; verification. [Unpublished; obtained from Professor Jørgen Amdahl].

Aas-Jakobsen, K. (2015). User manual windsim. `http://www.aas-jakobsen.net/download/windsim/User%20manual%20Windsim.pdf`. [Online; accessed 30-April-2018].

Aas-Jakobsen, K. and Strømmen, E. (2001). Time domain buffeting response calculations of slender structures. Journal of Wind Engineering and Industrial Aerodynamics, 89(5):341 – 364.

AASHTO (2014). Aashto lrfd bridge design specifications. [Revision 3].

Abdelgawad, A., Anwar, A., and Nassar, M. (2013). Snap-through buckling of a shallow arch resting on a two-parameter elastic foundation. Applied Mathematical Modelling, 37(16):7953 – 7963.

Amdahl, J. (2010). Tmr4205 buckling and ultimate strength of marine structures. Chapter 7: Plastic Methods of Analysis.

Amdahl, J. (2014). Tmr4167 marin tenikk 2 - konstruksjoner. [Compendium in TMR4167 Marin Tenikk 2].

Cheung, M. and Babcock, C.D., J. (1970). An energy approach to the dynamic stability of arches. Journal of Applied Mechanics, Transactions ASME, 37(4):1012–1018. cited By 11.

Det Norske Veritas (2010a). Dnv-rp-c204 - design against accidental loads. `https://rules.dnvgl.com/docs/pdf/DNV/codes/docs/2010-10/RP-C204.pdf`. [Online; accessed 10-October-2017].

Det Norske Veritas (2010b). Dnv-rp-c205 - design against accidental loads. `https://rules.dnvgl.com/docs/pdf/dnv/codes/docs/2010-10/rp-c205.pdf`. [Online; accessed 12-April-2018].

Det Norske Veritas (2010c). Dnv-rp-f205 - global performance analysis of deepwater floating structures. `https://rules.dnvgl.com/docs/pdf/DNV/codes/docs/2010-10/RP-F205.pdf`. [Online; accessed 27-April-2018].

Det Norske Veritas (2014). Dnv-os-j101 - design of offshore wind turbine structures. `https://rules.dnvgl.com/docs/pdf/DNV/codes/docs/2014-05/Os-J101.pdf`. [Online; accessed 5-May-2018].

Engineering ToolBox (2018). Beams - fixed at both ends - continuous and point loads. `https://www.engineeringtoolbox.com/beams-fixed-both-ends-support-loads-deflection-d_809.html`. [Online; accessed 28-May-2018].

Faltinsen, O. M. (1990). SEA LOADS ON SHIPS AND OFFSHORE STRUCTURES. CAMBRIDGE.

Fan, W., Liu, Y., Liu, B., and Guo, W. (2016). Dynamic ship-impact load on bridge structures emphasizing shock spectrum approximation. Journal of Bridge Engineering, 21(10). cited By 1.

Fan, W., Yuan, W., Yang, Z., and Fan, Q. (2011). Dynamic demand of bridge structure subjected to vessel impact using simplified interaction model. Journal of Bridge Engineering, 16(1):117–126. cited By 18.

Graff, K. F. (1975). Wave Motion in Elastic Solids. Dover Publications.

Greco, M. (2016). Tmr 4215: Sea loads. [Unpublsihed; lecture notes from TMR4215].

Haver, S. (2017). Metocean modelling and prediction of extremes. Technical report, Haver & havet and University of Stavanger and NTNU. [Compendium in TMR4195].

Irgens, F. (1999). Fasthetslære. Tapir, 6 edition.

Jones, N. (2011). Structural impact, second edition, volume 9781107010963. Cambridge University Press. cited By 0.

Kounadis, A., Raftoyiannnis, J., and Mallis, J. (1989). Dynamic buckling of an arch model under impact loading. Journal of Sound and Vibration, 134(2):193 – 202.

Langen, I. and Sigbjörnsson, R. (1979). Dynamisk analyse av konstruksjoner. Tapir.

Larsen, C. M. (2014). TMR4182 Marin Dynamikk. Akademika Forlag.

Lehn, E. (2009). Tidsserier - sampling, filtrering og analyse. `http://www.ivt.ntnu.no/imt/courses/tmr7/resources/Tidsserier_v07.pdf`. [Online; accessed 26-april-2018].

Leira, B. J. (2015). TMR4170 Marine Structures Basic Course. Akademika Forlag.

Marine Traffic (2018a). Maersk flensburg. `https://www.marinetraffic.com/no/ais/details/ships/shipid:123015/mmsi:209762000/imo:9252773/vessel:MAERSK_FLENSBURG`. [Online; accessed 13-February-2018].

Marine Traffic (2018b). Wilson ross. `https://www.marinetraffic.com/en/ais/details/ships/shipid:284951/mmsi:248379000/imo:7382495/vessel:WILSON_ROSS`. [Online; accessed 13-February-2018].

Marine Traffic (2018c). Wilson saga. `https://www.marinetraffic.com/en/ais/details/ships/shipid:146397/mmsi:212893000/imo:8918461/vessel:WILSON_SAGA`. [Online; accessed 13-February-2018].

Marintek (2001). Usfos gettting started. `http://www.usfos.no/manuals/usfos/theory/documents/Getting_Started.pdf`. [Online; accessed 12-October-2017].

Marintek (2010). Usfos hydrodynamics - theory and description of use. `http://www.usfos.no/manuals/usfos/theory/documents/Usfos_Hydrodynamics.pdf`. [Online; accessed 21-April-2018].

Marintek (2015). Usfos user's manual. `http://usfos.no/manuals/usfos/users/documents/Usfos_UM_06.pdf`. [Online; accessed 21-April-2018].

Moan, T. (2001). Design of offshore structures : Vol. 1 : Design procedures and criteria.

Moan, T. (2003). TMR4190 Finite Element Modelling and Analysis of Marine Structures. Akademika Forlag. [Chapter 12, Learning material in TMR4305].

Moe, O. H. (2016). Analysis and design of bjørnafjorden tlp supported suspension bridge subjected to large ship collisions and extreme environmental loads. Master's thesis, Norwegian University of Science and Technology.

Myrhaug, D. (2005). TMR4235 Stochastic Theory of Sealoads. Akademika Forlag.

Myrhaug, D. (2007). TMR4180 Marin Dynamikk - Uregelmessig sjø. Akademika forlag. [Compendium in TMR4180 Marin Dynamikk].

Myrhaug, D. (2014). Oceanography; Wind Waves. Akademika forlag.

Norconsult AS (2017a). K7 bjørnafjorden end-anchored floating bridge; appendix a – drawings binder. [Unpublished; obtained from Professor Jørgen Amdahl].

Norconsult AS (2017b). K7 bjørnafjorden end-anchored floating bridge; appendix b – global analyses. [Unpublished; obtained from Professor Jørgen Amdahl].

Norconsult AS (2017c). K7 bjørnafjorden end-anchored floating bridge appendix d – design of bridge girder. [Norconsult AS for Statens vegvesen Region vest].

Norconsult AS (2017d). K7 bjørnafjorden end-anchored floating bridge; appendix e – pontoon and column structural sizing and design. [Unpublished; obtained from Professor Jørgen Amdahl].

Norconsult AS (2017e). K7 bjørnafjorden end-anchored floating bridge; appendix j – ultimate resistance of bridge girder. [Unpublished; obtained from Professor Jørgen Amdahl].

Norconsult AS (2017f). K7 end-anchored floating bridge appendix a - model. [Unpublished; obtained from Professor Jørgen Amdahl].

Norsk Standard (2008). Eurokode 1: Laster på konstruksjoner - del 1-7: Almenne laster - ulykkeslaster.

NORSOK (2004). Norsok standard n-004 - design of steel structures. `http://www.standard.no/pagefiles/1145/n-004.pdf`. [Online; accessed 4-September-2017].

NORSOK (2007). Norsok standard n-003 - actions and action effects. `http://www.ivt.ntnu.no/imt/courses/tmr4195/literature/Standards%20and%20Recommendations/N-003e2.pdf`. [Online; accessed 2-September-2017].

NORSOK (2010). Norsok standard n-001, integrity of offshore structures. `http://www.standard.no/pagefiles/17477/n-001r7.pdf`. [Online; accessed 2-September-2017].

Pan, Z., Vada, T., and Hanssen, F.-C. (2013). A mesh dependency study for the mean drift forces by pressure integration. volume 9. cited By 2.

Pedersen, P. T. and Zhang, S. (1998). On impact mechanics in ship collisions. Marine Structures, 11(10):429 – 449.

Pettersen, B. (2004). TMR4247 Marin Teknikk 3 Hydrodynamikk. Akademika Forlag.

Pi, Y.-L. and Bradford, M. (2008). Dynamic buckling of shallow pin-ended arches under a sudden central concentrated load. Journal of Sound and Vibration, 317(3-5):898–917. cited By 30.

Standing, R., Brendling, W., and Wilson, D. (1987). Recent developments in the analysis of wave drift forces, low-frequency damping and response. IN: OTC 87, PROC. NINETEENTH ANNUAL OFFSHORE TECHNOL. CONF., (HOUSTON, U.S.A.: APR. 27-30, 1987), 2 , Richardson, U.S.A., Offshore Technol. Conf., 1987, Paper OTC 5456:307–315. cited By 2.

Statens Vegvesen (2016). Design basis sbt-pgr-ba-211-001-0. `https://www.vegvesen.no/_attachment/1607161/binary/1145773?fast_title=Bj%C3%B8rnafjorden+Suspension+Bridge+(TLP)+Design+Basis.pdf`. [Online; accessed 23-May-2018].

Statens Vegvesen (2017a). The e39 coastal highway route. `https://www.vegvesen.no/en/roads/Roads+and+bridges/Road+projects/e39coastalhighwayroute;jsessionid=6FC6EB2832C26222977C579B9C97015F`. [Online; accessed 10-December-2017].

Statens Vegvesen (2017b). The e39 coastal highway route; benefits for freight transport. `https://www.vegvesen.no/_attachment/2044360/binary/1213584?fast_title=Benefits+for+freight+transport+-+E39+coastal+highway+route.pdf`. [Online; accessed 10-December-2017].

Statens Vegvesen (2017c). The e39 coastal highway route choice of technology for fjord crossings. `https://www.vegvesen.no/_attachment/2044359/binary/1217358?fast_title=Choice+of+technology+for+fjord+crossings.pdf`. [Online; accessed 10-December-2017]].

Statens Vegvesen (2017d). Fjordkryssing - bjørnafjorden. `https://www.vegvesen.no/Europaveg/e39stordos/fjordkryssing-bjornafjorden`. [Online; accessed 10-December-2017].

Sørensen, S. I. (2010). Betongkonstruksjoner. Fagbokforlaget.

Yu, T., Yang, J., Reid, S., and Austin, C. (1996). Dynamic behaviour of elastic-plastic free-free beams subjected to impulsive loading. International Journal of Solids and Structures, 33(18):2659 – 2680.

Yu, Z., Amdahl, J., and Storheim, M. (2016). A new approach for coupling external dynamics and internal mechanics in ship collisions. Marine Structures, 45(Supplement C):110 – 132.

# Appendices

# Appendix A

# Modelling of the Bridge

## A.1 Cable properties

Table A.1: Properties of the cables in the various cable pairs. The cable pairs are numbered from the south end of the bridge.

| Cable pair number | Cross-sect. area $[mm^2]$ | Diameter $[mm]$ | Eff.Young's modulus $[GPa]$ | Poiss. ratio | Thermal exp. coeff. $[1/^\circ C]$ | Temp. western cable $[^\circ C]$ | Temp. eastern cable $[^\circ C]$ |
|---|---|---|---|---|---|---|---|
| 1 | 11656 | 121.8 | 177.54 | 0.3 | 1.20e-05 | -229.5 | -91.8 |
| 2 | 11245 | 119.7 | 178.37 | 0.3 | 1.20e-05 | -228.3 | -91.3 |
| 3 | 10824 | 117.4 | 179.18 | 0.3 | 1.20e-05 | -227.2 | -90.9 |
| 4 | 10405 | 115.1 | 179.98 | 0.3 | 1.20e-05 | -226.1 | -90.4 |
| 5 | 10001 | 112.8 | 180.76 | 0.3 | 1.20e-05 | -225.1 | -90.0 |
| 6 | 8625 | 104.8 | 181.53 | 0.3 | 1.20e-05 | -224.1 | -89.6 |
| 7 | 8241 | 102.4 | 182.28 | 0.3 | 1.20e-05 | -200.8 | -80.3 |
| 8 | 7859 | 100.0 | 183.02 | 0.3 | 1.20e-05 | -199.9 | -79.9 |
| 9 | 11719 | 122.2 | 184.43 | 0.3 | 1.20e-05 | -198.3 | -79.3 |
| 10 | 7294 | 96.4 | 185.77 | 0.3 | 1.20e-05 | -196.8 | -78.7 |
| 11 | 6928 | 93.9 | 187.03 | 0.3 | 1.20e-05 | -195.3 | -78.1 |
| 12 | 6569 | 91.5 | 188.21 | 0.3 | 1.20e-05 | -194.0 | -77.6 |
| 13 | 6210 | 88.9 | 189.31 | 0.3 | 1.20e-05 | -300.0 | -120.0 |
| 14 | 5844 | 86.3 | 190.31 | 0.3 | 1.20e-05 | -298.3 | -119.3 |
| 15 | 5493 | 83.6 | 191.23 | 0.3 | 1.20e-05 | -296.7 | -118.7 |
| 16 | 5142 | 80.9 | 192.05 | 0.3 | 1.20e-05 | -295.4 | -118.1 |
| 17 | 4807 | 78.2 | 192.78 | 0.3 | 1.20e-05 | -294.2 | -117.7 |
| 18 | 4479 | 75.5 | 193.40 | 0.3 | 1.20e-05 | -209.4 | -83.8 |
| 19 | 4173 | 72.9 | 193.92 | 0.3 | 1.20e-05 | -208.8 | -83.5 |
| 20 | 3899 | 70.5 | 194.35 | 0.3 | 1.20e-05 | -208.3 | -83.3 |
| 21 | 3670 | 68.4 | 194.66 | 0.3 | 1.20e-05 | -207.9 | -83.2 |
| 22 | 7004 | 94.4 | 194.88 | 0.3 | 1.20e-05 | -207.7 | -83.1 |
| 23 | 6996 | 94.4 | 194.88 | 0.3 | 1.20e-05 | -290.8 | -116.3 |
| 24 | 3670 | 68.4 | 194.66 | 0.3 | 1.20e-05 | -291.1 | -116.5 |
| 25 | 3899 | 70.5 | 194.35 | 0.3 | 1.20e-05 | -291.6 | -116.7 |
| 26 | 4166 | 72.8 | 193.92 | 0.3 | 1.20e-05 | -292.3 | -116.9 |
| 27 | 4463 | 75.4 | 193.40 | 0.3 | 1.20e-05 | -209.4 | -83.8 |
| 28 | 4784 | 78.0 | 192.77 | 0.3 | 1.20e-05 | -210.1 | -84.1 |
| 29 | 5112 | 80.7 | 192.05 | 0.3 | 1.20e-05 | -295.4 | -118.2 |
| 30 | 5447 | 83.3 | 191.23 | 0.3 | 1.20e-05 | -296.7 | -118.7 |
| 31 | 5798 | 85.9 | 190.31 | 0.3 | 1.20e-05 | -298.3 | -119.3 |
| 32 | 6149 | 88.5 | 189.31 | 0.3 | 1.20e-05 | -300.0 | -120.0 |
| 33 | 6493 | 90.9 | 188.21 | 0.3 | 1.20e-05 | -301.8 | -120.7 |
| 34 | 6836 | 93.3 | 187.03 | 0.3 | 1.20e-05 | -303.9 | -121.6 |
| 35 | 7187 | 95.7 | 185.77 | 0.3 | 1.20e-05 | -306.1 | -122.4 |
| 36 | 7538 | 98.0 | 184.43 | 0.3 | 1.20e-05 | -220.3 | -88.1 |
| 37 | 7889 | 100.2 | 183.02 | 0.3 | 1.20e-05 | -222.1 | -88.9 |
| 38 | 8225 | 102.3 | 181.53 | 0.3 | 1.20e-05 | -224.1 | -89.6 |
| 39 | 8576 | 104.5 | 179.98 | 0.3 | 1.20e-05 | -226.1 | -90.5 |
| 40 | 9888 | 112.2 | 178.37 | 0.3 | 1.20e-05 | -228.3 | -91.3 |
| 41 | 10269 | 114.3 | 176.69 | 0.3 | 1.20e-05 | -230.6 | -92.2 |
| 42 | 10651 | 116.5 | 174.97 | 0.3 | 1.20e-05 | -233.0 | -93.2 |
| 43 | 11017 | 118.4 | 173.19 | 0.3 | 1.20e-05 | -235.6 | -94.2 |
| 44 | 11398 | 120.5 | 171.37 | 0.3 | 1.20e-05 | -238.3 | -95.3 |

## A.2 Added mass for pontoons

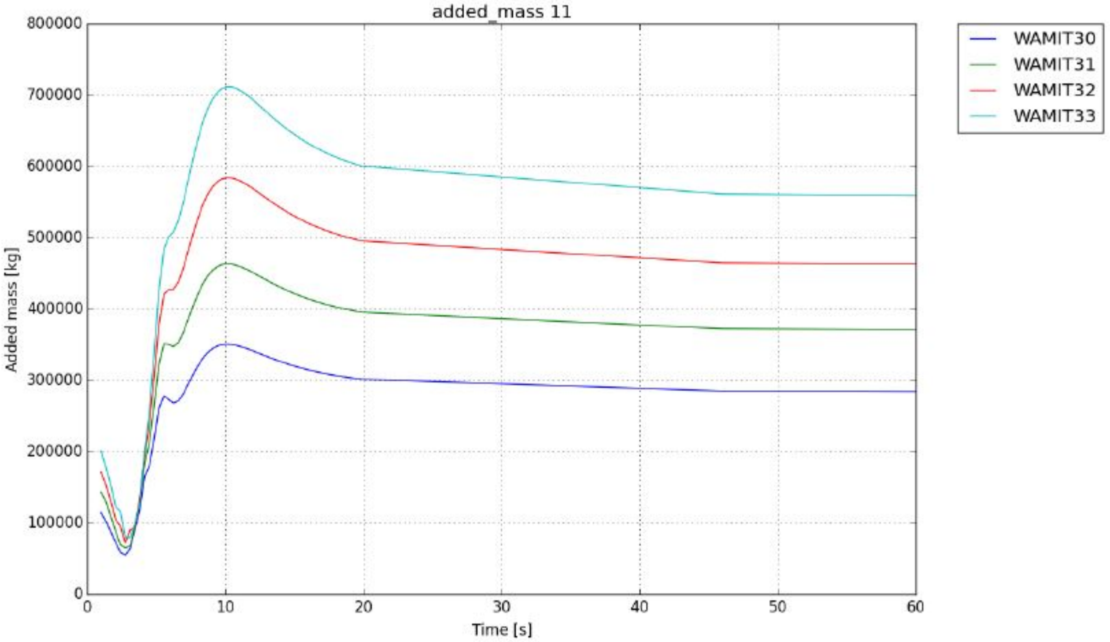

Figure A.1: Added mass in surge as a function of oscillation period. WAMIT30 is the smallest pontoon, WAMIT33 is the largest pontoon. From: (Norconsult AS, 2017f).

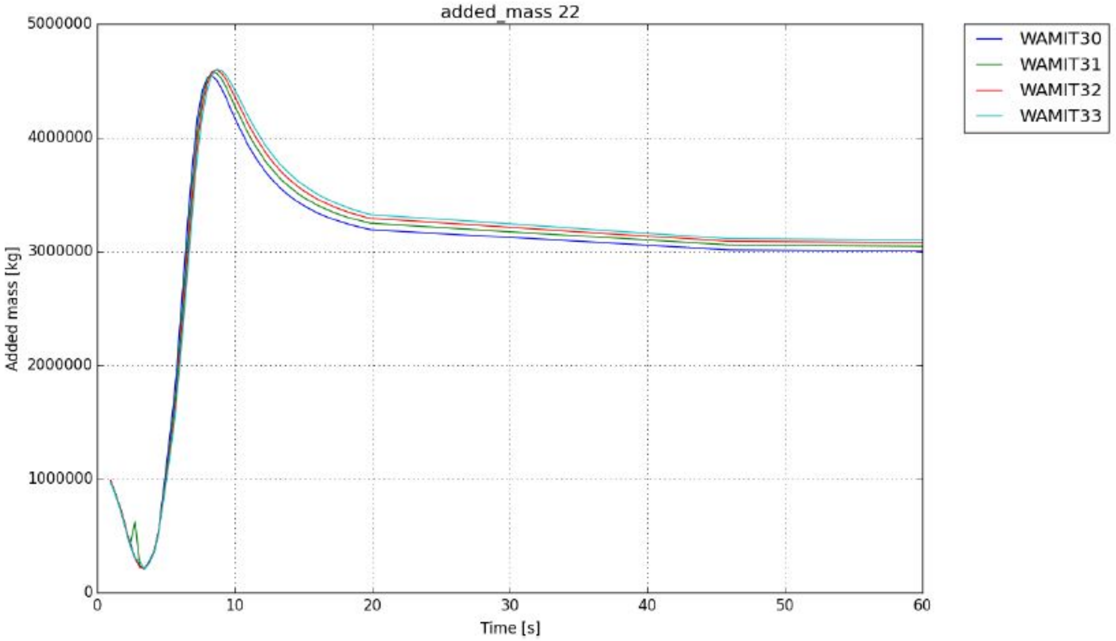

Figure A.2: Added mass in sway as a function of oscillation period. WAMIT30 is the smallest pontoon, WAMIT33 is the largest pontoon. From: (Norconsult AS, 2017f).

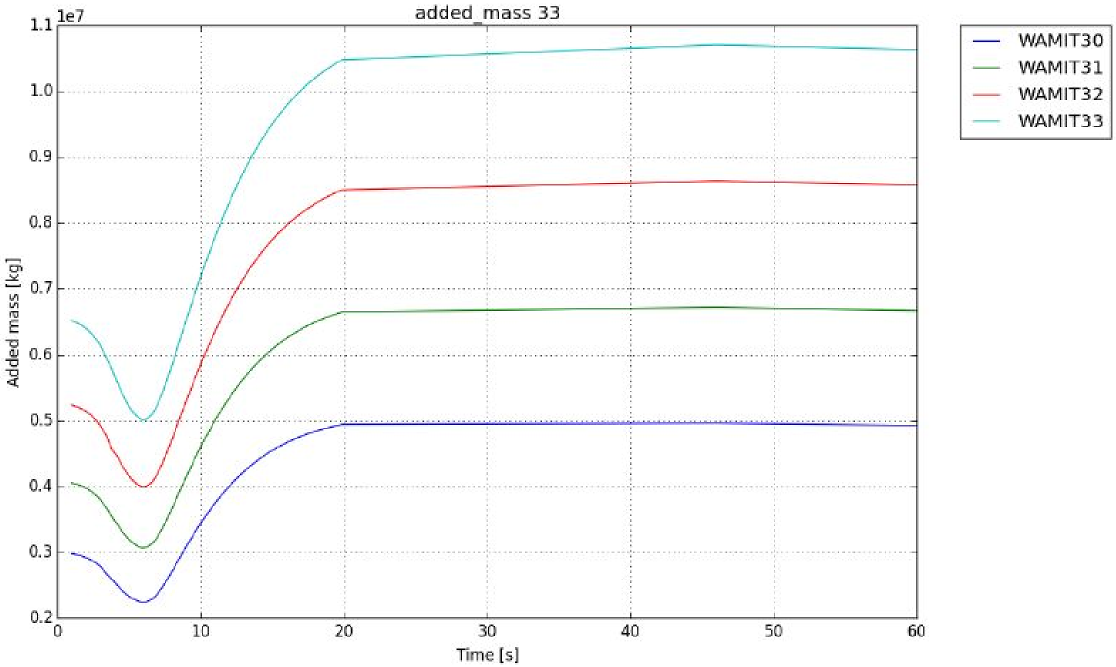

Figure A.3: Added mass in heave as a function of oscillation period. WAMIT30 is the smallest pontoon, WAMIT33 is the largest pontoon. From: (Norconsult AS, 2017f).

# Appendix B

# Eigenmodes

## B.1 Illustrations of a selection of eigenmodes

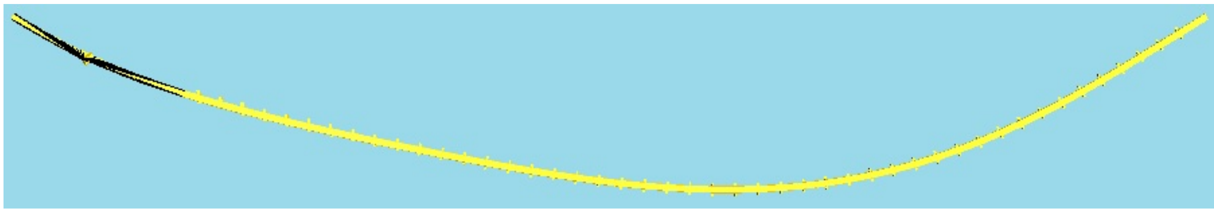

Figure B.1: Illustration of eigenmode 1.

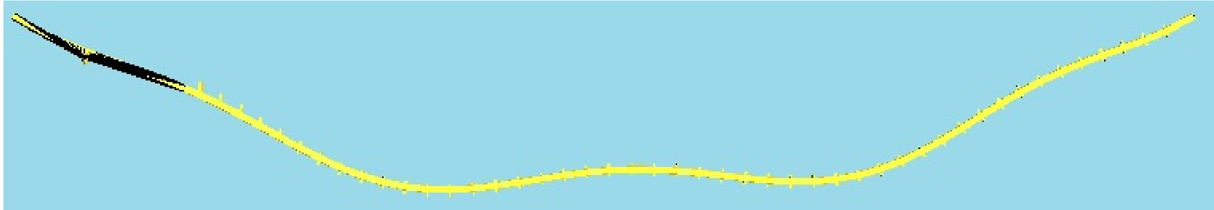

Figure B.2: Illustration of eigenmode 4.

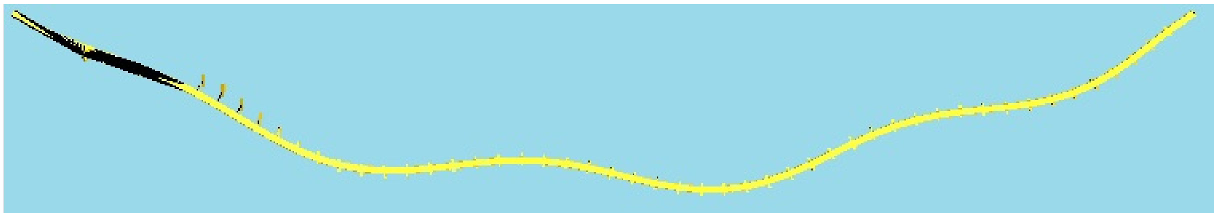

Figure B.3: Illustration of eigenmode 5.

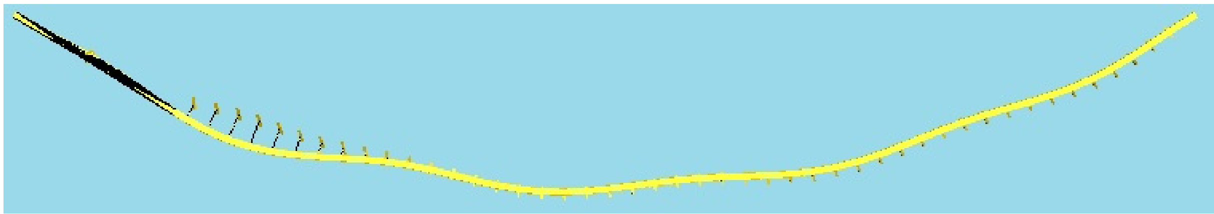

Figure B.4: Illustration of eigenmode 9.

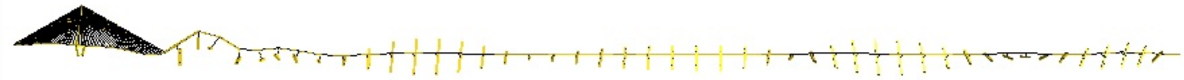

Figure B.5: Illustration of eigenmode 19.

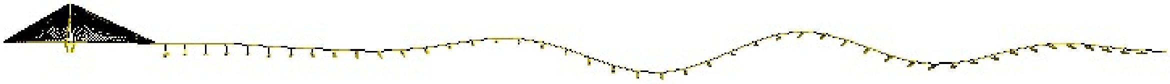

Figure B.6: Illustration of eigenmode 23.

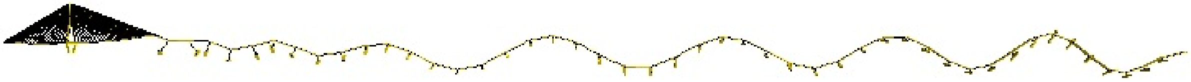

Figure B.7: Illustration of eigenmode 31.

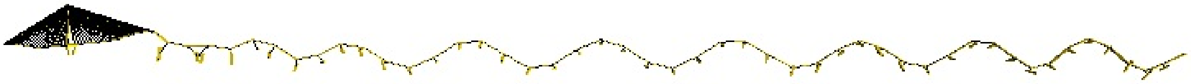

Figure B.8: Illustration of eigenmode 35.

## B.2 Eigenmodes found in USFOS

Table B.1: The first 20 eigenmodes of the USFOS model. The valid range for the applied added mass is given in the last column.

| **Eigenmode** | **Eigenperiod** [$s$] | **Description of motion** | **Valid period range for the added mass** |
|---|---|---|---|
| 1 | 119.61 | Horizontal, 2 half waves | $t > 40\ s$ |
| 2 | 62.29 | Horizontal, 3 half waves | $t > 40\ s$ |
| 3 | 36.30 | Horizontal, 4 half waves | $t > 40\ s$ |
| 4 | 25.24 | Horizontal, 5 half waves | $t > 40\ s$ |
| 5 | 17.74 | Horizontal<br>Torsional in high bridge | $t > 40\ s$ |
| 6 | 16.66 | Horizontal<br>Torsional in high bridge | $t > 40\ s$ |
| 7 | 13.65 | Horizontal<br>Torsional in high bridge | $t>40\ s$ |
| 8 | 11.15 | Horizontal and Torsional | $5\ s<t<10\ s$ |
| 9 | 10.68 | Horizontal and Torsional | $5\ s<t<10\ s$ |
| 10 | 9.10 | Horizontal and Torsional | $5\ s<t<10\ s$ |
| 11 | 8.31 | Horizontal and Torsional | $5\ s<t<10\ s$ |
| 12 | 7.74 | Torsional (and Horizontal) | $5\ s<t<10\ s$ |
| 13 | 6.99 | Torsional (and Horizontal)<br>Vertical in high bridge | $5\ s<t<10\ s$ |
| 14 | 6.82 | Torsional (and Horizontal)<br>Vertical in high bridge | $5\ s<t<10\ s$ |
| 15 | 6.69 | Vertical in high bridge<br>(Torsional and Horizontal) | $5\ s<t<10\ s$ |
| 16 | 6.60 | Vertical in high bridge<br>(Torsional and Horizontal) | $5\ s<t<10\ s$ |
| 17 | 6.40 | Vertical in high bridge | $5\ s<t<10\ s$ |
| 18 | 6.37 | Vertical in high bridge | $5\ s<t<10\ s$ |
| 19 | 6.32 | Vertical in high bridge | $5\ s<t<10\ s$ |
| 20 | 6.22 | Vertical in high bridge | $5\ s<t<10\ s$ |

Table B.2: Eigenmode 20 to 40 obtained with the USFOS model. The valid range for the applied added mass is given in the last column.

| **Eigenmode** | **Eigenperiod** $[s]$ | **Description of motion** | **Valid period range for the added mass** |
|---|---|---|---|
| 21 | 6.14 | Vertical in high bridge | 5 $s$<t<10 $s$ |
| 22 | 6.08 | Vertical in high bridge | 5 $s$<t<10 $s$ |
| 23 | 6.00 | Vertical in low bridge | 5 $s$<t<10 $s$ |
| 24 | 5.99 | Vertical in low bridge | 5 $s$<t<10 $s$ |
| 25 | 5.99 | Vertical in low bridge | 5 $s$<t<10 $s$ |
| 26 | 5.99 | Vertical in low bridge | 5 $s$<t<10 $s$ |
| 27 | 5.99 | Vertical in low bridge | 5 $s$<t<10 $s$ |
| 28 | 5.99 | Vertical in low bridge | 5 $s$<t<10 $s$ |
| 29 | 5.98 | Vertical in low bridge | 5 $s$<t<10 $s$ |
| 30 | 5.96 | Vertical in low bridge | 5 $s$<t<10 $s$ |
| 31 | 5.94 | Vertical in low bridge | 5 $s$<t<10 $s$ |
| 32 | 5.90 | Vertical over entire bridge span | 5 $s$<t<10 $s$ |
| 33 | 5.86 | Vertical over entire bridge span | 5 $s$<t<10 $s$ |
| 34 | 5.81 | Vertical over entire bridge span | 5 $s$<t<10 $s$ |
| 35 | 5.80 | Vertical over entire bridge span | 5 $s$<t<10 $s$ |
| 36 | 5.74 | Vertical over entire bridge span | 5 $s$<t<10 $s$ |
| 37 | 5.72 | Vertical over entire bridge span | 5 $s$<t<10 $s$ |
| 38 | 5.64 | Vertical over entire bridge span | 5 $s$<t<10 $s$ |
| 39 | 5.57 | Vertical over entire bridge span | 5 $s$<t<10 $s$ |
| 40 | 5.47 | Vertical over entire bridge span | 5 $s$<t<10 $s$ |

## B.3 Eigenmodes from USFOS analysis compared to results obtained with alternative software

Table B.3: Eigenmodes obtained in USFOS compared to eigenmodes obtained in 3DFloat.

| **USFOS analysis** | | | **3DFloat analysis** | **Norconsult AS (2017f)** | |
|---|---|---|---|---|---|
| **Mode** | **Period** [$s$] | **Description of motion** | **Mode** | **Period** [$s$] | **Description of motion** |
| 1 | 119.61 | Horizontal, 2 half waves | 1 | 119.90 | Horizontal |
| 2 | 62.29 | Horizontal, 3 half waves | 2 | 61.97 | Horizontal |
| 3 | 36.30 | Horizontal, 4 half waves | 3 | 34.80 | Horizontal |
| 4 | 25.24 | Horizontal, 5 half waves | 4 | 23.74 | Horizontal |
| 5 | 17.74 | Horizontal and Torsional | 5 | 16.37 | Horizontal |
| 6 | 16.66 | Horizontal and Torsional[1] | 6 | 14.00 | Horizontal&Torsional[2] |
| 7 | 13.65 | Horizontal and Torsional[1] | 7 | 12.07 | Horizontal&Torsional[2] |
| 8 | 11.31 | Horizontal and Torsional | 8 | 9.86 | Horizontal&Torsional[2] |
| 9 | 10.68 | Horizontal and Torsional | 9 | 9.36 | Horizontal&Torsional[2] |
| 10 | 9.10 | Horizontal and Torsional | 10 | 7.99 | Horizontal&Torsional[2] |
| 11 | 8.31 | Horizontal and Torsional | 11 | 7.94 | Horizontal&Torsional[2] |
| 12 | 7.74 | Torsional (and Horizontal) | 12 | 6.87 | Vertical in high bridge |
| 13 | 6.99 | Torsional (and Horizontal) Vertical in high bridge | 13 | 6.69 | Vertical in high bridge |
| 14 | 6.82 | Torsional (and Horizontal) Vertical in high bridge | 14 | 6.82 | Torsional |
| 15-22 | 6.69-6.08 | Vertical in high bridge Torsion in modes 16-18 | 15-20 | 6.45-6.03 | Vertical in high bridge |
| 23-31 | 6.00-5.94 | Vertical in low bridge | 21-26 | 5.99-5.97 | Vertical in low bridge |
| 32-50 | 5.90-4.70 | Mostly vertical modes Motions in the whole bridge | 27-50 | 5.96-4.37 | Mainly vertical modes Motions in the whole bridge |

[1] Torsion mainly in floating high bridge.
[2] Torsion in floating high bridge.

# Appendix C

# Ship Collision

## C.1 Force-deformation curves

### C.1.1 Pontoon collision

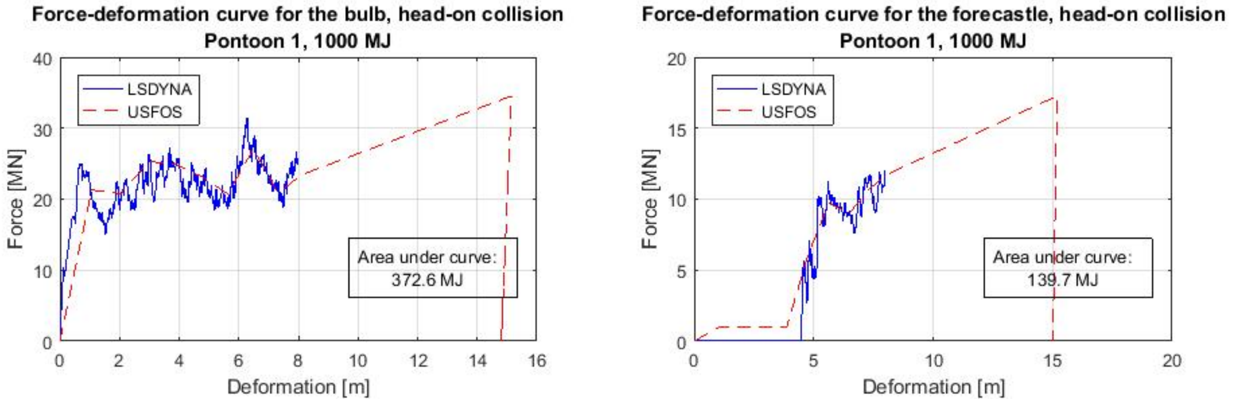

(a) Bulb

(b) Forecastle

Figure C.1: Measured force-deformation relationship in collision springs compared to curve from LSDYNA. Collision scenario 1.

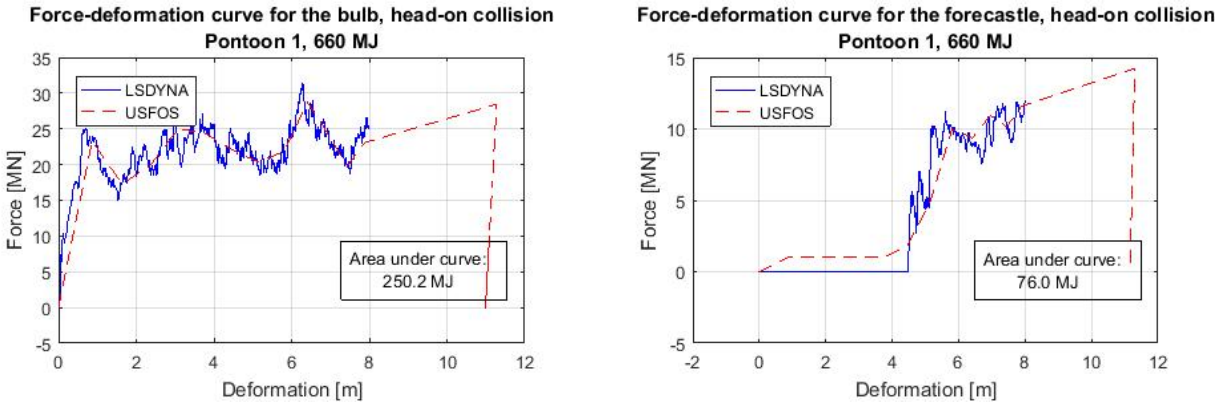

(a) Bulb (b) Forecastle

Figure C.2: Measured force-deformation relationship in collision springs compared to curve from LSDYNA. Collision scenario 2.

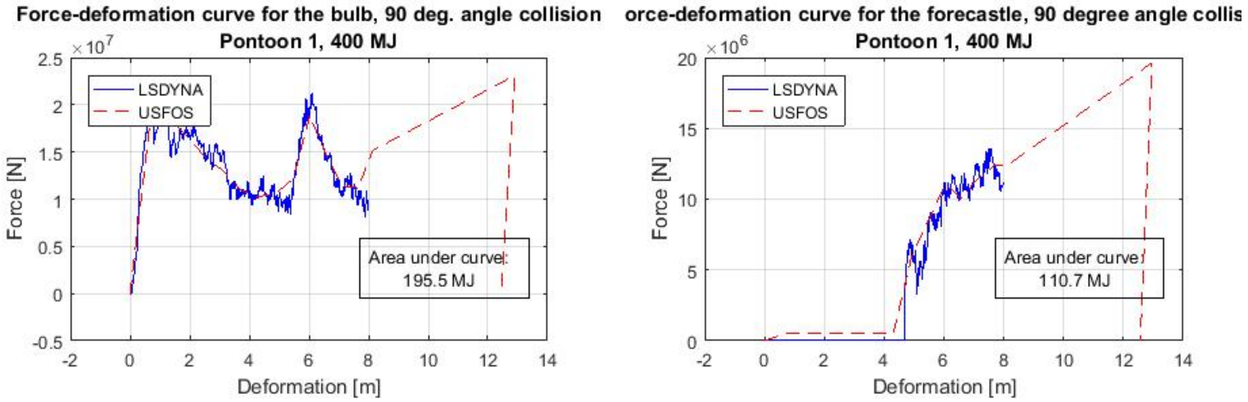

(a) Bulb (b) Forecastle

Figure C.3: Measured force-deformation relationship in collision springs compared to curve from LSDYNA. Collision scenario 3.

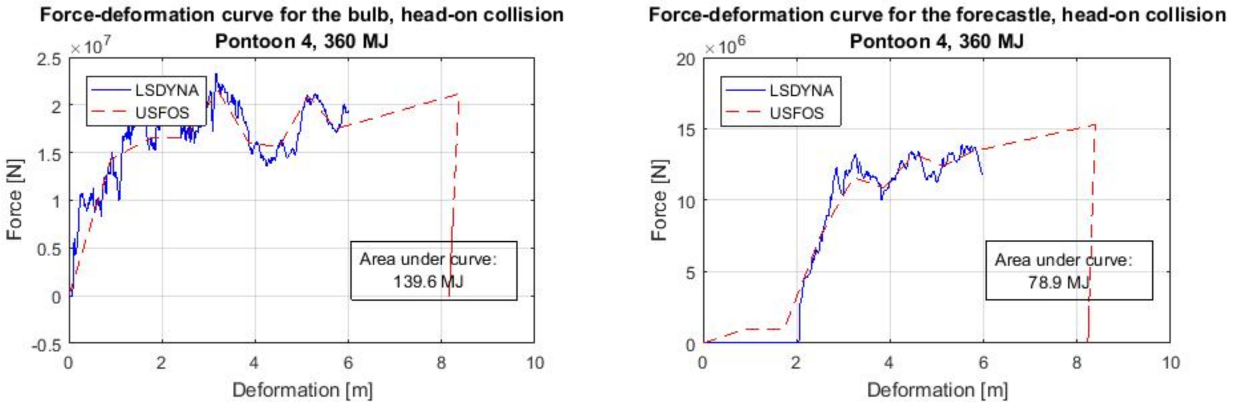

(a) Bulb

(b) Forecastle

Figure C.4: Measured force-deformation relationship in collision springs compared to curve from LSDYNA. Collision scenario 4.

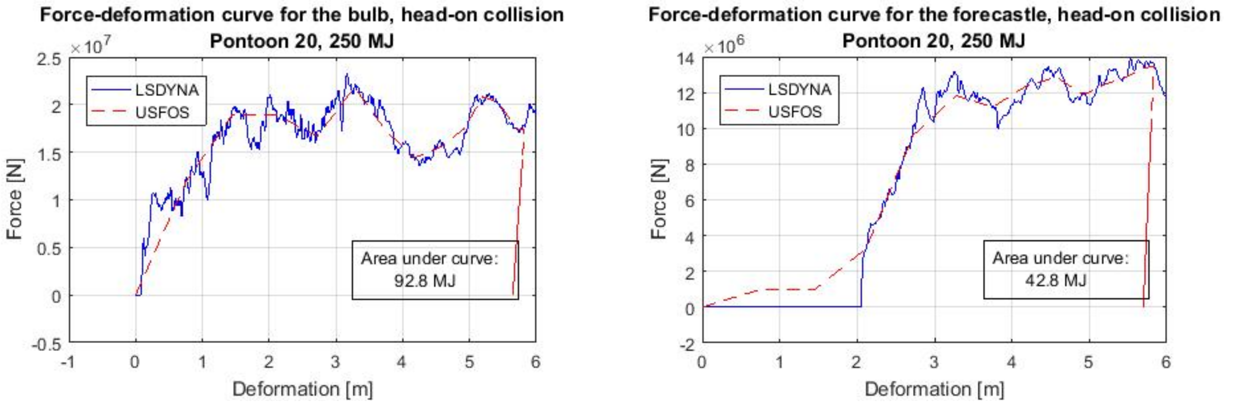

(a) Bulb

(b) Forecastle

Figure C.5: Measured force-deformation relationship in collision springs compared to curve from LSDYNA. Collision scenario 5.

### C.1.2 Pontoon collision - new pontoon design

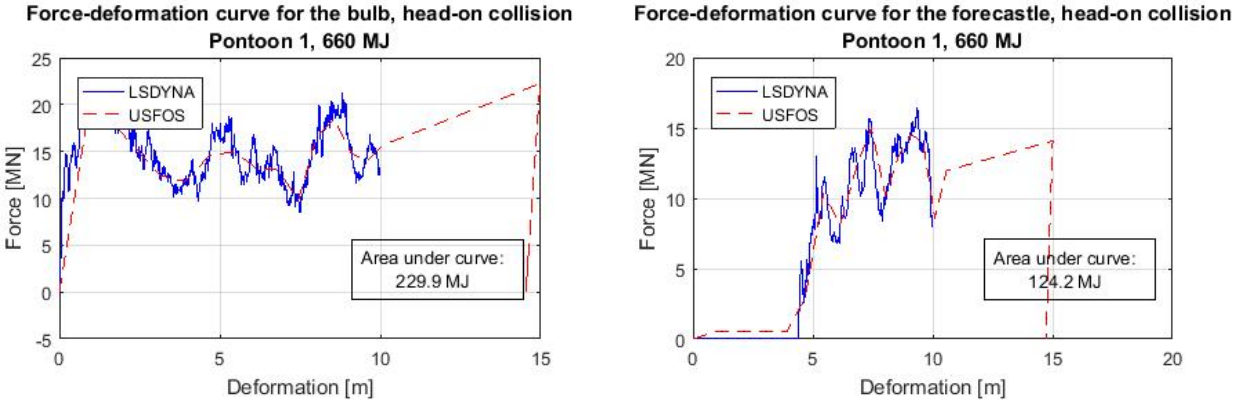

(a) Bulb

(b) Forecastle

Figure C.6: Measured force-deformation relationship in collision springs compared to curve from LSDYNA. Collision scenario 2, new pontoon design.

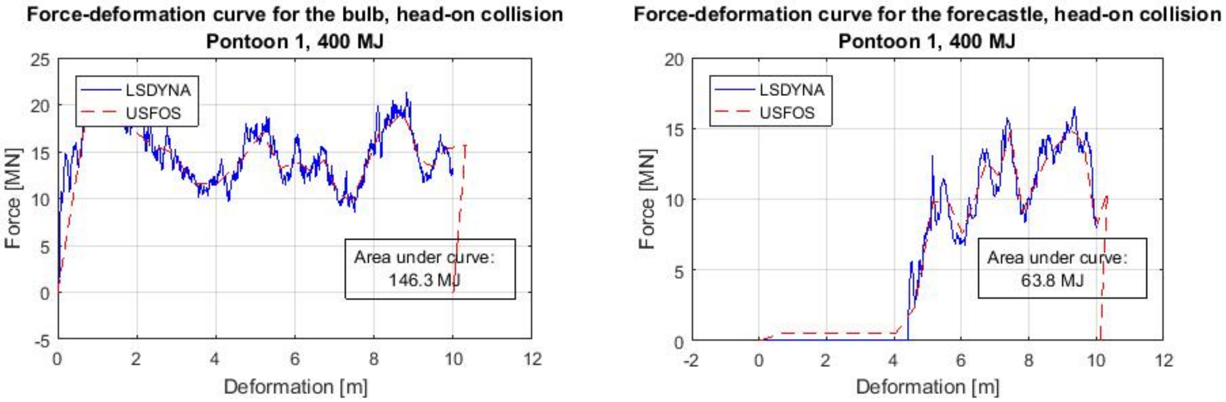

(a) Bulb

(b) Forecastle

Figure C.7: Measured force-deformation relationship in collision springs compared to curve from LSDYNA. Collision scenario 2a, new pontoon design.

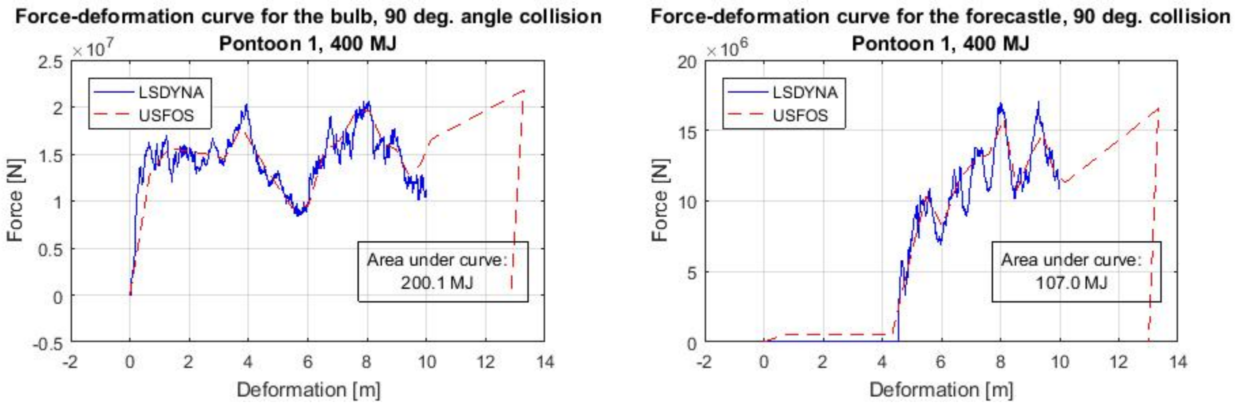

(a) Bulb

(b) Forecastle

Figure C.8: Measured force-deformation relationship in collision springs compared to curve from LSDYNA. Collision scenario 3, new pontoon design.

### C.1.3 Alternative extrapolations of the force-deformation curves for the new pontoon design

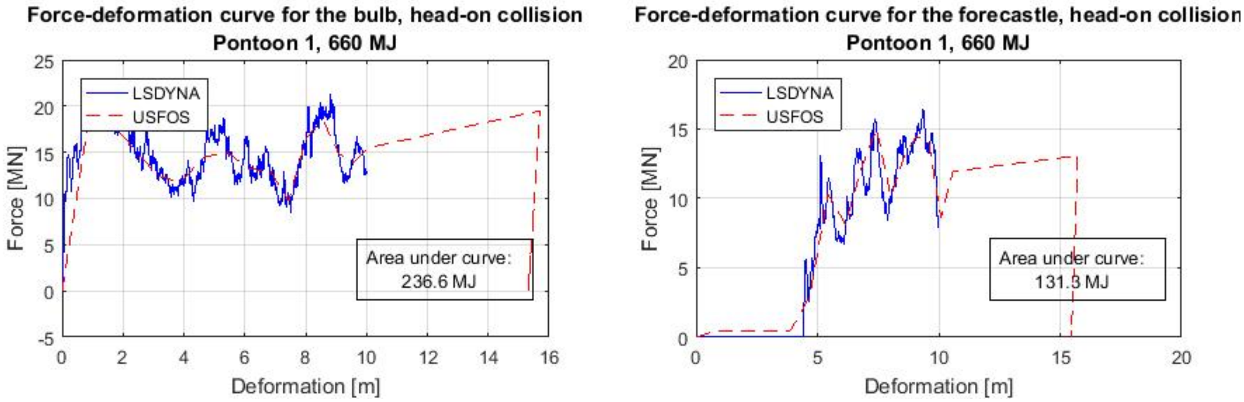

(a) Bulb

(b) Forecastle

Figure C.9: Measured force-deformation relationship in collision springs compared to curve from LSDYNA. Collision scenario 2, new pontoon design; flat extrapolation.

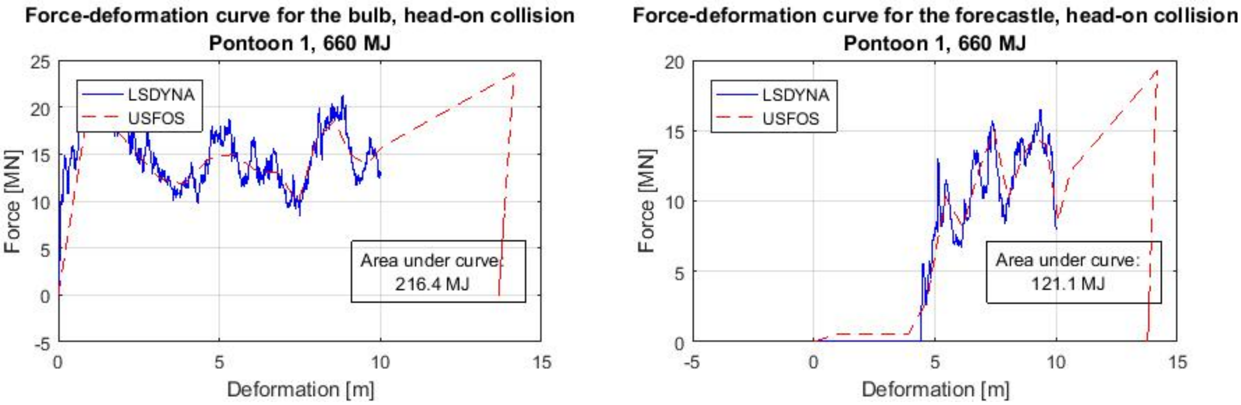

(a) Bulb

(b) Forecastle

Figure C.10: Measured force-deformation relationship in collision springs compared to curve from LSDYNA. Collision scenario 2, new pontoon design; steep extrapolation.

### C.1.4 Girder collision

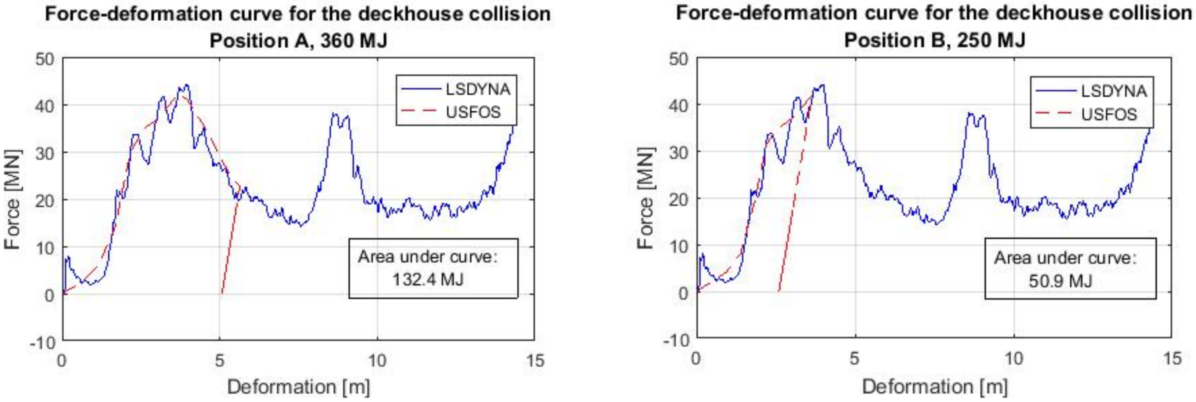

(a) Location A, collision energy 360 $MJ$

(b) Location B, 250 $MJ$

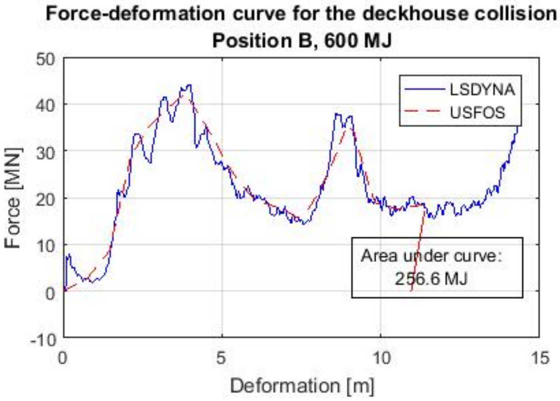

(c) Location B, 600 $MJ$

Figure C.11: Force-deformation curves for the collisions between deckhouse and girder.

## C.2 Force history plots

### C.2.1 Pontoon collision

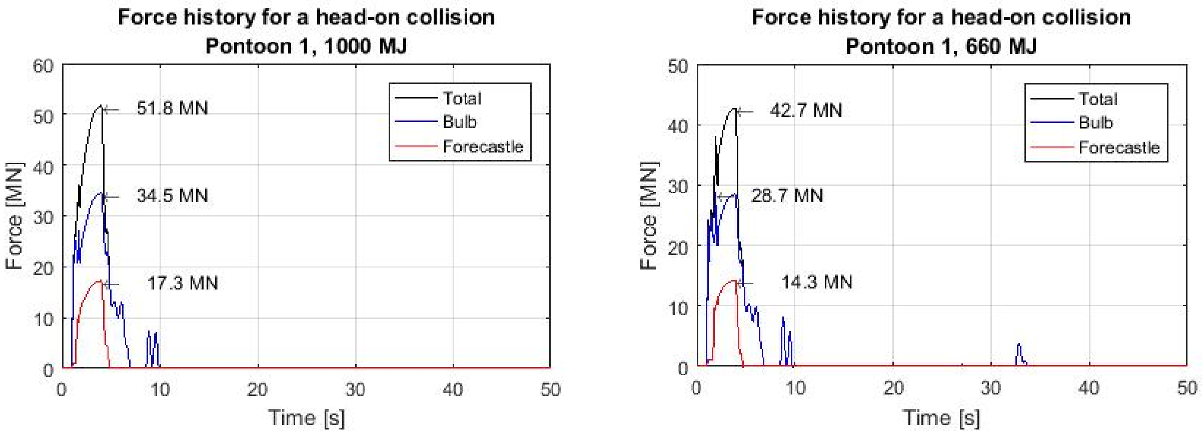

(a) Collision scenario 1

(b) Collision scenario 2

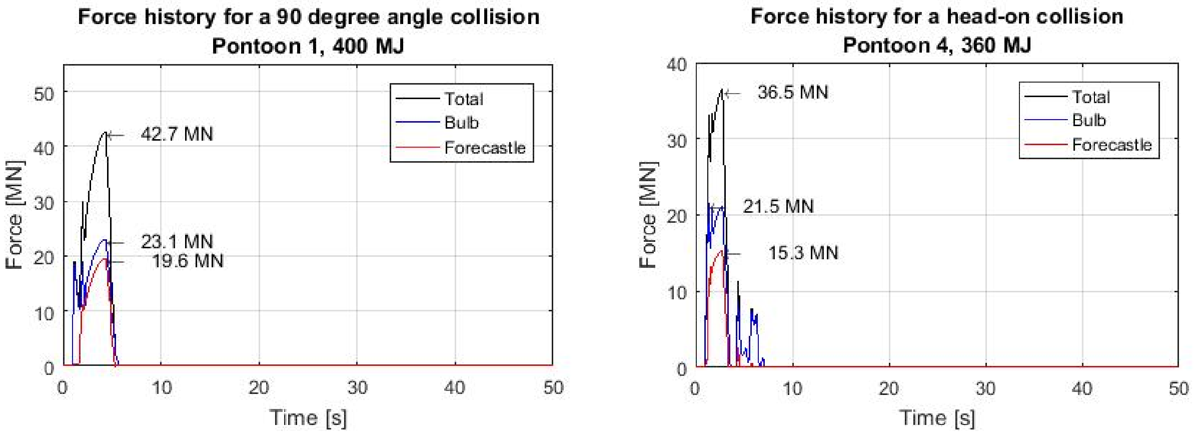

(c) Collision scenario 3

(d) Collision scenario 4

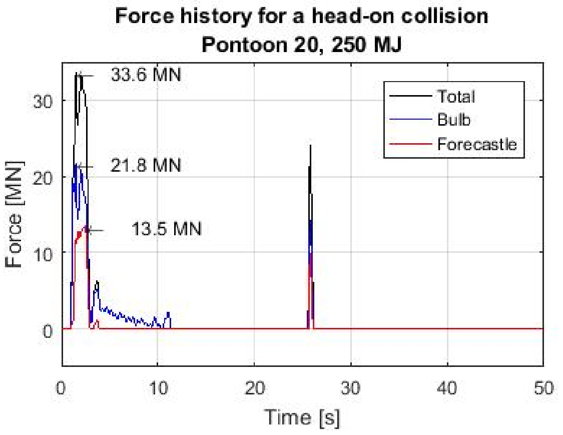

(e) Collision scenario 5

Figure C.12: Force histories for the collision springs in USFOS analyses. Pontoon collisions.

### C.2.2 Pontoon collision - new pontoon design

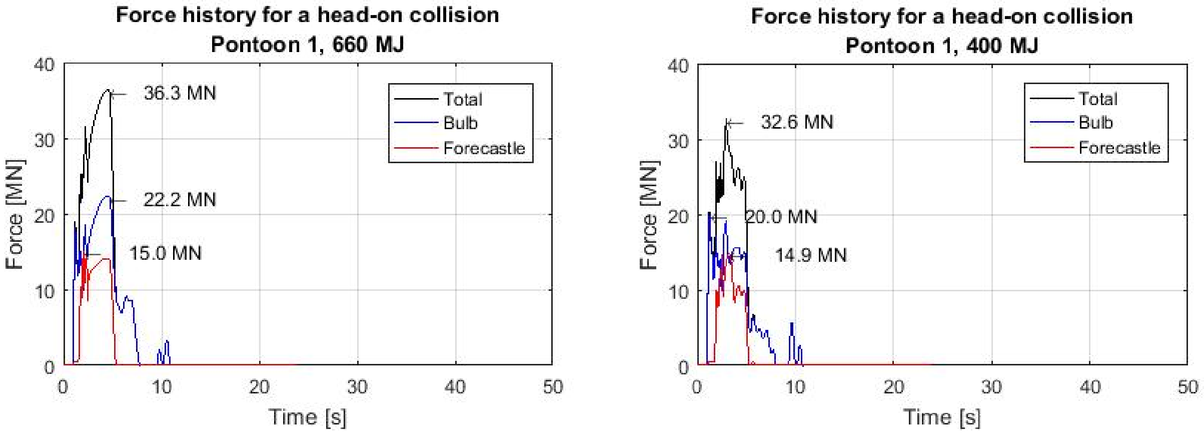

(a) Collision scenario 2

(b) Collision scenario 2a

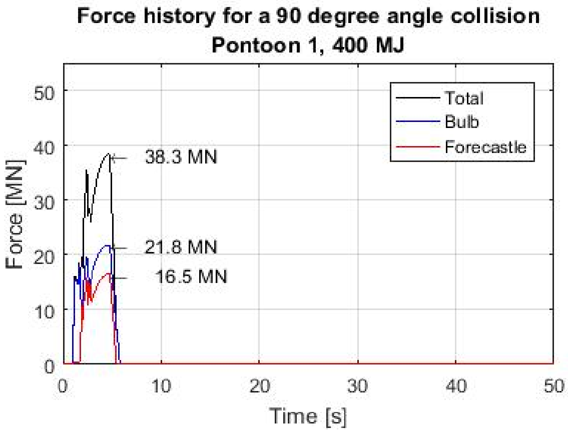

(c) Collision scenario 3

Figure C.13: Force histories for the collision springs obtained with USFOS analyses. Pontoon collisions with the new pontoon design.

### C.2.3 Girder collision

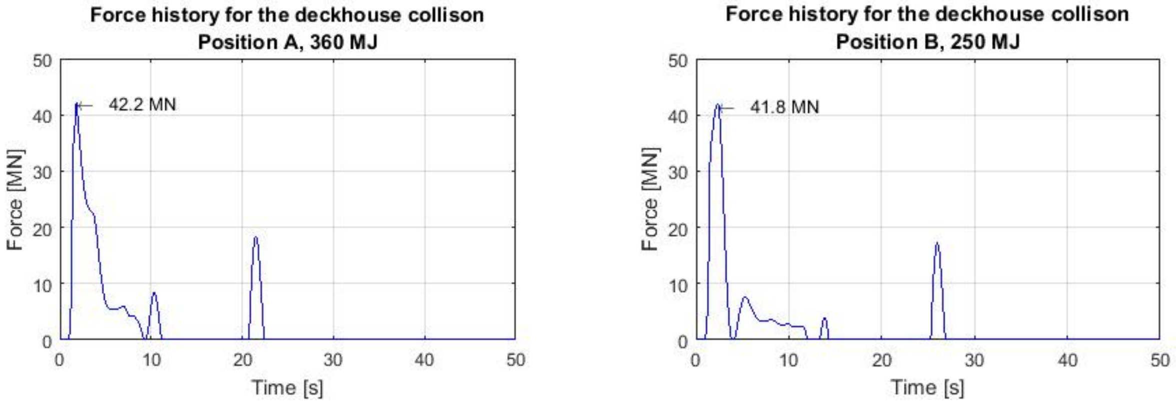

(a) Location A, collision energy 250 $MJ$

(b) Location B, 360 $MJ$

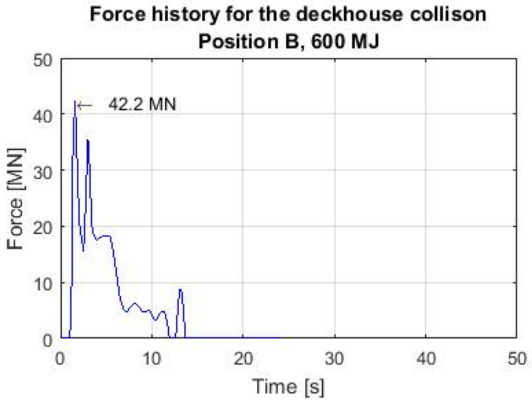

(c) Location B, 600 $MJ$

Figure C.14: Force histories for the collision springs obtained with USFOS analyses. Girder collisions.

## C.3 Bending waves in the floating high bridge

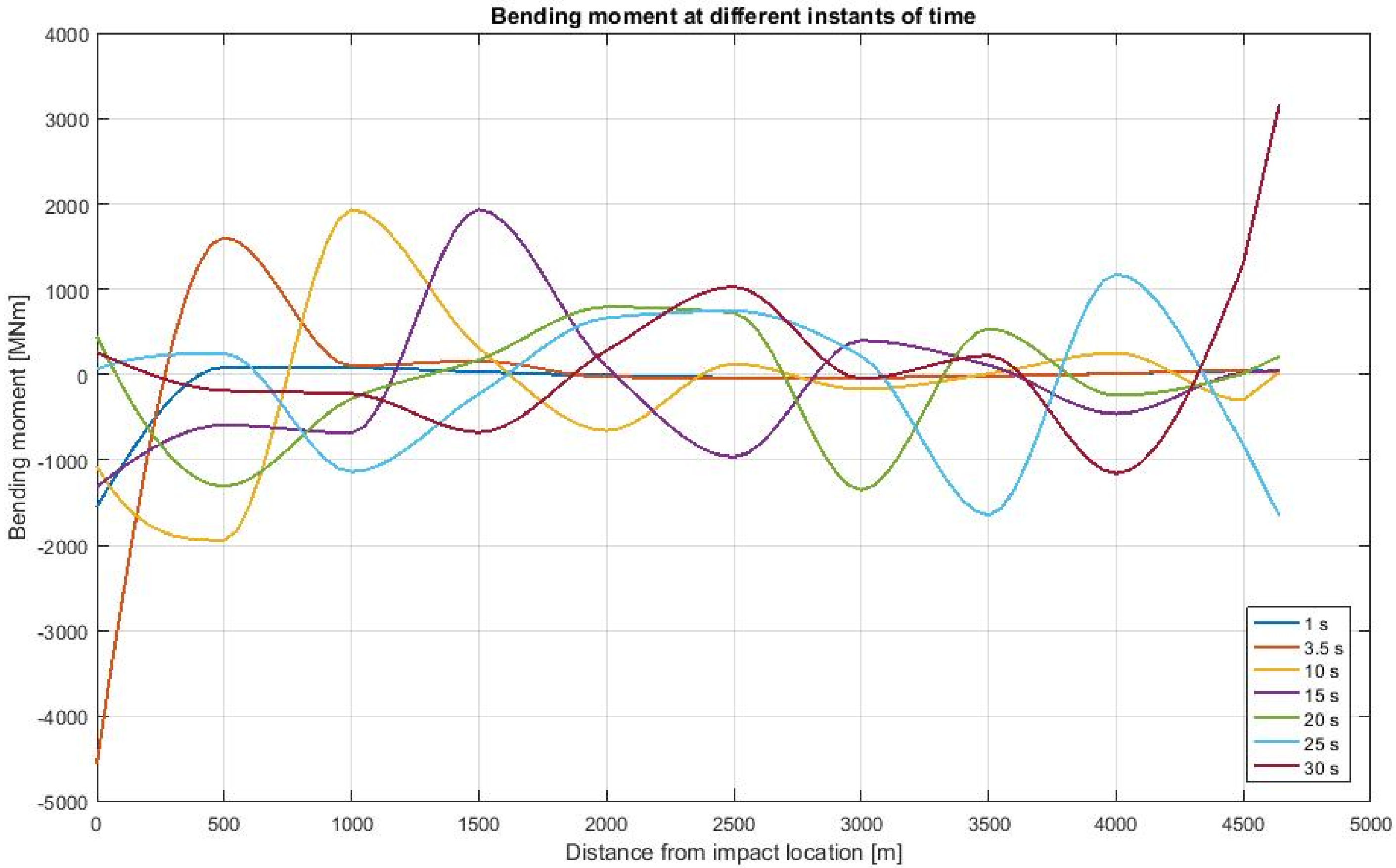

Figure C.15: Bending moment in the bridge girder at the north side of the impact point, time interval 1. Collision scenario 1, structural damping included.

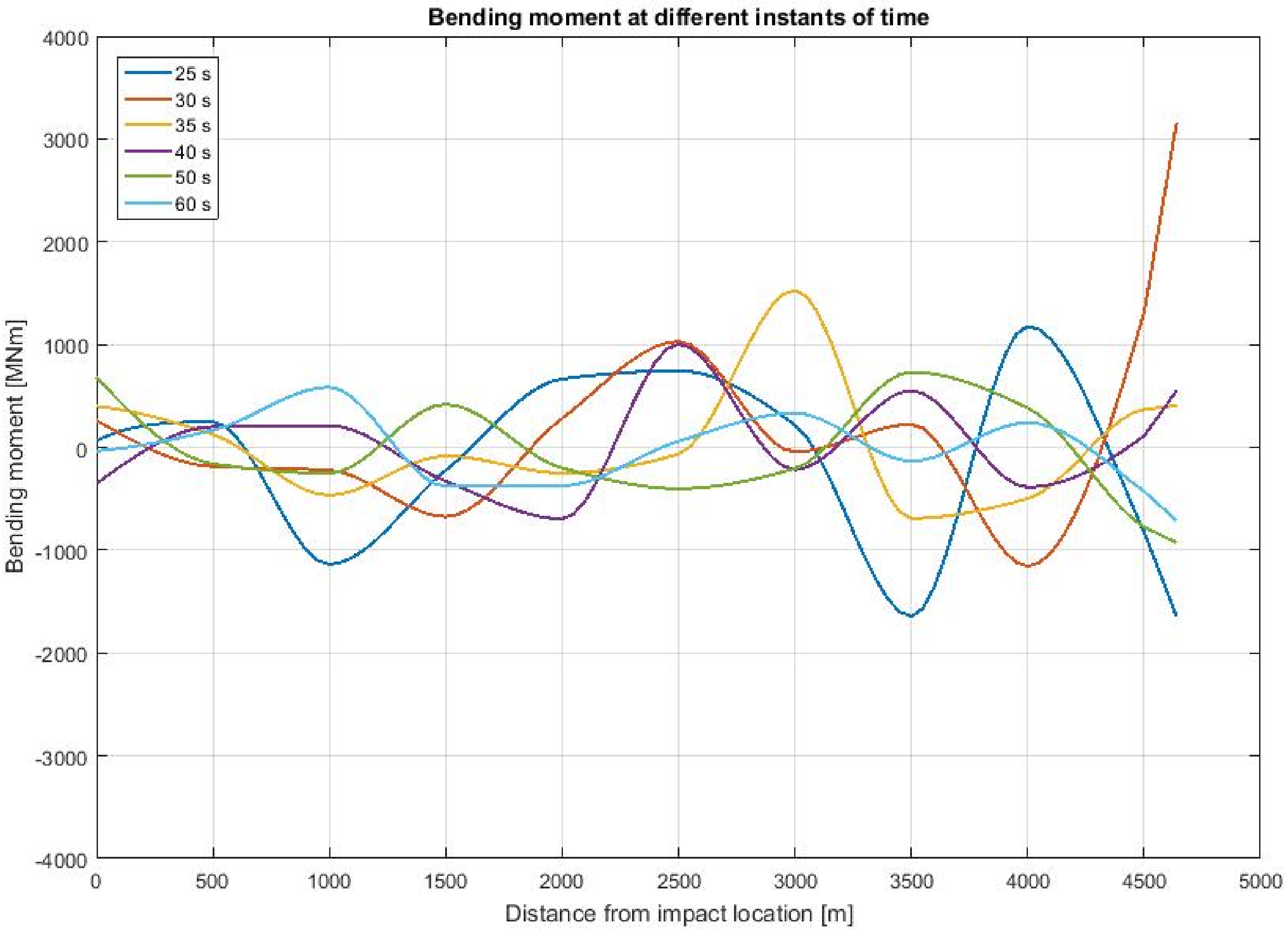

Figure C.16: Bending moment in the bridge girder at the north side of the impact point, time interval 2. Collision scenario 1, structural damping included.

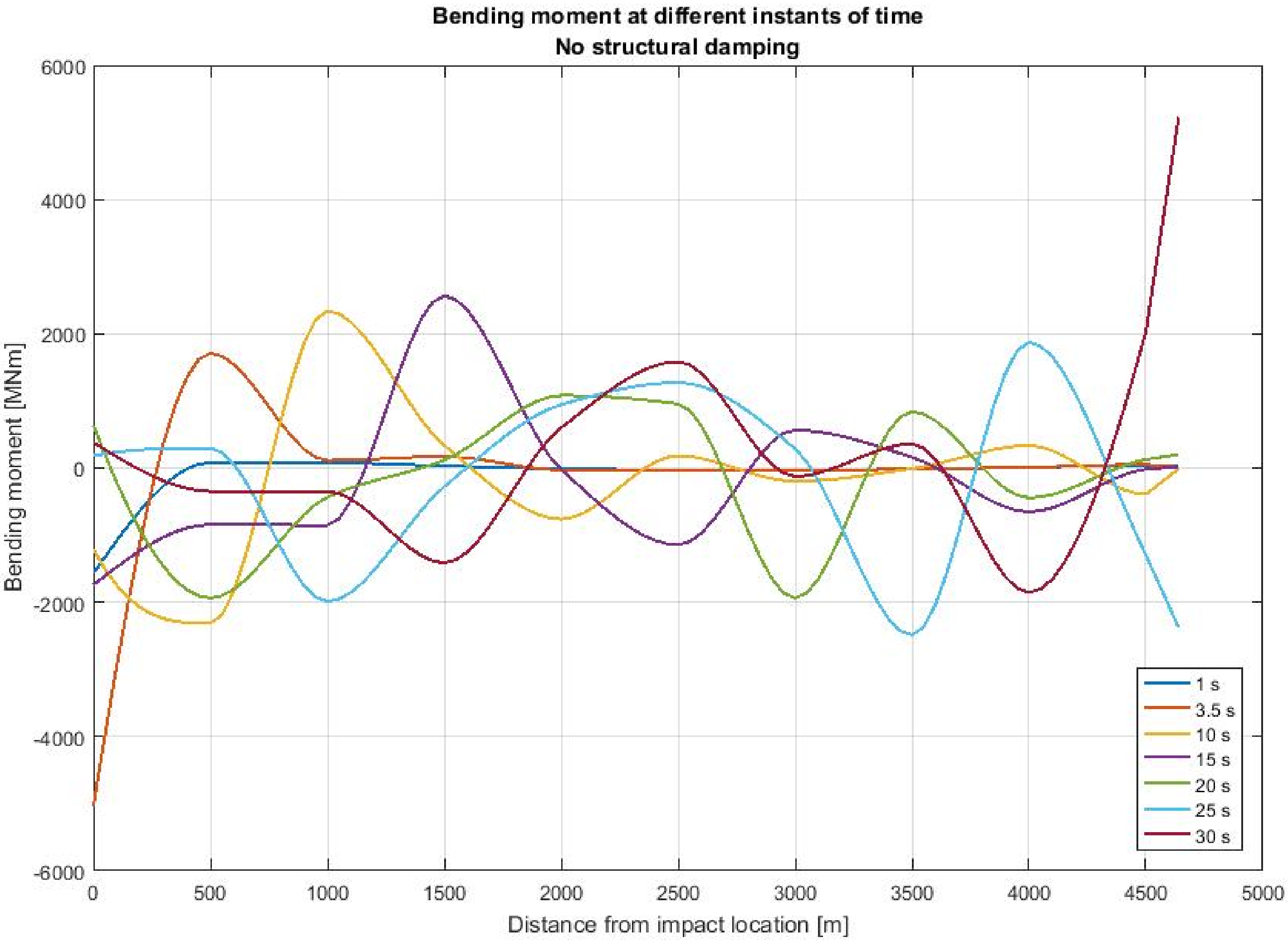

Figure C.17: Bending moment in the bridge girder at the north side of the impact point. Collision scenario 1, structural damping NOT included.

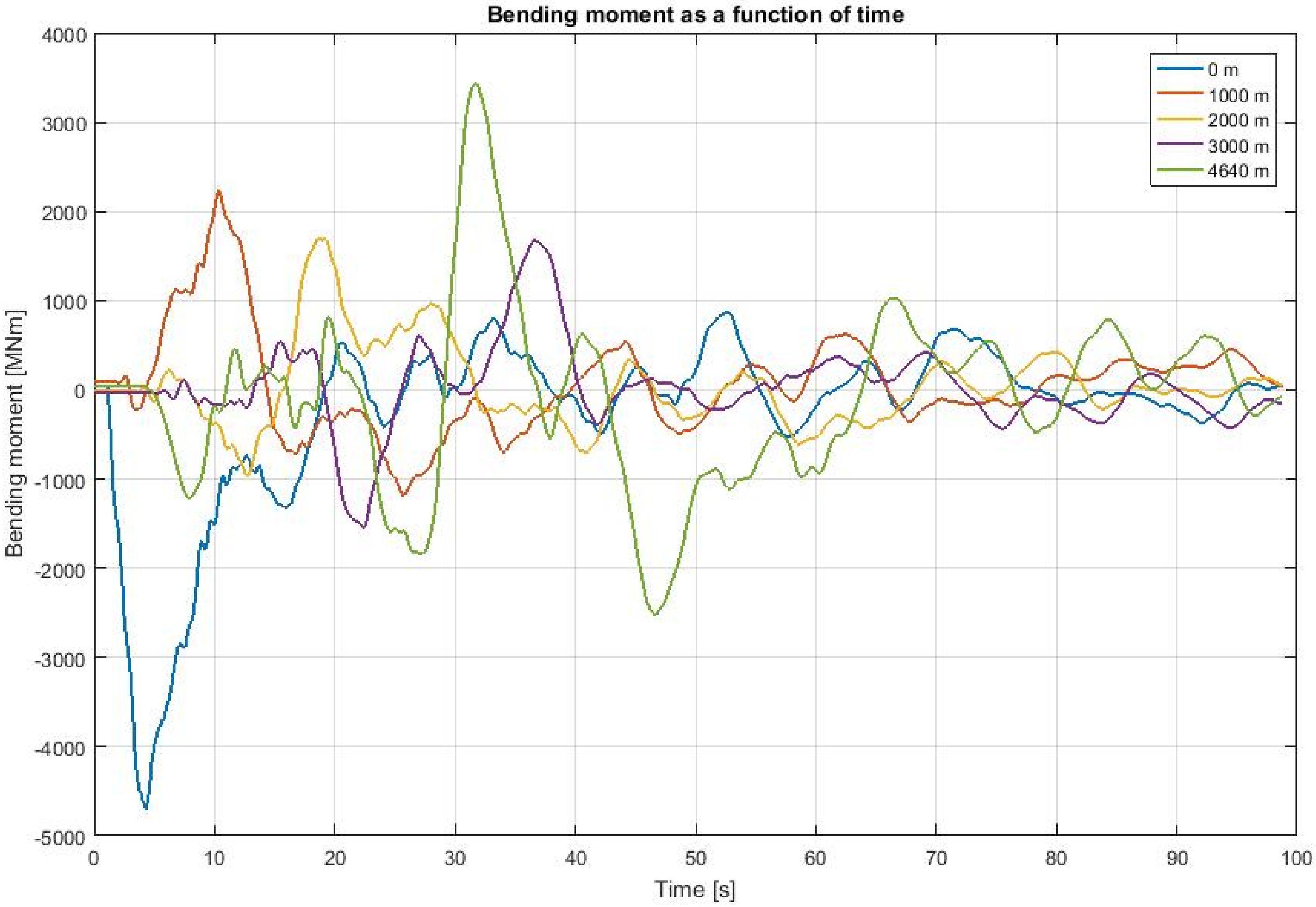

Figure C.18: Bending moment about the strong axis of the bridge girder, given as a function of time at a selection of locations. Position given by distance from the struck pontoon.

# Appendix D

# Wave Loads on Pontoons

## D.1 Comparison of linear transfer functions obtained with different mesh sizes

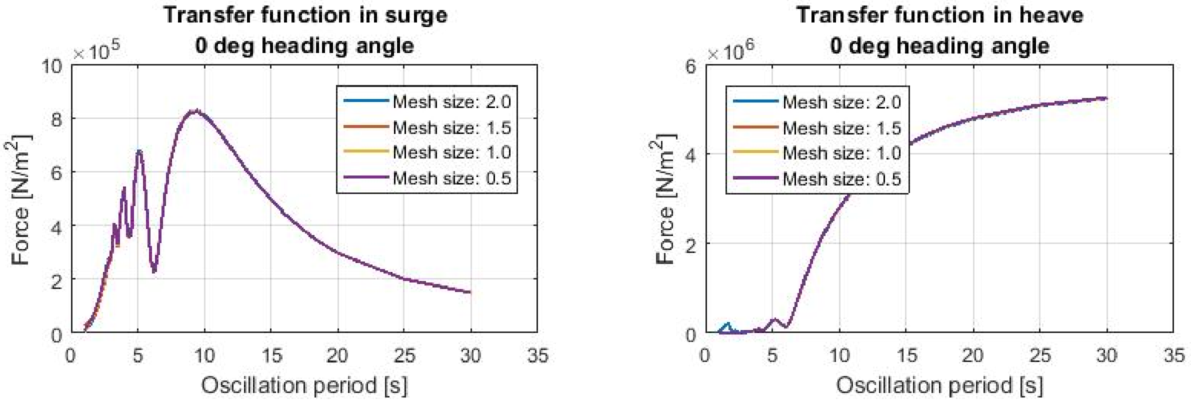

(a) Surge (b) Heave

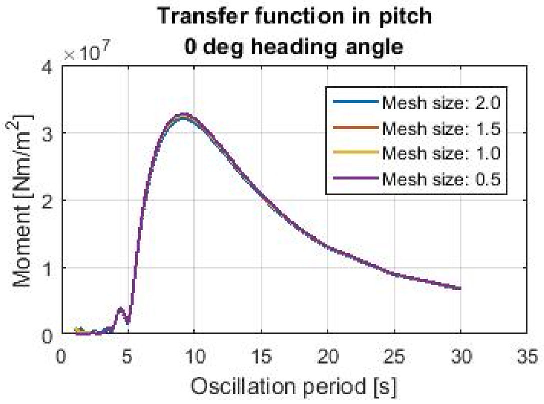

(c) Pitch

Figure D.1: Non-zero transfer functions for a head-on wave with four different mesh sizes, pontoon type 4.

## D.2 Linear transfer functions for a selection of heading angles

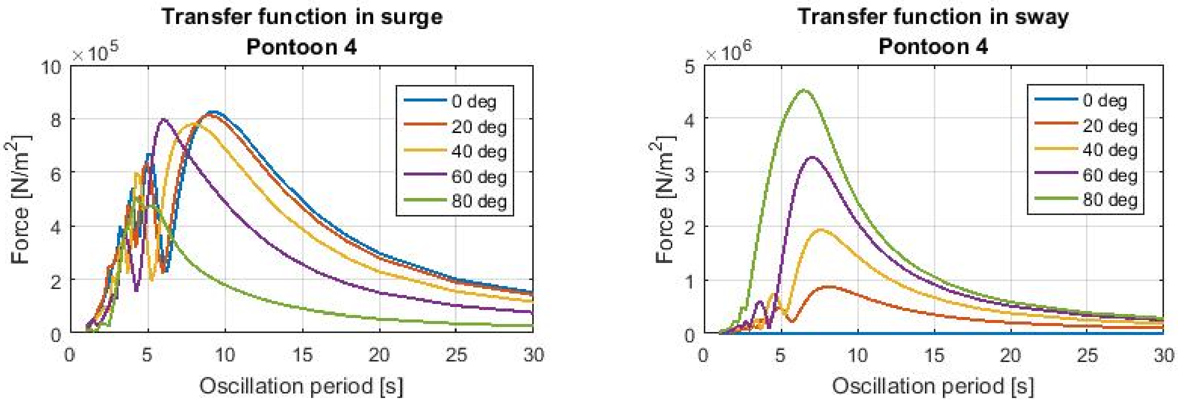
Transfer function in surge Pontoon 4

Transfer function in sway Pontoon 4

(a) Surge

(b) Sway

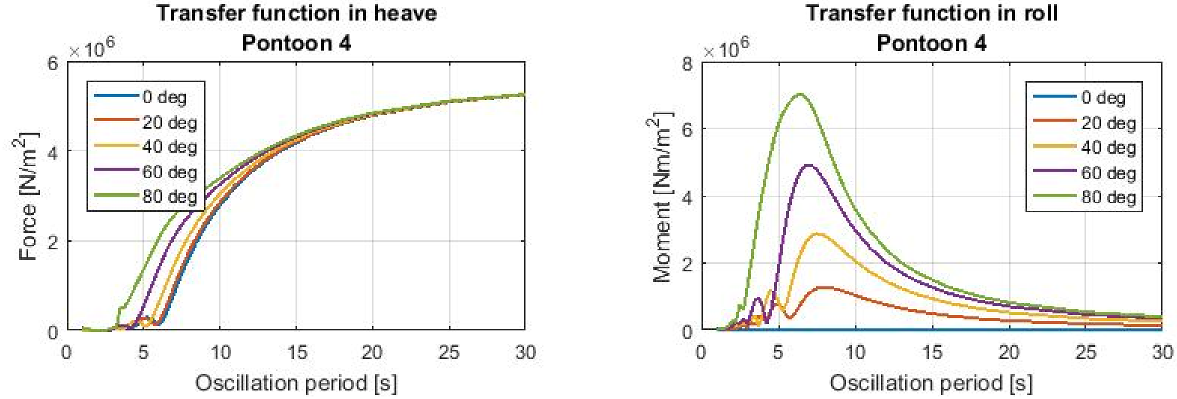
Transfer function in heave Pontoon 4

Transfer function in roll Pontoon 4

(c) Heave

(d) Roll

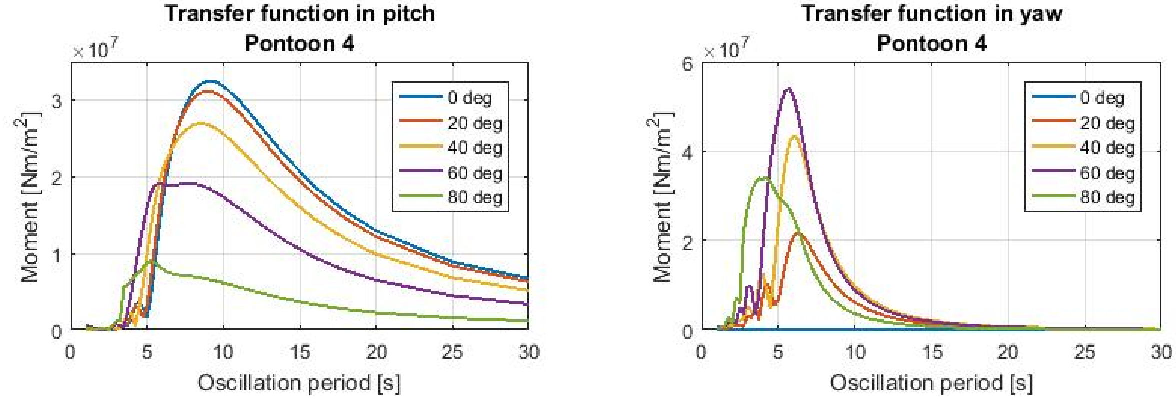
Transfer function in pitch Pontoon 4

Transfer function in yaw Pontoon 4

(e) Pitch

(f) Yaw

Figure D.2: Transfer functions for pontoon 4 for a selection of heading angles.

## D.3 Mean drift coefficients

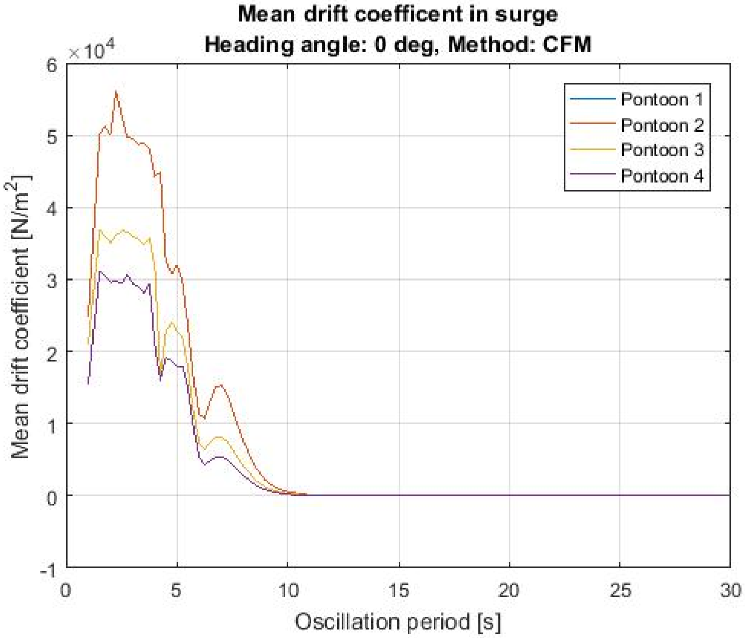

(a) Mean drift coefficient in surge obtained by conservation of fluid momentum in WADAM. Angle of incident wave: 0°

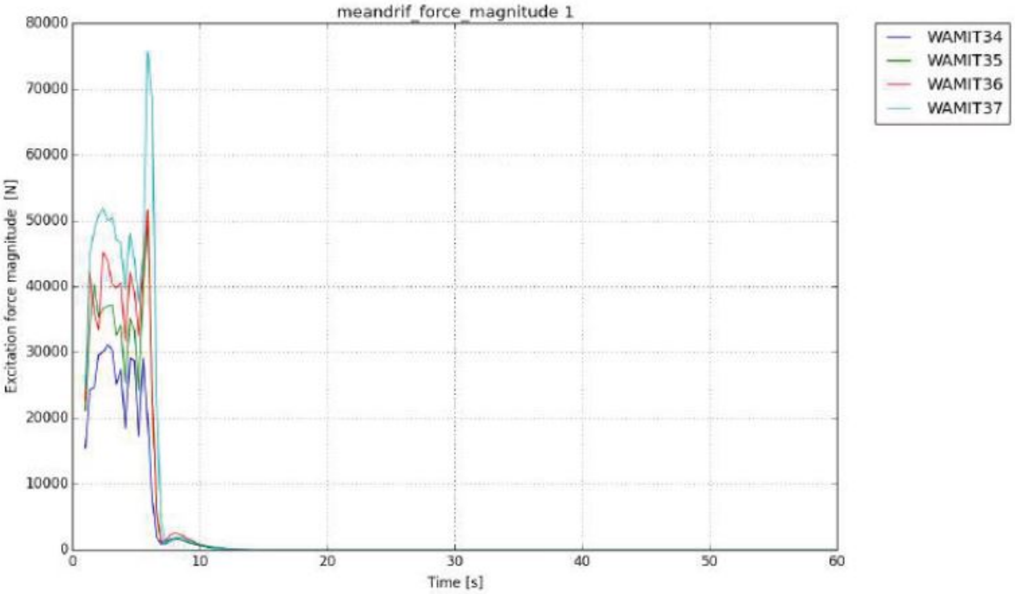

(b) Mean drift coefficient in surge obtained by Norconsult in WADAM, from: (Norconsult AS, 2017b). Angle of incident wave: 0°

Figure D.3: Mean drift coefficient in surge compared to coefficient obtained by Norconsult. Angle is relative to the longitudinal axis of the pontoon.

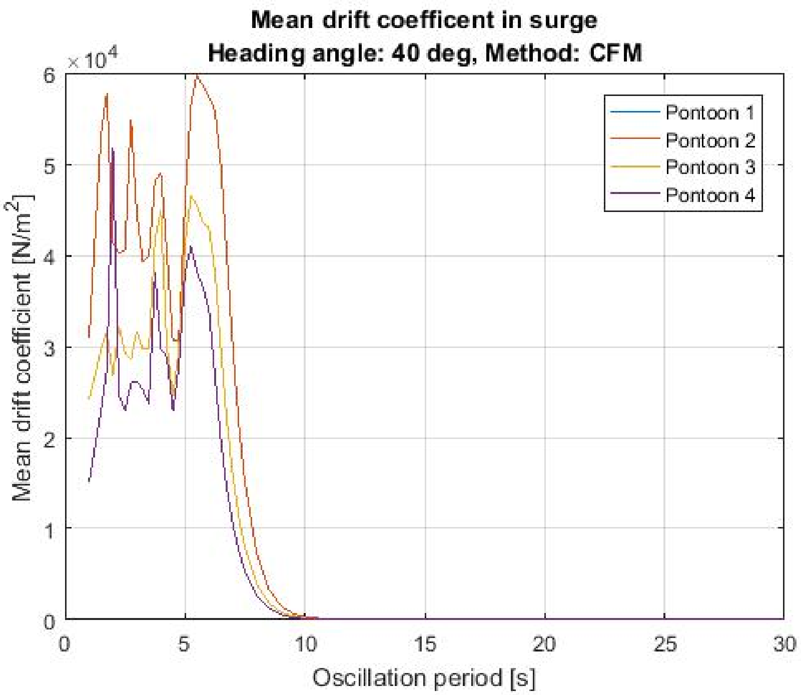

(a) Mean drift coefficient in surge obtained by conservation of fluid momentum in WADAM. Angle of incident wave: 40°

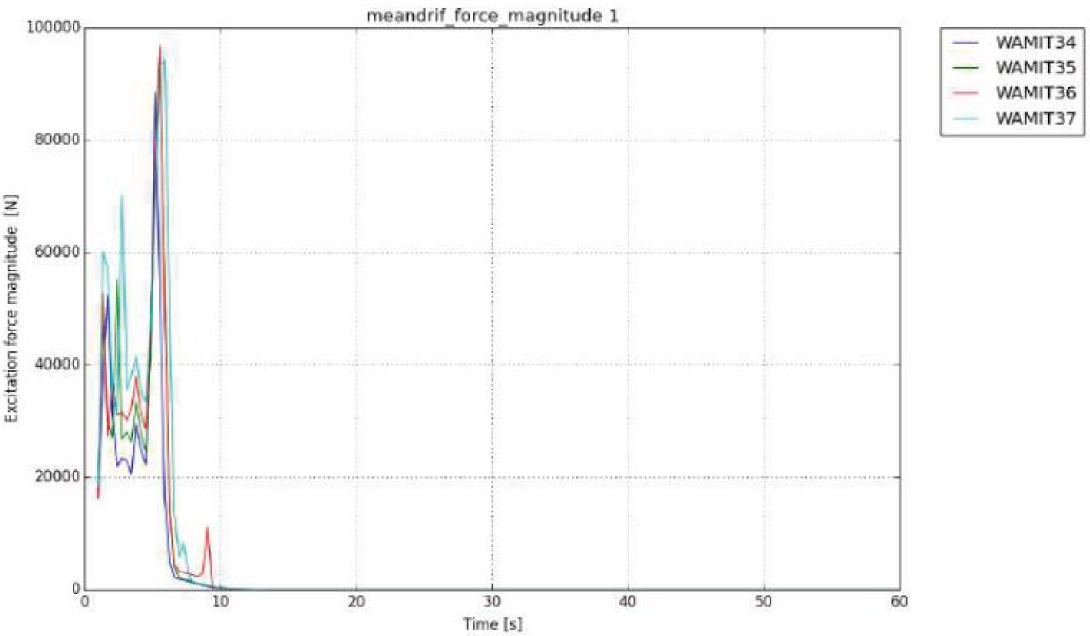

(b) Mean drift coefficient in surge obtained by Norconsult in WADAM, from:(Norconsult AS, 2017b). Angle of incident wave: 45°

Figure D.4: Mean drift coefficient in surge compared to coefficient obtained by Norconsult. Angle is relative to the longitudinal axis of the pontoon.

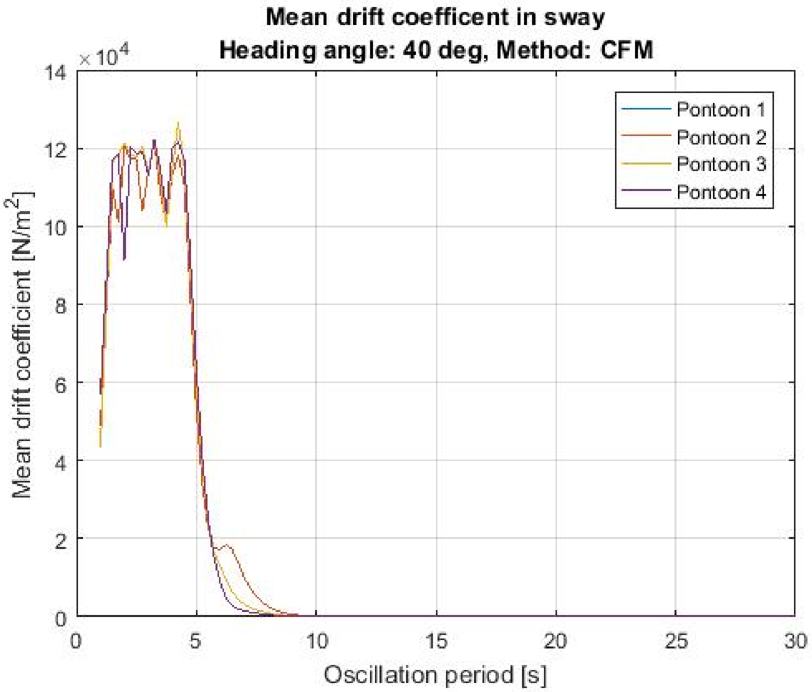

(a) Mean drift coefficient in sway obtained by conservation of fluid momentum in WADAM. Angle of incident wave: 40°

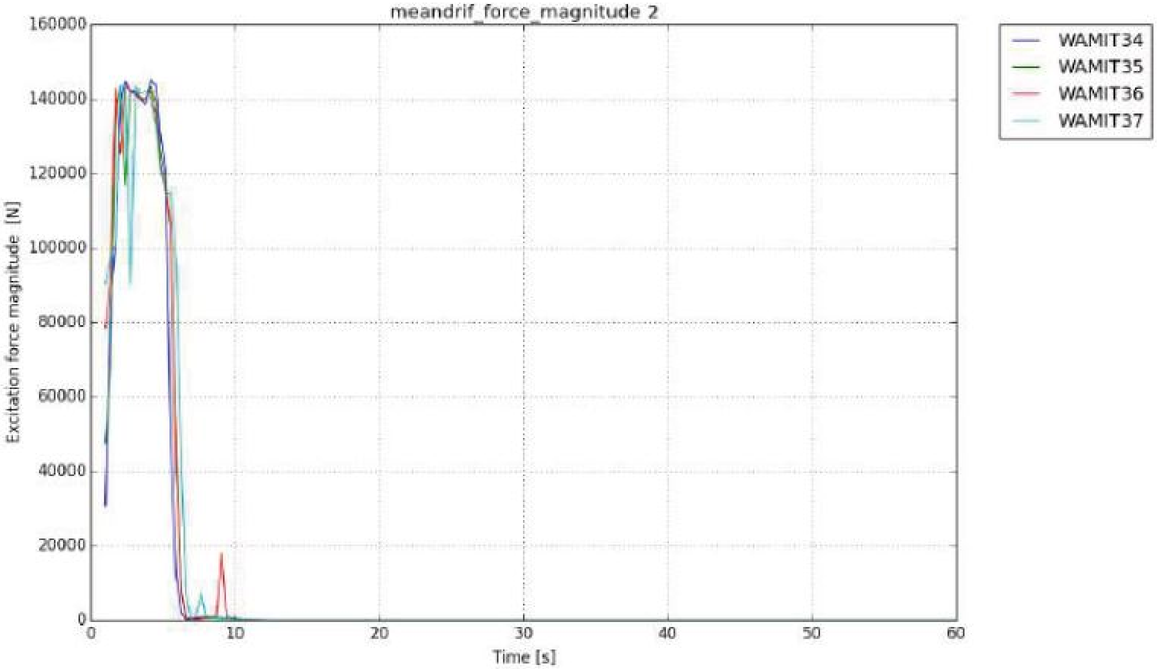

(b) Mean drift coefficient in sway obtained by Norconsult in WADAM, from: (Norconsult AS, 2017b). Angle of incident wave: 45°

Figure D.5: Mean drift coefficient in sway compared to coefficient obtained by Norconsult. Angle is relative to the longitudinal axis of the pontoon.

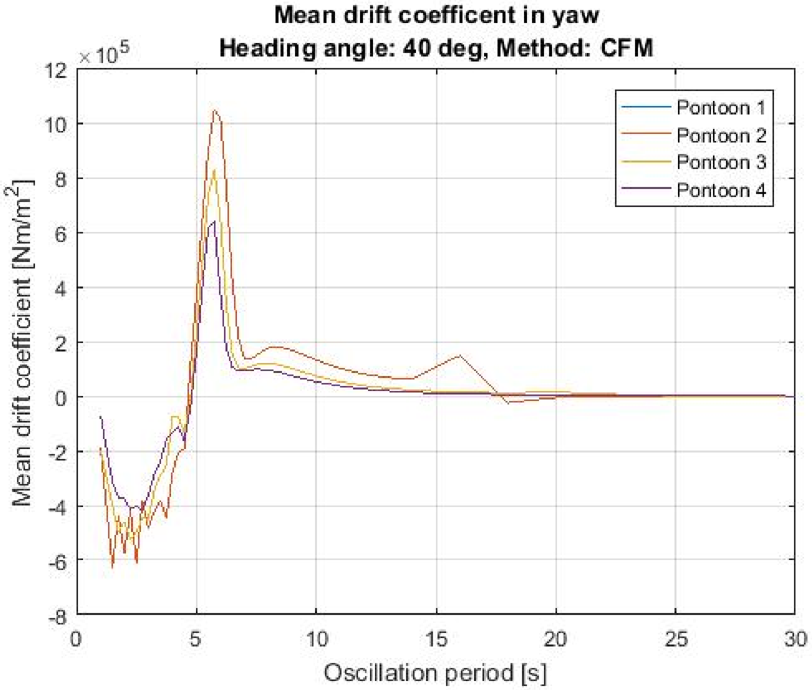

(a) Mean drift coefficient in yaw obtained by conservation of fluid momentum in WADAM. Angle of incident wave: 40°

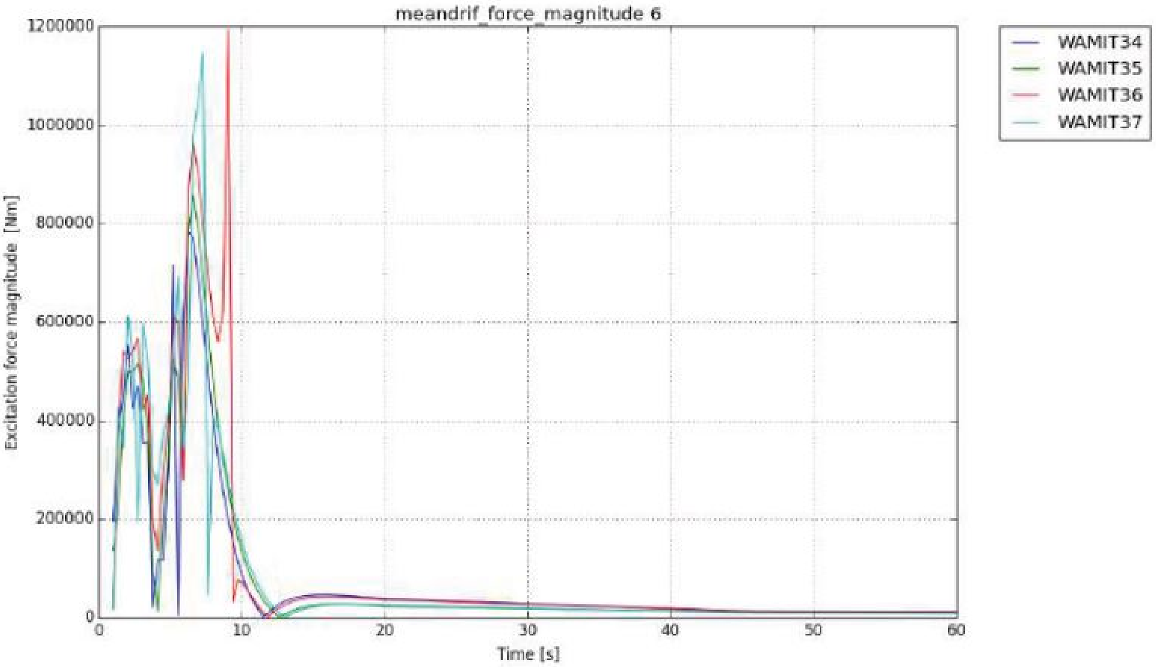

(b) Mean drift coefficient in yaw obtained by Norconsult in WADAM, from: (Norconsult AS, 2017b). Angle of incident wave: 45°

Figure D.6: Mean drift coefficient in yaw compared to coefficient obtained by Norconsult. Angle is relative to the longitudinal axis of the pontoon.

## D.4 Force spectra

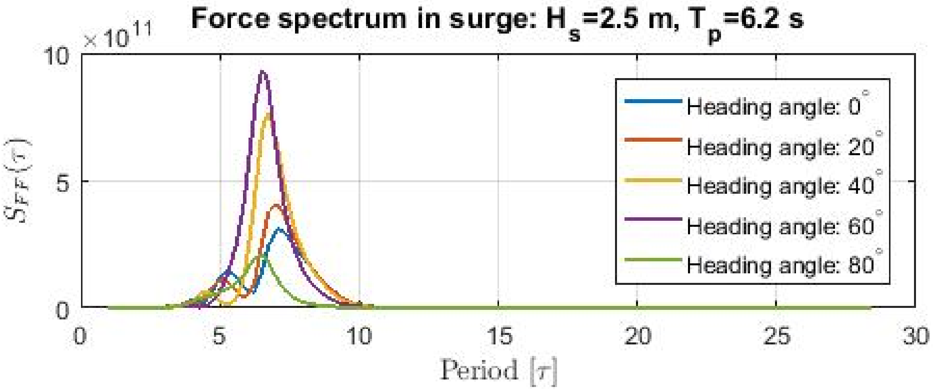

(a) Surge

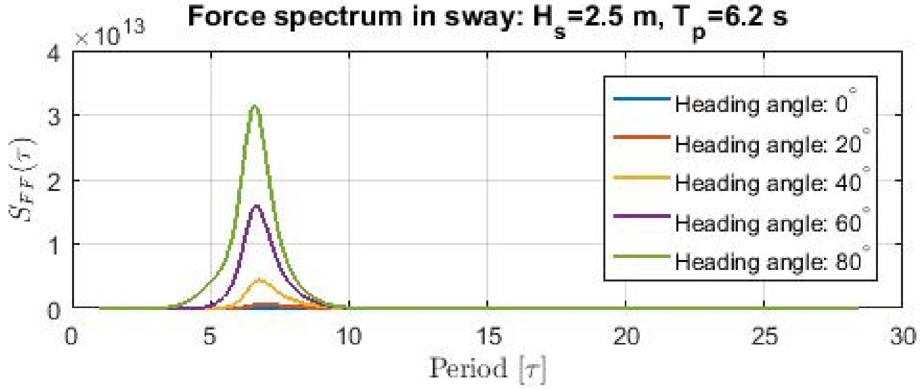

(b) Sway

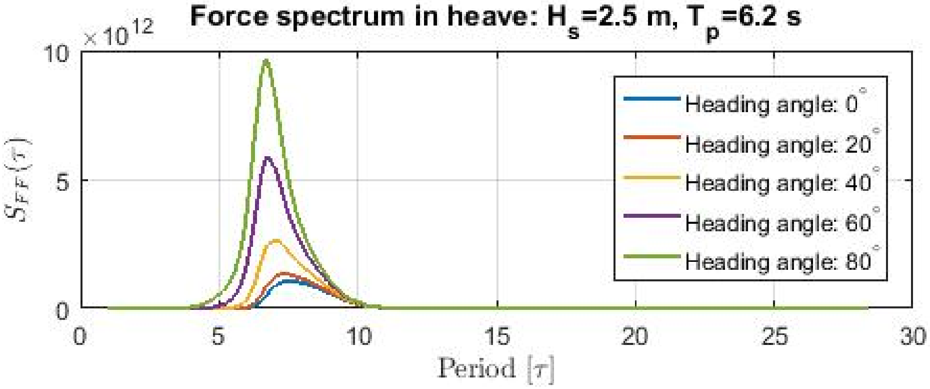

(c) Heave

Figure D.7: Force spectrum for pontoon type 4, force 1, 2 and 3. Motion according to the pontoon's local coordinate system. Heading angle relative to pontoon longitudinal axis.

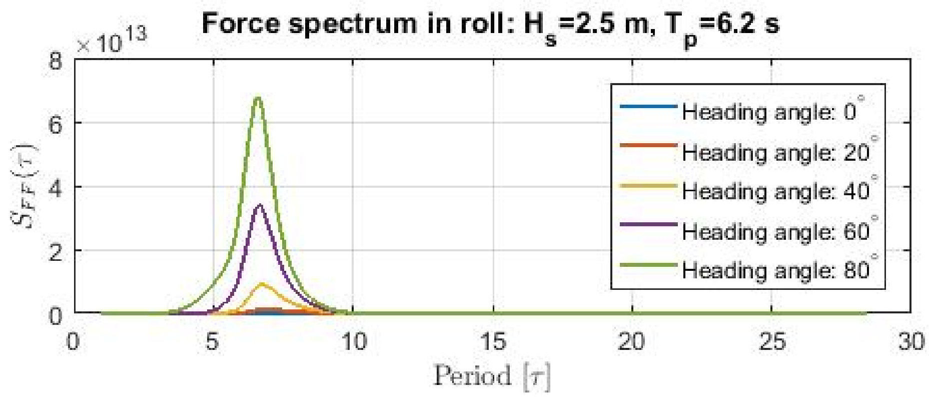

(a) Roll

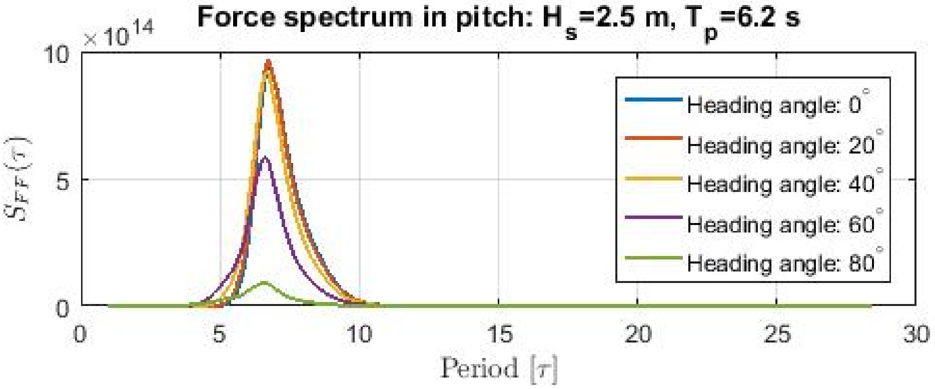

(b) Pitch

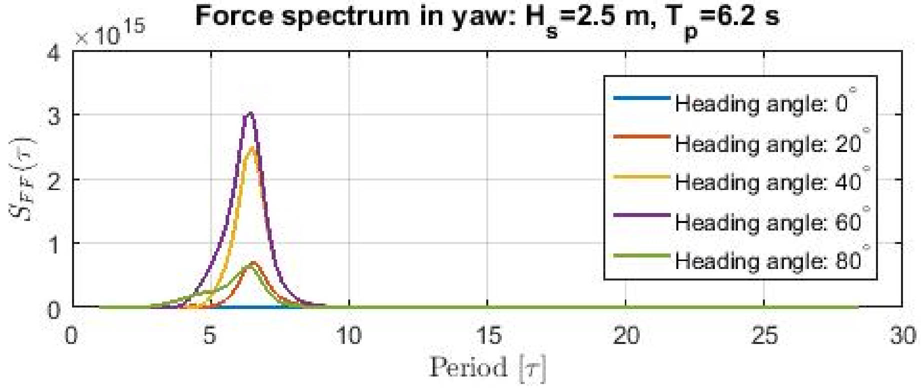

(c) Yaw

Figure D.8: Force spectrum for pontoon type 4, force 4, 5 and 6. Motion according to the pontoon's local coordinate system. Heading angle relative to pontoon longitudinal axis.

# Appendix E

# Example of Wave Forces on a Single Pontoon

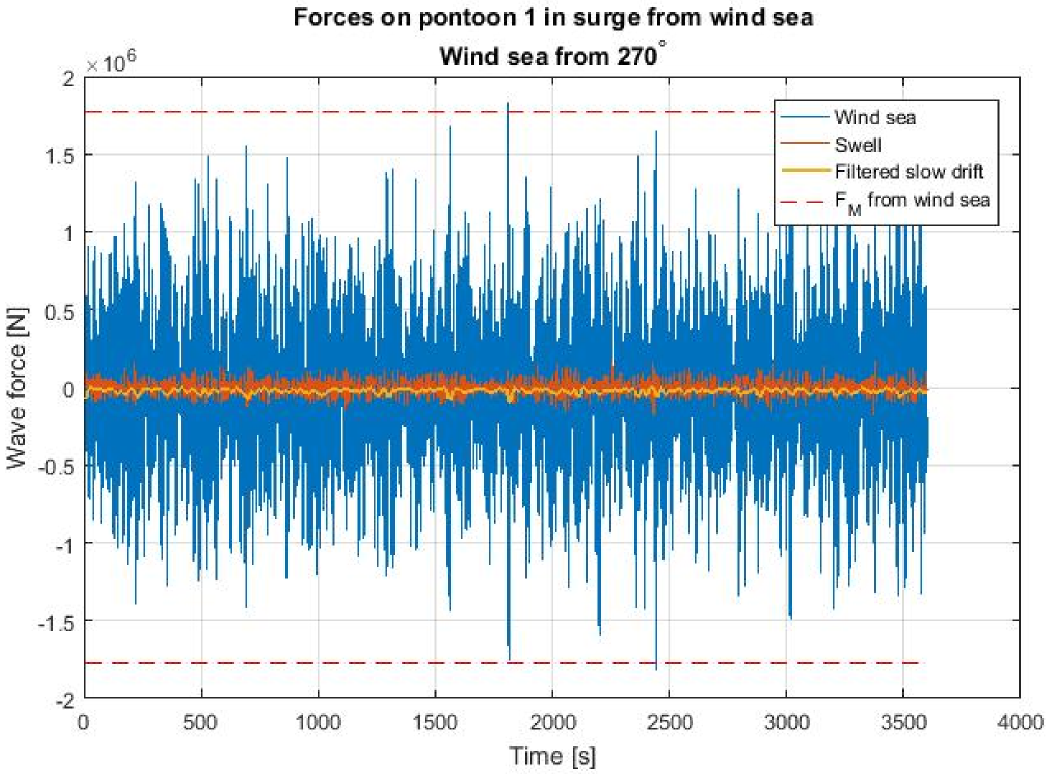

Figure E.1: Example of wave force in 100-year sea state with wind sea from 270° and swell from 330°. Direction of incoming waves defined in figure 7.1. Force history in local surge for pontoon 1. Characteristic 1-hour wave load from wind sea indicated by dashed line.

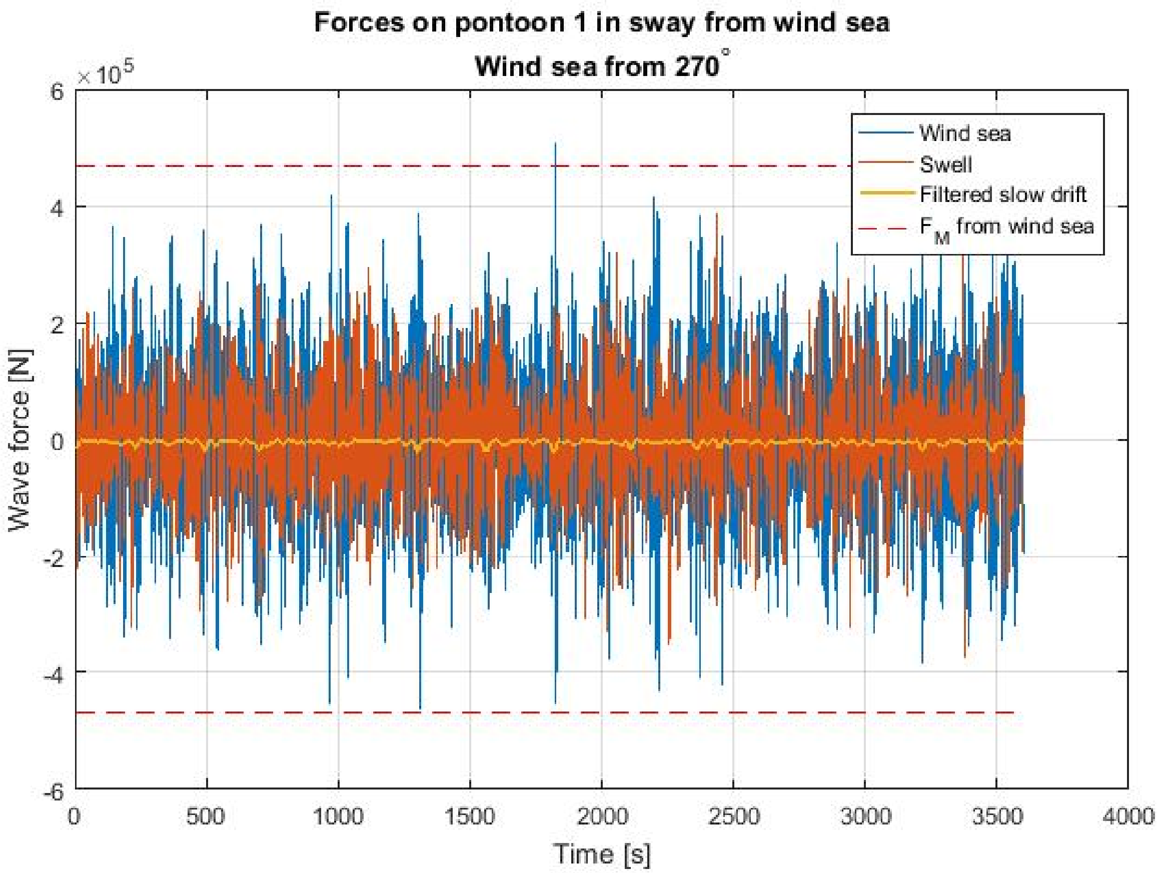

Figure E.2: Example of wave force in 100-year sea state with wind sea from 270° and swell from 330°. Direction of incoming waves defined in figure 7.1. Force history in sway for pontoon 1. Characteristic 1-hour wave load from wind sea indicated by dashed line.

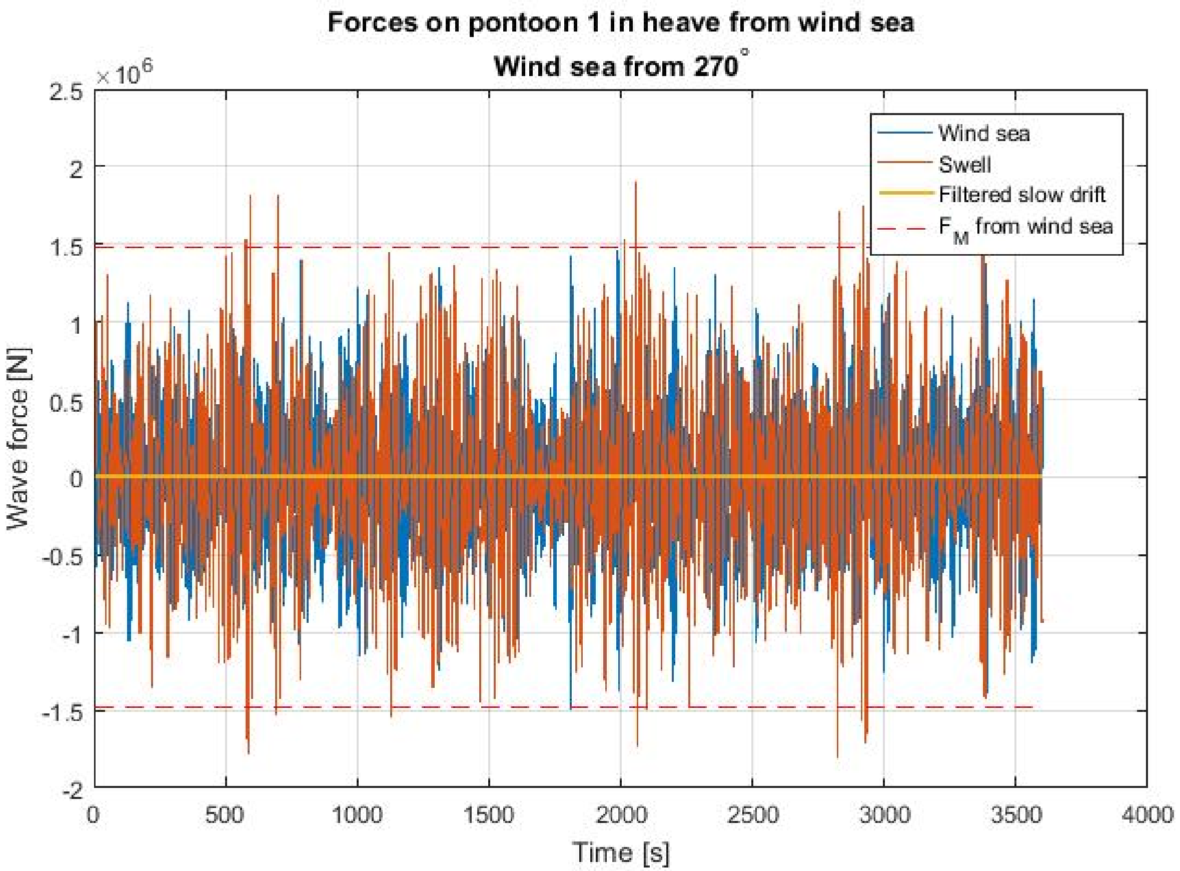

Figure E.3: Example of wave force in 100-year sea state with wind sea from 270° and swell from 330°. Direction of incoming waves defined in figure 7.1. Force history in local heave for pontoon 1. Characteristic 1-hour wave load from wind sea indicated by dashed line.

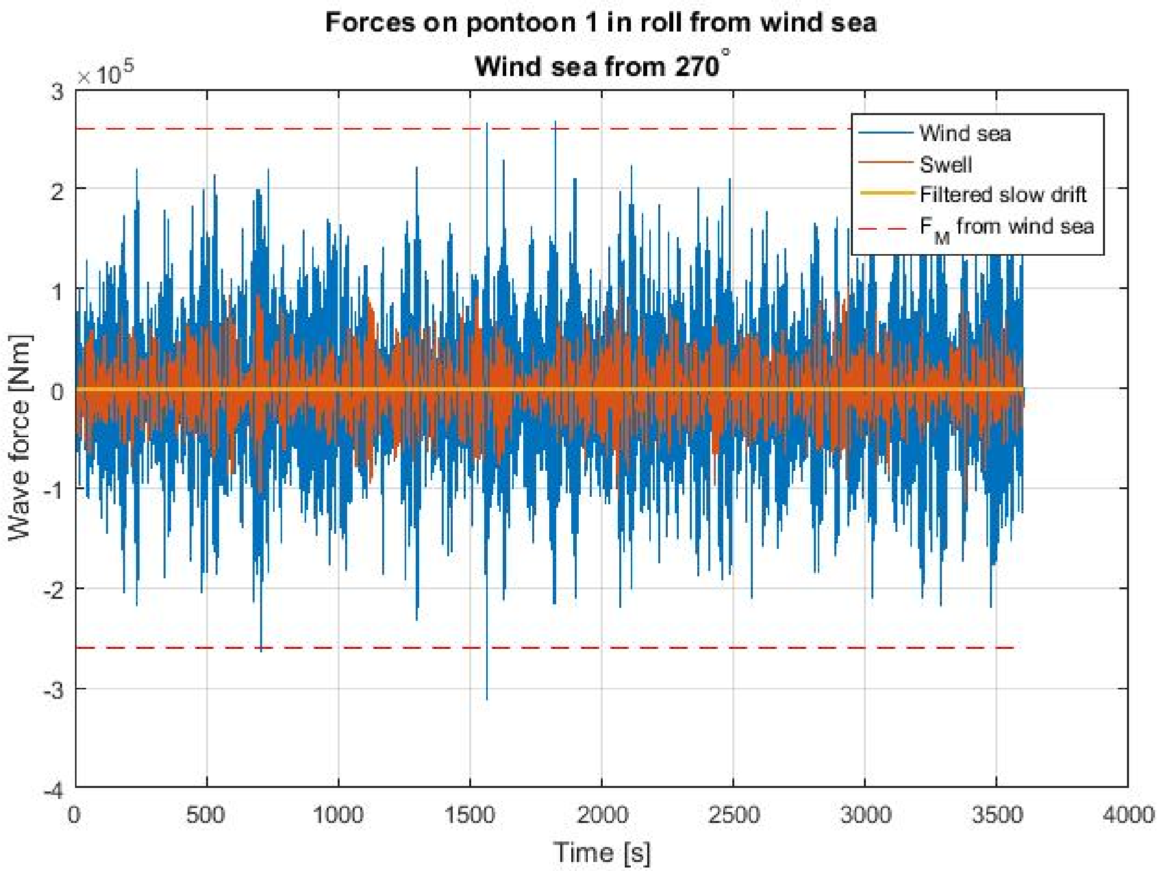

Figure E.4: Example of wave force in 100-year sea state with wind sea from 270° and swell from 330°. Direction of incoming waves defined in figure 7.1. Force history in local roll for pontoon 1. Characteristic 1-hour wave load from wind sea indicated by dashed line.

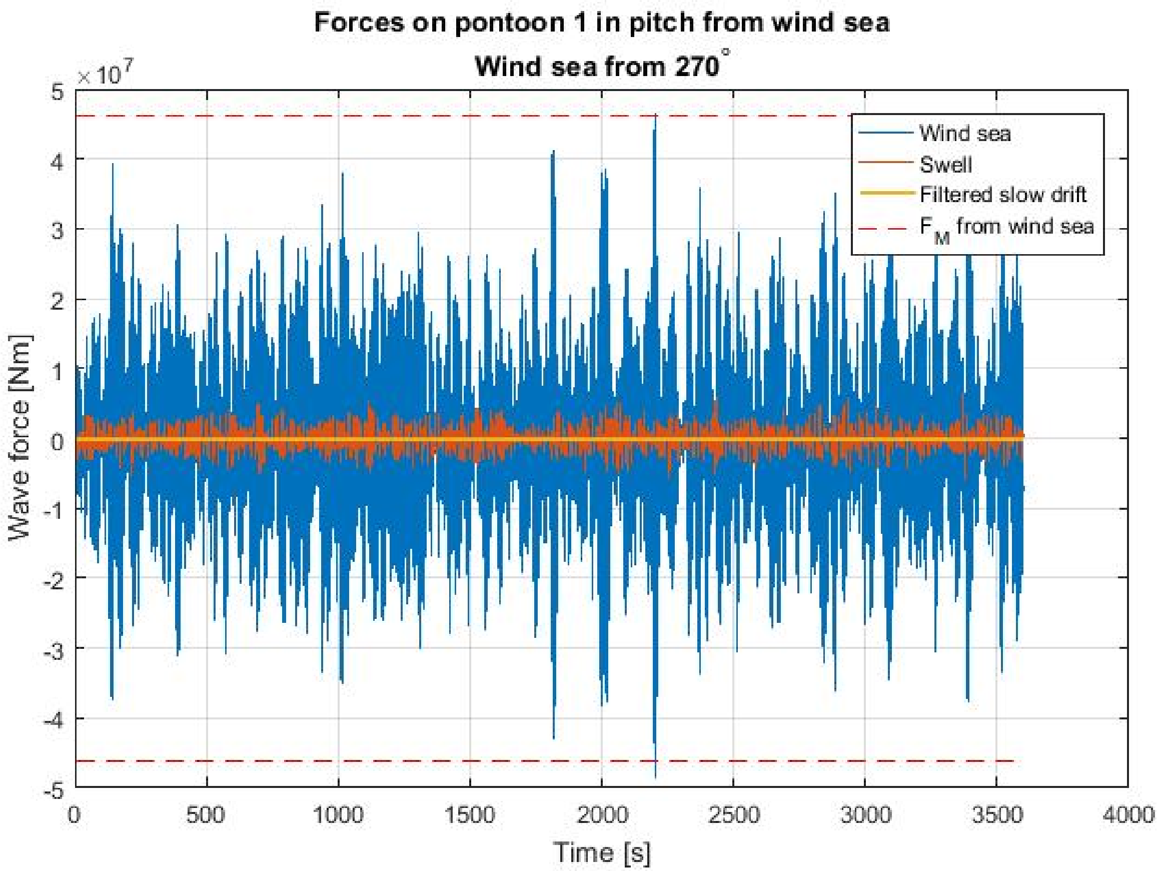

Figure E.5: Example of wave force in 100-year sea state with wind sea from 270° and swell from 330°. Direction of incoming waves defined in figure 7.1. Force history in local pitch for pontoon 1. Characteristic 1-hour wave load from wind sea indicated by dashed line.

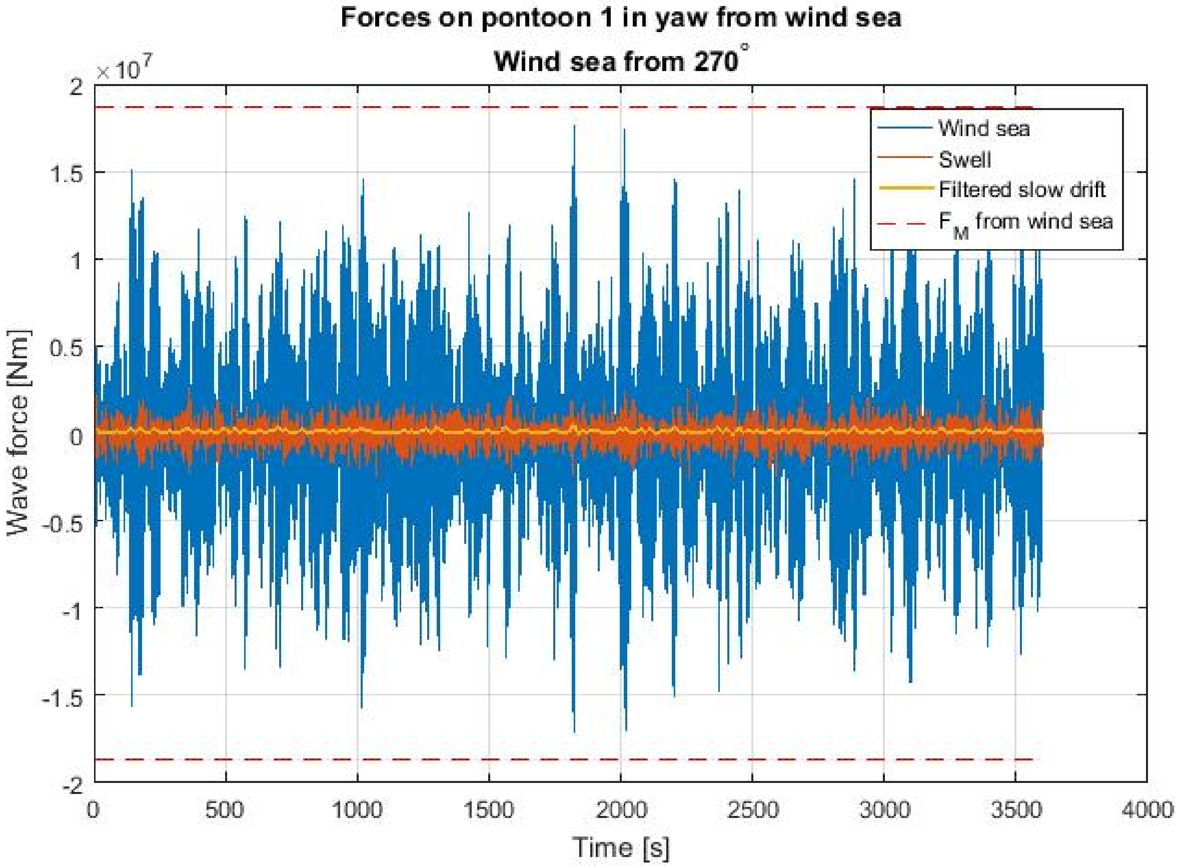

Figure E.6: Example of wave force in 100-year sea state with wind sea from 270° and swell from 330°. Direction of incoming waves defined in figure 7.1. Force history in local yaw for pontoon 1. Characteristic 1-hour wave load from wind sea indicated by dashed line.